Monazite solid solutions - Characterisation of structural, thermal and physical properties

Von der Fakultät für Georessourcen und Materialtechnik
der Rheinisch-Westfälischen Technischen Hochschule Aachen

zur Erlangung des akademischen Grades eines

Doktors der Naturwissenschaften

genehmigte Dissertation

vorgelegt von **M.Sc. Angewandte Geowissenschaften**

Antje Hirsch

aus Neubrandenburg

Berichter: Univ.-Prof. Dr. rer. nat. Georg Roth
Univ.-Prof. Dr. Björn Winkler

Tag der mündlichen Prüfung: 06. April 2018

Diese Dissertation ist auf den Internetseiten der Universitätsbibliothek online verfügbar.

Abstract

The aim of this extensive characterisation at ambient and non-ambient conditions was to obtain insight into the structural, chemical and physical behaviour of monazite and to complement the knowledge of monazite solid solutions. Monazite (LnPO$_4$) has been proposed as a promising host matrix for the long-term storage of long-lived radionuclides. Six monazite solid solutions (La$_{1-x}$Pr$_x$PO$_4$, Pr$_{1-x}$Nd$_x$PO$_4$, Pr$_{1-x}$Sm$_x$PO$_4$, Nd$_{1-x}$Eu$_x$PO$_4$, Nd$_{1-x}$Sm$_x$PO$_4$, and Sm$_{1-x}$Gd$_x$PO$_4$) were synthesised as powder samples, single crystals and ceramics. To model trivalent actinides in the monazite structure, lanthanides (Ln) were used as surrogates.

Powder samples were prepared using a solid state reaction with an excess of $NH_4H_2PO_4$. Single crystals were grown from these powders using the high-temperature solution (flux) method. Crystals were obtained by evaporation of the Li_2MoO_4 flux material and/or temperature reduction. Ceramics were produced after cold isostatic pressing by a two-step sintering procedure.

Structural investigations using X-ray diffraction showed a linear increase of the lattice parameters $\vec{a}$, $\vec{b}$, and $\vec{c}$, the unit cell volume, and the Ln-O bond lengths with increasing Ln radius, while the monoclinic angle β decreased. The PO$_4$ tetrahedron was found to be a 'rigid body' because of constant P-O bond lengths and O-P-O angles. This 'rigidity' led to geometric constraints within the chain structure of monazite yielding an increasing distortion of the LnO$_9$ polyhedron with increasing Ln radii. The wave numbers of the P-O modes, observed by Raman spectroscopy, decreased with increasing Ln radius which was attributed to the increase in the Ln-O bond lengths.

Single crystals were found to be inclusion-free and showed no sign of zoning in electron micro-probe analyses. At high pressure, the coordination of the Ln changed from nine to twelve oxygens which was accompanied by an increase of the Ln-O bond lengths and a rapid decrease in the unit cell volume. The structure type found using high-pressure single-crystal diffraction is the post-barite type in space group $P2_12_12_1$.

Ceramics were homogeneous and highly dense (up to 95 % of the theoretical densities). The thermal expansion coefficients measured on the powders showed an increase with increasing Ln radii. Thermal expansion coefficients of the ceramics obtained from dilatometry were strongly influenced by the microstructure of the samples. The elastic moduli obtained from ultrasound spectroscopy on the ceramics decreased with increasing Ln radius. Both, the thermal expansion coefficients and the elastic moduli depended on the density of the ceramics and, hence, on the degree of sintering.

The enthalpy of solution, measured with high-temperature drop solution calorimetry, and the deduced standard enthalpies of formation increased with increasing Ln radius. The

molar heat capacity, the standard molar entropy and the molar entropy change decreased with increasing *Ln* radius as seen in low-temperature microcalorimetry. An increasing Schottky contribution to the molar heat with increasing Pr content was attributed to the excitation of *f*-orbital electrons of the Pr^{3+} ion.
These extensive investigations show that monazite can form thermodynamically stable, ideal solid solutions from La to Gd without a miscibility gap. This is essential when considering monazite as a potential ceramic matrix material for nuclear waste.

Kurzfassung

Das Ziel dieser detailierten Charakterisierung bei Umgebungs- und Nicht-Umgebungsbedingungen war, Einsicht in das strukturelle, chemische und physikalische Verhalten von Monaziten zu erhalten und das Wissen über Monazitmischkristallsysteme zu ergänzen. Monazit ($Ln\mathrm{PO_4}$) wurde als vielversprechende Gastmatrix für die Langzeitspeicherung von langlebigen Radionukliden vorgeschlagen.
Sechs Monazitmischkristallsysteme ($\mathrm{La_{1-x}Pr_xPO_4}$, $\mathrm{Pr_{1-x}Nd_xPO_4}$, $\mathrm{Pr_{1-x}Sm_xPO_4}$, $\mathrm{Nd_{1-x}Eu_xPO_4}$, $\mathrm{Nd_{1-x}Sm_xPO_4}$ und $\mathrm{Sm_{1-x}Gd_xPO_4}$) wurden als Pulver, Einkristalle und Keramiken hergestellt. Um dreiwertige Actinoide in der Monazitstruktur zu simulieren, wurden Lanthanoide (Ln) als Stellvertreter verwendet.
Pulverproben wurden über eine Festphasenreaktion mit einem Überschuss an $\mathrm{NH_4H_2PO_4}$ synthetisiert. Aus diesen Pulvern wurden Einkristalle über die Hochtemperaturlösungs-(Flux-)methode gezüchtet. Kristalle wurden durch Verdampfung des Flussmittels $\mathrm{Li_2MoO_4}$ und/oder Temperaturerniedrigung gewonnen. Keramiken wurden nach kaltisostatischem Pressen durch ein zweistufiges Sinterverfahren dargestellt.
Untersuchungen der Monazitstruktur mittels Röntgenbeugung zeigten eine lineare Zunahme der Gitterparameter $\vec{a}$, $\vec{b}$ und $\vec{c}$, des Elementarzellvolumens und der Ln–O-Bindungslängen mit steigendem Ln-Radius, während der monokline Winkel β kleiner wurde. Da die P–O-Bindunslängen und O–P–O-Winkel konstant blieben, konnte das $\mathrm{PO_4}$-Tetraeder als 'starrer Körper' beschrieben werden. Diese 'Starrheit' führte zu geometrischen Zwängen innerhalb der Kettenstruktur von Monazit, sodass bei zunehmendem Ln-Radius eine zunehmende Verzerrung des $Ln\mathrm{O_9}$-Polyeders erfolgte. Die Wellenzahlen der P–O-Schwingungen, die mittels Ramanspektroskopie untersucht wurden, nahmen mit steigendem Ln-Radius ab, was in der Zunahme der Ln–O-Bindungslängen begründet ist.
Einkristalle konnten ohne Einschlüsse hergestellt werden und zeigten kein Zeichen von Zonierungen in Mikrosondenuntersuchungen. Bei hohem Druck änderte sich die Koordination des Ln von neun zu zwölf Sauerstoffen, welches mit einem Anstieg der Ln–O-Bindungslängen und einer schnellen Abnahme des Elementarzellvolumens einher ging. Der Strukturtyp konnte mittels Einkristallröntgenbeugung unter Hochdruck als Post-Baryt-Typ in der Raumgruppe $P2_12_12_1$ bestimmt werden.
Keramiken waren homogen und hochdicht (mit bis zu 95 % der theoretischen Dichten). Die thermischen Ausdehnungskoeffizienten von Pulvern zeigten eine Zunahme mit steigendem Ln-Radius. Dilatometrisch bestimmte thermische Ausdehnungskoeffizienten der Keramiken waren stark vom Gefüge der Proben abhängig. Die Elastizitätsmoduln, die über Ultraschallspektroskopie an Keramiken bestimmt wurden, nahmen mit

steigendem *Ln*-Radius ab. Sowohl die thermischen Ausdehnungskoeffizienten als auch die Elastizitätsmoduln hingen von der Dichte der Keramiken und, folglich, vom Sintergrad ab.
Die Lösungsenthalpie, gemessen mittels Hochtemperaturlösungskalorimetrie, sowie die daraus abgeleiteten Standardbildungsenthalpien stiegen mit steigendem *Ln*-Radius. Die molare Wärmekapazität, die molare Standardentropie und die molare Entropieänderung nahmen ab mit steigendem *Ln*-Radius, wie durch Tieftemperaturmikrokalorimetrie bestimmt werden konnte. Ein zunehmender Schottky-Beitrag zur molaren Wärme mit steigendem Pr-Gehalt konnte der Anregung von *f*-Orbitalelektronen des Pr^{3+}-Ions zugeordnet werden.
Diese umfangreichen Untersuchungen zeigen, dass Monazit thermodynamisch stabile, ideale Mischkristallreihen von La bis Gd ohne Mischungslücke bilden kann. Dies ist wesentlich bei der Bewertung der Eignung von Monazit als mögliches keramisches Matrixmaterial für nuklearen Abfall.

Acknowledgement

First of all, I would like to thank my thesis adviser, Prof. Georg Roth, for the opportunity to do this work and for always having an open ear for my questions. For all his support, discussions and expertise I am very grateful. I would also like to thank Prof. Björn Winkler for his help and the great discussions in Frankfurt and for taking on the task of second reviewer.
I am very thankful to my supervisor Lars Peters for his effective guidance during the research, the analyses, and the paper publication progresses. The whole time until the very last minute, he was supporting me with explanations, discussions and 'disentanglement' of my thoughts. Thanks also for the proofreading and the encouraging comments to improve my work and me.
From the Institute of Crystallography in Aachen, I would like to thank the whole team for the never-ending support and the pleasant coffee breaks. Thank you, Angelika von Berg, Ellen Nowack, Rolf Becker, Heiko Mahnke and Joseph Ernst, for the smooth organisation in the institute whether in the chemical or furnace laboratories or the hard- and software; Andreas Neumann for the talks about monazite and for sharing your ideas; Andrzej Grzechnik for your introduction into *Jana* and the help during my single-crystal evaluation; Bernd Liebeck and Vera Vasylyeva for your encouragement and the help with the *IPDS II*; and Sophie-Charlotte Lappe for your proofreading and your time to discuss my English and, again, for the help with my presentation to win a poster award.
I want to thank the crystallography team in Frankfurt for the nice stays with lots of work and still lots of fun. Thanks to Eiken Haussühl for the dilatometry support and the help with the evaluation, and Alexandra Friedrich for the introduction and the time at the OAS; Johannes Bauer for the PPMS measurements and the explanations around it; Thomas Bernert for giving up your time at DESY and for your bad jokes; Nadine Schrodt for the wonderful time at the SEM and your encouragement. My dearest appreciations go to Javier Ruiz-Fuertes, Igor Alencar Vellame and Anja Thust for all the shared time in the laboratories, on the conferences and on our holidays, for the proofreading and the detailed feedback, for your explanations and your support during the whole time.
Special thanks to my colleagues at the Institute of Energy and Climate Research (IEK6) at the Forschunszentrum Jülich, the Mineral Engineering Institute at the RWTH Aachen University, the Institute of Geosciences of the Christian-Albrechts-Universität zu Kiel, the Department of Earth Sciences at the ETH Zürich, and the Peter A. Rock Thermochemistry Laboratory and NEAT OUR, University of California at Davis: Especially, I would like to thank Philip Kegler for taking my samples to the USA, for the ananlyses and the time to help me understand. Thanks for your ability to kicking my ass and cheering me

up at the same time. Further thanks go to Christian Schreinemachers, Anna Shelyug, Sergey Ushakov and Alexandra Navrotsky for the calorimetric measurements and the help during the publication of the results. I want to thank Hilde Curtius and Zaina Paparigas for the IR measurements, Petra Schott and Lise Loison for the High-Temperature XRD measurements, and Peter Appel and Barbara Mader for the nice time in Kiel at the EPMA. Special thanks to Nico Küter for his preparation of my EPMA samples and that you can be bribed with liquorice. Charlotte Schausten helped a lot with her explanations about sintering and I would like to thank her for the encouraging phone calls and the nice time at the conferences. Big thanks go to Stefan Neumeier for the coordination of the BMBF project and the evenings at the conferences where we exchanged so many ideas. I am very grateful to Julia Heuser for her constant support, discussions and proofreading. Thanks for your motivation, the tasty food and ideas.
Also, I do not want to miss to thank all the student assistants as well as the bachelor and master students: Annika Schumacher, Noel Ladenthin, Jörg Schoel, Zafer Kuleci and David Bigdeli for preparing and examining your own solid solutions and that I was allowed to use your samples and your data; Larissa Butz for the wonderful time at the office, for shared food and a lot of laughter; Christa Claßen for the best written lab book and your endurance in the preparations; Laura Ritterbach for the time in the lab and your strange sweaters; Marcus Große for not being 'my' student assistant but still cheering me up in the office and Jonas Werner for all the tips in Inkscape and for a lot of interesting talks. Enormous thanks go to my friends (Maike, Mü, Lisa, Agnes, Christina, Sarah, Steffen and those mentioned before) for your distraction at the game nights, for short and long holidays, and for being there for me. Thanks to Conny for your calm and gentle support, the hugs and the motivation within every word.
I am very grateful to have a loving and supportive family. Thanks to Anke for all the wonderful childhood memories and that you are as annoying as I am. Mama und Papa, ich danke euch dafür, dass ihr euch über all die Jahre immer gefreut habt, wenn ich euch auch immer nur kleine Sachen erzählt habe. Ich danke euch für die fortwährende Unterstützung und dass ihr mich zu dem gemacht habt, was ich heute bin. Danke auch an Oma, wo auch immer du bist, dass du immer stolz auf mich warst und mich doch noch ein bisschen zur Lehrerin gemacht hast...
My biggest thanks go to my loving and caring wife, Katja, who is always there for me and is a constant source of happiness and motivation. Thanks for all the support and the help over all these years and thanks for putting up with me even when I sing too much.

To all of you: thank you very much!

This work was made possible by the financial support from the Bundesministerium für Bildung und Forschung (BMBF) (*02NUK021E*).

Contents

Abstract i

Kurzfassung iii

Acknowledgement v

List of Abbreviations xi

List of Figures xiii

List of Tables xvii

1 Introduction 1
- 1.1 Nuclear waste . . . 1
- 1.2 Aim of this work . . . 9
- 1.3 Monazite and Xenotime . . . 10
  - 1.3.1 Monazite . . . 12
  - 1.3.2 Xenotime . . . 14

2 Material and Methods 17
- 2.1 Synthesis . . . 17
  - 2.1.1 Possible synthesis routes for LnPO$_4$ powder . . . 17
  - 2.1.2 Solid state synthesis of monazite powders . . . 18
  - 2.1.3 Synthesis of monazite single crystals . . . 19
  - 2.1.4 Synthesis of monazite ceramics . . . 21
- 2.2 Characterisation methods . . . 21
  - 2.2.1 Chemical analysis . . . 21
    - 2.2.1.1 Electron probe micro analysis . . . 21
    - 2.2.1.2 Scanning electron microscopy . . . 22
  - 2.2.2 Thermal analysis . . . 23
  - 2.2.3 X-ray diffraction . . . 23
    - 2.2.3.1 Powder X-ray diffraction at ambient conditions . . . 23
    - 2.2.3.2 Synchrotron powder X-ray diffraction . . . 24
    - 2.2.3.3 High-temperature powder X-ray diffraction . . . 24
    - 2.2.3.4 Evaluation of the powder diffraction data . . . 25
    - 2.2.3.5 Single-crystal X-ray diffraction at ambient conditions . . . 25

2.2.3.6 High-pressure single-crystal X-ray diffraction 26
2.2.3.7 Evaluation of the single crystal diffraction data 26
2.2.4 Spectroscopy 27
2.2.4.1 Infrared spectroscopy 27
2.2.4.2 Raman spectroscopy 27
2.2.4.3 Ultrasound spectroscopy 27
2.2.4.4 Fluorescence spectroscopy 28
2.2.4.5 Optical absorption spectroscopy 28
2.2.5 Determination of the density 29
2.2.6 Dilatometry 29
2.2.7 High-temperature drop solution calorimetry 30
2.2.8 Low-temperature microcalorimetry 31
2.2.9 Second-harmonic generation 31

3 Results and Discussion **33**
3.1 Room temperature characterisation of powders 33
3.1.1 Chemical analyses 33
3.1.2 Thermal characterisation of the powder samples 37
3.1.3 Structural investigations 38
3.1.4 Spectroscopy 45
3.1.5 Summary on room temperature characterisation of powders 53
3.2 Monazite single crystals 54
3.2.1 Optimisation of the flux growth procedure 54
3.2.2 Chemical characterisation 57
3.2.3 Structural investigations 59
3.2.4 Optical absorption spectroscopy 66
3.2.5 Summary on room temperature characterisation of single crystals . 67
3.3 Structural characterisation at non-ambient conditions 68
3.3.1 High-pressure behaviour of $LaPO_4$ 68
3.3.2 Monazite ceramics 74
3.3.2.1 Sintering and Microstructure 74
3.3.2.2 Thermal expansion from HT-XRD 77
3.3.2.3 Thermal expansion from dilatometry 80
3.3.2.4 Mechanical properties 81
3.3.3 Summary on non-ambient characterisation of monazite 85
3.4 Thermodynamic properties of monazite 86
3.4.1 HT solution calorimetry 86
3.4.2 Microcalorimetry and fluorescence spectroscopy 90
3.4.2.1 Heat capacity 90
3.4.2.2 Schottky contribution 93
3.4.2.3 Energy level scheme of Pr^{3+} 94
3.4.3 Summary on thermodynamic properties of monazite 98

4 Summary and Conclusion **99**

5 Outlook **103**

6 Appendix **105**

Bibliography **145**

List of Abbreviations

The following abbreviations are used within the text and the captions of tables and figures (see List of Tables and List of Figures).

α, α_m, α_V	general, average (mean) and volumetric coefficient of thermal expansion
a_i: $\vec{a}, \vec{b}, \vec{c}, \beta$	lattice parameters of monazite
AD	angular distortion
BLD	bond length distortion
BSE	back-scattered electrons
$C^0_{p,m}$	standard molar heat capacity at constant pressure
c_{ij}: c_{11}, c_{44}	elastic stiffness coefficients: longitudinal and shear acoustic velocity
C_{ex}	excess molar heat capacity at constant pressure
C_p	heat capacity at constant pressure
$C_{p,m}$	molar heat capacity
$\Delta H_{289.15\,\mathrm{K}}$	standard enthalpy change
ΔH_{ds}	enthalpy of solution
ΔH^0_f: $\Delta H^0_{\mathrm{f,el}}$, $\Delta H^0_{\mathrm{f,ox}}$	standard enthalpy of formation: from the elements and from the oxides
ΔH_{mix}	standard enthalpy of mixing
ΔT	temperature change
DSC	differential scanning calorimetry
η	Poisson's ratio
E	Young's modulus
EPMA	electron probe micro analysis
FWHM	full width at half maximum
G	shear modulus
GoF	quality criterion for Rietveld analyses: Goodness of fit
H_V	Vickers micro hardness
HLW	high-level waste
HP	high pressure
HT	high temperature
HTSM	high-temperature solution method
ILW	intermediate-level waste
IR	infra-red

K	bulk modulus
LaPr	$La_{1-x}Pr_xPO_4$
LLW	low-level waste
Ln	Lanthanide
LT	low temperature
ν_1	symmetric stretching mode of PO_4
ν_2	symmetric bending mode of PO_4
ν_3	asymmetric stretching mode of PO_4
ν_4	asymmetric bending mode of PO_4
n_{obs}, n_{un}	number of observed and unique reflections
n_{prm}	number of parameters
NdEu	$Nd_{1-x}Eu_xPO_4$
NdSm	$Nd_{1-x}Sm_xPO_4$
OAS	optical absorption spectroscopy
OFZM	optical floating zone method
ϕ	percentage pore volume
PAV	polyhedral angle variance
PrNd	$Pr_{1-x}Nd_xPO_4$
PrSm	$Pr_{1-x}Sm_xPO_4$
ρ: ρ_m, ρ_e	density: measured and expected
$R_{int}, R^1, \omega R^2$	quality criteria for Rietveld analyses: internal, unweighted and weighted residual R-value
R_{wp}	quality criterion for powder Rietveld analyses: weighted R-value for the whole pattern
REE	rare earth element
RT	room temperature
$S^0_{298.15\,\mathrm{K}}$	standard molar entropy
SEM	scanning electron microscopy
SNF	spent nuclear fuel
SHG	second-harmonic generation
SmGd	$Sm_{1-x}Gd_xPO_4$
SynRoc	synthetic rock
TAV	tetrahedral angle variance
TGA	thermogravimetric analysis
V_{uc}	volume of the unit cell
x_{Ln}	Ln content
x, y, z	fractional coordinates for atoms
XRD	X-ray diffraction

List of Figures

1 Introduction

1.1 Elements in SNF after moderate burn-up . . . 3
1.2 Element categories in SNF after moderate burn-up . . . 4
1.3 Decay scheme of ^{238}U . . . 5
1.4 Element groups that influence the radioactivity of SNF. . . . 5
1.5 Stability fields of monazite and xenotime . . . 9
1.6 Phase diagram of La_2O_3 and P_2O_5 . . . 11
1.7 Monazite structure and AO_9-PO_4^{3-} chain . . . 13
1.8 Xenotime structure and AO_8-PO_4^{3-} chain . . . 15

3 Results and Discussion

3.1 BSE image of monazite powder samples . . . 34
3.2 BSE images of impurities in monazite powders . . . 36
3.3 Thermogravimetric analyses of LaPr . . . 37
3.4 Monazite structure along $\vec{b}$ . . . 39
3.5 Lattice parameters of various solid solutions . . . 40
3.6 Unit cell volume of various solid solutions . . . 40
3.7 Volume and excess volume of LaPr . . . 42
3.8 *Ln*-O bond lengths in LaPr . . . 43
3.9 P-O bond lengths for LaPr . . . 43
3.10 Coulomb repulsion in the LnO_9-PO_4 chain . . . 44
3.11 IR spectra of LaPr . . . 46
3.12 IR mode in LaPr . . . 46
3.13 Raman spectrum of $PrPO_4$ . . . 47
3.14 Raman spectra showing the influence of fluorescence . . . 48
3.15 Raman modes in LaPr, PrSm and NdSm . . . 50
3.16 Raman modes in comparison to literature values . . . 51
3.17 FWHM of Raman modes in LaPr, PrSm and NdSm . . . 52
3.18 Evaporated flux material . . . 55
3.19 Monazite single crystals . . . 56
3.20 Crystals of LaPr . . . 56
3.21 BSE images of a $La_{0.6}Pr_{0.4}PO_4$ and a $La_{0.4}Pr_{0.6}PO_4$ single crystal . . . 57
3.22 La and Pr content along cross-sections of a $La_{0.6}Pr_{0.4}PO_4$ single crystal . . . 58

3.23 La and Pr content along cross-sections of a $La_{0.4}Pr_{0.6}PO_4$ single crystal . . 58
3.24 Change of atomic positions of *Ln* and O^3 60
3.25 Average *Ln*-O bond lengths from single-crystals diffraction of three solid solutions 61
3.26 Individual *Ln*-O bond lengths from single-crystals diffraction of three solid solutions 61
3.27 O-P-O angles and Coulomb repulsion 62
3.28 BLD of *Ln*-O and P-O bonds 63
3.29 TAV and AD 64
3.30 PAV for LnO_9 65
3.31 Optical absorption spectra of LaPr 66
3.32 Evolution of the $(5k\bar{2})$ reflection family of $LaPO_4$ with pressures 69
3.33 SHG signal of $LaPO_4$ vs. pressure 70
3.34 Reciprocal lattice of LP and HP phase of $LaPO_4$ 71
3.35 Projections of the monazite and post-barite structure 71
3.36 Pressure dependence of $\vec{a}$, $\vec{b}$, $\vec{c}$ and β in $LaPO_4$ 73
3.37 Pressure dependence of V_{uc} and the mean La-O bond length 73
3.38 SEM micrographs and grain size distributions of LaPr 75
3.39 Average grain size of LaPr ceramics 76
3.40 Contour plot of the HT-diffraction data for $LaPO_4$ 77
3.41 HT behaviour for $La_{0.5}Pr_{0.5}PO_4$ 79
3.42 α of the lattice parameters of LaPr 79
3.43 α of the powder samples and final ceramics 81
3.44 K, E, G, and η of LaPr and LaEu 82
3.45 H_V and K/G of LaPr and LaEu 84
3.46 $\Delta H_{\mathrm{ds,973\,K}}$ and ΔH_{mix} of LaPr 89
3.47 Molar heat capacity of $LaPO_4$ and $PrPO_4$ 91
3.48 Molar heat capacity of LaPr up to 30 K 91
3.49 Molar heat capacity at 298.15 K of LaPr 92
3.50 $S^0_{298.15\,\mathrm{K}}$ and $\Delta H_{298.15\,\mathrm{K}}$ of LaPr 93
3.51 C_{ex} of LaPr 94
3.52 Fluorescence spectra of a $La_{0.8}Pr_{0.2}PO_4$ single crystal 95
3.53 Energy level schemes for $^3H_4$ ground state of the Pr^{3+} ion 96
3.54 Schottky contribution of $PrPO_4$ 96

6 Appendix

A.1 Vibrational modes of PO_4 112
A.2 La and Pr content in a $La_{0.8}Pr_{0.2}PO_4$ single crystal (1) 122
A.3 La and Pr content in a $La_{0.8}Pr_{0.2}PO_4$ single crystal (2) 122
A.4 La and Pr content in a $La_{0.8}Pr_{0.2}PO_4$ single crystal (3) 123
A.5 La and Pr content in a $La_{0.6}Pr_{0.4}PO_4$ single crystal (1) 124
A.6 La and Pr content in a $La_{0.6}Pr_{0.4}PO_4$ single crystal (2) 124
A.7 La and Pr content in a $La_{0.6}Pr_{0.4}PO_4$ single crystal (3) 125
A.8 La and Pr content in a $La_{0.4}Pr_{0.6}PO_4$ single crystal (1) 126

A.9 La and Pr content in a $La_{0.4}Pr_{0.6}PO_4$ single crystal (2) 126
A.10 La and Pr content in a $La_{0.4}Pr_{0.6}PO_4$ single crystal (3) 127
A.11 La and Pr content in a $La_{0.2}Pr_{0.8}PO_4$ single crystal (1) 128
A.12 La and Pr content in a $La_{0.2}Pr_{0.8}PO_4$ single crystal (2) 128
A.13 La and Pr content in a $La_{0.2}Pr_{0.8}PO_4$ single crystal (3) 129
A.14 Chemical analyses (mapping) by EPMA on a $La_{0.6}Pr_{0.4}PO_4$ crystal 130
A.15 Chemical analyses (mapping) by EPMA on $La_{0.4}Pr_{0.6}PO_4$ crystal 131
A.16 Wave length of peak positions from OAS (part 1) 140
A.17 Wave length of peak positions from OAS (part 2) 140
A.18 Ultrasound resonance spectra of $LaPO_4$ 143

List of Tables

1 Introduction
1.1 Classification of nuclear waste 2
1.2 Host matrices in nuclear waste management 8

2 Material and Methods
2.1 Monazite solid solutions 18
2.2 Diffractometers and measuring parameters 24

3 Results and Discussion
3.1 Results of EPMA analyses (part 1) 35
3.2 Results of EPMA analyses (part 2) 35
3.3 Structure refinements on $LaPO_4$ 38
3.4 Legend for figures 3.5 and 3.6 41
3.5 Zonal and serial reflection conditions of $LaPO_4$ HP phase 69
3.6 Percentage change in the lattice parameters between 298 K and 1373 K . . 78
3.7 Legend for figures 3.44 and 3.45 83
3.8 Thermochemical cycle of LaPr 87
3.9 HT solution calorimetry results for LaPr 88
3.10 Energy levels of the $^3H_4$ ground state of the Pr^{3+} ion 97

6 Appendix
A.1 Reactants for powder systems 105
A.2 Flux material 105
A.3 Results of all EPMA analyses 106
A.4 Lattice parameters of LaPr from powder XRD 107
A.5 Lattice parameters of PrSm from powder XRD 107
A.6 Lattice parameters of PrNd from powder XRD 108
A.7 Lattice parameters of NdSm from powder XRD 108
A.8 Lattice parameters of NdEu from powder XRD 109
A.9 Lattice parameters of SmGd from powder XRD 109
A.10 *Ln*-O bond lengths for LaPr 110
A.11 P-O bond lengths for LaPr 111

A.12 Wave numbers of LaPr from IR spectroscopy . . . 113
A.13 Wave numbers of LaPr, PrSm, and NdSm from Raman spectrocopy . . . 114
A.14 Explanation of Mulliken representations . . . 115
A.15 Wave numbers of LaPr from Raman spectroscopy . . . 115
A.16 Wave numbers of PrSm from Raman spectroscopy . . . 116
A.17 Wave numbers of NdSm from Raman spectroscopy . . . 116
A.18 FWHM of Raman modes in LaPr . . . 117
A.19 FWHM of Raman modes in PrSm . . . 117
A.20 FWHM of Raman modes in NdSm . . . 118
A.21 Flux growth conditions (part 1) . . . 119
A.22 Flux growth conditions (part 2) . . . 120
A.23 Results from single-crystal XRD on LaPr . . . 132
A.24 Results from single-crystal XRD on NdSm . . . 133
A.25 Results from single-crystal XRD on NdEu . . . 134
A.26 *Ln*-O bond lengths in single crystals . . . 135
A.27 P-O bond lengths in single crystals . . . 136
A.28 O-P-O angles in single crystals . . . 137
A.29 BLD, TAV and AD for single crystals . . . 138
A.30 PAV for single crystals . . . 139
A.31 Asymmetric unit of monazite and post-barite structure . . . 141
A.32 ρ and c_{ij} of LaPr for pre-ceramics and final ceramics . . . 142
A.33 α of the lattice parameters of LaPr as a function of the Pr content . . . 142

Chapter 1: Introduction

1.1 Nuclear waste

Radioactive waste management is a current, pressing topic of research since this waste is one of the most hazardous waste types to deal with in our times. Its sources are widespread and not only range from nuclear power plants to defence material, but also include nuclear material used in hospitals and universities. It also comprises radioactive waste from commercial research activities, industrial use of isotopes and mining, as well as refining of uranium ore (Wicks and Bickford, 1989; Roy, 1982; Donald *et al.*, 1997).

Radioactive waste can be classified according to its type of radiation and its radiotoxicity which influences the handling procedure. In general, four types of ionising radiation can be distinguished that have to be considered when studying radioactive waste: α-, β-, γ-, and neutron radiation. Hedin (1997) summarised these radiations and their impact on humans. The disintegration of an element is called radioactivity and is measured in Becquerel (Bq) [1]. Depending on the type, each radiation may be harmful for humans, animals and plants. To measure this harmfulness of some radionuclides, the term radiotoxicity is used. In addition to the type of radiation and its energy, radiotoxicity includes the reception, resorption and retention behaviour within an organism (Gompper *et al.*, 2010). For radiotoxicity, a radiation source can be classified as external or internal depending on whether the radiation is emitted outside or inside the body. Both may damage or even kill cells or an entire organism. For humans being exposed to radiation, mostly the nervous system, the gastrointestinal tract or the bone marrow are affected. Low radiation doses yield cancer while higher doses may even cause death, with a lethal dose of 5000 mSv (Sv: Sievert) [2]. So far, such doses only occurred after the detonations of atomic bombs during the Second World War and in the Chernobyl accident (Hedin, 1997). The Fukushima nuclear disaster yielded far lower doses.
The most concerning portion of radioactive waste in terms of radioactivity stems from the commercial use of nuclear energy. In 2015, 441 nuclear power plants worldwide delivered 382.9 GW of electrical energy (International Atomic Energy Agency (IAEA), 2016). In Germany in 2016, 8 power plants were in regular operation and 9 in continuous non-power operation. They delivered a gross output of 13.1 % and a basic load of 33.7 % of the power generation in Germany (Deutsches Atomforum e. V. (DAtF), 2016). The

[1] 1 Bq is the activity of the number of nuclei in radioactive material that decay per second.

[2] 1 Sv is the equivalent biological effect of the deposition of 1 J of radiation energy in 1 kg of human tissue.

amount of burn-up (*i.e.* the fuel utilisation) is around 20 t per nuclear reactor and year and a sum of 10.500 t worldwide (Ewing, 2006; Gompper *et al.*, 2010). The generated nuclear waste must to be handled safely. Accordingly, nuclear waste management considers three categories of waste following the classification of the IAEA (see table 1.1). High-level nuclear waste (HLW) consists of spent nuclear fuel (SNF) and reprocesses or decommissioned nuclear weapons (also known as defence waste). Low-level waste (LLW) is generated in hospitals, laboratories and industries. Intermediate-level waste (ILW) comes from resins and chemical sludge. Both, LLW and ILW, are easier to handle, because they are much less radioactive (see table 1.1, Lumpkin, 2006; Oelkers and Montel, 2008). However, in Germany, radioactive waste is usually classified in terms of the generated heat: waste with a radioactivity level up to $10^{12}\,\mathrm{Bq/m^3}$ is called waste with negligible heat production, while waste with higher radioactivity is named heat-producing waste ("Arbeitskreis Abfallmanagement" des VGB (Vereinigung der Großkesselbesitzer) PowerTech e.V., 2011).

Table 1.1 Classification of nuclear waste according to the IAEA (International Atomic Energy Agency): LLW: low-level waste, ILW: intermediate-level waste, HLW: high-level waste. Volume and radioactivity fractions of the total radioactive waste according to Lumpkin (2006); Oelkers and Montel (2008) and typical activity according to the "Arbeitskreis Abfallmanagement" des VGB (Vereinigung der Großkesselbesitzer) PowerTech e.V. (2011).

Category	Typical activity [$\mathrm{Bq/m^3}$]	Volume fraction of the total radioactive waste	Radioactivity fraction of the total radioactive waste
LLW	$<10^{11}$	90 %	1 %
ILW	10^{10} to 10^{15}	7 %	4 %
HLW	$>10^{14}$	3 %	95 %

In Germany, 300.000 $\mathrm{m^3}$ of radioactive waste will be generated by 2040. 90 % of it will be LLW and ILW which can be directly disposed without high effort (Röhlig *et al.*, 2012). However, the challenge for nuclear waste management will be to deal with the approximately 29.000 $\mathrm{m^3}$ of heat-producing waste (ILW and HLW), which produces 99 % of the total radioactivity (Röhlig *et al.*, 2012). Mainly SNF and weapons-grade Pu are of high concern. During the operation of nuclear power plants and due to the radioactive series of decay processes of U and Pu, a wide range of elements and isotopes is generated. Three major categories of elements are generated during the fission of U. When ^{235}U or ^{239}Pu capture neutrons, their nucleus splits generating fission fragments and additional neutrons concomitant with energy release. The fission products range from Se to Gd. The second type of elements are generated by neutron capture and β-decay. The resulting elements are heavier than U and therefore called transuranium elements. They mainly include Np, Pu, Am, and Cm, also known as minor actinides. The third group are activation products like ^{14}C and ^{36}Cl from cladding material of the reactor as well as shielding material like ^{60}Co, ^{63}Ni or ^{210}Pb which may get radioactive due to neutron capture (Bruno and Ewing, 2006; Geckeis *et al.*, 2012). However, many

of these activation products are also generated during β-decay. Here, they are considered to be fission products. An overview of the different elements in spent nuclear fuel after moderate burn-up is given in figure 1.1. According to Kleykamp (1985), the elements can occur in different forms. Some elements like Sr, Zr, the lanthanides, and the transuranium elements form solid solutions with UO_2. Fission products can be found as dispersed bubbles (Xe or Kr gases), as metallic immiscible precipitates (*e.g.* Mo, Tc) or as oxide precipitates (*e.g.* Rb_2O, Cs_2O). However, 95 % of the SNF are still UO_2. A representation of the remaining elemental composition of the secondary products of SNF is given in figure 1.2.

H																	He
Li	Be											B	C	N	O	F	Ne
Na	Mg											Al	Si	P	S	Cl	Ar
K	Ca	Sc	Ti	V	Cr	Mn	Fe	Co	Ni	Cu	Zn	Ga	Ge	As	Se	Br	Kr
Rb	Sr	Y	Zr	Nb	Mo	Tc	Ru	Rh	Pd	Ag	Cd	In	Sn	Sb	Te	I	Xe
Cs	Ba	*	Hf	Ta	W	Re	Os	Ir	Pt	Au	Hg	Tl	Pb	Bi	Po	At	Rn
Fr	Ra	**	Rf	Db	Sb	Bh	Hs	Mt	Ds	Rg	Cn	Nn	Fl	Mc	Lv	Ts	Og

*	La	Ce	Pr	Nd	Pm	Sm	Eu	Gd	Tb	Dy	Ho	Er	Tm	Yb	Lu
**	Ac	Th	Pa	U	Np	Pu	Am	Cm	Bk	Cf	Es	Fm	Md	No	Lr

Figure 1.1 Elements in spent nuclear fuel (SNF) after moderate burn-up after Geckeis *et al.* (2012). Red: Uranium; green: Transuranium elements or minor actinides (in total 1.1 wt.%); yellow: fission products (in total 3.3 wt.%); blue: cladding material.

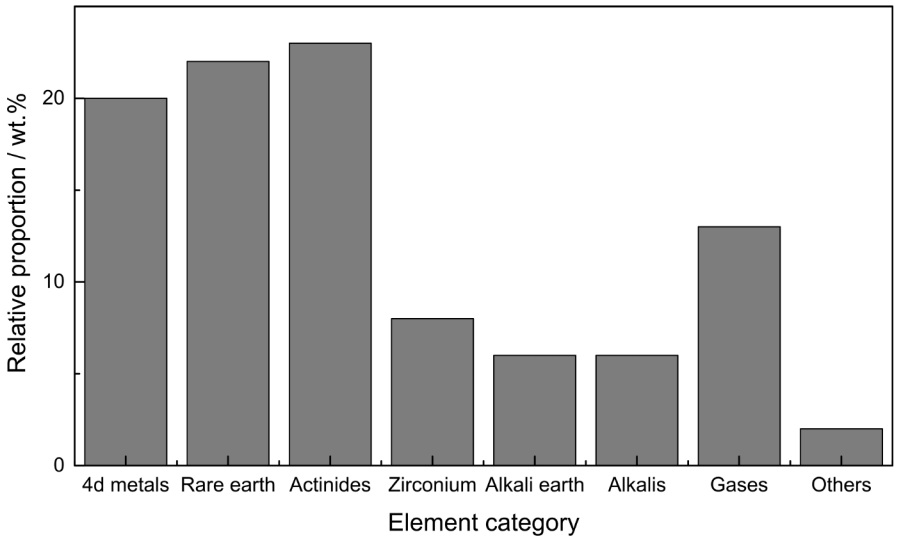

Figure 1.2 Element categories of secondary products in spent nuclear fuel (SNF) after moderate burn-up after Buck *et al.* (2004) and Oversby (1994). 95 % of the SNF are still UO_2. (Bruno and Ewing, 2006).

After SNF is removed from the reactor, the radioactivity is about 10^{17} Bq per ton fuel, after a moderate burn-up. Two aspects may change the element composition of SNF. Various elements arise along the decay chain of ^{238}U until the stable isotope ^{206}Pb is formed (fig. 1.3). The fission products constitute 3.3 wt.% of the SNF (Geckeis *et al.*, 2012). Many of these have short half-lives. In the first hundreds of years after disposal, the prominent elements are ^{129}I, ^{137}Cs and ^{90}Sr. The β- and γ-radiation associated with their decay contributes the most to both, the radioactivity and the heat after the burn-up (Bruno and Ewing, 2006; Oelkers and Montel, 2008). After 500 years for up to 100.000 years, ^{243}Am, ^{240}Pu, and ^{239}Pu are the main contributors to radioactivity, radiotoxicity and heat production. This is due to the accumulation of these elements during the U and Pu decay. After 100.000 years, Np and its daughter elements and fission products are the main newly generated elements and the main contributors to radioactivity in the SNF (Bruno and Ewing, 2006; Oelkers and Montel, 2008).
Within the first thousand years after removal from the reactor, radioactivity and radiotoxicity drop significantly (Ewing, 2006). The initial heat production of 1000 kW/t SNF ($\sim 10^{18}$ Bq/t) is reduced to 1 kW/t ($\sim 10^{15}$ Bq/t) after 10 years decreasing the specific activity to 1 ‰ of the initial activity value (Hedin, 1997; Röhlig *et al.*, 2012). This radioactivity decrease is shown in figure 1.4. Finding a host matrix for the long-lived radionuclides is the main goal in nuclear waste management. Elements of special interest are those with long half-life, high radiotoxicity and high mobility like U, Pu, the minor actinides and the long-lived fission products (Bruno and Ewing, 2006). The matrix should be chemically and physically stable without any transformation into amorphised phases (Lumpkin, 2006).

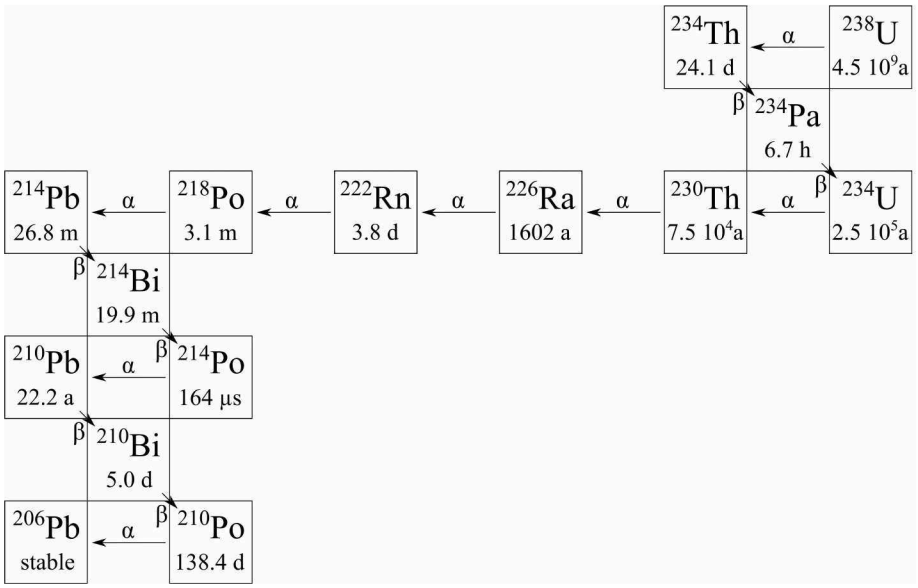

Figure 1.3 Decay scheme of ^{238}U after Hedin (1997) and Abdelouas (2006) with half-lives in seconds (s), minutes (m), days (d) and years (a). Main decay processes are indicated as α and β, while γ-emitters are not presented

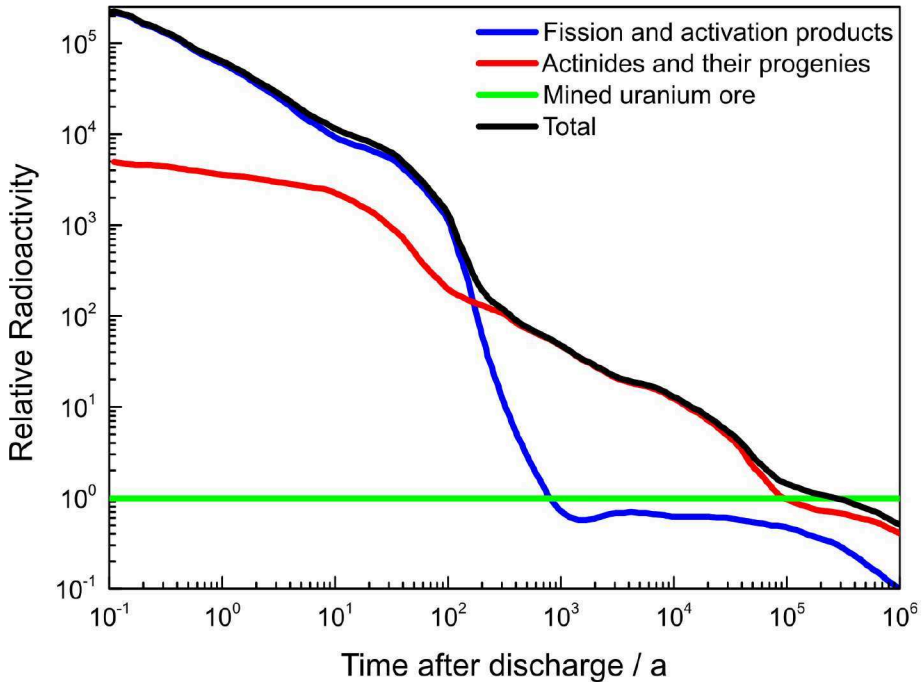

Figure 1.4 Element groups that influence the chronological sequence of the relative radioactivity of spent nuclear fuel (SNF) based on the radioactivity of mined uranium ore after Hedin (1997).

For final storage, the waste needs to be 'conditioned'. This includes the treatment and packing of radioactive waste according to the Radiation Protection Ordinance (Strahlenschutzverordnung). *Conditioning* itself is the incorporation of radionuclides into a waste matrix like ceramics or glass. There are some alternatives to reduce the hazardous potential of nuclear waste before storage. While *Partitioning* refers to separation of long-lived radionuclides from fuel elements, *Transmutation* is the transformation of radiotoxic elements into stable nuclides or into other radionuclides that may be easier to handle. This can be done by irradiation using a high-flux neutron source for example. Both processes drastically shorten the time needed until nuclear waste achieves the radiotoxicity level of natural U. However, to guarantee this decrease, the reprocessing (*i.e.* partitioning and transmutation) needs to be highly efficient. Additionally, a lot of additional ILW and LLW is created (Gompper *et al.*, 2010; Deutsche Arbeitsgemeinschaft Endlagerforschung (DAEF), 2014).
France, Great Britain and Japan use the *PUREX* (Plutonium and Uranium Recovery by EXtraction) method or modifications of it to selectively separate U and Pu from minor actinides and fission products. Since the Atomic Energetic Law (Atomgesetz) in Germany was changed in 2005, only direct final disposal is allowed for SNF ("Arbeitskreis Abfallmanagement" des VGB (Vereinigung der Großkesselbesitzer) PowerTech e.V., 2011; Röhlig *et al.*, 2012). The aim of these repositories is to retain nuclear waste (especially radiotoxic and chemotoxic material) for at least one million years (Röhlig *et al.*, 2012; Deutsche Arbeitsgemeinschaft Endlagerforschung (DAEF), 2014). The repository should hinder and/or slow down any migration of the radionuclides to guarantee long-term safety for human and environment (Röhlig *et al.*, 2012). In Germany, there is no such repository yet, but several places and concepts are under investigation. Repositories are going to be in a depth of some hundred meters in a geologically quiet area (*e.g.* a region without earthquakes). Their design will strongly depend on the kind of waste that should be stored, its physical and chemical properties and the type and amount of radionuclides. Another important factor for repositories is how long control and/or service is supposed to be available and if the waste shall be retrievable for any future use or reprocessing (Röhlig *et al.*, 2012).
Especially the long-lived radionuclide ^{239}Pu requires long-term isolation because of its significant radiotoxicity. It is generated as a daughter nuclide during the α-decay of Np and U. The energy of these α-particles and of the recoiling nuclei are high enough to cause modifications in the surrounding material (like structural changes or even amorphisation). Additionally, Pu has a high potential for criticality, *i.e.* an uncontrolled nuclear chain reaction.
A host matrix for these radionuclides needs to be found that will be thermodynamically stable in the given set-up (McCarthy *et al.*, 1978b). Chemical processes within the repository may be dissolution and precipitation of material, sorption of nuclides or redoxreactions with the surrounding material or incoming water. Additionally, complexation, radiolysis and microbiological reactions as well as gas or colloid formations need to be taken into account (Geckeis *et al.*, 2012). The desired material should be highly durable in terms of leaching and should show a high grade of chemical flexibility to incorporate the different types of radionuclides generated during the decay of U and Pu. From the economical point of view, the preferential host matrix should enable a high

waste loading and should be easy and cheap to produce to be available in large quantities (Boatner and Sales, 1988). In addition, a favourable waste form should barely react to radiation resulting from actinides and their fission products. Potential waste forms are, for example, borosilicate glass (*e.g.* McCarthy, 1977; Grambow, 2006), SynRoc (*e.g.* Ringwood *et al.*, 1979a,b) or ceramics (*e.g.* Lumpkin, 2006).

The currently used nuclear waste form is borosilicate glass. Experimental and theoretical studies on natural and synthetic analogues have been conducted for about 40 years. It is used in many countries like France, the USA, the UK, Russia, Belgium, Germany, and Japan because it can be easily processed on industrial scale (*e.g.* Ewing *et al.*, 1995; Stefanovsky *et al.*, 2004; Weber *et al.*, 2009; Deissmann *et al.*, 2012). Borosilicate glass can accommodate a wide variety of waste-stream compositions whilst being stable against radiation or thermal and chemical perturbations. The main oxides are SiO_2 and B_2O_3. Several other oxides are often added like Al_2O_3, Na_2O, CaO, MgO, Li_2O, and TiO_2 (in variable amounts). Radioactive waste from reprocessing can either be added directly to the glass in form of solutions or after drying. Then, the glass is poured in a steel mold. Since the material is reprocessed, usually only a few percent of U and Pu are left within this waste form. In total, a waste load of up to 20 wt% of waste oxides (consisting of around 30 elements) can be achieved. Most of the radionuclides are homogeneously dispersed in the glass. However, not all elements are easily incorporated such as ^{129}I. Furthermore, noble metals and platinoids, like Pd, Ru and Rh, are non-soluble in these glasses. They usually separate or precipitate as metallic or oxide particles (Grambow, 2006; Geckeis *et al.*, 2012; Ewing *et al.*, 1995).

Advantages of borosilicate glasses are their low probability of devitrification and the low diffusion rate of radionuclides. Additionally, the corrosion rate is very low when it is exposed to ground water (Grambow, 2006). In a repository with an intact barrier to incoming water, Geckeis *et al.* (2012) expect the first contact with ground water in around 10.000 years. This time range is estimated by taking into account the dissolution rate of steel and mechanical rupture of the packing material within the disposal. Some other similar glasses have been investigated like lanthanide borosilicate glasses, phosphate glasses or alkali-tin-silicate glasses (*e.g.* Donald *et al.*, 1997; Stefanovsky *et al.*, 2004; Harrison *et al.*, 2008). All in all, borosilicate glass is preferred because of the long time of experience in working with this material.

Since the 1970s, ceramics are investigated as alternative host matrices (McCarthy, 1977), especially because ceramics can consist of more than one phase. These multi-phase ceramics are very promising contestants since their combined properties may compensate for their disadvantages (Men *et al.*, 2013). Ringwood *et al.* (1979a,b) proposed a natural-like polyphase approach to immobilise nuclear waste. They developed a synthetic rock (SYNROC) composed of TiO_2, BaO, ZrO_2, Al_2O_3 and CaO. Minerals formed in this matrix are mainly zirconolites, perovskites and Ba-hollandites. Because of this chemical and mineralogical variety, SYNROC can accommodate many different radionuclides from different waste streams yielding a waste load of up to 20 wt% (Ewing *et al.*, 1995). Other polyphase and single-phase waste forms are summarised in Lumpkin (2006) and some are shown exemplarily in table 1.2.

Table 1.2 Possible host matrices according to their most important characteristics in nuclear waste management. Modified after Lumpkin (2006). +: High; -: Low; o: Medium.

Mineral name	Chemical formula	Aqueous durability	Chemical flexibility	Waste loading	Radiation tolerance
Brannerite	UTi_2O_6	o	o	+	-
Kosnarite	$NaZr_2(PO_4)_3$	o	o	o	-
Monazite	$LnPO_4$	+	o	+	+
Perovskite	$(Ca,Sr)TiO_3$	-	o	-	o
Pyrochlore	$Gd_2(Ti,Hf)_2O_7$	+	+	+	-−+
Titanate	$CaTiSiO_5$	o	o	-	-
Zircon	$ZrSiO_4$	+	o	-(?)	-

In comparison to borosilicate glass, the main advantage of ceramic matrices is their crystallinity. This means that the radionuclides can be incorporated on defined sites in the crystal structure forming a dilute solid solution (Ewing *et al.*, 1995; Lumpkin, 2006). Polyphase ceramics offer the possibility of incorporating a large range of radionuclides. They are adaptable for different waste stream compositions. In contrast, single-phase waste forms are optimised for waste stream compositions with one or few types of radionuclides. Secondary phases may form in single-phase ceramics, for example due to uncontrolled impurities. However, single-phase waste forms are used to obtain a better understanding of the physico-chemical behaviour related to the incorporation of specific radionuclides (Ewing and Lutze, 1991; Ewing *et al.*, 1995; Ewing, 2007; Muller *et al.*, 2002).
Several properties are required for a safe nuclear waste form. First of all, the host matrix needs to be solid, stable and durable as well as easy to store or to dispose. Therefore, the elements in the waste need to be immobilised by dissolution or encapsulation. By this means, the matrix should withstand the heat caused by the decay of the fission products. For elements with a high criticality like ^{239}Pu, neutron absorbers like Gd or Hf may be added to the waste form (Deissmann *et al.*, 2012). A multi-barrier system aims to prevent contamination of the biosphere. These barrier systems must be non-breakable containers and over-packs (like metal canisters) in over-pack material covered with inert overfill (Donald *et al.*, 1997; Marples, 1988; Wicks, 1985; McCarthy *et al.*, 1978b). Deep boreholes (300 m to 1000 m) should lower the risk of incoming water. The barrier system should be stable under repository conditions, not leading to any reactions with the surrounding material. The system is supposed to maintain stability against leaching and transport of radionuclides in case of percolating water, as well as against breakdown of the geological setting due to unpredictable events like earthquakes.

1.2 Aim of this work

In this thesis, rare-earth element (REE) phosphates are discussed. Monazite, as suggested by many authors, is a very promising single-phase waste matrix for the immobilisiation of long-lived radionuclides such as Pu and Am (*e.g.* McCarthy *et al.*, 1978b; Boatner *et al.*, 1980; Kelly *et al.*, 1981; Davis *et al.*, 1981; Boatner and Sales, 1988; Ewing and Lutze, 1991; Oelkers and Montel, 2008). Petek *et al.* (1981) point out that it is more economical to use mixed REE phosphates (*i.e.* monazite solid solutions) compared to any other pure *Ln* phosphate. Hence, monazite solid solutions were investigated via different methods to get a detailed insight into the structural, chemical and physical behaviour of this material. This thesis aims to combine and compare structural characterisation at ambient and non-ambient conditions with thermodynamic properties. Additionally, the influence of different synthesis conditions for the growth of single crystals is studied. To do so, powder samples, single crystals, and ceramics of monazite solid solutions have been investigated. Lanthanides are used as surrogates to model the behaviour of actinides. This is because their size, their outer electron configurations and their chemical behaviour is comparable to trivalent actinides or Pu (*e.g.* Boatner and Sales, 1988; Aloy *et al.*, 2001; Terra *et al.*, 2006, 2008, and see fig. 1.5).

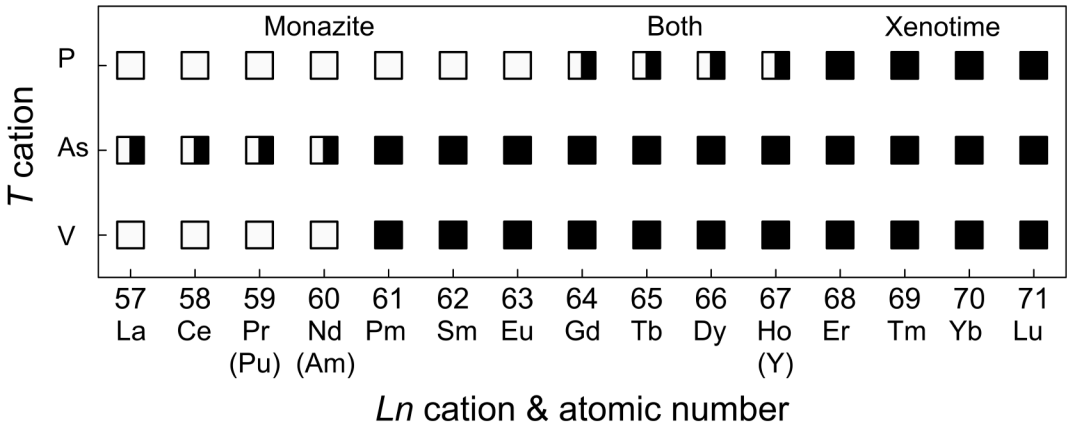

Figure 1.5 Stability fields of monazite (open symbols) and xenotime (black symbols) structure type for $LnXO_4$ (X: P, As, V) after Ushakov *et al.* (2001) and Kolitsch and Holtstam (2004). Y, Pu and Am are included because of similar ionic radii. Divided symbols mark elements that can form both structure types.

1.3 Monazite and Xenotime

Monazite and xenotime are naturally occurring REE orthophosphates with the general formula $Ln\mathrm{PO_4}$. In monazite, Ln are the light REE (La-Gd) and in xenotime, Ln are the heavy REE (Tb-Lu, and Y). Both minerals occur universally as accessory minerals in plutonic and metamorphic rocks like granites, gneisses, granitoids, pegmatites and rhyolites (*e.g.* Gramaccioli and Segalstad, 1978; Kato, 1958; Hutton, 1951; Boatner and Sales, 1988). They influence and control the REE distribution in igneous melts (Rapp and Watson, 1986; Ni *et al.*, 1995; Lacomba-Perales *et al.*, 2010). Among phosphates, they are two of the most refractory and insoluble materials (Ushakov *et al.*, 2001). Another form of appearance of these minerals in nature is in hydrothermally formed vein deposits, in pegmatitic fluids (Boatner and Sales, 1988; McCarthy *et al.*, 1978b) or in alluvial or beach sands (Leonardos, 1974).
As indicated in figure 1.5, Gd and Ho can be found in both structures, monazite and xenotime, respectively. This dimorphic area depends on the T cation which may substitute for $\mathrm{P^{5+}}$ so the general formula can be written as $LnT\mathrm{O_4}$ (Botto and Baran, 1982; Kolitsch and Holtstam, 2004). The phase which is formed also depends on the synthesis route. Van Emden *et al.* (1996) show via powder X-ray diffraction (XRD) that monazite and xenotime are usually separated by a miscibility gap.
Monazite and xenotime are intermediate phases in the system $Ln_2\mathrm{O_3}$ - $\mathrm{P_2O_5}$ with a molar ratio of 1:1. Kropiwnicka and Znamierowska (1988) investigated the system of $\mathrm{La_2O_3}$ and $\mathrm{P_2O_5}$ (fig. 1.6) and found four other stable compositions ($\mathrm{La_5PO_{10}}$, $\mathrm{La_3PO_7}$, $\mathrm{LaP_3O_9}$ and $\mathrm{LaP_5O_{14}}$). The phase diagram for the other light REE resembles that of the sytem $\mathrm{La_2O_3}$ - $\mathrm{P_2O_5}$. A hydrated $\mathrm{LaPO_4}$ compound, rhabdophane ($\mathrm{LaPO_4}\times\ \mathrm{H_2O}$), can be transformed into monazite at temperatures above 850 K (Mitchell, 1965; Dooley Jr and Hathaway, 1961).
In comparison to monazite, xenotime is not as suitable as waste form (*e.g.* McCarthy *et al.*, 1978b; Boatner *et al.*, 1980; Kelly *et al.*, 1981; Davis *et al.*, 1981; Boatner and Sales, 1988; Ewing and Lutze, 1991; Oelkers and Montel, 2008).

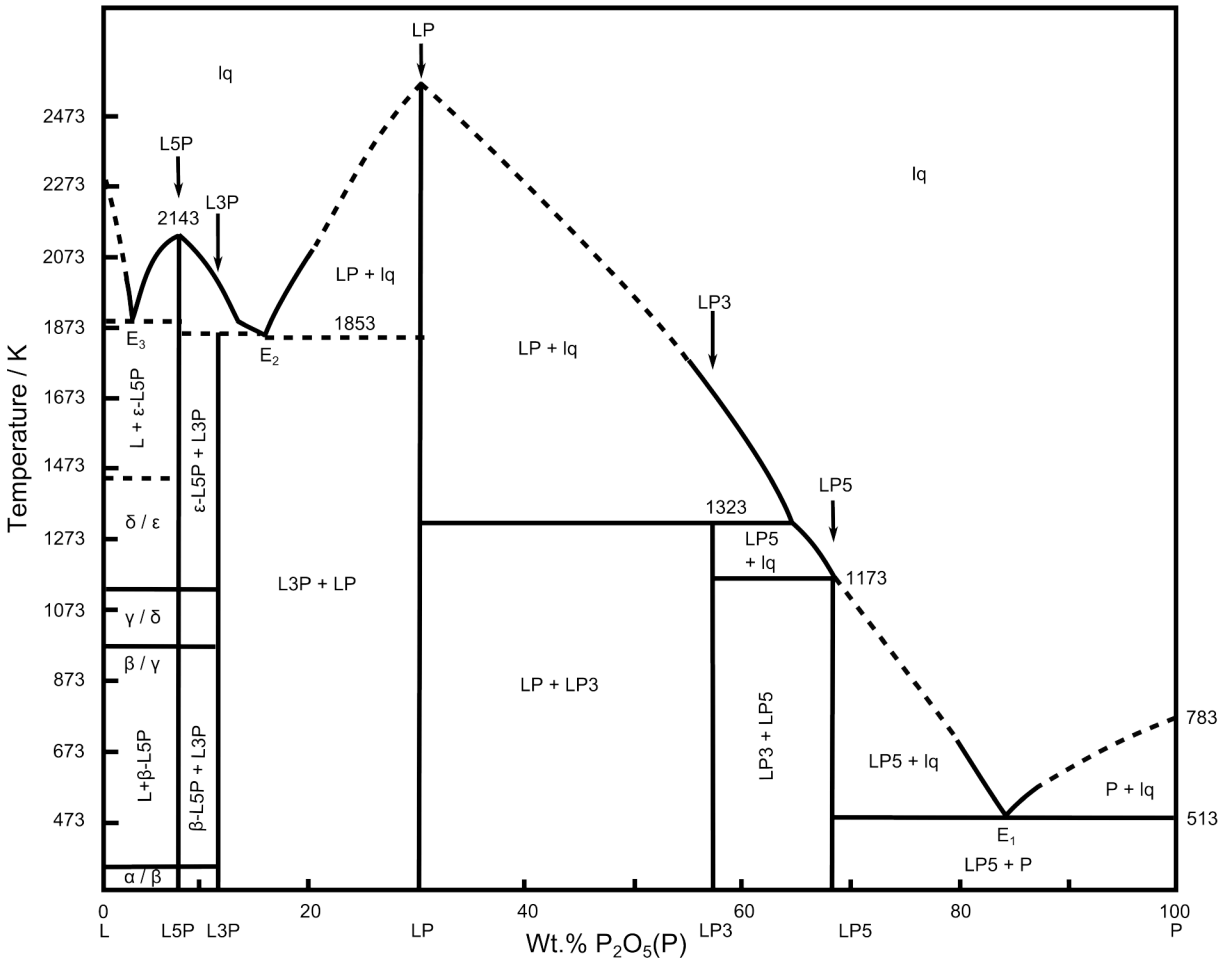

Figure 1.6 Phase diagram of La_2O_3 (L) and P_2O_5 (P) at 1 bar after Kropiwnicka and Znamierowska (1988). Mixed phases are La_5PO_{10} (α-ϵ L5P), La_3PO_7 (L3P), $LaPO_4$ (LP), LaP_3O_9 (LP3), LaP_5O_{14} (LP5). lq: liquid. E: eutectics.

1.3.1 Monazite

The name *monazite* is derived from Greek $\mu o \nu \alpha \zeta \epsilon \iota \nu$ (*monazein*, to be solitary) referring to the naturally separately occurring crystals which are geologically extremely stable (Boatner, 2002). The oldest monazites can be found in Brazil, Canada and the Himalayas, showing ages of around two billion years and being initially formed during the Precambrian (Leonardos, 1974; Schärer and Deutsch, 1990; Copeland *et al.*, 1988). This suggests that monazite is extremely stable against weathering, sedimentation and metamorphic processes (Boatner and Sales, 1988; Floran *et al.*, 1981; Haaker and Ewing, 1981). As a result of the natural incorporation of up to 15 wt % UO_2 and up to 32 wt % ThO_2, respectively, monazite accumulates radiogenic Pb during α- and β-decay of theses elements (Gramaccioli and Segalstad, 1978; Peiffert *et al.*, 1996; Clavier *et al.*, 2011). Consequently, it is used in geochronology (Copeland *et al.*, 1988; Gardés *et al.*, 2006). However, these decay processes yield high radiation damage due to α-decay which could lead to metamictisation (Boatner and Sales, 1988). Introduced by Broegger (1893), this term refers to the amorphisation of a material. Nevertheless, natural monazite with these high levels of active U and Th is rarely found in a metamict state (Ewing, 1975, 1977; Ewing and Haaker, 1980). This implies that monazite can retain its structure despite decay processes (Boatner *et al.*, 1980; McCarthy *et al.*, 1978a; Bregiroux *et al.*, 2007b; Ewing and Haaker, 1980). Since the mineral exhibits a low critical temperature of recrystallisation, no amorphisation can be introduced by ion-irradiation because the recrystallisation process is faster than the accumulation of radiation damage which is also known as 'self-annealing' (Meldrum *et al.*, 1996, 1997b,a, 1998, 1999, 2000). However, swelling has been reported as a result of He retention (Seydoux-Guillaume *et al.*, 2002, 2004; Seydoux-Guillaume *et al.*, 2012).

First structural investigations by Mooney (1948) and high precision structural determinations by Ni *et al.* (1995) revealed the monoclinic structure ($P\,2_1/n$, Z = 4) of monazite-type $Ln PO_4$ compounds and a relatively high density (≈ 5.1 g/cm^3).

The P^{5+} cations are four-fold coordinated by O^{2-}. The Ln^{3+} cations are surrounded by nine O (Beall *et al.*, 1981; Mullica *et al.*, 1984, 1985a,b). The LnO_9 coordination polyhedron can be described as a *pentagonal interpenetrating tetrahedral polyhedron* with nine different *Ln*-O bonds lengths. The LnO_9 polyhedra are bidental bonded to the PO_4 tetrahedra (Mullica *et al.*, 1984, 1985b,a, 1986), which share edges with the LnO_9 polyhedra forming chains along the [001] direction (Ni *et al.*, 1995, fig. 1.7 on the right). The LnO_9 themselves are sharing corners with each other and connected so that the chains are linked in the $a-b$-plane (fig. 1.7 on the left, Lumpkin, 2006). As a result of this polyhedral arrangement, four of the nine oxygen atoms in the *Ln*-O_9 polyhedron are connected to PO_4 while the remaining five oxygen atoms (in the equatorial plane of the *Ln*-O_9 polyhedron) bridge to five surrounding chains which has been called *locking effect* (Mullica *et al.*, 1984, 1985b,a, 1986). All PO_4 tetrahedra are isolated and do not connect to each other.

Structurally, all atoms are situated on general positions (Wyckoff position: 4e). Because the number of formula units per unit cell (Z) is four, *Ln* and P are situated on one crystallographic site each, whereas O takes four crystallographic non-equivalent sites (O^1, O^2, O^3 and O^4). All oxygen atoms are three-fold coordinated by two *Ln* and one P,

each, except for O^2. The latter is connected by one additional *Ln* cation. Within these thirteen bonds, the bond character of *Ln*-O is dominantly ionic, while the P-O bonds are more covalent (Li *et al.*, 2009). In each group, the coordination number of the oxygen influences the covalent fraction of the bonds. As a result, all O^2-bonds are less covalent than the others. A lower coordination number yields shorter bonds, while a higher one results in longer bonds with lower bond strength.
The relatively large *Ln* cations cause a structural distortion causing a rotation of the PO_4 tetrahedra (Lacomba-Perales *et al.*, 2010). Usually, *Ln* cations are trivalent but the irregular nine-fold coordination is able to accommodate different cations in terms of size and valence state without imposing severe constraints on the symmetry, size or charge of the cation (Beall *et al.*, 1981; Boatner and Sales, 1988; Aloy *et al.*, 2001). This allows for incorporations of trivalent actinides Pu, Am, Cm, Bk, Cf or Es (see Clavier *et al.*, 2011, and references therein). By compensating through defects like vacancies or by coupled substitution, mono-, di- and tetravalent cations can be incorporated at the *Ln* site (Peiffert *et al.*, 1996). Additionally, P can be substituted by Si, V, As or Cr in a direct replacement or by double substitution on the P- and the *Ln*-site. However, pure Si 'end-members' are barely found and only $PaSiO_4$ and $ThSiO_4$ have been reported to form the monazite structure (Hutton, 1951; Keller, 1963; Myasoedov *et al.*, 2010). An extensive review on various compositions with monazite-structure was given by Clavier *et al.* (2011).

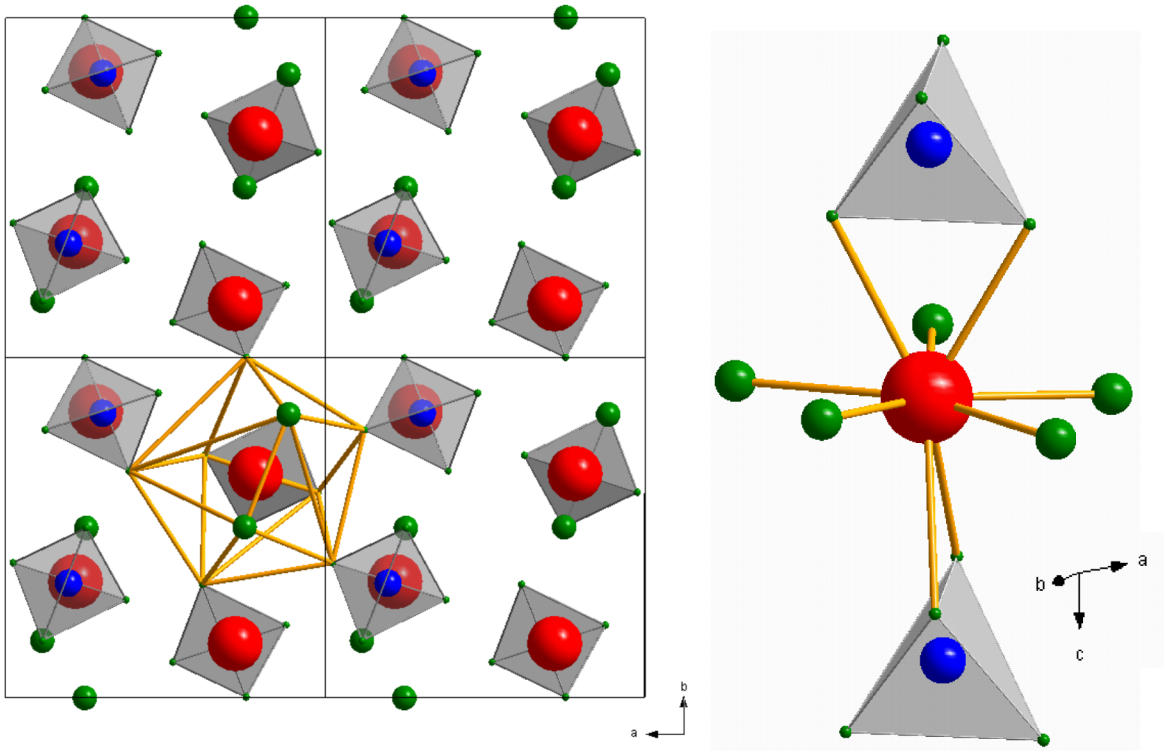

Figure 1.7 Left: Monazite structure projected along [001] after Ni *et al.* (1995). Right: AO_9-PO_4 chains running along the [001] direction forming a *pentagonal interpenetrating tetrahedral polyhedron* after Mullica *et al.* (1984). In red: *Ln*; in blue: P; in green: O.

Monazite shows high melting temperatures of around 2100 K to 2300 K (Hikichi and Nomura, 1987). In addition to a high resistance to radiation damage (Trachenko, 2004), monazite also shows high resistance to aqueous corrosion (Boatner and Sales, 1988).
Aside from its relevance in geochronology and as possible host matrix for nuclear waste, monazite has various other applications such as luminophor, laser or light emitter (*e.g.* Dong *et al.*, 2010; Chen *et al.*, 1997) or as ionic or protonic conductor (*e.g.* Gallini *et al.*, 2005; Amezawa *et al.*, 2001; Kitamura *et al.*, 2006). Combined with other materials like Al_2O_3, monazite is used as an interlayer in oxide-oxide composites in applications at high temperatures like for turbine engines (*e.g.* Davis *et al.*, 2000; Mogilevsky *et al.*, 2007). Another application are environmentally-friendly and inorganic pigments made of monazite (Masui *et al.*, 2004; Bělina *et al.*, 2007). Monazite is also economically important as the major source for the world's Th supply (Boatner and Sales, 1988).
Concerning nuclear waste management, Petek *et al.* (1981) found a significantly higher waste loading for monazite than for borosilicate glass. Additionally, the dissolution rate of monazite in destilled water at 363 K is 1000 times lower than the one of these glasses (Sales *et al.*, 1983). Monazite also performs better in retaining Cs and Sr during leaching (Petek *et al.*, 1981). According to Boatner and Sales (1988) when preparing defence-waste loaded ceramics, monazite exhibits a relatively low sintering temperature ($\approx$1173 K) which is advantageous if monazite is to be produced as a waste matrix in industrial processes. However, the sintering of commercial-waste loaded monazite ceramics takes place at elevated temperatures (>1450 K) and sintering adds will be needed to lower these temperatures. This is crucial for fission products like Cs, Ru and Mo which may get lost due to volatilisation during the synthesis. A radioactive off-gas system might be required (Boatner and Sales, 1988). The main advantage for using monazite in nuclear waste management is the possibility to incorporate and retain a broad range of elements of the decay products of U and Pu.

1.3.2 Xenotime

The word *xenotime* comes from Greek $\kappa\epsilon\nu o\sigma$ (vain, apparent, foreign) and $\tau\iota\mu\eta$ (honor, value). This *vainglory* stands for the original claim of a newly found element which was later found out to be the already known Y. Over time, the name changed to its contemporary form (*e.g.* Boatner, 2002).
Structural investigations of xenotime were done by Milligan *et al.* (1982, 1983b,a) and Ni *et al.* (1995). Xenotime has the same number of PO_4 tetrahedra and LnO_x polyhedra in the unit cell as monazite. While in monazite, the *Ln* atom is nine-fold coordinated, in xenotime, *Ln* is eight-fold coordinated by O and the structure is the tetragonal zircon ($ZrSiO_4$) structure ($I4_1/amd$, Z = 4; Ni *et al.*, 1995; Lumpkin, 2006). Similar to monazite, the LnO_8 polyhedra and the PO_4 tetrahedra form alternating edge-sharing chains along [001] and are linked in the (100) plane (fig 1.8, Ni *et al.*, 1995; Lacomba-Perales *et al.*, 2010).
Xenotime is approximately 10 % less dense than monazite (Lumpkin, 2006) and it is not as stable as monazite concerning the chemical durability and radiation damage.

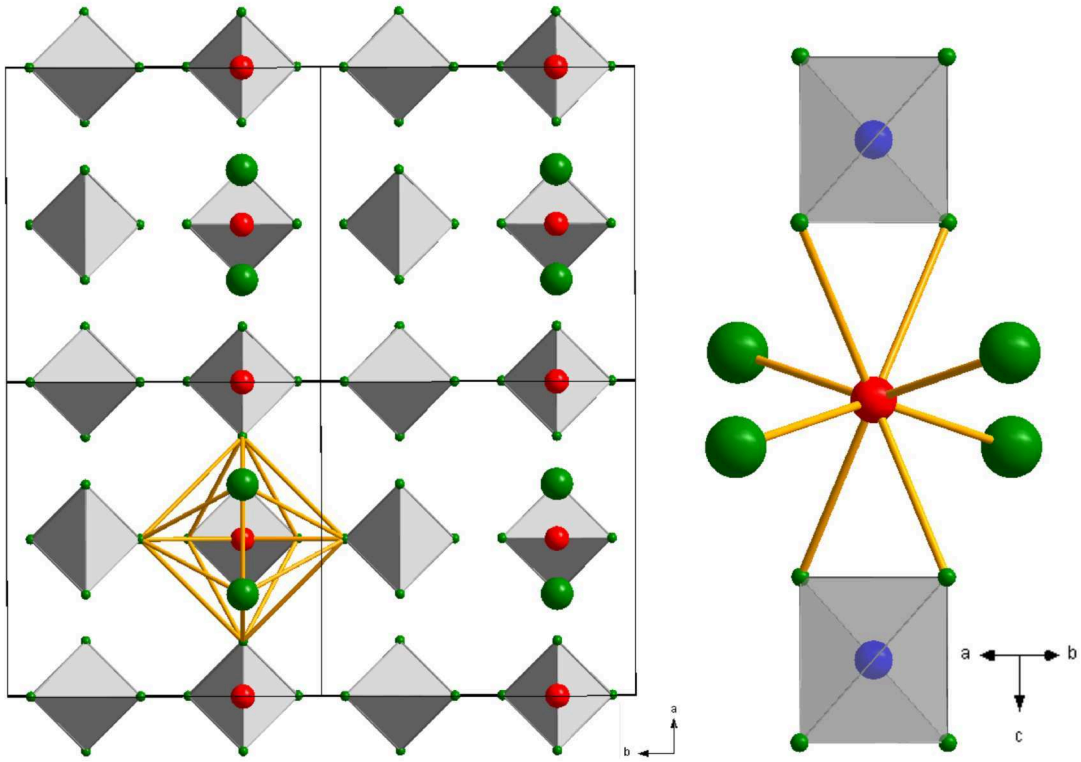

Figure 1.8 Left: Xenotime structure projected along [001] after (Ni *et al.*, 1995). Right: AO_8-PO_4 chains running along the [001] direction after Mullica *et al.* (1984). In red: *Ln*; in blue: P; in green: O.

Chapter 2: Material and Methods

In this chapter, the experimental procedures used for this thesis are described. At first, the synthesis of the samples will be given, followed by the description of the analytical methods.

2.1 Synthesis

In the following, the preparation of powders, single crystals and ceramics is described. In a first step, powders were synthesised by a solid state reaction. These powders were used to grow single crystals using a high-temperature solution. Additionally, the powders were used to produce ceramics via cold-isostatic pressing and a two-step sintering procedure.

2.1.1 Possible synthesis routes for *Ln*PO_4 powder

There are various routes to prepare monazite and xenotime synthetically. Lucas *et al.* (2004b), Lucas *et al.* (2004a), Bělina *et al.* (2009) and Schlenz *et al.* (2013) gave overviews of possible synthesis routes like hydrothermal synthesis, sol-gel route, wet chemical precipitation or high-temperature solid-state reactions. Depending on the synthesis route, various physico-chemical properties of monazite or xenotime can be influenced, among them chemical composition and homogeneity, crystalline structure, grain size and morphology, thermal and sintering behaviour (Lucas *et al.*, 2004a; Boatner, 2002).
For hydrothermal synthesis, autoclaves are filled with *Ln*- and P-precursor phases in a molar ratio *Ln*:P = 1:1. As *Ln* source, nitrates are used, while PO_4 is added via $NH_4H_2PO_4$, $(NH_4)_2HPO_4$ or H_3PO_4. These educts react in a sodium hydroxide solution within the autoclave for several hours at around 473 K. After washing with diluted HNO_3 to dissolve additionally formed *Ln* hydroxides, the material is washed with deionised water and then dried at slightly elevated temperatures. Monazite formed by this route shows low crystallinaty (*e.g.* Karkhanavala, 1956; Meyssamy *et al.*, 1999; Zhang *et al.*, 2003; Yan *et al.*, 2010).
Sol-gel reactions were described by Bo *et al.* (2001), Rajesh *et al.* (2004) and Poitrasson *et al.* (2004). These approaches use various reactants as *Ln* and P sources forming the sol which is gelatinised over a certain time. This method is more time consuming compared to the other methods but leads to well defined crystals.
For the precipitation method, *Ln* chlorides or hydroxides and $NH_4H_2PO_4$, NaH_2PO_4 or H_3PO_4 can be used (*e.g.* Chen and Mah, 1997; Lucas *et al.*, 2002, 2004b; Boakye *et al.*, 2001; Rajesh *et al.*, 2004; Nuñez *et al.*, 2010). As a byproduct, *Ln*P_3O_9 (meta-phosphate)

can be formed (Lucas *et al.*, 2002). In most cases the hydrated orthophosphate form Rhabdophane ($LnPO_4 \cdot xH_2O$) is precipitated. This compound then needs to be washed, dried and calcined at temperatures between 773 to 1073 K (Lucas *et al.*, 2004a). Especially for solid solutions, this method yields very homogeneous cation distributions and pure phases without contamination of oxides.
Educts in the solid state synthesis are as diverse as in the hydrothermal synthesis. *Ln* sources are oxides, chlorides and carbonates. As a source for P, $(NH_4)_2HPO_4$ or $NH_4H_2PO_4$ can be used. Starting materials are ground, homogenised and heat treated at temperatures above 1273 K (*e.g.* Bělina *et al.*, 2009; Hikichi *et al.*, 1978a,b, 1980, 1990; Montel *et al.*, 2006; Bregiroux *et al.*, 2007a; Cho *et al.*, 2009). Solid state reactions usually lead to a direct formation of monazite or xenotime, but with the possibility of forming byproducts.

2.1.2 Solid state synthesis of monazite powders

Powder samples of various solid solutions were prepared by solid state reaction essentially following the procedure of Bregiroux *et al.* (2007a). This route was chosen, because monazite is produced directly without any intermediate products. The solid solutions synthesised in this study are listed in table 2.1 and will be referred to as listed in there. The general reaction equation for the synthesis of a monazite solid solution containing two light REE (A and B) is:

$$(1-x)\,A_2O_3 + x\,B_2O_3 + 2\,NH_4H_2PO_4 \rightarrow 2\,A_{1-x}B_xPO_4 + 2\,NH_3\uparrow + 3\,H_2O\uparrow \qquad (2.1)$$

Table 2.1 Monazite solid solutions synthesised in this thesis with their chemical formula and the abbreviation used in the text. The order of the elements is according to increasing atomic number. For all solid solutions, samples were prepared in intervals of $\Delta x = 0.1$.

Chemical formula	Abbreviation	Reference
$La_{1-x}Pr_xPO_4$	LaPr	Hirsch *et al.* (2017) and this thesis
$Pr_{1-x}Nd_xPO_4$	PrNd	Claßen, pers. comm. (2015), and this thesis
$Pr_{1-x}Sm_xPO_4$	PrSm	Bigdeli (2016) and this thesis
$Nd_{1-x}Sm_xPO_4$	NdSm	Kuleci (2015) and this thesis
$Nd_{1-x}Eu_xPO_4$	NdEu	Schumacher (2016) and this thesis
$Sm_{1-x}Gd_xPO_4$	SmGd	Ladenthin (2017) and this thesis

The reactants used are given in table A.1 in the Appendix. Manufacturer and purity of the educts is given. *Ln* oxides are known for their hygroscopic behaviour, this was compensated for either by annealing the raw material or by using the loss on ignition (LOI) determined at 1273 K. The initially used Pr_2O_3 showed a negative weight loss (*i.e.* a weight gain) probably because of the valence change from Pr^{3+} in Pr_2O_3 to Pr^{4+} in PrO_2. When opening the sealed Pr_2O_3, the green colour changed to brownish within a few hours. This change is probably due to water uptake of the material or due to valance

change. However, the change at first concerns only the powder surface. Since the LOI for Pr_2O_3 was negative, it was not included in the initial weight calculation for the sample synthesis.
Previous stoichiometric experiments often yielded phosphate deficient phases (see fig. 1.6, Weigelt, 2011; Zaddach, 2013). Therefore, an excess of 10 wt% of $NH_4H_2PO_4$ with respect to the stoichiometric formula was used aiding the formation of pure monazite. The high vapour pressure of P_4O_{10} at elevated temperatures leads to an evaporation of the excess P_4O_{10}. The mixtures of the reactants were homogenised manually in a agate mortar and pressed in pellets. The so produced raw material was then heat treated in Al_2O_3 crucibles at 1523 K for 12–24 h in ambient atmosphere.
Powder samples were prepared in $\Delta x = 0.1$ and used for chemical and thermal characterisations, structural investigations and high-temperature drop solution calorimetry.

2.1.3 Synthesis of monazite single crystals

For the growth of monazite single crystals, two routes were investigated in this thesis: the optical floating zone method (OFZM) and the high-temperature solution (flux) method (HTSM).
Previous experiments were carried out using an optical floating zone furnace (*FZ-T-10000-H-II-VP, Crystal Systems Inc.* using OFZM (Weigelt, 2011; Zaddach, 2013). OFZM is used in purification processes and for growth of metals, alloys and semiconductor compounds (Pamplin, 1980; Wilke, 1963). This method is a vertical, crucible-free crystal growth method developed by Keck and Golay (1953), Emeis (1954), and Theuerer (1962). The heat source are halogen lamps and the heat is focussed by ellipsoidal mirrors. Two sintered, polycrystalline rods of the sample material are moved through the hot zone of the furnace. The melt is held in place between the two rods by surface tension (Schildknecht, 1964; Dabkowska and Dabkowski, 2010). OFZM yields contamination-free crystals of high chemical purity but can only be performed on congruently melting substances. Crystal size is essentially controlled by the diameter of the rods (Dabkowska and Dabkowski, 2010). Visual observation of the growth process is possible, however, without direct control of the temperature.
Although $SmPO_4$ has the lowest melting temperature of $LnPO_4$ monazites (2189±20 K, Hikichi and Nomura, 1987), the heating power of the given furnace set-up was not sufficient to melt the rods. In the previous works of Weigelt (2011) and Zaddach (2013), $Sm_{0.85}(Ca,Ce)_{0.15}PO_4$ was used to check if the incorporation of Ca and Ce might lower the liquidus to a temperature accessible with the given furnace. However, neither of the two compounds did melt and no crystals could be grown. Therefore, no further attempts were made to grow single crystals by OFZM.
Instead, HTSM was used to grow crystal for this work. HTSM is used for substances with high melting points and/or low solubility in water (Wilke, 1963; Elwell and Scheel, 2000). Molten salts or oxides are usually used as flux materials. This method requires a crucible that, on the one hand, limits the size of the final crystals, but, on the other hand, allows for a highly precise control of the crystal growth parameters due to the small growth rates. During the growth procedure, the desired material needs to be dissolved in the flux first. Crystallisation can be achieved either by spontaneous nucleation or by

using a seed crystal (Elwell, 1980; Carvajal *et al.*, 2010). Supersaturation of the flux may be accomplished by slow cooling of the solution, by evaporation of the flux or by increasing the concentration of the solute while keeping the temperature constant (Elwell, 1980; Wilke and Bohm, 1988; Elwell and Scheel, 2000; Carvajal *et al.*, 2010). At the end of the experiment, the crucible is either decanted to remove flux material and to prevent a thermal shock of the crystals or directly removed from the oven to "freeze" the flux material. The flux is then dissolved by water or acids to remove the grown crystals (Wilke and Bohm, 1988; Carvajal *et al.*, 2010). Usually, crystals grown via HTSM show higher concentration of impurities but a lower concentration of defects, dislocations and reduced thermal stress in comparison to other growth techniques like OFZM (Elwell, 1980; Elwell and Scheel, 2000; Carvajal *et al.*, 2010).
Several authors used $Pb_2P_2O_7$ (lead pyrophosphate) as flux material (*e.g.* Feigelson, 1964; Wanklyn, 1972; Smith and Wanklyn, 1974; Wanklyn, 1977, 1978; Rappaz *et al.*, 1980, 1981; Beall *et al.*, 1981; Milligan *et al.*, 1982, 1983b,a; Wanklyn, 1983; Boatner and Sales, 1988). This lead phosphate was first used by Wickham (1962) as a high-temperature flux because of its lower volatility compared to other lead-containing flux materials. Since lead is toxic, the lower volatility reduces health risks explicitly. Wanklyn (1983) described that the composition of Pb-fluxes influences the habit of the resulting crystals: A higher availability of oxygen (due to the dissociation of PbO in the molten state) and of oxides yields smaller PO_4 complexes in the flux. The diffusion of small complexes is faster so the growth rate of the crystal increases. The grown crystals are fewer in number, larger and equidimensional (Wanklyn, 1983).
Cherniak *et al.* (2004) developed a Pb-free flux growth routine using Li_2CO_3 and MoO_3 to grow $Ln PO_4$ crystals. The molar ratio is:

$$75 : 25 : 2 \equiv MoO_3 : Li_2O : LnPO_4. \tag{2.2}$$

They describe similar observations to those made by Wanklyn (1983) for their crystals: The more basic oxides (Li_2O) are present in the flux, the smaller the PO_4 complexes will be, while more MoO_3 yields larger, highly charged anions which might impede the growth and influence the size and habit of the crystals (Cherniak *et al.*, 2004). In this thesis, the effects of different flux systems (*i.e.* different molar ratios of the flux components) were investigated.
For the growth procedure, the mixture of flux material and monazite powder was filled in a Pt crucible. The crucibles were put in a chamber furnace at ambient pressure and kept isothermally at about 1173 K for more than 12 h to assure the melting of the whole flux material and, by that, entire homogenisation of the mixture. The temperature was then raised to the starting temperature for complete dissolution of the monazite powder in the flux and then slowly cooled down using a ramp. Afterwards, the crucibles were removed from the furnace to finally cool down in air. Flux composition, temperature range, and cooling rate were varied in several experiments as shown in table A.22 in the Appendix. Additionally, experiments with open and closed Pt crucibles were carried out to investigate the influence of evaporation of the flux material on the growth of single crystals (also indicated in table A.22 in the Appendix). In most cases, the lid was placed on top of the crucible so that the crucible was not completely sealed. In one experiment, the lid was welded to the crucible to ensure a tightly closed crucible. The grown single

crystals were removed from the flux material by dissolving the latter with pure water in an ultrasonic bath at slightly elevated temperatures (up to 323 K). All chemicals used as flux material are listed in table A.2 in the Appendix.
Single crystals were analysed via spectroscopy, microcalorimetry, X-ray diffraction and second-harmonic generation measurements.

2.1.4 Synthesis of monazite ceramics

The procedure to make LaPr ceramics used for this thesis was also presented in Thust *et al.* (2017). Pure LaPr monazite powders with compositions $x_{\mathrm{Pr}} = 0$, 0.3, 0.5, 0.8, and 1 were used. These powders were ground manually to decrease the grain size and to homogenise the material, and then filled in rubber tubes while continuously compacting the powder. Compaction is necessary to avoid holes within the rod and to assure sintering. The tubes were then evacuated using a conventional vacuum pump and pressed isostatically at 60 MPa for 15 min at ambient temperature. After removing the tubes, green bodies were pre-sintered at 1273 K for 20 h. For further characterisation, these pre-ceramics were cut into cylinders. They were used for scanning electron microscopy (SEM) analysis and for dilatometry. Densities of the pre-ceramics were calculated from the volume and mass of each sample. They were not measured via Archimedes' principle to avoid contamination with water which might have influenced the following sample procedure. In a second step, the samples were re-sintered at 1673 K for additional 15 h. These final ceramics were analysed by SEM, dilatometry, and ultrasound spectroscopy. Densities of these samples were then determined via Archimedes' principle.

2.2 Characterisation methods

In this section, the different analytical techniques used for characterisation of powders, single crystals and ceramics will be described briefly.

2.2.1 Chemical analysis

Electron probe micro analysis (EPMA) and scanning electron microscopy (SEM) were used for chemical characterisation of powders and single crystals, as well as for characterisation of the microstructure of the ceramics.

2.2.1.1 Electron probe micro analysis

EPMA was performed on a *JEOL JXA 8900 R* instrument at the Christian-Albrechts-Universität zu Kiel as presented here and in Hirsch *et al.* (2017). The electron beam had a diameter of 1 μm, operating at a current of 40 nA and an acceleration voltage of 20 kV. For the measurements, powder and single crystal samples were embedded in Laromin resin in plastic mounts. The embedded crystals were polished for further analyses. All samples were carbon-coated to avoid charging effects. $CePO_4$ (USNM 168484), $LaPO_4$ (USNM 168490), $PrPO_4$ (USNM 168493), $NdPO_4$ (USNM 168492), and $SmPO_4$ (USNM 168494) were used as calibration standards for P, La, Pr, Nd, and Sm, respectively (Smithsonian

Institution, Washington: Jarosewich and Boatner, 1991).
For chemical characterisation of the LaPr powder samples, 15 different spots were analysed for each sample (Hirsch *et al.*, 2017), while for PrNd, PrSm and NdSm, up to 50 spots per sample were analysed. Three (empirical) factors were taken into account following Terra *et al.* (2003) to check if a measurement should be included in the evaluation:

- The sum of all elements had to be between 96 % and 102 %.
- The deviation from the expected value for each composition of the percentage ratio Ln_1/Ln_2 had to be between 50-150 % (ideal case: 100 %; this value represents the homogeneous distribution of the two lanthanide ions).
- The ratio $(Ln_1{+}Ln_2)$/P had to be between 0.80 and 1.40 (ideal case in monazite: ΣLn/P = 1:1; this ratio gives indication about other lanthanide phosphate phases present in the sample).

Note that the sum of the elements should ideally be 100 %. Errors are calculated from standard deviations (statistical or random errors). Values larger than 100 % are due to the *CITZAF* software (Armstrong, 1995) that was used for the matrix correction (representing systematic errors). A deviation from ideal behaviour could point, for example, to a possible miscibility gap. However, deviations that led to an exclusion of the data are most probably due to porosity: Underlying pores which were not visible at the surface might have been filled with embedding material and, by that, may have influenced the results for the Ln_1/Ln_2 ratio.
Space-resolved analyses were done on LaPr single crystals. For profiles on three crystals per composition ($x_{\mathrm{Pr}} = 0; 0.2; 0.4; 0.6; 0.8$), two approximately perpendicular line scans were measured where one line was chosen along the longest dimension of the crystal. Measurements were carried out every 30 μm for 1 min per step. Additionally, two crystals ($x_{\mathrm{Pr}} = 0.4; 0.6$) were chosen for mapping the chemical composition in a larger area. Measurements covered an area of 900 × 900 μm in intervals of 1.5 μm with 1 min/step.

2.2.1.2 Scanning electron microscopy

SEM was carried out on a *LOT-QuantumDesign Phenom^{TM} ProX* desktop SEM at the Institute of Geosciences, Goethe University Frankfurt, as presented in this thesis and in Thust *et al.* (2017). The instrument was equipped with a thermionic CeB_6 source and a high sensitivity multi-mode back-scattered electron (BSE) detector. Acceleration voltage was adjusted to 10 kV and 15 kV for imaging and energy dispersive X-ray spectroscopy (EDS), respectively. For the analysis, samples were placed on a graphite holder without conductive coating. Both, *pre-ceramics* and *final ceramics* were polished using Al_2O_3 and diamond paste. Afterwards, the samples were thermally etched for 4 h at 1273 K to remove polishing residues and to enhance the contrast between grain boundaries during imaging. Analysis of the microstructure of the ceramics was done using *ImageJ* (Rasband, 1997-2016) to evaluate grain shape and homogeneity. The method of the best fitting ellipses according to Heilbronner and Barrett (2013) was used to estimate grain sizes. To validate the results, the *lineal intercept method* after Wurst and Nelson (1972) was used.

2.2.2 Thermal analysis

Thermogravimetric analyses and differential scanning calorimetry (TGA and DSC) were performed on a *Netzsch STA 449 F3 Jupiter* system at the Institute of Crystallography, RWTH Aachen University, to check if the samples showed any phase transitions or reactions like water loss between room temperature and 1373 K (Hirsch *et al.*, 2017, and this thesis). Approximately 30 mg per sample were heated in a corundum crucible. The heating cycle was from room temperature to 1373 K with a rate of 10 K/min, then the temperature was kept constant for 10 min before cooling down with the same rate. Corundum was used as a reference material. To correct the base line, a blank run with an empty crucible was made. According to the manufacturer, the instrumental precision is 1.5 K for temperature, 0.01 mg for mass, and 50 nV for voltages in DSC.

2.2.3 X-ray diffraction

In a first step, conventional X-ray diffraction (XRD) at ambient conditions was performed to check phase purity and to obtain lattice parameters for the solid solution members of powder and single crystal samples. Additionally, synchrotron powder XRD was used for LaPr for structural refinements using high-quality data. At non-ambient conditions, high-temperature powder XRD was used to determine thermal expansion of LaPr, and high-pressure single crystal synchrotron XRD to detect possible pressure-induced phase transitions in $LaPO_4$.

2.2.3.1 Powder X-ray diffraction at ambient conditions

Different diffractometers were used at the Institute of Crystallography, RWTH Aachen University, for the room temperature (RT) characterisation of the monazite solid solutions. In table 2.2, an overview of these diffractometers and the operational conditions is given.
The *PANalytical X' pert Pro* diffractometer in Bragg-Brentano θ-θ-geometry was equipped with Cu-tube and Ni-filter, yielding Cu $K_{\alpha 1,2}$ radiation, and an *X'celerator* semiconductor strip detector. The *Philips PW1820* diffractometer was equipped with a Cu $K_{\alpha 1,2}$ source, a secondary monochromator (pyrolytic (002) graphite) and a single scintillation detector. Since Sm and Eu are known for their fluorescence under Cu radiation (energy of Cu $K_{\alpha 1}$: 8.048 keV; energy of the Sm and Eu L_I-edge: 7.707 and 8.024 keV, respectively), a secondary monochromator was used. All diffractometers operated at 40 mA and 40 kV.

Table 2.2 Diffractometers and operational conditions used for each solid solution.

Name	Diffractometer	2θ	$\Delta\ 2\theta$	Time	Reference
LaPr	*X'Pert Pro*	10 - 110°	0.008°	37 s/step	-
PrNd	*X'Pert Pro*	10 - 110°	0.008°	40 s/step	Claßen, pers.comm. (2015)
SmGd	*X'Pert Pro*	10 - 110°	0.008°	60 s/step	Ladenthin (2017) and herein
NdSm	*PW1820*	10 - 110°	0.02°	2 s/step	Kuleci (2015) and herein
PrSm	*PW1820*	10 - 110°	0.02°	15 s/step	Bigdeli (2016) and herein
NdEu	*PW1820*	5 - 110°	0.02°	15 s/step	Schumacher (2016) and herein

2.2.3.2 Synchrotron powder X-ray diffraction

As shown in Hirsch *et al.* (2017), synchrotron XRD was performed on LaPr powder samples at the High Resolution Powder Diffraction Beamline P02.1 on PETRA III (DESY, Hamburg). The system was equipped with a Si(111) monochromator and a *PerkinElmer XRD1621* fast area detector. The wavelength was given as $\lambda = 0.207120$ Å. CeO_2 (NIST 674b) and Si (NIST 640d) were used as calibrants. Both, samples and calibrants, were placed in SiO_2-glass capillaries of 0.5 mm diameter. Measurements under ambient conditions and at 100 K were recorded for 10 s and 100 s, respectively, while spinning the capillaries. The program *Fit2D41* (Hammersley *et al.*, 1996) was used to adjust the sample-to-detector distance (given as 2020.668 mm) for the Si calibrant and to integrate the two-dimensional diffraction data. Note that both, wavelength and sample-to-detector distance, were obtained from a single measurement on Si. Since both parameters are correlated, no standard deviations can be given.

2.2.3.3 High-temperature powder X-ray diffraction

To determine the thermal expansion of LaPr as presented in chapter 3.3.2 and in Thust *et al.* (2017), *in-situ* high-temperature (HT) XRD was performed on five powder samples ($x_{\mathrm{Pr}} = 0; 0.3; 0.5; 0.7; 1$) on a *Bruker D8 Advanced DaVinci* diffractometer in Bragg-Brentano θ-θ-geometry at the Institute for Mineral Engineering at the RWTH Aachen University. This system was equipped with a *LynxEye* semiconductor strip detector. To achieve high temperatures, an *Anton Paar HTK 2000* high-temperature chamber was installed, operating with a Pt heating strip. An internal corundum standard was added to each sample. The sample-to-standard ratio was 2:1. Acetone was added and then the mixture dropped onto the Pt plate of the resitance furnace. Due to evaporation of the acetone, a smooth and even sample surface was achieved. The Pt plate was heated electrically from 298 K to 1373 K and cooled back down. Every 25 K while heating and every 50 K on cooling, a diffractogram was taken from 10 to 80° 2θ with $\Delta 2\theta = 0.03°$ and 19.2 s/step. At 298 K and 1373 K, two long-time measurements were performed using 96 s/step. Since Al_2O_3 was a mixture of α and γ phase, both structures were used for the refinement (Ishizawa *et al.*, 1980; Zhou and Snyder, 1991). Soft bond lengths restraints were used for PO_4 tetrahedra during the refinement.

2.2.3.4 Evaluation of the powder diffraction data

For structural refinements of all powder XRD data, the Rietveld method (Rietveld, 1967) as implemented in the program *Topas Academic V. 5* was used (Coelho, 2000). During the refinements, the following parameters were allowed to vary: a background polynomial (6 to 12 coefficients), a modified pseudo-Voigt profile function (Thompson *et al.*, 1987), reflection asymmetry, and sample height. Lattice parameters, fractional coordinates for all sites and isotropic thermal displacement parameters were allowed to vary. As a structural model for monazite, data from Ni *et al.* (1995) was used. While for synchrotron measurements, the data were evaluated directly, refinements of conventional XRD measurements were done using restraints for the PO_4 tetrahedron.
Errors obtained by the Rietveld method tend to be underestimated (Scott, 1983; Bérar and Lelann, 1991). However, no correction was done because the (usually assumed) underestimation of the e.s.d.s cannot be quantified.
For the HT XRD data, α-Al_2O_3 and γ-Al_2O_3 (Ishizawa *et al.*, 1980; Zhou and Snyder, 1991) were used as structural models for the internal standard as shown in Thust *et al.* (2017). For the plate furnace, the Pt model of Waseda *et al.* (1975) with a preferred orientation described by spherical harmonics was included. The results of the refinements were used to calculate linear coefficients of thermal expansion (α) for all lattice parameters and the unit cell volume (V_{uc}). To do this, the data were fitted with *OriginPro9.0* (OriginLab, n.d.) using the following formula:

$$a_i(T) = a_{i,0} + a_{i,0} \cdot \alpha \Delta T \tag{2.3}$$

with

$$\alpha(T) = A_X + B_X \Delta T \tag{2.4}$$

where $a_i(T)$ and $a_{i,0}$ represent $\vec{a}$, $\vec{b}$, $\vec{c}$, β and V_{uc}, at temperature T and at 1273 K, respectively (Krishnan *et al.*, 1979). A_X and B_X are fit parameters. Normalised lengths and volume changes were calculated after Haussühl (1983):

$$\frac{\Delta a_i}{a_{i,0}} = \frac{a_i(T) - a_{i,0}}{a_{i,0}} \tag{2.5}$$

To compare these values with the ones obtained from dilatometry (see section 2.2.6), the thermal expansion for the volume (α_V) was divided by three in order to obtain an average coefficient (α_m).

2.2.3.5 Single-crystal X-ray diffraction at ambient conditions

For structure refinement and, particularly, to obtain accurate fractional coordinates of the atoms, single crystal diffraction was performed at the Institute of Crystallography, RWTH Aachen University, on *IPDS I* and *IPDS II* diffractometers from *STOE*. Both use Mo $K_{\alpha 1,2}$ and two-dimensional imaging-plate detectors. While *IPDS I* is a one-circle diffractometer (rotation axis omega) with a maximum of 66° in 2θ, *IPDS II* is a two-circle diffractometer with $2\theta_{max} = 77°$. The generator was operated at 50 kV and 25 mA for both.
Since *Ln* ions are known for their high absorption, most single crystals were smoothed in

a box covered with sand paper using compressed air. Spherically shaped crystals of less than 0.1 μm were then glued on glass capillaries (diameter: 0.1 μm). All measurements were performed from 0 to 180° ω in $\Delta\omega$ steps of 1° with an exposure time of 1 min per acquisition. In *IPDS II*, two runs with these conditions were carried out using $\phi = 0°$ and $\phi = 90°$. The distance between crystal and detector in *IPDS I* and *IPDS II* was 90 mm and 80 mm, respectively. *X-Area* (Stoe & Cie GmbH, 2013) was used for data evaluation.

2.2.3.6 High-pressure single-crystal X-ray diffraction

High-pressure (HP) single crystal XRD for this thesis was presented in Ruiz-Fuertes *et al.* (2016). Two $LaPO_4$ single crystals were chosen for HP experiments which were performed using *Boehler-Almax* diamond-anvil cells (DACs). The diamonds in this set-up have a culet size of 350 μm. The sizes of the $LaPO_4$ crystals were about 40×40×10 μm. They were separately loaded in a hole of 130 μm in diameter of a W-gasket which was pre-indented to 40 μm thickness. For the pressure determination according to Mao *et al.* (1986), additional synthetic ruby chips were loaded in each DAC. Liquid Ne was used as a quasi-hydrostatic pressure-transmitting medium (Klotz *et al.*, 2009). HP XRD experiments were performed at the Extreme Conditions Beamline P02.2 on PETRA III (DESY, Hamburg). This set-up used a wavelength of $\lambda = 0.2907$ Å, focussing the beam to 5×5 μm. It was equipped with a *PerkinElmer XRD1621* flat-panel detector. The sample-to-detector distance was 451 mm. Collecting diffraction images by 1° ω-scanning, experiments were carried out using the following pressures: 8.0(1), 12.9(1), 16.7(1), 21.2(1), 27.1(1) and 31.2(2) GPa. Again, wavelength and sample-to-detector distance were obtained from one Si measurement and no standard deviations can be calculated.

2.2.3.7 Evaluation of the single crystal diffraction data

Room temperature single crystal diffraction data was analysed using *X-Area* (Stoe & Cie GmbH, 2013) to determine the unit cell, for integration, and data reduction applying Lorentz and polarisation correction. For crystals that were not smoothed into sperical form, anisotropic absorption was corrected using *X-Red* (Stoe & Cie GmbH, 2012) after an optimisation of the crystal facets via *X-Shape* (Stoe & Cie GmbH, 2013). Afterwards, structure refinements were carried out using either *SHELXL97* (Sheldrick, 2015) or *Jana2006* (Petříček *et al.*, 2008).
For evaluation of the HP data as shown in Ruiz-Fuertes *et al.* (2016), the images were converted using the procedure of Rothkirch *et al.* (2013). Reflections were indexed and intensity data reduction was done using the software *CrysAlisPro* (Agilent, 2013). The crystal structures at the studied pressures were solved using the Patterson method with the program *SHELXS97* (Sheldrick, 2008). The refinement was carried out using *SHELXL97* (Sheldrick, 2008).

2.2.4 Spectroscopy

Infrared (IR) and Raman spectra were recorded on powders to obtain local information of the PO_4 tetrahedron depending on substitution within the monazite structure. Ultrasound spectroscopy was used on ceramic samples to obtain elastic stiffness coefficients, while fluorescence spectroscopy on a single crystal of $PrPO_4$ was performed to determine the energy level scheme of Pr^{3+}. Optical absorption spectroscopy was used to evaluate the influence of substitution on the Pr absorption bands in LaPr single crystals.

2.2.4.1 Infrared spectroscopy

IR spectroscopy was performed on LaPr powders on a *Bruker AXS EQUINOX FT-IR* spectrometer at Forschungszentrum Jülich as described in Hirsch *et al.* (2017). For the measurement, 1 mg of powder was mixed with 250 mg KBr and pressed into pellets. Spectra were recorded in the wave number range of 4000-400 cm^{-1} with a resolution of 4 cm^{-1}. The search for local minima was done with *OriginPro 9.0.0G* (OriginLab, n.d.).

2.2.4.2 Raman spectroscopy

Raman spectroscopy as given in Hirsch *et al.* (2017) was performed on a *Renishaw RM-1000* spectrometer at the Institute of Geosciences, Goethe University Frankfurt. The system was equipped with a 20× objective and an 1800 grooves/mm grating. It was operated in quasi-backscattering geometry without polarisation analysis. The exciting source was a Nd:YAG laser ($\lambda = 532$ nm, output power: 2 mW on the sample) filtered by *Notch* filters. The system was calibrated using the band at 520.2 ± 0.5 cm^{-1} of a silicon wafer (Parker *et al.*, 1967). The powder samples were placed on a glass plate and planished. Spectra were recorded either in the wave number range of 100 to 1200 cm^{-1} during 10 s or in static mode between 530 to 1380 cm^{-1} for 10 accumulations of 1 s each. The resolution was 2 cm^{-1}. The silicon mode used for calibration was expected at 520.0 cm^{-1} and found to be at 523.5 cm^{-1}, 521.0 cm^{-1} and 520.5 cm^{-1} for LaPr, PrSm and NdSm, respectively. This shift was corrected before starting the further data evaluation. Peak fitting and calculations of the full width at half maximum (FWHM) were carried out with *OriginPro 9.0.0G* (OriginLab, n.d.). In the peak analyses of the monazite spectra, a pseudo-Voigt profile for each mode was employed after background removal.

2.2.4.3 Ultrasound spectroscopy

Plane-wave/parallel-plate ultrasound spectroscopy was done at the Institute of Geosciences, Goethe University Frankfurt. It was employed to measure the propagation of longitudinal and shear waves in order to determine the elastic stiffness coefficients of the final ceramics (Thust *et al.*, 2017). A detailed description of the set-up is given by Arbeck *et al.* (2010). Since the sintered samples were found to be isotropic and homogeneous (see chapter 3.3.2), it was not necessary to orientate the samples for the measurements. By exciting mechanical oscillations in the sample using ultrasound transducers (α-quartz with x- and y-cuts) and an impedance analyser (*Agilent 4395A*) for analysis, resonance

frequencies were generated. To assure the acoustic coupling of sample and transducer, paraffin oil or resin was used. Sound velocities ν_s can be determined from:

$$\nu_s = 2d(\Delta f) \tag{2.6}$$

where d is the thickness of the sample and Δf the separation between two neighbouring resonance frequencies (Haussühl and Tillmanns, 1997). The sound velocities can then be converted into elastic stiffness coefficients (c_{ij}) using the density (ρ) by solving of the Christoffel equation according to Haussühl (1983) and Yadawa *et al.* (2009):

$$c_{ij} = \frac{\rho}{\nu_s^2} \tag{2.7}$$

The longitudinal and shear elastic stiffness coefficients (c_{11} and c_{44}) were determined in order to calculate elastic properties like bulk modulus (K; eq. 2.8), shear modulus (G; eq. 2.9), Poisson's ratio (η; eq. 2.10), and Young's modulus (E; eq. 2.11) (Levy *et al.*, 2001).

$$K = c_{11} - \frac{3}{4}c_{44} \tag{2.8}$$

$$G = c_{44} \tag{2.9}$$

$$\eta = \frac{3K - 2G}{6K + 2G} \tag{2.10}$$

$$E = 2G(1 + \eta) \tag{2.11}$$

2.2.4.4 Fluorescence spectroscopy

To obtain the electronic energy level scheme of Pr^{+3} in $PrPO_4$, fluorescence spectroscopy was performed on a set-up equipped with a grating monochromator (*Acton SpectraPro 2300i, Princeton*) and a *Princeton Instruments Pixis 256E CCD* camera. As described in Bauer *et al.* (2016), the fluorescence was excited using a Q-switched Nd:YAG laser (*Continuum Surelite III-19*) with a pulse length of 10 ns at 10 Hz. The laser produces a third-harmonic wavelength and pumped an optical parametric oscillator (*Spectra Physics versaScan 120/MB*). To avoid self-quenching as described by Sokólska *et al.* (2000), the sample containing the least amount of Pr^{3+} was chosen. The laser wavelength ($474.5\,\text{nm} \mathrel{\hat{=}} 21{,}075\,\text{cm}^{-1}$) prevented excitation of higher energy levels like $^3P_1$ or $^3P_2$. For a better assignment of the energy levels, the crystal was measured in two orientations with respect to the laser incidence. Calibration was done measuring the emission of a Ne lamp, which revealed an accuracy of the wavelengths of ± 0.05 nm. Using Lorentzian functions, barycentres of the emission lines were determined.

2.2.4.5 Optical absorption spectroscopy

For optical absorption spectroscopy (OAS), a modified universal microscope spectrophotometer *USMP-80* from *Zeiss* was used. The polarising microscope was equipped with

a 10× ultrafluar objective and a condenser as well as two lamps (a xenon lamp with 75 W and a tungsten lamp with 100 W for 330-450 nm and 400-1000 nm, respectively). A threefold grating (*SP-2357, Acton Research*) was used on the illuminated side and a photomultiplier (*R5108, Hamamatsu*) was used as detector. Both, monochromator and detector were controlled via a *SpectraHub interface* from *Roper Scientific*. Measurements on LaPr single crystals ($x = 0.2$; 0.4; 0.6; 0.8; 1.0) with the W-lamp used an entrance slit of 250 μm, an exit slit of 50 μm, an aperture of 2.5 and a high voltage of 1.020 V at the photomultiplier. The acquisition time was 100 ms per step in a range of 400-650 nm in 0.2 nm steps.

2.2.5 Determination of the density

Usually, sample densities are determined via Archimedes' principle with water as immersion liquid at ambient temperature. However, the density of the pre-ceramics was not measured this way, because these samples were not fully densified and could have been destroyed by water so that a second sintering step might have been impossible as described in Thust *et al.* (2017). To calculate the density (ρ) from mass (m) and volume (V) of the sample, pre-ceramics were weighted and their size measured. The density of the final ceramics was determined using Archimedes' principle. For this purpose, the samples were measured five to six times, to estimate uncertainties, at a temperature of 293.5 to 295.7 K. The expected density from structural data (ρ_e) was calculated using the following equation:

$$\rho_e = \frac{m}{V} = \frac{M \cdot Z}{N_A \cdot V_{uc}} \tag{2.12}$$

where m is the mass and V the volume, M the molar mass of the solid solution member, Z the number of formula units per unit cell, N_A the Avogadro constant, and V_{uc} the volume of the monoclinic unit cell calculated from data from Ni *et al.* (1995).

Using the expected and the measured density of the sample (ρ_m either determined geometrically or obtained from Archimedes principle), the percentage pore volume (ϕ) was calculated:

$$\phi = (1 - \frac{\rho_m}{\rho_e}) \cdot 100. \tag{2.13}$$

2.2.6 Dilatometry

Linear coefficients of thermal expansion (α) for LaPr ceramics were determined using dilatometric measurements at the Institute of Geosciences, Goethe University Frankfurt. The procedure is published in Thust *et al.* (2017).

After determining density and pore volume, all ceramic samples were used for dilatometric measurements. The dilatometer was a *Netzsch DIL 402C* push rod dilatometer. It was equipped with a high temperature furnace (type 6.2191-26 from *Netzsch*). Air was used as purge gas and ceramic corundum rods as calibrants. Data were collected on heating from RT to 1373 K and on cooling down to room temperature using a rate of 2 K/min.

Accuracy of the data is estimated to be 3 % according to the corundum measurements. Data were fitted using a 3^{rd} order polynomial by Haussühl (1983):

$$\frac{l - l_0}{l_0}(T) = A_D + B_D(T - T_{ref}) + C_D(T - T_{ref})^2 + D_D(T - T_{ref})^3 \tag{2.14}$$

In this formula, A_D is the intercept with the y-axis, while B_D, C_D, D_D are the linear, quadratic and third-order thermal expansion coefficients, respectively (the subscript D is used to distinguish these fitting parameters from the ones used for the HT XRD). T_{ref} is the reference temperature of 1273 K as used in Thust *et al.* (2015). Thermal expansion values were then calculated using the first derivative $\alpha = \frac{d\frac{l-l_0}{l_0}}{dT}$.

2.2.7 High-temperature drop solution calorimetry

HT drop solution calorimetry was used to obtain thermodynamic parameters which are presented in Hirsch *et al.* (2017). Measurements on LaPr were performed using a custom-built *Tian-Calvet*-type twin calorimeter at the Peter A. Rock Thermochemistry Laboratory, University of California in Davis (USA) (Navrotsky, 1977, 1997, 2014). In this calorimeter, two sample chambers were used to determine the heat flow generated at constant temperature when a sample is dropped into a molten solvent (isoperibol set-up, Navrotsky, 2014). The heat flow signal is influenced by the heating of the sample after dropping from room temperature to the solvent temperature as well as by the heat consumed during the solution of the sample in the solvent (enthalpy of solution, ΔH_{ds}). Additionally, any reactions taking place in the solvent like valence changes also contribute to the signal. The resulting heat-flow is measured by the calorimeter.
20 g of the solvent (sodium molybdate: $3\,Na_2O \cdot MoO_3$) were filled in each of the two Pt-crucibles on either side of the calorimeter. To assure an oxidising environment and to controll the oxygen fugacy, the melt was stirred at 973 K by 'bubbling' with oxygen with a rate of 5.9 ml/min. According to Navrotsky (2014), this enhances dissolution and prevents local saturation of the solvent. Additionally, an O_2 gas flow with 40 ml/min was flushed through the calorimeter chamber generating a constant gas environment above the solvent to remove any evolved gases. The calibration of the calorimeter was done by measuring the heat content of α-Al_2O_3 pellets and cross checked by TiO_2 pellets and compared to results by Navrotsky (2014). Before the measurements, all samples were thermally treated at 1073 K for at least 8 h to remove any surface water. For the measurement of ΔH_{ds}, approximately 5 mg of each LaPr sample were pressed into cylindrical pellets. 8-10 pellets per composition were dropped into the solvent to increase accuracy and to assure reliability. For the analysis, only those measurements were used during which the signal returned to the baseline (Ushakov *et al.*, 2001). On average, it took 30 minutes to return to the initial level This time depends not only on the enthalpy change / specific heat capacity, but also on the dissolution rate and the time constant of the calorimeter. The heat-flow signal was integrated over time using the software *Calisto SETARAM* to determine ΔH_{ds}. The achievable accuracy of ΔH_{ds} is in the range of 1 kJ/mol. By employing appropriate thermochemical cycles (see table 3.8 in section 3.4.1), enthalpies of formation from oxides and elements as well as the enthalpy of mixing were calculated.

The methodology is essentially the same as that used for prior experiments on rare earth phosphates and related materials (Ushakov *et al.*, 2001).

2.2.8 Low-temperature microcalorimetry

Low-temperature (LT) microcalorimetry on LaPr single crystals ($x_{\mathrm{Pr}} = 0$; 0.2; 0.4; 0.6; 0.8; 1) was used to measure the heat capacity (C_p) and to calculate standard enthalpy change ($\Delta H_{298.15\,\mathrm{K}}$) and standard molar entropy ($S^0_{298.15\,\mathrm{K}}$).
As described in Bauer *et al.* (2016), inclusion free single crystals with masses between 4-20 mg were selected. Since all examined crystal samples revealed at least one well developed natural face, no additional preparation was needed to ensure thermal contact with the sample platform. However, since this technique needs a strongly coupling medium (grease) to couple the sample to the platform and the thermal behaviour of the grease needs to be considered, a prior run with grease only was performed before each measurement. Heat capacities were measured with a *Quantum Design Physical Properties Measurement System* in a temperature range of 2-395 K with data collection in 150 temperature steps. At each of these steps, three responses to a heat pulse were measured. The temperature difference was gradually increased logarithmically between two measurement steps from low to high temperature. Data analysis was done using the *Quantum Design MultiVu* software. For fitting, three temperature ranges were used with two seventh order polynomials and one Haas-Fisher function (Haas Jr. and Fisher, 1976) with

$$C_p = h_0 + h_1 \cdot T + h_2 \cdot T^{-2} + h_3 \cdot T^{-0.5} + h_4 \cdot T^2. \tag{2.15}$$

As reference materials, Al_2O_3 (SRM-720) and Cu (Alfa Aesar, 99.999 %) were used to determine the accuracy of the heat capacity measurements. While a comparison of the Al_2O_3 data with data of Ditmars *et al.* (1982) showed a deviation of 2 % between 50-395 K and 6 % below 50 K, the heat capacity data for Cu compared to Lashley *et al.* (2003) showed deviations of < 1 % between 40-300 K and ≈ 2 % below 40 K.

2.2.9 Second-harmonic generation

As a probe for detecting phase transformations of $LaPO_4$ at high pressure (HP), second-harmonic generation (SGH, also known as frequency doubling) was used as a non-linear optical process that is sensitive to structural changes. SHG, as described in Ruiz-Fuertes *et al.* (2016), is only allowed within non-centrosymmetric space groups, *i.e.* systems without a center of inversion. Even though the SHG signal can also be zero in non-centrosymmetric space groups, the occurrence of a SHG signal undoubtedly indicates non-centrosymmetry. Bayarjargal and Winkler (2014) gave a summary on the use of SHG for high-pressure experiments. SHG was measured using a Nd:YLF laser ($\lambda = 1054$ nm). The signals were measured at $\lambda_{2\omega} = 527$ nm in transmission geometry. The set-up is described in Bayarjargal *et al.* (2009). For measuring the SHG intensities, some $LaPO_4$ crystals were ground to fine powders and then compacted to pellets.

Chapter 3: Results and Discussion

The results discussed in the following chapter are grouped into four topics. The first part considers powder results and discusses which factors influence the monazite structure within solid solutions of monazite compounds. The following section deals with single crystals covering the whole range of experiments from the crystal growth to room temperature structural analyses. The third part describes non-ambient characterisation where high-pressure and high-temperature studies are presented. The last section discusses thermodynamic properties, mainly focussing on calorimetric investigations.

3.1 Room temperature characterisation of powders

In this section, the influence of substituting different *Ln* cations on the monazite structure is described. The samples were first subjected to chemical and thermal characterisation, after which they were analysed using RT XRD and spectroscopic methods (IR and Raman).

3.1.1 Chemical analyses

The aim of the chemical analysis was to answer the following questions:

- Did the precursors fully convert into monazite?
- What is the composition of the powders?
- How homogeneous are they?

The monazite solid solutions LaPr, PrSm, PrNd, and NdSm were analysed by EPMA with respect to their chemical composition. For measurements, non-porous areas of uniform grey 'colour' were chosen. These areas needed to be at least 5 μm in diameter to assure that the activation volume of the beam was always inside the volume that was to be analysed and not, for example, within the embedding material. For PrNd and NdSm, it was hard to find such regions and in those cases, no measurements could be performed. Within all of the four investigated solid solutions, the grains were found to be aggregates of micron-sized crystallites (fig. 3.1). They were highly porous which is probably due to the loss of H_2O and NH_4 during the synthesis (see chapter 2.1.2).
The influence of the porosity of the samples is clearly seen in the three empirical parameters by Terra *et al.* (2003) (see subsection 2.2.1). Most of the measurements

on NdSm yielded elemental compositions summing up considerably more than 100 %. After a re-calibration, the results were corrected down by 1 %. Still many results showed higher sums. Therefore, in the case of NdSm, the range of considering a measurement as 'acceptable' was extended to 98.5 to 102.6 %.
For PrNd, barely any useful measurements were possible. The grains were too small and the material too porous and too heterogeneous for this spatially resolved chemical characterisation method to yield useful results.

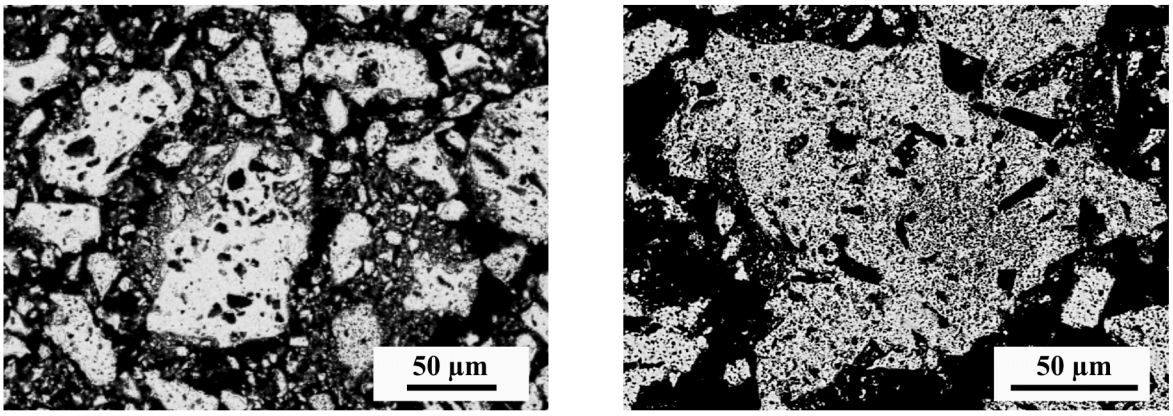

Figure 3.1 Back-scattered electron (BSE) images of monazite powder samples (left: $La_{0.8}Pr_{0.2}PO_4$; right: $Pr_{0.5}Nd_{0.5}PO_4$). All grains are highly porous.

As described in subsection 2.2.1, only those measurements were taken into account that fit the parameters by Terra *et al.* (2003). Tables 3.1 and 3.2 show the chemical compositions of LaPr, PrSm and NdSm calculated from the EPMA data. Table A.3 in the Appendix gives the results when no selection criteria are applied. A clear deviation can be found between the results for all and for the selected measurements. This means, that the errors are much larger when all measurements are taken into account compared to the calculation based on the selection criteria. This can be explained by porous areas or by impurities that were not seen during the selection of the measurement spot. This yields wrong calculations of the compositions. Especially the solid solutions containing Sm seen to be influenced because the Ln_1/Ln_2 ratios calculated from all measurements are higher than those from the selected ones. This might be due to the matrix correction. Yet, the mayor issue for these deviations is the high porosity of the samples. As those measurements not fitting the above mentioned criteria were excluded because the yield unreliable data, the following discussion will focus only on the results of the selected ones.

Table 3.1 Results of EPMA analyses for atomic fraction (*i.e.* the composition, x) and Ln_1/Ln_2 ratios in LaPr, PrSm, and NdSm solid solutions (as described in subsection 2.2.1, according to Terra *et al.*, 2003). The nomial (nom.) and calculated values are presented. Errors (standard deviation) are given in brackets.

x (nom.)	x_{Pr} (LaPr)	x_{Sm} (PrSm)	x_{Sm} (NdSm)	Ln_1/Ln_2 (nom.)	La/Pr (LaPr)	Pr/Sm (PrSm)	Nd/Sm (NdSm)
0.0	0.00(1)	0.00(1)	0.00(1)	-	-	-	-
0.1	0.09(1)	0.10(1)	0.09(2)	9	10(2)	10(1)	9(1)
0.2	0.20(5)	0.20(3)	0.20(3)	4	4(1)	4(6)	4.1(4)
0.3	0.28(3)	0.30(3)	0.29(3)	2.33	2.6(3)	2.3(2)	2.2(1)
0.4	0.40(3)	0.41(3)	0.39(4)	1.5	1.5(2)	1.5(1)	1.4(2)
0.5	0.52(5)	0.51(3)	0.49(3)	1	1.0(2)	1.0(1)	0.98(9)
0.6	0.63(6)	0.62(4)	0.58(4)	0.67	0.60(2)	0.6(9)	0.65(8)
0.7	0.71(5)	0.74(4)	0.69(2)	0.43	0.41(1)	0.36(6)	0.42(4)
0.8	0.81(2)	0.81(2)	0.80(2)	0.25	0.24(3)	0.24(2)	0.25(4)
0.9	0.91(1)	0.91(1)	0.90(1)	0.11	0.10(1)	0.10(1)	0.10(3)
1.0	1.00(1)	0.00(1)	1.00(1)	-	-	-	-

Table 3.2 Results of EPMA analyses for the atomic ratio ΣLn/P in LaPr, PrSm, and NdSm solid solutions (as described in the text, according to Terra *et al.*, 2003). The nomial (nom.) and calculated values are presented with errors (standard deviation) in brackets. The number of measurements (n) as those selected (sel.) for the evaluation *e.g.* matching the selection criteria named in subsection 2.2.1 in comparison to the total number of measurements as given in brackets (all).

x (nom.)	(La+Pr)/P (LaPr)	(Pr+Sm)/P (PrSm)	(Nd+Sm)/P (NdSm)	n(LaPr) sel.(all)	n(PrSm) sel.(all)	n(NdSm) sel.(all)
0.0	1.1(1)	1.00(1)	0.98(3)	14(15)	48(50)	42(50)
0.1	0.96(1)	0.99(2)	0.99(2)	13(15)	38(50)	31(50)
0.2	0.95(7)	0.99(4)	0.99(3)	11(15)	42(50)	36(50)
0.3	0.95(4)	0.99(4)	0.99(3)	12(15)	41(50)	41(50)
0.4	0.94(5)	0.99(4)	1.00(6)	11(15)	41(50)	42(50)
0.5	0.95(8)	0.99(5)	1.00(5)	12(15)	37(50)	27(50)
0.6	0.95(9)	0.97(8)	0.99(6)	13(15)	35(50)	22(50)
0.7	0.95(7)	0.98(5)	0.99(4)	13(15)	31(50)	29(50)
0.8	0.96(3)	0.98(3)	0.99(5)	15(15)	32(50)	22(50)
0.9	0.93(8)	0.99(3)	0.97(3)	13(15)	39(50)	29(50)
1.0	0.97(1)	1.00(1)	0.97(1)	15(15)	33(50)	48(50)

Within 1σ, no deviation from the nominal composition was found for the measurements. This error represents the statistic or random errors achieved from the standard deviation. In the case of EPMA, systematic errors will mostly influence the values arising from imperfect calibration. However, there were some impurities in some samples of the solid solutions. Those areas were rather small as shown in figure 3.2 so that it was not possible to analyse their exact compositions. In the BSE images, these areas are brighter than the surrounding monazite. This is a sign of *Ln*-richer phases which means that these impurities are most probably phosphate loss phases due to the synthesis procedure.
The ratio of Ln_1/Ln_2 in all three solid solutions is, within the errors, in agreement with the expected value. Additionally, the ratio (Ln_1+Ln_2)/P remains constant. In conclusion, the samples can be considered to be single phase and homogeneous. Applying the selection criteria ensures that no phosphate excess or deficit phases were included in the calculations. On the basis of the Ln/P ratio, the impurities found in NdSm and PrNd (fig. 3.2) are most probably phosphate deficit phases like Ln_3PO_7. These phases form probably because the $NH_4H_2PO_4$ excess in the synthesis is not high enough to form pure monazite and the system may have lost too much phosphate during the solid state reaction. Another explanation for the brighter areas is that the reaction was not finished so that *Ln*-richer areas remained in the samples. Still, it cannot be excluded that there are also phosphate excess phases present. However, no exact determination of the chemical composition of the impurities was possible with the given analysis.

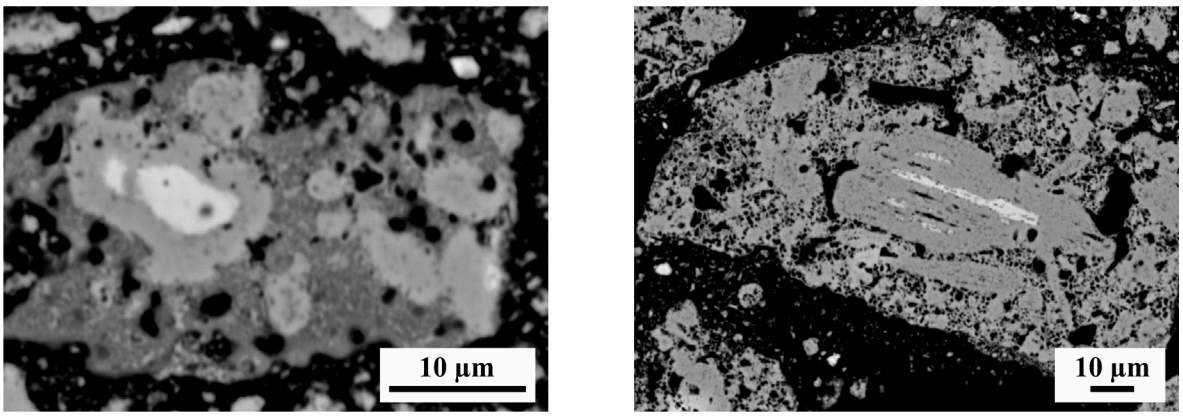

Figure 3.2 Back-scattered electron (BSE) images of monazite powder samples (left: $Pr_{0.3}Nd_{0.7}PO_4$, right: $Pr_{0.4}Nd_{0.6}PO_4$). The dark grey areas are monazite. The lighter grey parts are impurities. Since these impurities are rather small, their compositions could not be determined with sufficient accuracy.

3.1.2 Thermal characterisation of the powder samples

From the chemical analyses, some questions originated:

- Do the intragranular inclusions influence the thermal behaviour?
- Do possible PO_4 excess phases get lost during heating?
- Is there any absorption of H_2O or CO_2?

Thermal characterisation of LaPr using TG and DSC did not show any reaction or phase transition. All samples showed similar behaviour (see fig. 3.3). For the pure Pr end member, a deviation of ≈ 1 wt% from the behaviour of the other solid solution members was observed. However, after an additional heating cycle with the same parameters the thermal behaviour was essentially the same as for the other samples. This deviation from the other samples is probably due to the loss of adsorbed water or a surplus of P_4O_{10} due to the excess of $NH_4H_2PO_4$ during synthesis. Another influence might be the redox reaction of Pr^{3+}. Nevertheless, no indications for additional P or Pr phases were found within XRD analyses as presented in chapter 3.1.3.

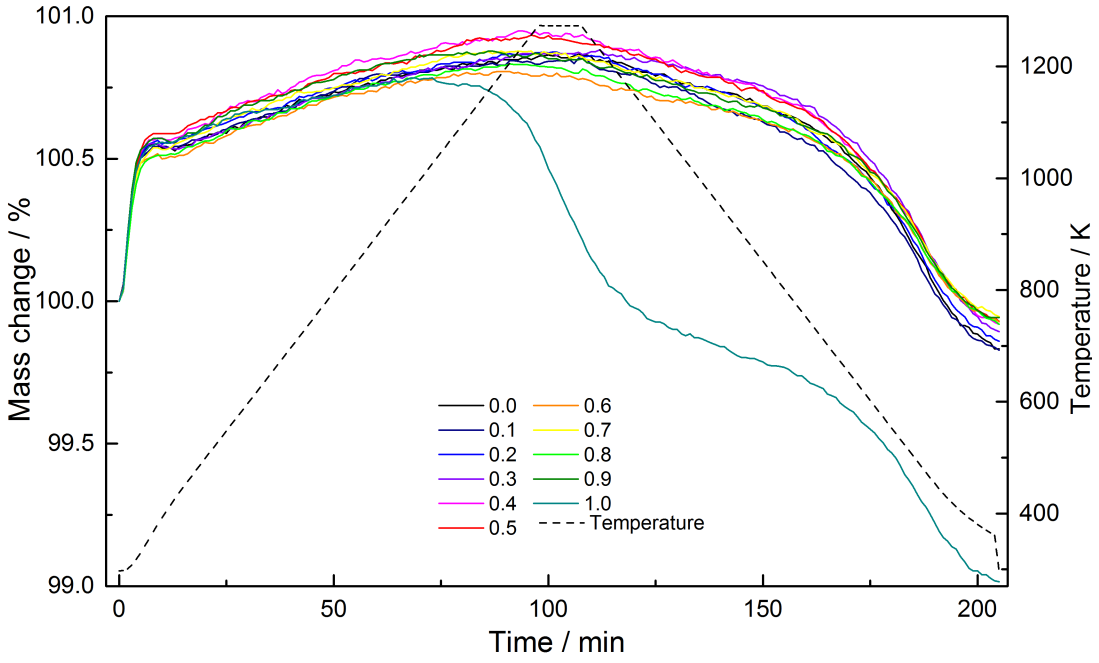

Figure 3.3 Thermogravimetric analyses of LaPr. The numbers represent the atomic fraction x_{Pr}. Except for the pure Pr end member, all compositions show similar behaviour. After a second heating cycle under the same conditions, the curve for $PrPO_4$ was the same as for the other solid solutions.

3.1.3 Structural investigations

XRD was used to answer the following questions:

- How does the *Ln* substitution influence the lattice parameters of monazite?
- How large are these changes within each solid solution and from the smallest to the largest end member?
- How do the bonds change upon substitution?
- Can the impurities be identified?

All solid solutions analysed with RT XRD were found to be pure monazite when synthesised with an excess of $NH_4H_2PO_4$. Although different conventional diffractometers were used, the lattice parameters are in very good agreement and equivalent within the uncertainties. For comparison, the results for $LaPO_4$ measured on different diffractometers are shown in table 3.3. The results are essentially similar to Ni *et al.* (1995). There is a significant difference between the results from Synchrotron XRD compared to the other ones. The errors given in table 3.3 are calculated from the correlation matrix during the least-squares procedure of the Rietveld method and are not physically meaningful. As described by Scott (1983) and Bérar and Lelann (1991), these errors would have to be multiplied by 3 or 4 to obtain a reasonable 1σ. However, this can only be done if the fit reaches low GoF values (close to 1). Additionally, the errors for the Synchrotron measurements are even more underestimated when calculating the intensity distribution from the 2D frames (Chall *et al.*, 2000). However, when calculating a significant error of 3σ, the values given in table 3.3 are comparable.

Table 3.3 Comparison of the lattice parameters from structural refinements on $LaPO_4$ for conventional diffraction and synchrotron data (short: 0.5 s/step; long: 1.5 s/step) in comparison to Ni *et al.* (1995): lattice parameters ($\vec{a}$, $\vec{b}$, $\vec{c}$, β), volume of the unit cell (V_{uc}) and quality criteria for powder Rietveld analyses (R_{wp}: R-value for the whole pattern; GoF: goodness of fit).

	X'pert Pro	*D8* (short)	*D8* (long)	Synchrotron	Ni *et al.* (1995)
$\vec{a}$	6.83951(8)	6.8355(5)	6.8355(5)	6.84133(8)	6.8313(10)
$\vec{b}$	7.07435(8)	7.0732(5)	7.0738(3)	7.07590(8)	7.0705(9)
$\vec{c}$	6.51053(7)	6.5068(4)	6.5070(3)	6.51233(7)	6.5034(9)
β	103.2865(8)	103.278(5)	103.282(3)	103.2892(9)	103.27(1)
V_{uc}	306.581(6)	306.19(4)	306.28(2)	306.811(6)	305.73(7)
R_{wp}	7.405	12.94985	8.11359	2.975	-
GoF	0.990	-	-	0.862	-

Effective ionic radii according to Shannon (1976) were calculated for comparison of the different solid solutions. For this purpose, the radii of the end members have been

averaged according to the x-value in the chemical formula. For LaPr, the synchrotron data are used in the following. A view on the monazite structure along the $\vec{b}$ axis is shown in figure 3.4.

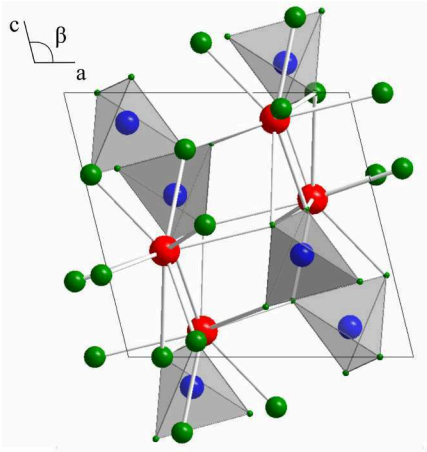

Figure 3.4 Monazite structure projected along [010] ($\vec{b}$) after Ni et al. (1995). In red: *Ln*; in blue: P; in green: O.

Within all monazite solid solutions, an increase in $\vec{a}$, $\vec{b}$ and $\vec{c}$ as well as an increase in the unit cell volume can be seen from pure $GdPO_4$ to pure $LaPO_4$, while β decreases (fig. 3.5 and fig. 3.6). The results can also be found in the tables A.4 for LaPr, A.5 for PrSm, A.6 for PrNd, A.7 for NdSm, A.8 for NdEu, and A.9 for SmGd in the Appendix. Reproducibility was proven because many end members were synthesised within several solid solutions and measured on different diffractometers and still yield essentially the same lattice parameters within the standard deviation. An almost ideal behaviour can be seen reflecting results from earlier workers for pure endmembers (*e.g.* Ni *et al.*, 1995; Thiriet *et al.*, 2005; Mullica *et al.*, 1985b,a; Ushakov *et al.*, 2001; Bregiroux *et al.*, 2007a; Hikichi, 1991) and for solid solutions (*e.g.* Arinicheva *et al.*, 2014; Thust *et al.*, 2015; Terra *et al.*, 2003; de Biasi *et al.*, 1987; Yang *et al.*, 2009; Hou *et al.*, 2009; Kitamura *et al.*, 2004; Ferhi *et al.*, 2008; Yang *et al.*, 2014; Yaiphaba *et al.*, 2010; Popa *et al.*, 2007; Wang *et al.*, 2014; Zeng *et al.*, 2014). The lanthanide contraction (the decrease of the ionic radii with increasing atomic number: from La^{3+} (1.216 Å) to Gd^{3+} (1.107 Å), Shannon, 1976) is seen in a decrease of the lattice parameters from La to Gd, or, as given in figures 3.5 and 3.6, in an increase from Gd to La. The slight decrease of β is a consequence of the changing lattice parameters. Figure 3.4 shows an illustration of the monazite structure detailing on β. The connection of the chains along $\vec{c}$ of subsequent LnO_9 and PO_4 polyhedra is within the $\vec{a}$-$\vec{b}$ plane. With increasing *Ln* radius, the chains seem to tilt towards the $\vec{a}$ axis which would result in the observed decrease of β. While the percentage increase from Gd to La for $\vec{a}$ and $\vec{c}$ is comparable (2.75(2) % and 2.70(2) %, respectively), the change in $\vec{b}$ is slightly higher (3.24(1) %), which can be seen in the slightly steeper increase. α and γ, however, are constrained by the space group symmetry to be 90°.

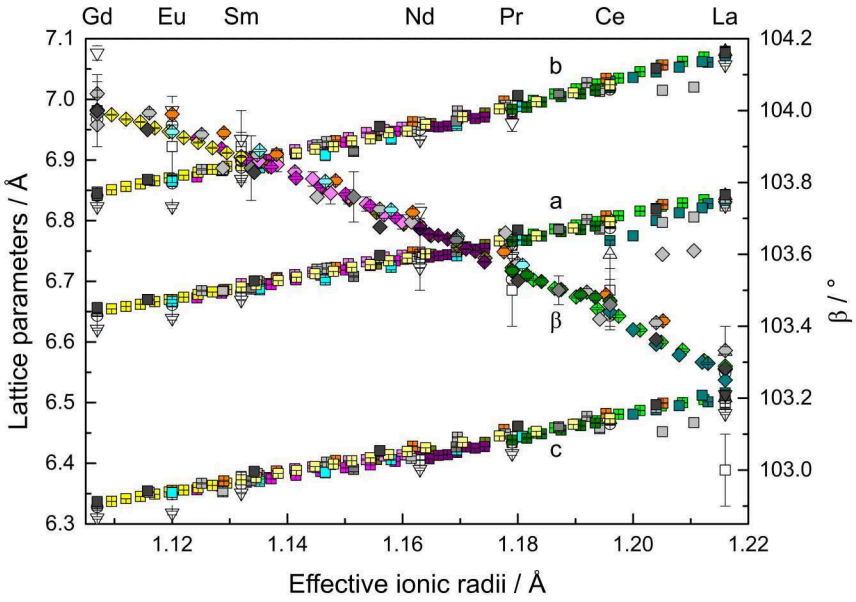

Figure 3.5 Lattice parameters of various monazite-type solid solution members vs. the effective ionic radius (Shannon, 1976) after Schlenz *et al.* (2017). For the explanation of the symbols see table 3.4. For this thesis, the solid solutions LaPr, PrNd, PrSm, NdSm, NdEu, and SmGd were synthesised.

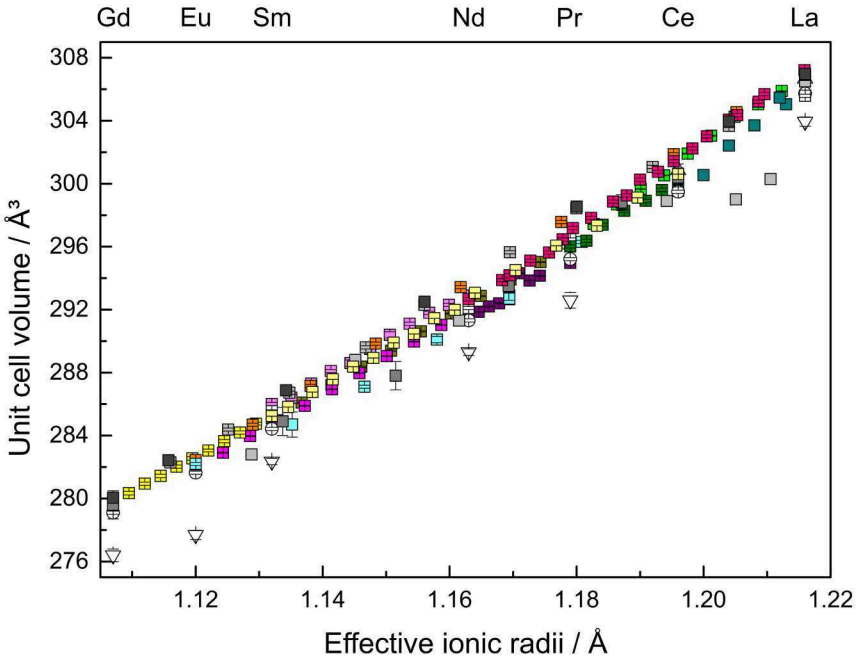

Figure 3.6 Unit cell volume of various monazite-type solid solution members vs. the effective ionic radius (Shannon, 1976). For the explanation of the symbols see table 3.4. For this thesis, the solid solutions LaPr, PrNd, PrSm, NdSm, NdEu, and SmGd were synthesised.

Table 3.4 Legend for figures 3.5 and 3.6 containing the symbol, the composition in terms of the abbreviated formula of the solid solution or the end members and the references.

Symbol	Chemistry	Reference
□	CeEu	Wang *et al.* (2014)
□	CeGd	Yang *et al.* (2014)
□	CePr	Zeng *et al.* (2014)
□	CeSm	Heuser (2015)
□	LaCe	de Biasi *et al.* (1987); Hou *et al.* (2009)
□	LaEu	Neumeier *et al.* (2017)
□	LaGd	Neumeier *et al.* (2017); Terra *et al.* (2003)
□	LaGd:Eu	Huittinen *et al.* (2017)
□	LaNd	Schlenz, per.comm. (2017)
□	LaPr	Hirsch *et al.* (2017), this work
□	NdEu	Schumacher (2016), this work
□	NdSm	Kuleci (2015), this work
□	PrNd	Claßen, pers.comm. (2015), this work
□	PrSm	Bigdeli (2016), this work
□	SmGd	Ladenthin (2017), this work
▽	end members	Mullica *et al.* (1984, 1985b,a)
○	end members	Ni *et al.* (1995)
△	end members	Terra *et al.* (2003)
□	end members	Ushakov *et al.* (2001)

Due to the higher quality of the synchrotron data compared to the measurements on conventional diffractometers (in terms of better counting statistics and higher angular resolution), the structural changes are discussed in the following on the basis of the synchrotron data. However, the absolute precision in the lattice parameters is the same. As reported in Hirsch *et al.* (2017) and shown in figure 3.7, there is a small deviation of the unit cell volume of LaPr from linear behaviour. This excess volume appears to be symmetrical around $x_{\mathrm{Pr}} = 0.5$. The reason for this is the non-ideal mixing due to the different cation sizes (2.8 % difference between La^{3+} and Pr^{3+}) yielding strain effects in the structure. Both, symmetric and asymmetric functions fit V_{ex}. However, since the deviation is rather small (about 0.15 %), none of the two can be explicitly chosen or ruled out.

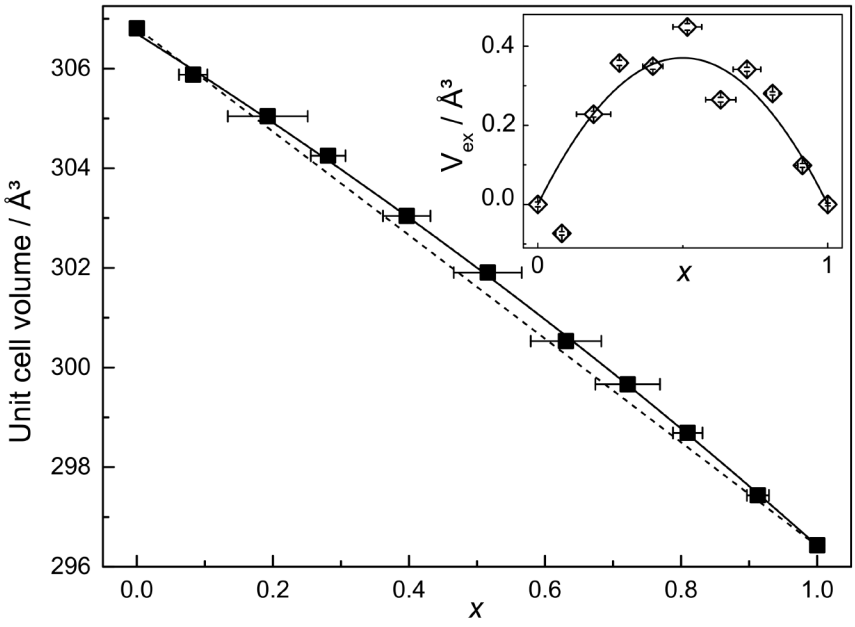

Figure 3.7 Volume and excess volume (V_{ex}) of LaPr against the Pr content x after Hirsch *et al.* (2017). All lines are guides to the eye. Errors bars may be smaller than the symbols.

Synchrotron data were used for calculating bond distances. However, though powder data is not of as high quality as single crystal data for evaluating these features, only the observed changes below will be discussed here. For further a discussion on bond lengths see subsection 3.2.3 concerning single crystal analysis.
Figures 3.8 and 3.9 show the different *Ln*-O and P-O bond lengths, respectively, obtained from the synchrotron data. Additionally, an average value is added. Tables A.10 and A.11 in the Appendix list these results. In figure 3.8 on the right, the atomic positions in the chain structure of monazite are shown.
The *Ln*–O^2 bond in the LnO_9 polyhedron is the longest within the structure and remains the longest throughout the whole solid solution. Following the nomenclature of Ni *et al.* (1995) and Mullica *et al.* (1986), this bond is located in the polyhedron chain between the LnO_9 and PO_4. The *Ln*–O^1 bond is notably shorter, although it is also part of the bidentate bonding (see fig. 3.8 on the right). The reason for this difference might be the slight tilting of the polyhedra against each other. The average *Ln*–O bond length decreases with increasing Pr content due to the smaller ionic radius (La^{3+}: 1.216 Å; Pr^{3+}: 1.179 Å Shannon, 1976).
The mean distances (La–O: 2.573(8) Å and Pr–O: 2.532(6) Å) are slightly shorter than the expected ones calculated from Shannon (1976): 2.596 Å for La–O and 2.559 Å for Pr–O. This can be explained by some covalent character of the bonding which was also stated by Li *et al.* (2009). They show that O^2 has the least covalent bond character of all oxygen ions in the monazite structure resulting in longer bond lengths which is in agreement with these findings.
The P–O bond lengths scatter around the average which remains constant at ≈ 1.56 Å within the uncertainties (see table A.11 in the Appendix). The P–O^1 bond is slightly

longer than the other bonds. This matches the findings on *Ln*–O^1 being shorter than *Ln*–O^2 in the chain structure. The shorter bond length can be explained by the fact that the O^2 seems to be more attracted by P while O^1 is more attracted to *Ln* according to the results of Li *et al.* (2009).

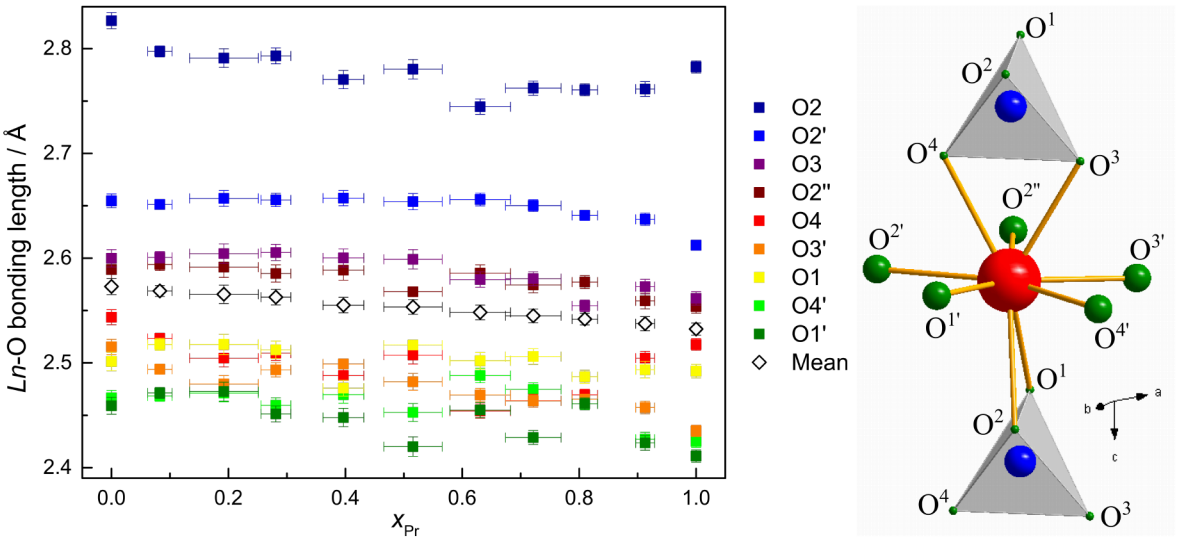

Figure 3.8 *Ln*-O bond lengths obtained from Synchrotron powder XRD on LaPr vs. the Pr content. The average *Ln*-O bond length is included as mean. Oxygen atoms are named according to Mullica *et al.* (1984) and Ni *et al.* (1995) and given on the right.

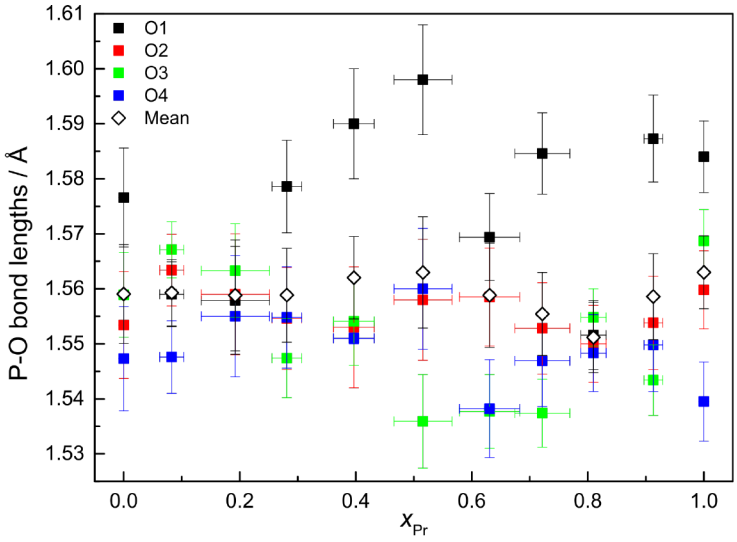

Figure 3.9 P-O bond lengths obtained from Synchrotron powder XRD on LaPr vs. the Pr content. Oxygen atoms are named according to Mullica *et al.* (1984) and Ni *et al.* (1995) and given in figure 3.8 on the right. The average P-O bond length is included as mean.

The PO_4 tetrahedron shows an angular distortion. For all members of the solid solution series, three angles are larger (up to 116.1(5)°) and three angles are smaller (down to 101.8(3)°) than the ideal intratetrahedra angle (109.5°). This can be explained by Coulomb repulsion between *Ln* and P. Both share two O atoms along the chain. The Coulomb repulsion therefore shortens the O–O edge length in-between the two cations (fig. 3.10). This distortion is known from pure monazite and monazite solid solutions (*e.g.* Mullica *et al.*, 1984, 1985a,b, 1990). Still no trend with changing composition was found within the experimental uncertainties. Concluding, the PO_4 tetrahedron in monazite can be seen, as expected, as a 'rigid body'. However, single crystal results will reveal more accurate structural features (see chapter 3.2.3).

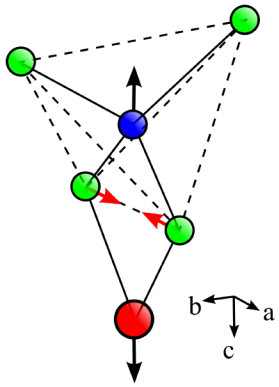

Figure 3.10 Detail of the monazite chain (In red: *Ln*; in blue: P; in green: O): The Coulomb repulsion (black arrows) in the LnO_9-PO_4 chains in monazite between *Ln* and P results in a shortening (red arrows) of the O–O edge between the cations.

3.1.4 Spectroscopy

Optical spectroscopy is in many respects complementary to XRD. In particular, it allows to study the local structure of the atoms. Open questions in this chapter resulting from XRD are:

- Do the PO_4 tetrahedra behave as 'rigid' as it seems from XRD?
- How does substitution on the *Ln* site influence the local structure?
- Do the PO_4-related modes change upon substitution?

To answer these questions, IR and Raman spectra were recorded. These two techniques are complementary because often different modes are activated. IR spectra typically reveal a lot of strongly overlapping modes, therefore, additional Raman spectra can help to answer the open questions stated above.
Generally, in IR spectra of monazites, only modes related to the PO_4 tetrahedron are visible, while in Raman spectra also some lattice contributions can be found. The principal PO_4 modes are depicted in figure A.1 in the Appendix. The symmetric and asymmetric bending modes ν_2 and ν_4 are low-energy modes and thus occur at a smaller wave number range because they need less energy to be excited. The higher energetic stretching modes ν_1 and ν_3 (symmetric and asymmetric, respectively) are visible in the higher wave number range. Except for ν_1, all modes are degenerate. For an ideal tetrahedron with the symmetry $\bar{4}3m$ (T_d), all degenerate modes would give the same frequency (Herzberg, 1945). However, since all atoms in monazite are located on general positions, the symmetry of the PO_4 tetrahedron is lowered to 1 (C_1). Hence, all degenerate modes may appear in the spectrum (*e.g.* Kitaev *et al.*, 2004; Silva *et al.*, 2006).
The IR spectra of all LaPr samples were very similar within the whole wave number range (fig. 3.11 on the left). The part of high wave numbers is influenced by broad bands of the symmetric and asymmetric stretching modes of water (ν_1: 3657 cm^{-1} and ν_3: 3756 cm^{-1}), the medium wave number part shows modes of CO_2 (ν_3: 2349 cm^{-1}, asymmetric stretching mode) and H_2O (ν_2: 1595 cm^{-1}, bending mode) (*e.g.* Jones, 1963). The presence of these modes can be explained by adsorbed H_2O or CO_2 because the KBr used for the preparation of the samples was not dried. Therefore, the main focus for the evaluation is the lower wave number part between 1200 to 400 cm^{-1} where all PO_4 modes occur (fig. 3.11 on the right).
All four IR active vibrations related to the PO_4 modes in monazite according to Hezel and Ross (1966) were observed. Figure 3.11 (right) shows the region of the IR spectra which can be attributed to the four different modes. Asymmetric (ν_3) and symmetric (ν_1) stretching modes yielded a broad band between 1094-993 cm^{-1} and a sharper band at 957-953 cm^{-1}, respectively. The broad signal between 621-538 cm^{-1} can be assigned to the asymmetric bending mode (ν_4) However, the symmetric bending mode (ν_2) only appears as a small shoulder of ν_4. The broadening of ν_3 and ν_4 is due to the degeneracy of the modes resulting in combination and /or overtone modes (Hezel and Ross, 1966).

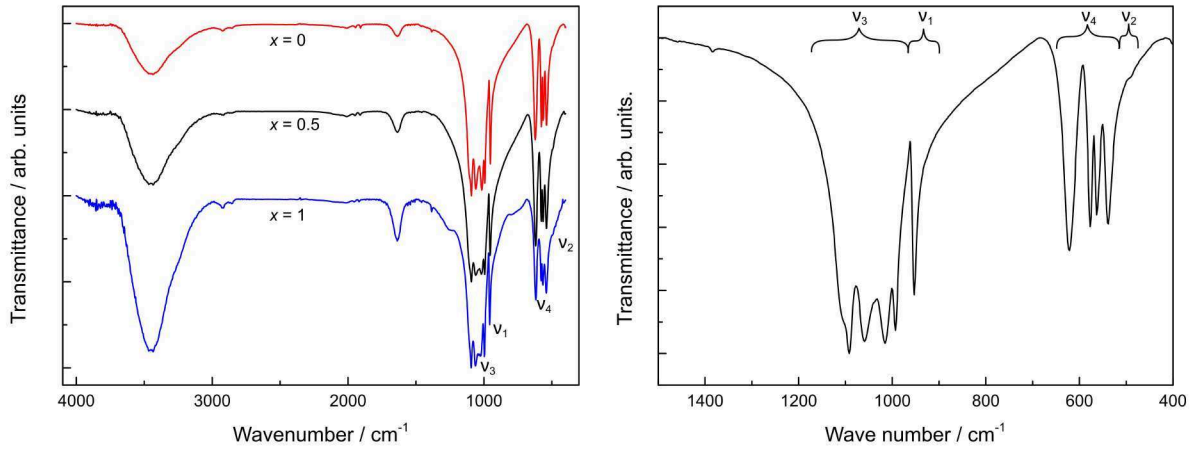

Figure 3.11 IR spectra of three LaPr members (left) and IR spectrum of the *fingerprint* region of $LaPO_4$ at small wave numbers (right). Indicated are the four bending and stretching modes $\nu_1, \nu_2, \nu_3, \nu_4$ of the PO_4 tetrahedra.

Because of the overlapping bands, the only possible way to analyse these modes was localising their minima. It was not possible to use line profiles for fitting the bands because of their overlap. For ν_2, the position was chosen by eye, because in most data sets, ν_2 was barely visible and it was not possible to obtain an exact minimum. Due to this kind of data processing, no clear change could be found in ν_2. Only ν_1 shows a slight increase with increasing Pr content (fig. 3.12). However, since the errors shown are only within 1σ, the apparent trend is hardly significant. The same holds true for ν_3 and ν_4. All results are also given in table A.12 in the Appendix. In general, the IR results are heavily biased due to the overlap in the bands which could not be resolved by data processing. Therefore, additional Raman spectroscopy was employed to understand the influence of substitution in monazite on the PO_4 tetrahedra.

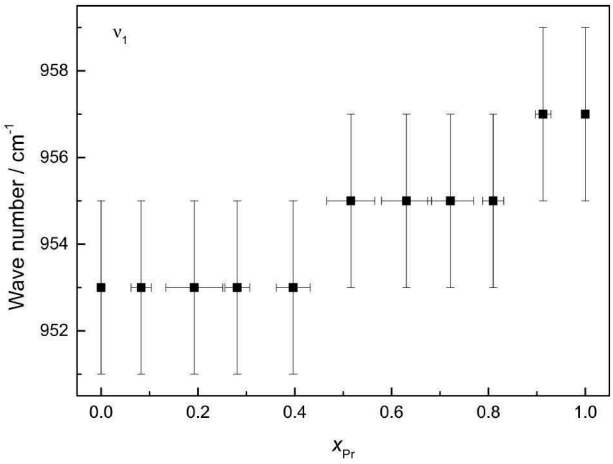

Figure 3.12 IR mode ν_1 in LaPr. With increasing Pr content, ν_1 shifts to higher wave numbers.

The Raman modes of monazite are divided into modes resulting only from PO_4 and modes resulting from the lattice in total (Begun *et al.*, 1981; Silva *et al.*, 2006; Ruschel *et al.*, 2012). According to factor group analysis, 36 Raman active modes are predicted, of which 21 were unambiguously identified (table A.13 in the Appendix). A representative Raman spectrum of $PrPO_4$ is given in figure 3.13.

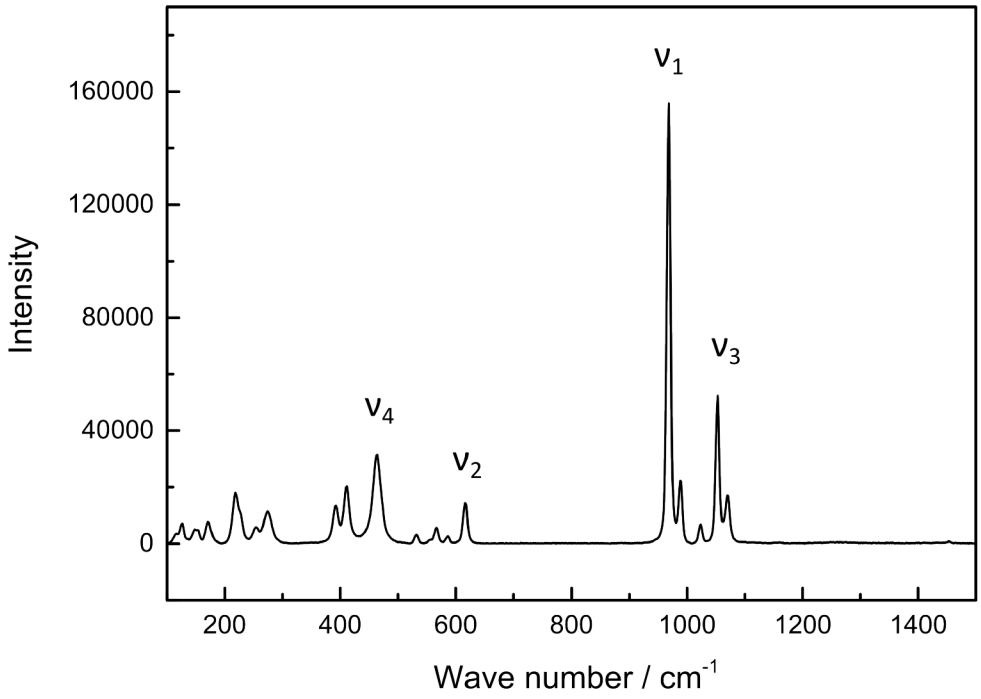

Figure 3.13 Raman spectrum of $PrPO_4$. Indicated are the four bending and stretching modes ν_1, ν_2, ν_3, and ν_4 of the PO_4 tetrahedra.

While most of the PO_4 modes are clearly discriminated, the lattice modes, especially in the lower wave number range, overlap. Therefore, not all modes could be found for all compositions. Furthermore, samples containing a higher amount of Sm were strongly influenced by fluorescence. This yielded additional modes at around 800, 930 and 1120 cm^{-1} (fig. 3.14).

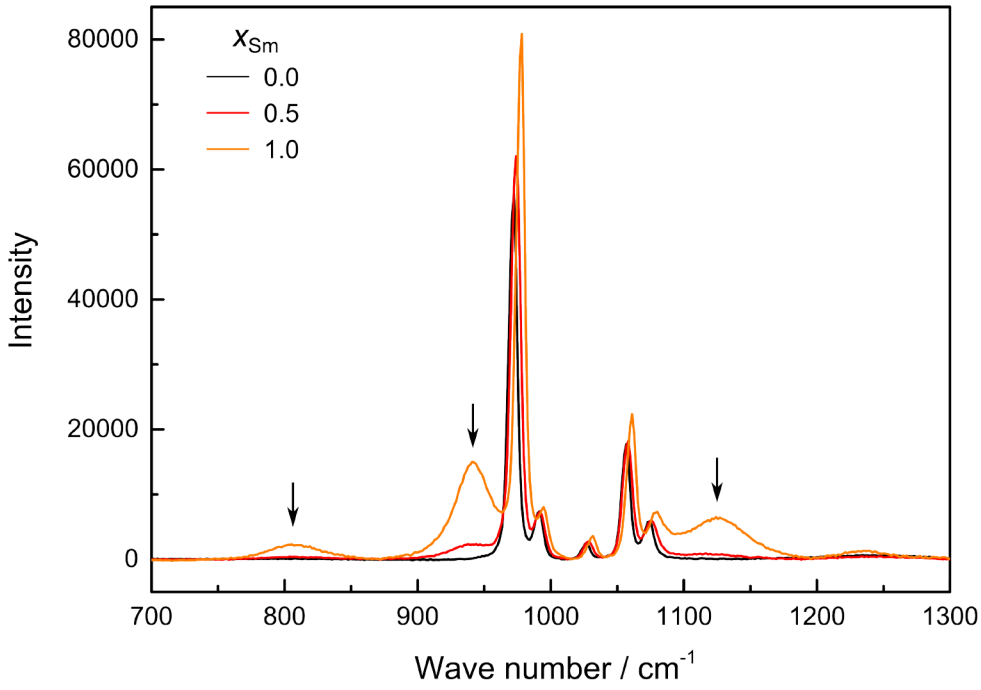

Figure 3.14 Raman spectra of NdSm showing the influence of fluorescence (marked with arrows) with increasing Sm content.

The most pronounced modes were those related to the phosphate group. The ν_1, ν_2, ν_3 and ν_4 are observed between 960-975 cm^{-1}, 460-470 cm^{-1}, 1050-1060 cm^{-1}, and 615-625 cm^{-1}, respectively. According to DFT calculations by Ruschel *et al.* (2012) and considering the assignment by Beall *et al.* (1981), ν_2 and ν_4 are influenced by the angles O^1-P-O^2 and O^3-P-O^4 whereas the stretching mode ν_1 is solely influenced by the bond distance P-O^2 and ν_3 depends on P-O^1 and P-O^3.

In all three solid solutions studied in this thesis (LaPr, PrSm, NdSm), the wave numbers of the PO_4 related modes decrease with increasing *Ln* radius (fig. 3.15). The results are also given in the tables A.15, A.16, and A.17 in the Appendix. Figure 3.16 shows the ν_1 mode of the three solid solutions in comparison to literature values by Heuser (2015), Begun *et al.* (1981), and Silva *et al.* (2006). The mismatch between the data presented here and those from the references is most probably due to calibration issues. Since the calibration for this set-up was done using the silicon mode (see section 2.2.4.2), accurate frequency values can be expected around 500 cm^{-1} but not around 1000 cm^{-1}. For this purpose, another calibration would be necessary (like plasma lines of HeNe (red) or Nd:YAG (green) lasers) which is not possible at the spectrometer used here.
The term 'blueshift' is often used to describe this behaviour. This means a shift to smaller wavelength, *i.e.* to larger wave numbers which can be seen in the figures 3.15 and 3.16 with decreasing ionic radii. This blueshift, although reported before, is still under discussion (*e.g.* Terra *et al.*, 2003; Chun-hua *et al.*, 2007; Ruschel *et al.*, 2012). It can be explained either by a compression of PO_4 tetrahedra (Begun *et al.*, 1981; Hobart *et al.*, 1983), or a contraction at the *Ln* cation site (Podor, 1995; Santos *et al.*, 2007).

In the first case, the PO_4 compression would result in a closer packing of the polyhedra and, therefore, yield shorter P-O distances. This would cause a shift of the modes to higher wave numbers (Begun *et al.*, 1981; Hobart *et al.*, 1983). In the second case, the contraction on the *Ln* site would yield a shortening of the *Ln*-O distances which would result in a shift to higher wave numbers (Podor, 1995; Santos *et al.*, 2007). Baran and Lavat (1982) show that the force constants of the P-O bonds decrease with increasing ionic radii from Gd to La. Santos *et al.* (2007) describe that for $LnVO_4$, the covalence of the V-O bonds decreases with increasing *Ln*-O distance which is similar for $LnPO_4$. The superposition of non-occupied atomic orbitals of the *Ln* and the highest-occupied molecular orbital (HOMO) of the PO_4 represents the chemical interaction between *Ln* and PO_4. The energy of the *Ln* atomic orbital increases with increasing ionic radii and approaches the energy of the HOMO. Therefore, the interaction (*i.e.* the force constant) between *Ln* and PO_4 decreases as the energy difference increases yielding a decrease of the frequencies of the internal modes and an increase of the *Ln*–O bond lenghts (Santos *et al.*, 2007).
Regarding the previously described behaviour of the bond distances (in section 3.1.3), the second explanation seems to be more likely: Since the *Ln*-O distances in LaPr show a decrease with increasing Pr content while the P-O bond lengths remain constant, the blueshift can be attributed to the contraction at the *Ln* site.

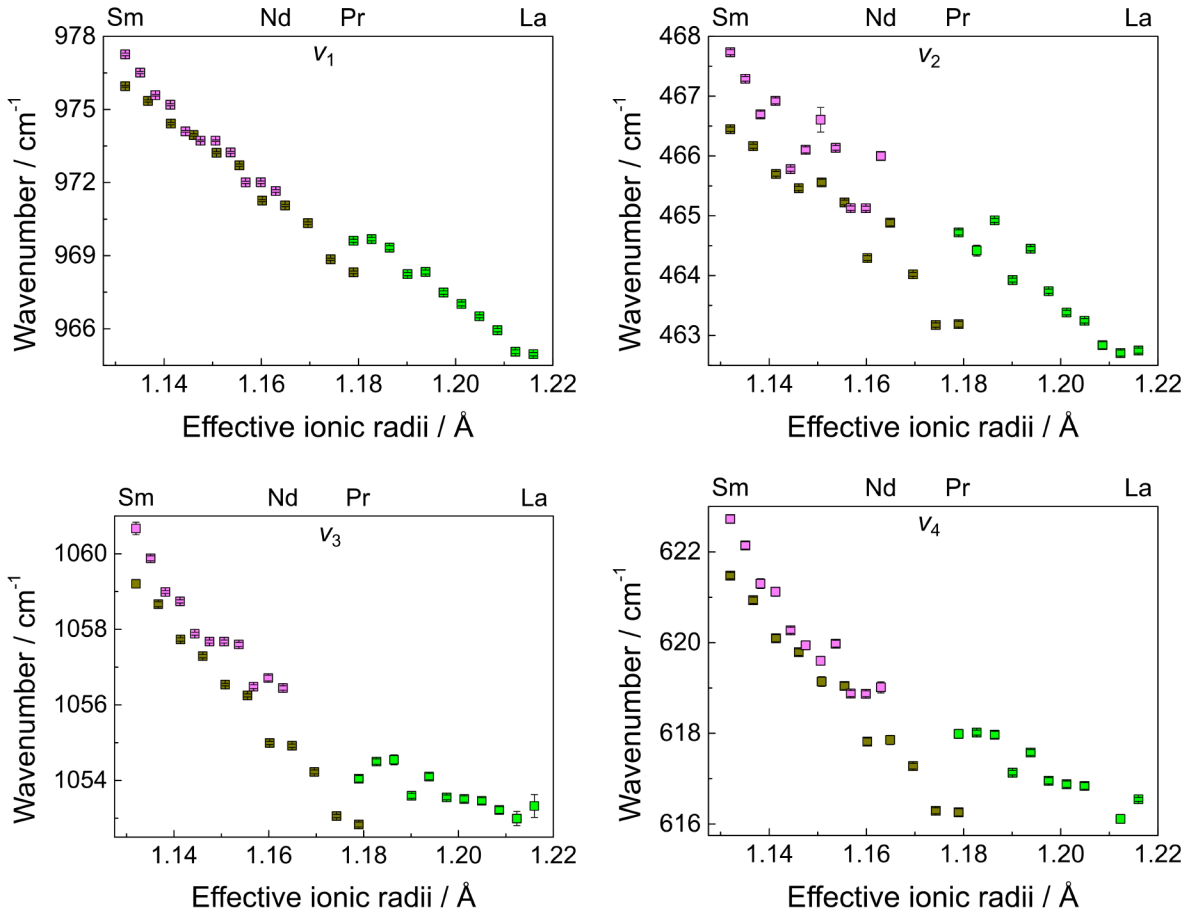

Figure 3.15 Raman modes in LaPr (bright green), PrSm (yellow-brown) and NdSm (pinkish) obtained in this thesis. All four modes show decreasing wave numbers with increasing ionic radius (Shannon, 1976).

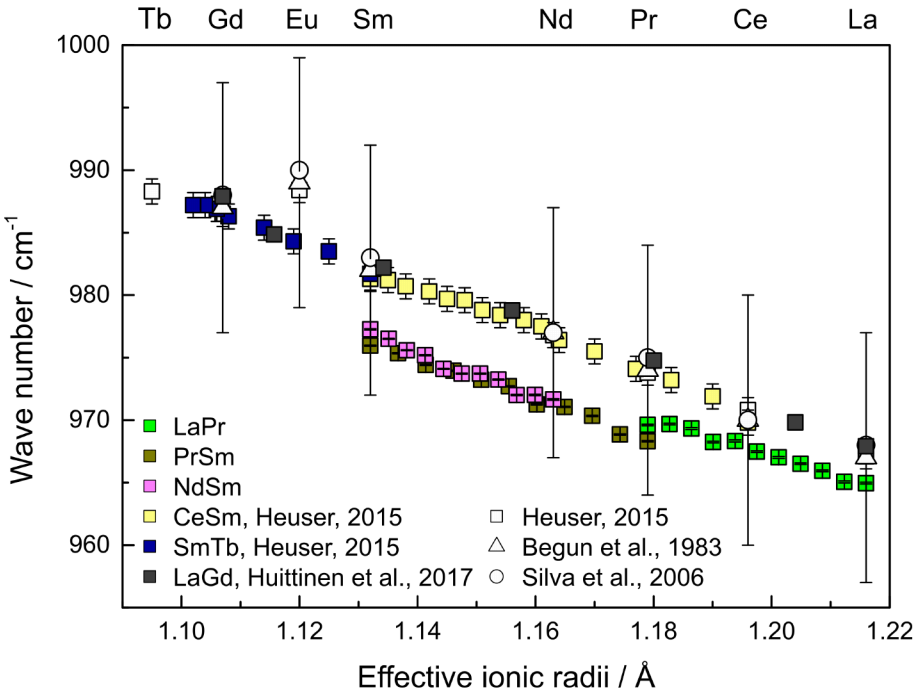

Figure 3.16 Raman modes ν_1 vs. effective ionic radius (Shannon, 1976): LaPr, PrSm, and NdSm from this thesis in comparison to literature values of Heuser (2015), Begun *et al.* (1981), Silva *et al.* (2006), and Huittinen *et al.* (2017).

The FWHM of the PO_4 modes of the three solid solutions are in the same range (fig. 3.17). The results are also given in the tables A.18, A.19, and A.20 in the Appendix. In most cases, the values for LaPr are slightly higher than those of the other two solid solutions. Some samples (like the pure $LaPO_4$ in LaPr which seems to be an outlier) showed much sharper profiles leading to much smaller FWHMs as seen for all four PO_4 modes. This may be explained by less porosity or larger grains of these samples. The broadening can also be explained by the disorder of the *Ln* cations within monazite structure as stated by Gouadec and Colomban (2007), Podor (1995), Raison *et al.* (2008), and shown by Huittinen *et al.* (2017). This means that the highest FWHM is expected for the samples with a Ln_1:Ln_2 ratio of 50:50. Additionally, the solid solution with the highest difference in the two *Ln* radii is expected to show a higher FWHM.
The FWHM of ν_1, ν_3 and ν_4 in dependence of the composition are mostly parabolic for all solid solutions. For LaPr, this behaviour is not as pronounced as for the other two solid solutions. For the FWHM of these modes, the influence of the disorder is clearly seen as the maxima of the parabolic behaviour for the three solid solutions are at $x = 0.5$. Although PrSm has the highest ionic-radii difference of 0.047, where one would expect the highest FWHM values, however, the largest FWHM are found in LaPr with an ionic-radii difference of 0.037 Å (Shannon, 1976). However, the FWHM of PrSm are more similar to ones in PrNd although the ionic-radii difference of the latter is close to LaPr (0.031 Å). The deviations are probably due to different porosities and grain sizes for the three solid solutions.

In contrast to the other three modes, the ν_2 mode is showing a linear trend. Huittinen *et al.* (2017) found the FWHM of the ν_2 mode in LaGd doped with Eu (LaGd:Eu) to be insensitive to the disorder and therefore independent of the composition of their solid solution. The FWHM of the ν_2 mode here seems to be only depending on the radius but not on the disorder.

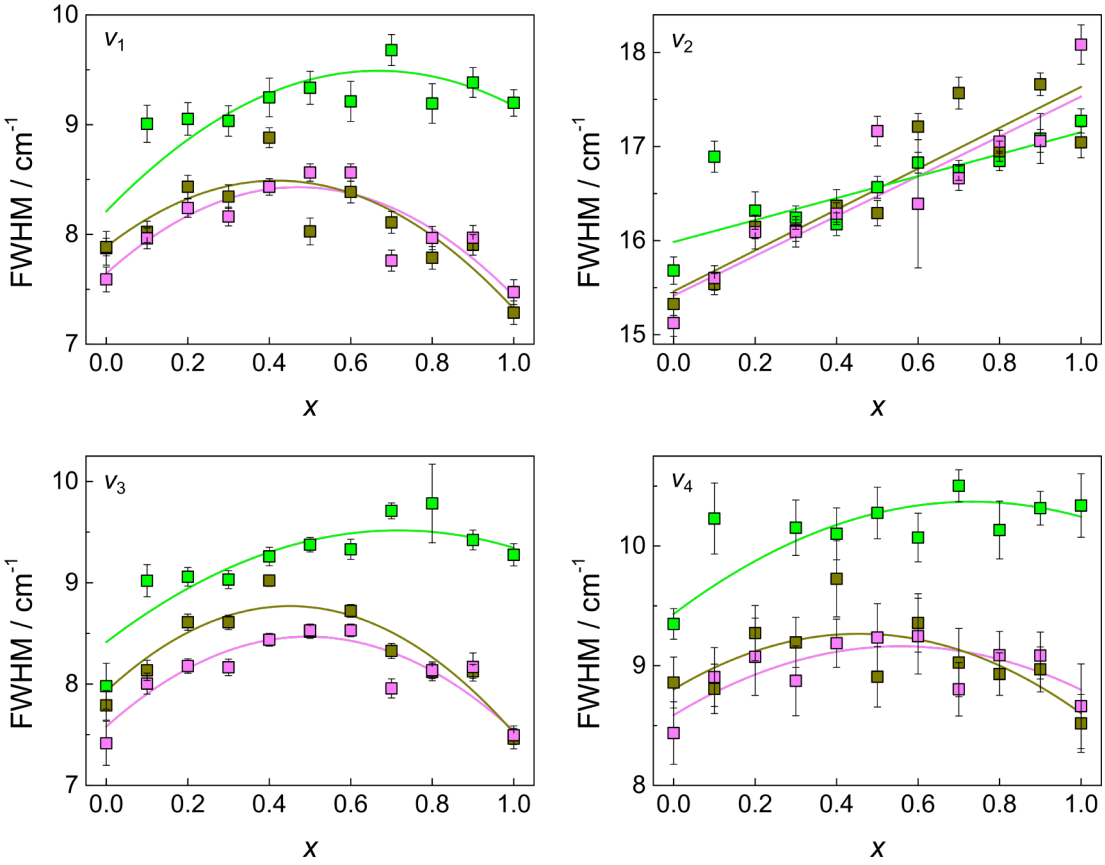

Figure 3.17 Comparison of the full widths at half maximum (FWHM) at the Raman modes in LaPr (bright green), PrSm (yellow-brown) and NdSm (pinkish). Note that x is the nominal chemical composition of the solid solutions as given in table 2.1 with x_{Pr}, x_{Sm} and x_{Sm} for the three solid solutions, respectively. Increasing x equals decreasing ionic *Ln* radius. The lines are fits to the data of the same colour and illustrate the trends.

3.1.5 Summary on room temperature characterisation of powders

Monazite solid solution powders of various compositions were produced by high-temperature solid state reaction. Since this technique is highly susceptible to impurities, it is necessary to homogenise the precursors well and to work with an excess of the phosphate donor to assure pure products and to prevent the formation of Ln_3PO_7. The grains of the as produced powders show high porosities that complicate chemical analyses via EPMA.

The structural changes in the solid solutions are due to the incorporation of smaller cations on the *Ln* site: with decreasing radius the lattice parameter and the unit cell volume decrease linearly. This decrease is due to the decreasing *Ln*-O bond lengths. The PO_4 tetrahedra are essentially rigid. The increase of the wave number of the PO_4 related modes in Raman spectroscopy with decreasing *Ln* radius can be attributed to the contraction on the *Ln* site.

3.2 Monazite single crystals

In this section, the findings for the single crystals are described. At first, the influence of the growth routine itself is discussed with regard to the optimisation of the growth procedure. Afterwards, chemical and XRD analyses are presented.

3.2.1 Optimisation of the flux growth procedure

Different flux compositions and temperature regimes were used to grow single crystals. In this section, the following aspects are discussed:

- How do the growth conditions (like cooling rate) influence the size, form and quality of the single crystals?
- What impact does an open crucible have in comparison to a tightly sealed one?
- What is the influence of the flux composition on the growth of the single crystals?

In order to evaluate the influences of these varying conditions, the crystals are compared with regard to their habit. All results are presented in detail in table A.22 in the Appendix. Growth experiments without a lid lead to many needle-shaped crystals at the furnace door (fig. 3.18). This probably happened because of precipitation of the evaporated flux material (Li_2MoO_4) at the coldest area of the furnace. The crystals form opaque and yellow aggregates. Isolated crystals are transparent and have a pearly lustre. Their longest dimension is about 2 mm by 5 mm while being rather thin (less than 1 mm). Furthermore, the outer parts of the uncovered crucibles were covered with crystals. These crystals were very flat (less than 1 mm) had a yellowish green colour. They could not be removed with water in ultrasonic bath nor with hydrochloric or nitric acid. Since monazite is not soluble in water but Li_2MoO_4 is, these crystals were most likely monazite crystals. This assumption, however, could not be checked because it was impossible to remove the crystals from the crucible for analysis.
Manually sealed crucibles also showed a few crystals on their outer part. However, these crystals could be completely dissolved in water indicating that they were evaporated and precipitated flux material.

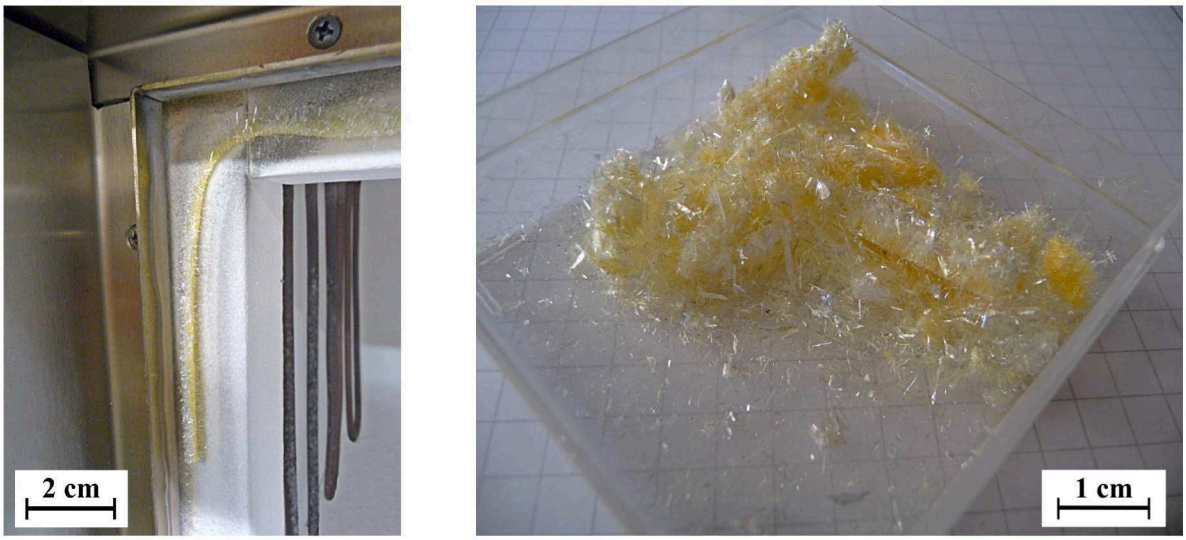

Figure 3.18 Evaporated flux material found on the door of the furnace (left). The crystals form opaque and yellow aggregates (right). Single crystals are transparent and have a pearly lustre. Their size is about 2 mm by 5 mm while being very thin (< 1 mm).

For some experiments, the flux material was partly removed by gently bending the crucible. Monazite crystals were only found at the bottom of the crucible because their density is higher than the one of the flux. The remaining flux material around the crystals was removed by dissolving it in water.
The monazite crystals were transparent and mostly free of inclusions. Figures 3.19 and 3.20 show crystals from selected growth experiments. Crystals with Nd show different colours under natural and artificial light which is due to several narrow absorption bands of Nd^{3+} (Bernstein, 1982). This is known as the alexandrite effect after the chrysoberyl ($BeAl_2O_4$) variety alexandrite where some Al atoms are replaced with Cr yielding a colour change between natural and artificial light.
Growth experiments with open crucibles (*i.e.* without a lid) yield in general fewer crystals than experiments with closed crucibles. Additionally, these crystals are smaller. This is because in this growth routines, a lot of the flux material evaporated.
Using a welded and, by this, a completely sealed crucible, crystals can be grown only due to temperature reduction. In contrast, performing a growth experiment in an open crucible at constant temperature (1273 K), crystals can be grown via evaporation. This yields the conclusion that it is possible to obtain monazite single crystals using either temperature reduction, evaporation or a combination of both factors.
Using a smaller cooling rate (indicated as ramp in table A.22 in the Appendix) while keeping the other growth conditions the same, the crystals grow larger. However, this might be coincidental since the growth of the crystals is mainly depending on the nucleation rate and the growth rate.
In order to evaluate the influence of the flux-to-sample ratio and to get a rough impression about the solubility of monazite within this flux composition, the Li:Mo ratio were kept constant. The crystal habit changes with varying flux:monazite ratio (Li_2MoO_4:MoO_3:$LnPO_4$). Using 25:50:1, the crystals are very small ($\ll 1$ mm). This

can simply be explained because there was to few material available to grow bigger crystals. By doubling the amount of monazite, transparent crystals are found to be thin needles to thin platelets with lengths of up to 5 mm for the needles and 2 mm for the platelets. Another doubling yielded a very large single crystal (1.3×0.4×0.3 cm, fig. 3.19 left). The crystal is colourless and transparent showing some inclusions. All facets look like grown crystal surfaces except the one that was in contact with air due to the low filling level of the crucible. Crystals grown by 25:50:8 are isometric with diameters between 0.2 to 2 mm. They are colourless and transparent (fig. 3.19 middle). In general, the higher the amount of monazite is, the higher is the availability of the material and, hence, the larger is the probability for large crystals to grow.
Compositional change of the educts for the flux seems to influence the habit of the crystals. Using Li_2CO_3 and MoO_3, crystals are mostly plate-like and flat (fig. 3.19 right), while crystals grown with Li_2MoO_4 and MoO_3 tend to be isometric (see table A.22 in the Appendix). Additionally, a higher amount of MoO_3 in the flux yields smaller crystals. This supports the findings of Cherniak *et al.* (2004): more Li_2O leads to smaller PO_4 complexes in the flux resulting in better diffusion and facilitating the growth, while more MoO_3 yields larger PO_4 complexes and a higher viscosity which impedes the growth (see subsection 2.1.3).

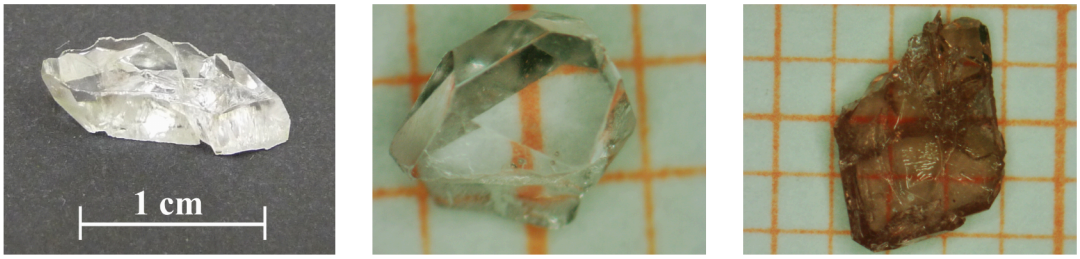

Figure 3.19 Left: Large single crystal of $LaPO_4$. Note that the crystal broke during the removal from the crucible. Middle: Typical isometric single crystal (here: $LaPO_4$) with natural grown faces. Right: Typical platelet single crystal (here: $Pr_{0.2}Nd_{0.8}PO_4$) with natural grown faces. Distance between two lines is 1 mm. Growth conditions can be found in table A.22 in the Appendix.

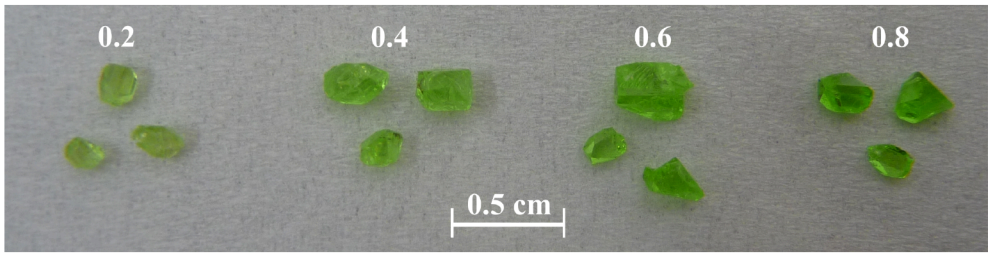

Figure 3.20 Isometric crystals of $La_{1-x}Pr_xPO_4$ with the compositions $x_{Pr} = 0.2$, 0.4, 0.6, 0.8 (left to right). The higher the Pr content, the more vivid the green. Growth conditions can be found in table A.22 in the Appendix.

3.2.2 Chemical characterisation

The following questions were addressed by chemical analyses via EPMA:

- What is the composition of and how homogeneous are the single crystals?
- Are there any inclusions of flux material?
- Do the crystals show signs of zonal growth?

The single crystals looked homogeneous in back-scattered electron (BSE) images (fig. 3.21). However, the spacial resolution of these images is not good enough to draw any conclusions about homogeneity. Most crystals of LaPr show naturally grown faces.

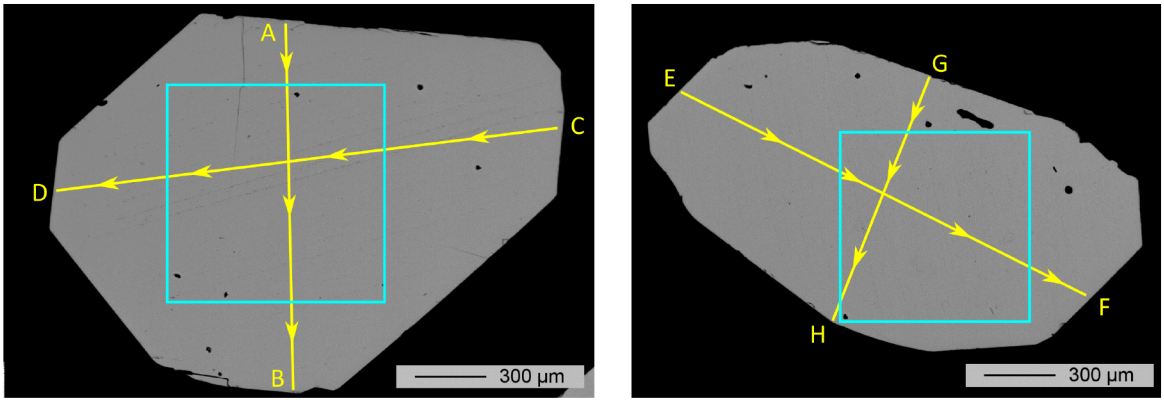

Figure 3.21 Back-scattered electron (BSE) images of a $La_{0.6}Pr_{0.4}PO_4$ (left) and a $La_{0.4}Pr_{0.6}PO_4$ (right) single crystal. Yellow lines indicate the line profiles (start and end points marked with letters A to H, arrows show the direction of the measurement, see fig. 3.22 and 3.23). Blue frames highlight the areas of the mappings (see figures A.14 and A.15 in the Appendix).

Profile analyses, indicated as yellow lines in figure 3.21, are shown in figures 3.22 and 3.23. The result of the other profiles can be found in the Appendix in the figures A.2 to A.12. The two crystals shown here have the highest compositional changes within their profiles. However, both profiles only show slight compositional variations within the error, meaning that the compositional change is not significant. Nevertheless, the profile A-B (fig. 3.22) shows a slight increase of 5 % within the error. This might indicate that there is a slight zonal growth which is, however, not supported by profile analyses on the other crystals of the same and different compositions. Still, this slight difference may arise due to the different melting temperatures of $LaPO_4$ and $PrPO_4$ (2345 K and 2211 K, respectively Hikichi and Nomura, 1987).
To further check for zoning, mappings (given as blue boxes in figure 3.21) were done on the same two crystals. However, the mappings did not reveal any significant indication for zoning (see figures A.14 and A.15 in the Appendix). Therefore, within the error, zoning can not be confirmed. Yet, zoning is expected to be seen best in systems with high differences in the ionic radii and in the melting temperatures. Thus, La and Pr might be too similar to yield zoning in the crystals.

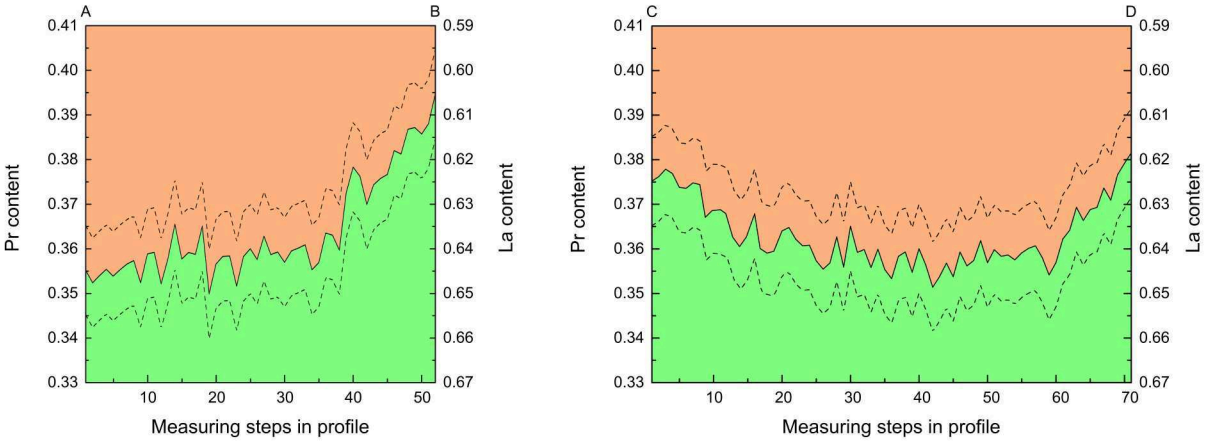

Figure 3.22 Atomic fraction of La (orange) and Pr (green) along cross-sections (A-B: left; C-D: right) of the $La_{0.6}Pr_{0.4}PO_4$ single crystal in figure 3.21 on the left. The solid black line represents the measured values while the dashed lines represent the error range of $\pm 1\,\%$. The short (A-B) profile shows an increase of about 5 % within the error. The longer (C-D) profile shows a parabolic shape. However, within the error, the compositional change in this direction is not significant.

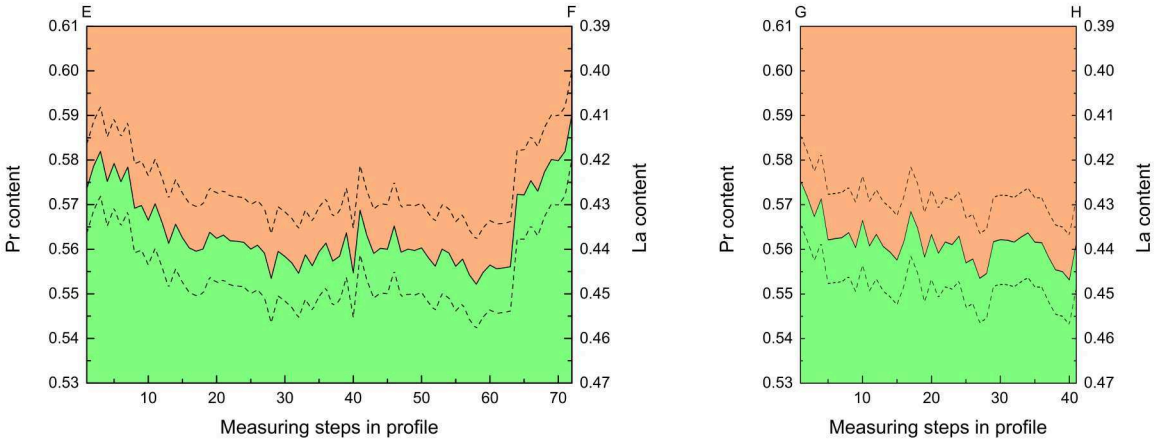

Figure 3.23 Atomic fraction of La (orange) and Pr (green) along the cross-sections (E-F: left; G-H: right) of the $La_{0.4}Pr_{0.6}PO_4$ single crystal in figure 3.21 on the right. The solid black line represents the measured values while the dashed lines represent the error range of $\pm 1\,\%$. There is no significant change in the composition within the errors in both profiles.

3.2.3 Structural investigations

In this section, data from LaPr, NdEu and SmNd single crystals are presented. XRD on single crystals was used to answer the following questions:

- How does the *Ln* substitution influence the lattice parameters of monazite?
- How do the fractional coordinates of the atoms change upon substitution?
- How do the bond lengths and angles change with different *Ln*?

Since there is no difference of the composition between powders and single crystals, the values for the lattice parameters were taken from the XRD results of the corresponding powder sample. In powder XRD, the peaks have a better angular resolution compared to the reflections obtained from single-crystal XRD. Also, powder XRD measurements are usually performed to much higher diffraction angles. In single-crystal XRD, the exact orientation of the crystal in the diffractometer is refined (orientation matrix) from a few observed reflection positions. Systematic errors from the *IPDS* diffractometers arise due to imperfect centring of the crystal at the goniometer head and because of uncertainty in the crystal-detector distance. Hence, the lattice parameters obtained from powder XRD are more precise. However, the determination of the fractional coordinates is more precise in single-crystal XRD because the complete three-dimensional space can be measured. There is no superposition of symmetry-equivalent reflections (with exactly the same interplanar distance of two lattice planes, *i.e.* d values) and no complete nor partial overlap of symmetry non-equivalent reflections (because of similar d spacings). Thus, the fractional coordinates can be obtained more precisely from single-crystal XRD since each reflection can is measured individually, and hence, individual relative intensities lead to more precise determination of fractional coordinates. This is because single-crystal XRD has better counting statistics and a larger dynamic range. This yields a better peak-to-background ratio and more reflections with higher angles (indices) can be measured. Additionally, the reflexes are measured in 3D and not projected in 1D as done in powder XRD. To conclude, the resolution of the d spacings is better in single-crystal XRD. On this basis, bond lengths and angles can also be determined more precisely. The results of the single-crystal XRD measurements are presented in the tables A.23, A.24, and A.25 in the Appendix.
Regarding the fractional coordinates (tables A.23, A.24, and A.25 in the Appendix for LaPr, NdSm, and NdEu, respectively), most remain almost constant (x_{Ln}, z_{P}, x_{O^2}, x_{O^3}, x_{O^4}, z_{O^2}, z_{O^4}) while some show only slight variations within errors (x_{P}, y_{P}, x_{O^1}, z_{O^1}, y_{O^1}, y_{O^2}, y_{O^3}, y_{O^4}). However, three coordinates are clearly influenced by changing composition. While y_{Ln} and z_{Ln} show an increase with increasing ionic *Ln* radius, z_{O^3} decreases (fig. 3.24).

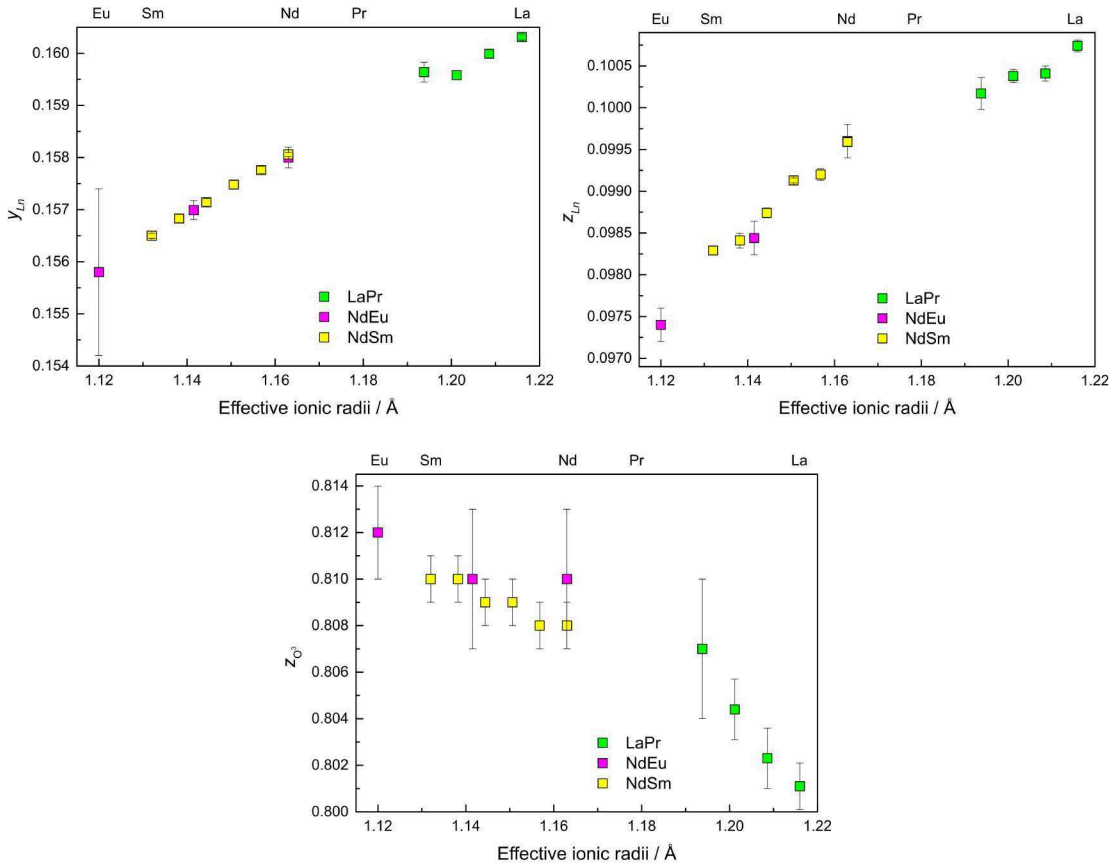

Figure 3.24 Change of atomic positions of *Ln* and O^3. With increasing ionic radius of *Ln*, the *y* and *z* position of the *Ln* cation shifts to higher values, while the *z* coordinate of the O^3 atom shifts to lower values.

The change in the fractional coordinates of the atoms is the response to the change of the unit cell parameters due to the different *Ln* radius. Usually, the required space for different atoms within a simple structure type is obtained by the change of the lattice parameters and not by the change of the coordinates. However, in monazite, this change of the fractional coordinates reflects the constraints arising from the structural arrangement of the atoms which will be discussed in the following regarding the bond lengths and angles as well as the coordination polyhedra.
All *Ln*-O bonds decrease with decreasing ionic radii (fig. 3.25 and table A.26 in the Appendix) which is due to the lanthanide contraction. Those bonds parallel to the monazite chain structure are significantly longer than those within the equatorial plane of the LnO_9 polyhedron. This is due to the attractive force of the P ion on the O ions. The *Ln*-O^2 bond is longer than the other three 'chain' oxygen atoms, leading to a tilt of the tetrahedra within the chain (fig. 3.26 on the left). The *Ln*-O^2 bonds within the equatorial plane are longer than the others (fig. 3.26 on the right). The O^2 bonds were characterised by Li *et al.* (2009) to be less covalent due to the higher coordination number compared to all other oxygens (see section 1.3.1).

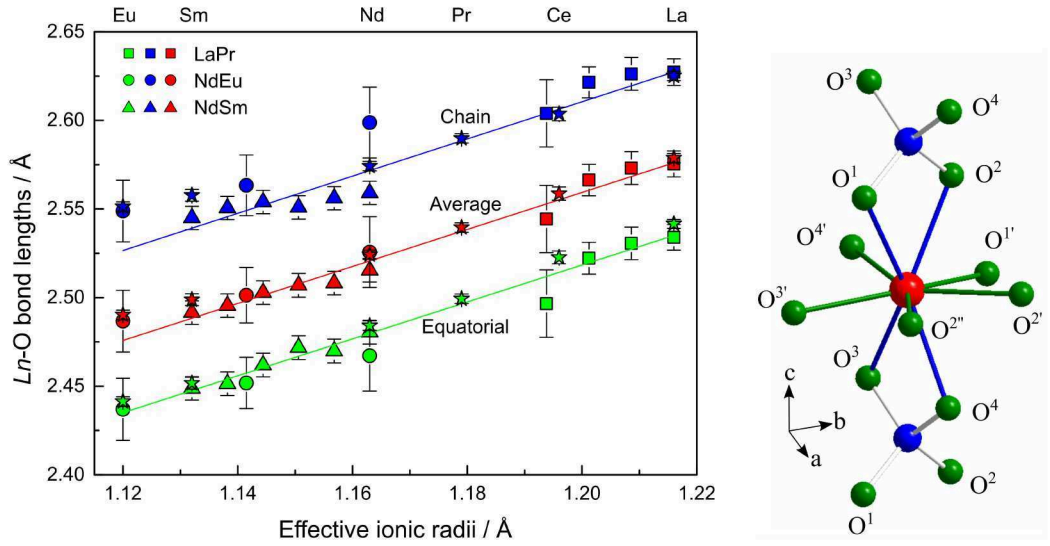

Figure 3.25 Average *Ln*-O bond lengths from single-crystals diffraction of three solid solutions (LaPr, NdEu, NdSm) vs. the effective ionic radius: In red, the average of all *Ln*-O bond distances is given. The average calculated from those bonds along $\vec{c}$ attached to the PO_4 tetrahedra are given in blue, while those within the equatorial plane are given in green. In the structural detail of the chain on the right, the corresponding bonds are also highlighted in blue and green. Stars represent data from Ni *et al.* (1995). Lines are guides to the eye. For NdEu, the influence of using the lattice parameters obtained by single-crystal XRD is seen in larger errors compared to the other solid solutions.

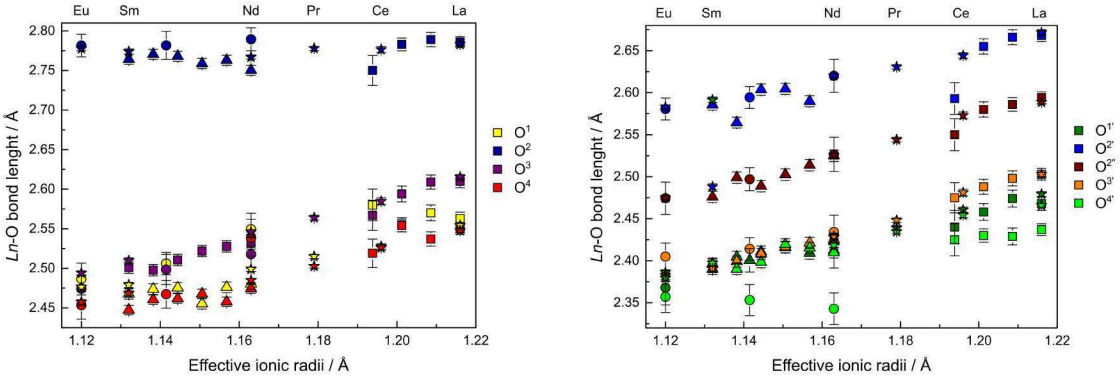

Figure 3.26 Individual *Ln*-O bond lengths from single-crystals diffraction of three solid solutions (LaPr: squares, NdEu: circles, NdSm: triangles) vs. the effective ionic radius. Stars represent data from Ni *et al.* (1995)

All P-O bonds are similar in length (table A.27 in the Appendix) and the O-P-O angles vary around 109.5° (fig. 3.27; table A.28 in the Appendix). This is the same as seen for the powders in chapter 3.1.3. However, there is a difference between those angles along the chain and 'perpendicular' to it. The latter, O^1-P-O^2 and O^3-P-O^4, are both smaller than the ideal angle, while the others (along the chain) are mostly larger than 109.5°. This 'compression' of the angles O^1-P-O^2 and O^3-P-O^4 yields the relaxation of the other angles. This compression is a result of the Coulomb repulsion of *Ln* and P as they share the edges O^1-O^2 and O^3-O^4 (see section 3.1.3).

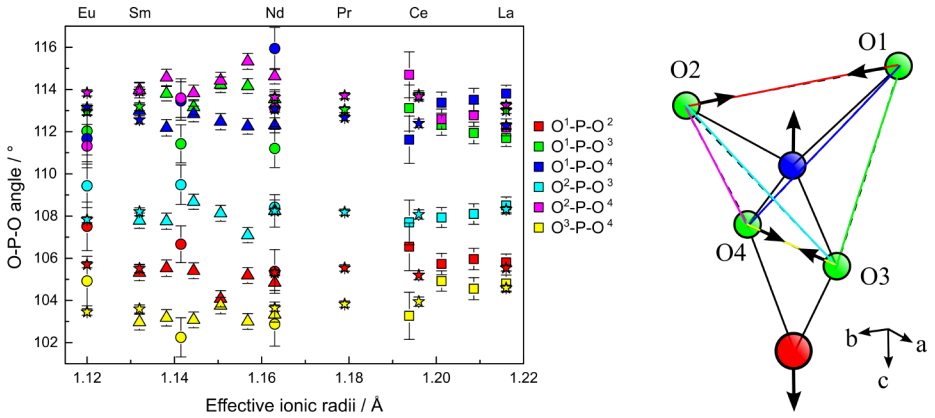

Figure 3.27 Left: O-P-O angles vs. the effective ionic radius (Shannon, 1976) obtained from single-crystal XRD on LaPr (squares), NdSm (triangles), and NdEu (circles); Right: Detail of the monazite chain (in red: Ln; in blue: P; in green: O) for a schematic representation of the Coulomb repulsion in the LnO_9-PO_4 chains in monazite between *Ln* and P resulting in smaller O^1-P-O^2 and O^3-P-O^4 angles compared to the other angles. The angles are marked along the edges that the two oxygen ions form in the same colour as on the left. Stars represent data from Ni *et al.* (1995)

Additionally, the bond length distortion (BLD) was calculated for the *Ln*-O and P-O polyhedra according to Renner and Lehmann (1986):

$$BLD = \frac{100}{n} \sum_{i=1}^{n} \frac{|\,(X-\mathrm{O})_i - (X-\mathrm{O})_m\,|}{(X-\mathrm{O})_m}\% \tag{3.1}$$

In this formula, n is the number of cation-anion bonds. $(X-\mathrm{O})_i$ is the length of a particular bond from cation X to oxygen, while $(X-\mathrm{O})_m$ is the mean value.
The BLDs for *Ln*-O bonds are presented in figure 3.28 (left) and in table A.29 in the Appendix. The BLDs range from 2.5 to 3.5 %. Within uncertainties, BLDs for all three solid solutions are comparable. The BLDs calculated for the P-O bonds (fig. 3.28 on the right and table A.29 in the Appendix) range from 0.5 to 2.5 %, hence, are smaller than the BLDs for the *Ln*-O bonds. This is expected, because the P-O bonds are stronger than the *Ln*-O bonds. No trend was observed for any of the three solid solutions.

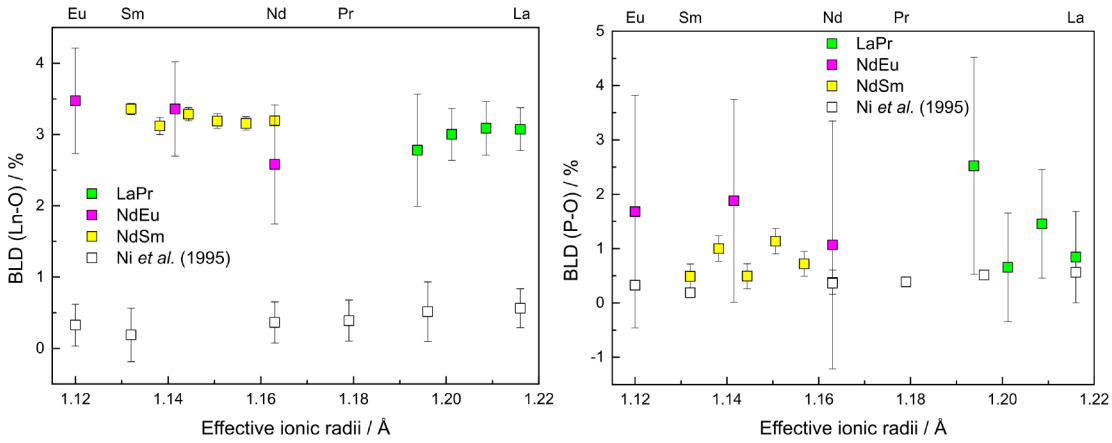

Figure 3.28 Bond length distortion (BLD) of *Ln*-O (left) and P-O (right) bonds calculated after Renner and Lehmann (1986) against the effective ionic radii (Shannon, 1976).

In a similar way, the tetrahedral angle variance (TAV, also known as quadratic elongation) and the angular distortion (AD) for the PO_4 tetrahedra were calculated after Robinson *et al.* (1971) and Baur (1974), respectively, to evaluate the distortion of the PO_4 tetrahedra:

$$TAV = \sum_{i=1}^{6} \frac{(\theta_i - 109.47°)^2}{5} \tag{3.2}$$

and

$$AD = \frac{100}{6} \sum_{i=1}^{6} \frac{|\,(\mathrm{O-P-O})_i - (\mathrm{O-P-O})_m\,|}{(\mathrm{O-P-O})_m}\% \tag{3.3}$$

Here, θ_i and $(\mathrm{O-P-O})_i$ are the individual angles and $(\mathrm{O-P-O})_m$ is the mean value. Note that in the calculation of the TAV, the divisor of 5 is calculated from the number of the intra-tetrahedra angles (6) minus 1. Results are given figure 3.29 and in table A.29 in the Appendix. The TAV is mostly larger than 10 ° and the AD is mostly higher than 2.5 %. There seems to be a decrease of both values with increasing ionic radius, indicating that the PO_4 tetrahedra in $LaPO_4$ are the least distorted because La^{3+} is the biggest of the lanthanides. The smaller the ionic radius of the *Ln* cation, the more the structure needs to adapt to this smaller ion yielding higher distortion. However, these changes are very small and, within the errors, no absolute trend can be confirmed.

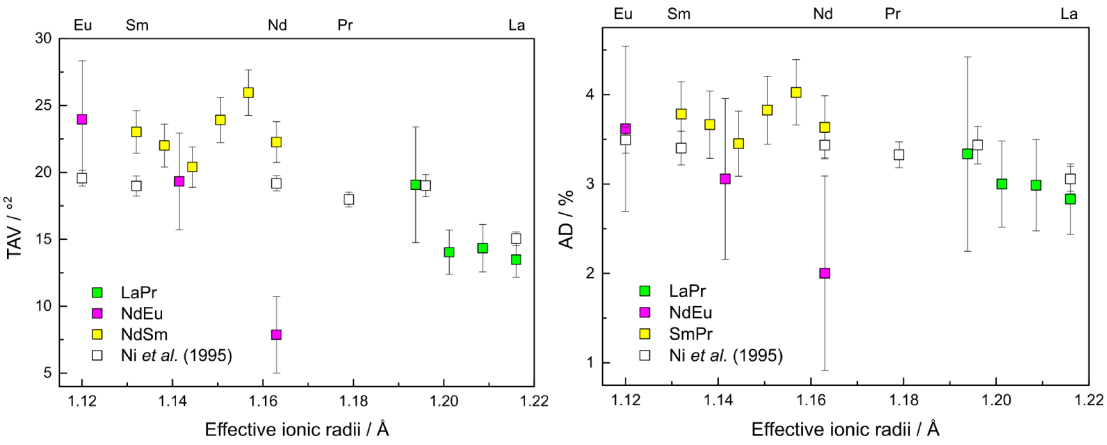

Figure 3.29 Tetrahedral angle variance (TAV, light) and angular distortion (AD, right) for the PO_4 tetrahedra calculated after Robinson *et al.* (1971) and Baur (1974), respectively, against the effective ionic radii (Shannon, 1976).

Analogue to the TAV of the PO_4 in equation 3.2, the polyhedral angle variance (PAV) of the LnO_9 polyhedra was calculated to evaluate the distortion of this polyhedron:

$$PAV = \sum_{i=1}^{36} \frac{((\mathrm{O} - Ln - \mathrm{O})_i - (\mathrm{O} - Ln - \mathrm{O})_m)^2}{35} \tag{3.4}$$

with the divisor 35 resulting from all 36 intra-polyhedral angles.
Since the LnO_9 polyhedron can be described as a *pentagonal interpenetrating tetrahedral polyhedron* (Mullica *et al.*, 1984, see subsection 1.3.1), the following two parts were taken into account to find the main influence on this distortion. The PAV of the 10 O-*Ln*-O angles in the equatorial plane linking the chains in the *a*-*b*-plane (PAV(E)) and those 6 connected to the PO_4 tetrahedra along the chain (PAV(T)) were calculated:

$$PAV(E) = \sum_{i=1}^{10} \frac{((\mathrm{O} - Ln - \mathrm{O})_i - (\mathrm{O} - Ln - \mathrm{O})_m)^2}{9} \tag{3.5}$$

$$PAV(T) = \sum_{i=1}^{6} \frac{((\mathrm{O} - Ln - \mathrm{O})_i - (\mathrm{O} - Ln - \mathrm{O})_m)^2}{5} \tag{3.6}$$

Again, the divisors result from the number of angles minus 1.
The results of these PAVs are presented in figure 3.30 and are also given in table A.30 in the Appendix. The general PAV (fig. 3.30 top) shows an increase with increasing ionic radii. It seems that smaller *Ln* ions fit better within the polyhedron causing less angular distortion. The values are smaller than the values for PAV(E) and PAV(T) because the angles connecting the equatorial atoms and the tetrahedral oxygens are not included in the calculation of PAV(E) and PAV(T). The distortion of the equatorial plane does not change with varying *Ln* radii. There are less constraints from the structural arrangement so that the repulsion of these oxygens maintains the pentagonal arrangement. Hence, the equatorial plane seems to rescale with varying *Ln* size. In contrast, the distortion for the O-*Ln*-O angles along the chain increases with increasing *Ln* radius. With larger *Ln*

ions, the chain is elongated and the *Ln*-O distances increase (as shown in fig. 3.25) which results in a larger angular distortion. Thus, this tetrahedral arrangement can be better described as a disphenoid. The larger distortion of this part of the LnO_9 polyhedron can be explained by the strong P-O bonds in the PO_4 tetrahedron. This tetrahedron puts large constraints on the O-O edge and keeps the oxygen atoms close to the P ion. Hence, the distortion of the LnO_9 polyhedron must adapt to those constraints. In conclusion, the structural description of the LnO_9 polyhedron is suitable when considering the saturation of the valence of the Ln^{3+} but not deficient for the description of the reaction of the structure to the incorporation of cations of different sizes.

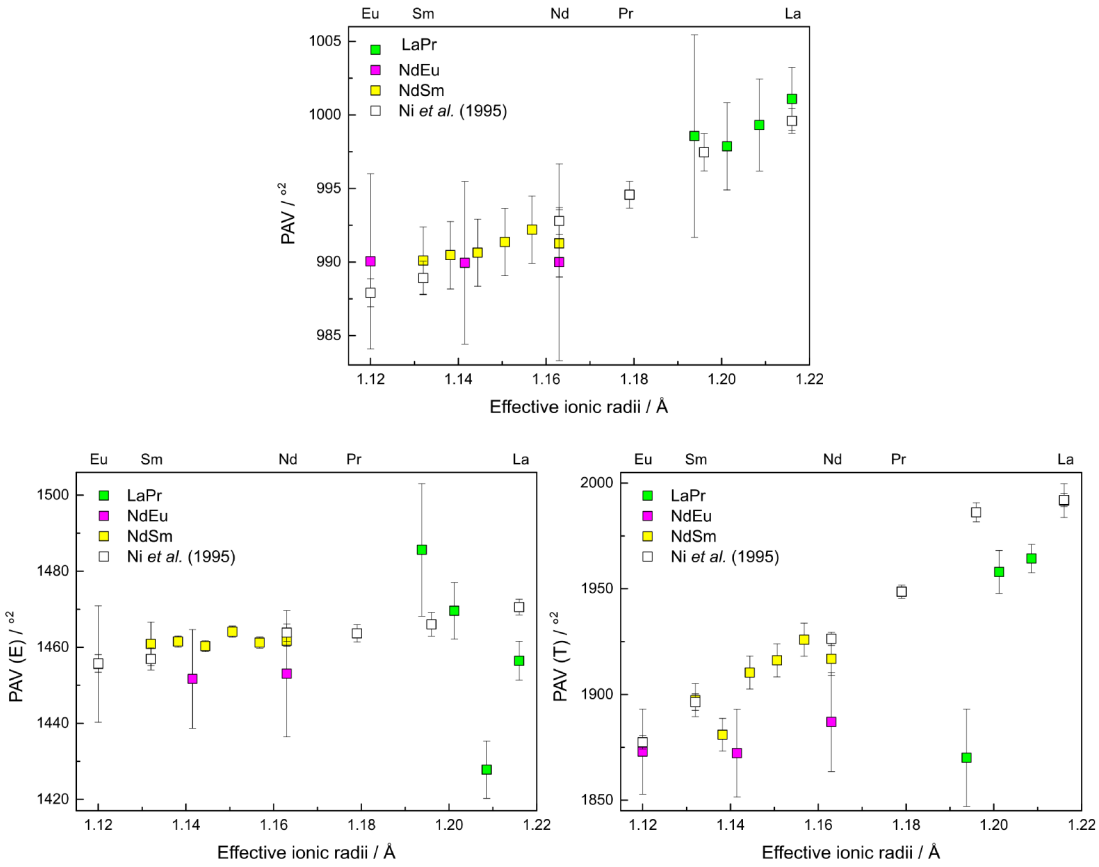

Figure 3.30 Polyhedral angle variance (PAV) for LnO_9 against the effective ionic radii (Shannon, 1976). Top: PAV for all O-*Ln*-O angles; bottom: PAV of the O-*Ln*-O angles in the equatorial plane (PAV(E); left) and those connected to the PO_4 tetrahedra (PAV(T); right).

3.2.4 Optical absorption spectroscopy

The following questions were addressed using optical absorption spectroscopy (OAS):

- How does Pr^{3+} influence the crystal field in $LaPO_4$?
- How does this influence change with increasing Pr content?

Optical absorption spectra are recorded when the excitation energy of $4f$ electrons of Ln^{3+} or their absorption bands are within the wavelength range of visible light. Since in LaPr only Pr^{3+} has $4f$ electrons (electron configuration in La: [Xe] $5d^1 6s^2$, in Pr: [Xe] $4f^3 6s^2$; [Xe] refers to the electron configuration in Xe), the optical absorption spectrum of $LaPO_4$ does not show any electron transitions. The two main parts of the optical absorption spectra (430 - 500 nm and 570 - 620 nm) of five samples of LaPr are shown in figure 3.31. Note that the spectra are stacked. Included are the electronic $4f$–$4f$ transitions in Pr^{3+} according to Horchani-Naifer and Férid (2009) resulting from the ground state $^3H_4$ ($^3H_4 \rightarrow {}^3P_0, {}^3P_1 + {}^1I_6, {}^3P_2, {}^1D_2$). Additionally, three peaks are marked and the instrumental resolution is added.
There is a slight change in the height of the absorption peaks, however, no trend with increasing Pr content could be observed. The slight change in height could be due to the fact that the background was not subtracted. More importantly, no change for the peak centres was found within the given uncertainty (see also fig. A.16 and A.17 in the Appendix). When the Pr content in $LaPO_4$ is relatively small, the influence of these 'defects' may be seen in a shift of these peak centers. However, within this work, the lowest Pr content of $x = 0.2$ was probably already too high so that the interactions between the Pr^{3+} ions are probably too high. This may explain the unchanging peak center positions.

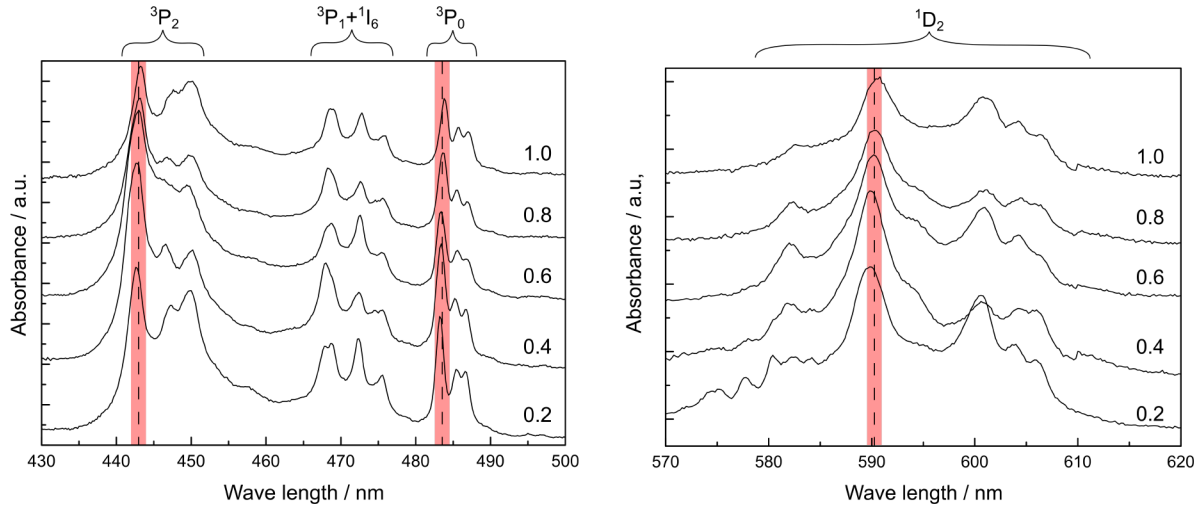

Figure 3.31 Stacked optical absorption spectra of LaPr with the electronic $4f$–$4f$ transitions ($^3H_4 \rightarrow {}^3P_0, {}^3P_1 + {}^1I_6, {}^3P_2, {}^1D_2$) in Pr^{3+} according to Horchani-Naifer and Férid (2009). The numbers give the Pr content (x_{Pr}). The dashed lines mark three peak positions. The red area shows the error due to the resolution of the instrument.

3.2.5 Summary on room temperature characterisation of single crystals

Monazite crystals can be grown by HTSM. The following essential conclusions can be drawn:

- Open crucibles yield smaller and fewer crystals due to enhanced evaporation of the flux.
- Crystals can be grown using temperature reduction and/or evaporation.
- The smaller the cooling rate, the larger the crystals due to a longer growth phase.
- The higher the amount of monazite in the flux, the more and the larger the crystals because of the higher nucleation rate and availability of material.
- The higher the MoO_3 content, the smaller the crystals, possibly due to inhibited growth.
- Flux composed of Li_2CO_3 and MoO_3 yields platelets, while flux composed of Li_2MoO_4 and MoO_3 yields isometric crystals.

The obtained single crystals were inclusion free and homogeneous. There seems to be no zoning in the composition.
Results from structural characterisation using the lattice parameters obtained by powder XRD show that the *Ln*-O bond lengths increase with increasing ionic radii. There are no constraints on the O-O distances in equatorial plane of the LnO_9 polyhedron resulting in no angular distortion in this plane. In contrast, the rigid PO_4 put strong restraints on the O-O edges connecting the LnO_9 polyhedra and the PO_4 tetrahedra within the chain. Hence, the angular distortion of the LnO_9 can be attributed to this structural unit. Additionally, the change in the fractional coordinates of *Ln* and O^3 can be attributed to the unequal change of the unit cell parameters due to the rigidity of the PO_4 tetrahedra. In OAS, the amount of Pr^{3+} substituted in $LaPO_4$ needs to be (significantly) lower than $x = 0.2$ to see influences of 'defects' resulting from the Pr^{3+} in the spectra.

3.3 Structural characterisation at non-ambient conditions

In this section, the influence of high temperatures and high pressures on the monazite structure will be presented. Additionally, physical and mechanical properties are discussed.

3.3.1 High-pressure behaviour of $LaPO_4$

The behaviour of $LaPO_4$ at high pressure was studied by Lacomba-Perales *et al.* (2010) by means of powder XRD. They observe a phase transition at 26.1 GPa to an orthorhombic phase, however they were unable to solve the high-pressure (HP) structure. This section addresses the following questions:

- What is the space group of the high-pressure phase?
- How does the structure look like?
- Which are the similarities and differences between the low-pressure monazite structure and the high-pressure phase?
- How do the fractional coordinates of the atoms change with increasing pressure?

As published in Ruiz-Fuertes *et al.* (2016) and shown in this section, it was now possible to determine this HP structure.
Three sections through the reciprocal space obtained from single-crystal diffraction frames were chosen to show the evolution of the $(5k\bar{2})$ reflections with increasing pressure (fig. 3.32). At lower pressure, the peaks are very sharp, while broadening occurs with increasing pressure. At 27.1(1) GPa, additional reflections indicate the presence of a second phase, *i.e.* a phase transition took place.

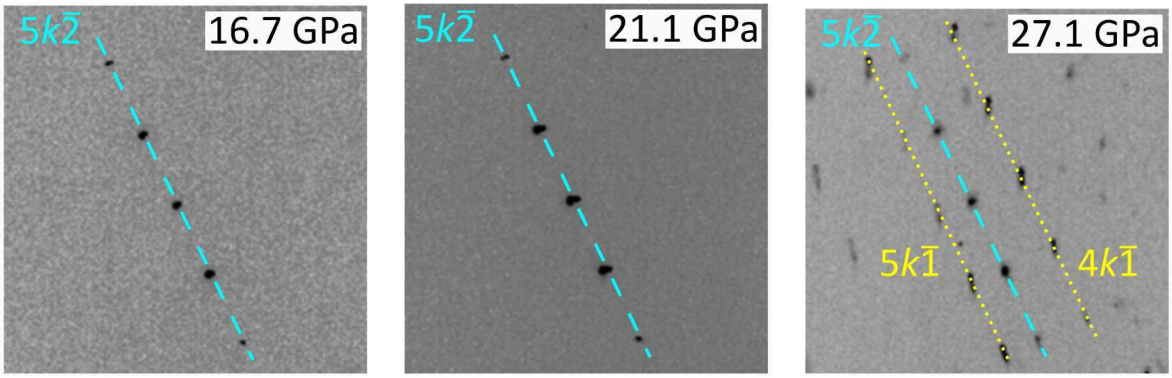

Figure 3.32 Evolution of the $(5k\bar{2})$ reflection family in sections through the reciprocal space of $LaPO_4$ at three different pressures obtained by single crystal diffraction. Light blue: low-pressure phase; yellow: high-pressure phase after Ruiz-Fuertes *et al.* (2016).

To determine the structure of this second phase, all reflections were analysed: 1188 reflections were found to belong to monazite, while 1073 additional reflections were observed at this pressure. These HP-phase reflections were indexed with an orthorhombic metric and tested for any reflection conditions concerning systematic extinction. As there is no indication for a lattice centering, the orthorhombic lattice must be primitive. The analysis of zonal and serial reflections is shown in table 3.5. According to table 3.5, there is no evidence for glide planes, while the extinction rules for 2_1 axes along $\vec{a}$, $\vec{b}$ and $\vec{c}$ are obeyed. Due to the crystal orientation along [001] parallel to the rotation axis of the diffractometer, a $2_1 \parallel \vec{c}$ can neither be confirmed nor excluded. This means that two space groups are possible for this set-up: $P2_12_12$ and $P2_12_12_1$. However, the probability of finding a structure with the space group $P2_12_12$ is much smaller than finding one in $P2_12_12_1$ (only 5 %). Thus, the structure was finally solved in $P2_12_12_1$.

Table 3.5 Zonal and serial reflection conditions for symmetry elements like 2_1 screw axes parallel to and a, b, c, n glide planes perpendicular to $\vec{a}$, $\vec{b}$ and $\vec{c}$ direction of $LaPO_4$ high-pressure phase at 27.1(1) GPa after Ruiz-Fuertes *et al.* (2016). Absence refers to reflections that were not detected, while violations mean reflections that are not allowed for a specific symmetry element. The used threshold to determine the reflections was $I/\sigma > 2$.

	$\vec{a}$				$\vec{b}$				$\vec{c}$			
Elements	2_1	b	c	n	2_1	a	c	n	2_1	a	b	n
Absence	8	16	19	19	7	34	36	32	0	114	121	121
Violations	0	12	9	11	0	13	23	24	0	70	97	73

A non-centrosymmetric space group was confirmed using second-harmonic generation (SHG) experiments (fig. 3.33): In the centrosymmetric space group of monazite, the SHG is forbidden. This means that the signal equals zero in the measurements. At the phase transition, the signal increases dramatically indicating non-centrosymmetry. Since a signal in SHG can result either from surface effects and defects or from the bulk itself,

the laser current, which is proportional to the laser power, was changed while measuring the SHG at constant pressure (29.2(1) GPa), which yielded a quadratic behaviour (inset in fig. 3.33). Following Bayarjargal and Winkler (2014), this unambiguously proves that the SHG signal originates from the bulk.

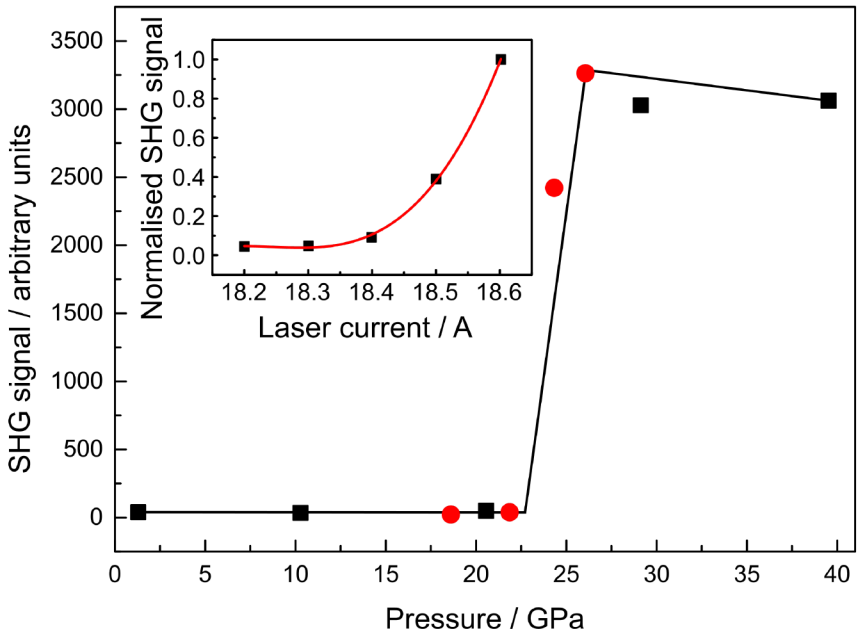

Figure 3.33 SHG signal of $LaPO_4$ vs. pressure. As an Inset: The normalised SHG signal at 29.2 GPa as a function of the laser current. Circles and squares mark two measurement cycles, solid lines are guides to the eye after Ruiz-Fuertes *et al.* (2016).

In figure 3.34, the overlap of the reflections of the two reciprocal lattices is presented to show the orientation relation between the monoclinic low-pressure and the orthorhombic high-pressure phase.
Lattice parameters and fractional atomic coordinates of the two coexisting phases at 27.1 GPa are given in table A.31 in the Appendix. The atomic arrangement of the HP phase is similar to the post-barite structure, the HP modification of $BaSO_4$ (Santamaría-Pérez *et al.*, 2011). Within this HP structure, P^{5+} remains four-fold coordinated by O^{2-} like in monazite, whereas the coordination number of La^{3+} increases from nine in monazite to twelve in the post-barite structure. A comparison of both structures is shown in figure 3.35.

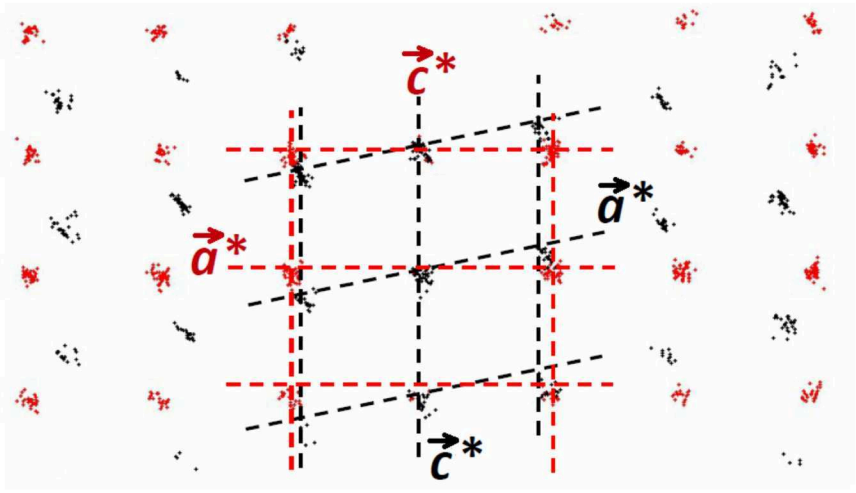

Figure 3.34 Reciprocal lattice along the $\vec{b}^*$ direction of the low- (black) and the high-pressure (red) phase of $LaPO_4$ at 27.1 GPa. Dots show the reflections, while unit cells are presented with broken lines after Ruiz-Fuertes *et al.* (2016). The black dots and unit cell show the monoclinic lattice of monazite, the red peaks and unit cell represent the orthorhombic HP phase.

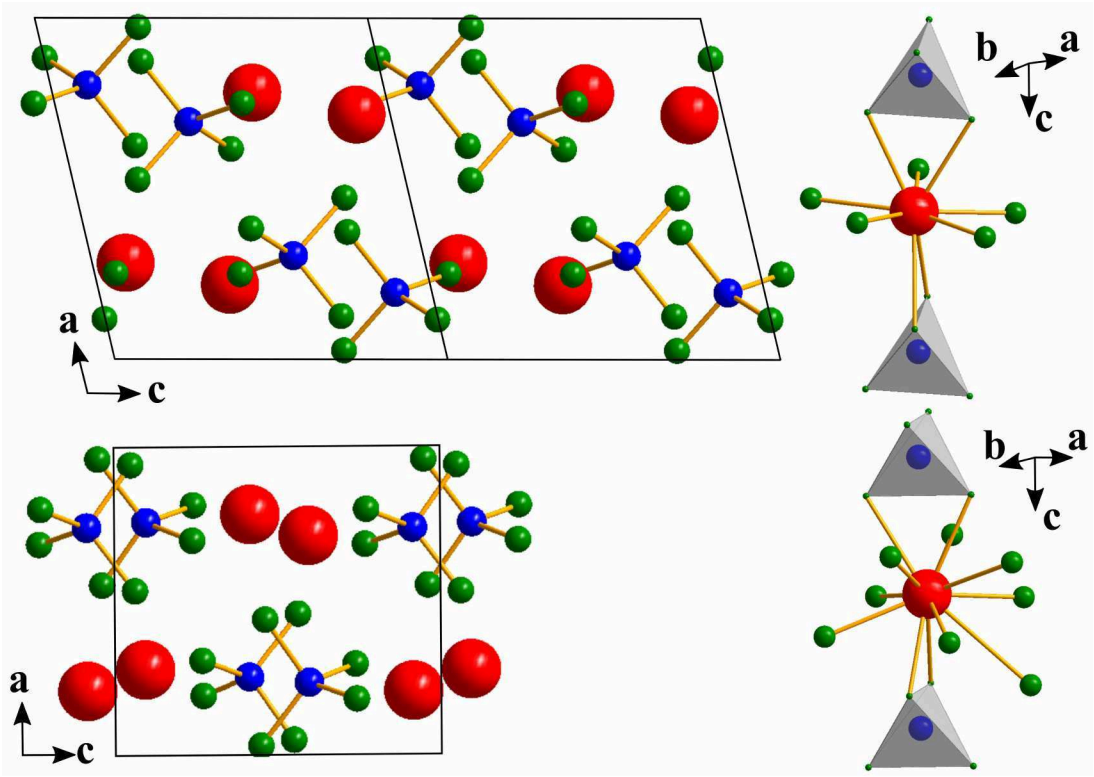

Figure 3.35 Projections along [010] and chain structures along [001] of the monazite-type structure (top) and the post-barite structure (bottom) of $LaPO_4$ at 27.1 GPa after Ruiz-Fuertes *et al.* (2016). Red: La^{3+}, blue: P^{5+}, green: O^{2-}; grey tetrahedra: PO_4.

The behaviour of the lattice parameters and the β angle are given in figure 3.36. Figure 3.37 shows the pressure dependence of the unit cell volume and the mean La-O bond lengths. Up to the phase transition at 27.1(1) GPa, all values decrease which is due to compression with increasing pressure. At the phase transition, a decrease of the unit cell is accompanied by a rapid decrease in $\vec{a}$ and an increase of the mean La-O bond lengths. The volume collapse can be explained by a repacking of the whole structure when the rigid PO_4 tetrahedra align along the (100) plane and the coordination number of La increases. To obtain the bulk modulus (K) for the monazite phase, a third-order Birch-Murnaghan equation of state was used to fit the volume of monazite at HP. The obtained value of $K = 125(3)$ GPa is lower than the value by Lacomba-Perales *et al.* (2010) from powder data: $K = 144(2)$ GPa. There are two possible explanations for this difference. The first is non-hydrostatic conditions during the measurement, the second is the nature of the sample itself. Since for both, the single crystal studied here and the powder samples from Lacomba-Perales *et al.* (2010), the same pressure-transmitting medium (Ne) was used, the deviation of K can not be associated to non-hydrostatic conditions. Powder samples from Lacomba-Perales *et al.* (2010) consist of several grains causing a decrease of the pressure effect on the unit cell volume due to inter-grain contacts. This means that the relative pressure on a single grain is lower and, because of that, the volume decrease at the same nominal external pressure is lower. This yields lower compressibility of the powder samples which is seen in a higher K.
An *ab initio* calculation (at a temperature of 0 K) for K yielded 111.5 (8) GPa. For more details on this calculation procedure, a description is given in Ruiz-Fuertes *et al.* (2016). Other calculations yield 100.00 and 103.66 GPa (Wang *et al.*, 2005; Ali *et al.*, 2016), respectively. These values are notably lower than the experimental result. According to Winkler and Milman (2014), this is typical for calculations based on density functional theory (DFT) and generalised gradient approximations (GGA). However, the value calculated in Ruiz-Fuertes *et al.* (2016) is slightly higher than other calculated values in the literature where slightly different approaches for DFT calculations were used. Li *et al.* (2009) used another theoretical approach to determine the bulk modulus from the lattice energy based on chemical bond theory (Phillips, 1970; Levine, 1973; Zhang *et al.*, 2007a,b). Their result is $K = 134.0$ GPa which is more reliable than the conventional calculations. It is in between the presented value of $K = 125(3)$ GPa and the one of Lacomba-Perales *et al.* (2010). Li *et al.* (2009) also calculated mean values for La-O (170.0–85.2 GPa) and P-O (990.0–1093.9 GPa). This shows that the influence of the La-O bond on the compression behaviour is larger because of the lower interaction potential between the two elements compared to P-O (Li *et al.*, 2009).
The phase transition from monazite to post-barite is a first-order transition because of the discontinuous change of the volume ($\approx 6\,\%$) at the phase transition. The compression during the transition is extremely anisotropic with $\vec{a}$ being the most compressible axis (86 % relative length change between ambient conditions and at 27.1 GPa) while the relative length changes for $\vec{b}$ and $\vec{c}$ are of similar magnitude (94 % and 95 %, respectively). This large decrease in $\vec{a}$ can be explained by the structural rearrangement: The polyhedra chain in monazite is parallel to $\vec{c}$, while the LaO_9 polyhedra are connected to each other within the $\vec{a} - \vec{b}$ plane as explained in section 1.3.1. The PO_4 tetrahedra are almost rigid and hardly yield to pressure by changing P-O bond lengths or O-P-O bond angles which

is confirmed by the calculations of Li *et al.* (2009). However, the LaO_9 polyhedra along $\vec{a}$ are far more compressible, hence, they can rearrange most easily (Lacomba-Perales *et al.*, 2010).

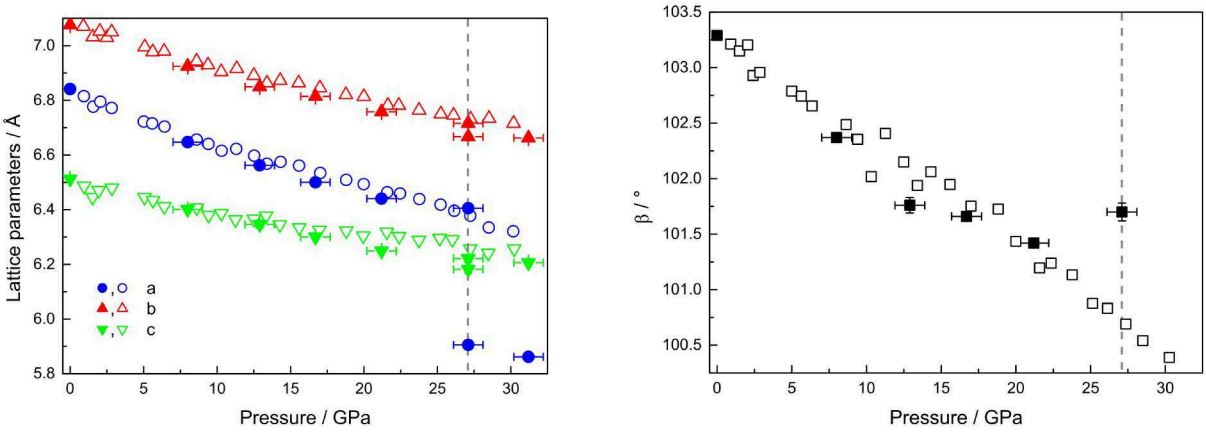

Figure 3.36 Pressure dependence of $\vec{a}$, $\vec{b}$, $\vec{c}$ (left) and β (right) of monazite-type $LaPO_4$ after Ruiz-Fuertes *et al.* (2016). Filled symbols are single-crystal data, while open symbols are powder XRD data of the metastable monazite form from Lacomba-Perales *et al.* (2010). Error bars are smaller than the symbols. The dashed, vertical line represents the pressure of the phase transition.

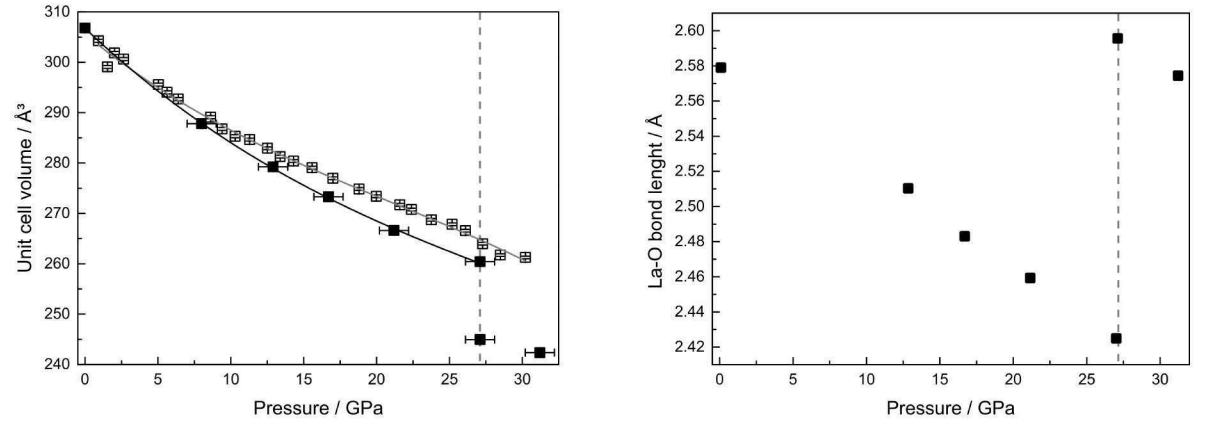

Figure 3.37 Pressure dependence of the unit cell volume (left) and the mean La-O bond length (right) after Ruiz-Fuertes *et al.* (2016). Filled symbols are single-crystal data, while open symbols are powder XRD data of the metastable monazite form from Lacomba-Perales *et al.* (2010). The dashed, vertical line represents the pressure of the phase transition. Black and grey solid lines represent fitted third-order Birch-Murnaghan equation of states. In some cases, the error bars are smaller than the symbols.

3.3.2 Monazite ceramics

In this section, the results of HT XRD measurements and dilatometry on LaPr are presented to focus on the following aspects:

- What is the microstructure and the grain size distribution of the ceramics after each sintering step?
- How do the ceramics change from the first sintering to the second sintering step?
- Are there any compositional influences on the microstructure and density?
- Are there (compositional) differences in the coefficients of thermal expansion (α) in powders and ceramics?
- How do the elastic properties of ceramics behave upon substitution?

The results have also been published in Thust *et al.* (2017).

3.3.2.1 Sintering and Microstructure

All pre-ceramics were soft and fragile. After the second sintering step, the final ceramics were dense and mechanically stable. SEM images of three samples in the state of pre- and final ceramic (a-c and d-f, resepectively) are shown in figure 3.38. All samples are homogeneous and no local clustering of a specific grain size was found. The histograms (g-i) in figure 3.38 show the grain distribution for the major grain axis. This means that that the results for the longest axis are presented. For the pre-ceramics, results were only obtained by the lineal intercept method by Wurst and Nelson (1972). For the method of the best fitting ellipses by Heilbronner and Barrett (2013), the SEM images did not reveal enough detail. However, grain sizes of final ceramics could be obtained by both methods.
Figure 3.39 shows the average grain size for the complete LaPr series. While the pre-ceramics barely show any variation with composition in their microstructure, grain shape, and grain size, the final ceramics show a slight increase in the grain sizes especially for intermediate compositions. However, within the errors, there is no deviation between the average grain sizes obtained by the two different methods used to determine them. The increase of the grain size might be due to enhanced sintering behaviour of these samples. Yet, since the melting temperature of the intermediate compositions are expected to decrease linearly from $LaPO_4$ to $PrPO_4$ (2345±20 K and 2211±20 K, respectively, Hikichi and Nomura, 1987), the higher grain sizes of the intermediates are not associated with a better sintering due to reduced melting temperatures.
The densities (see subsection 2.2.5) of the pre-ceramics are between 57 and 64 % of the theoretical densities, while those of the final ceramics are significantly higher (94.3–99.3 %; see table A.32 in the Appendix). This indicates a good response to sintering which is an advantage for monazite as a nuclear waste form (Dacheux *et al.*, 2013). Additionally, the high density and the low porosity are essential to create a low effective surface for any incoming leachants to cause corrosion (Boatner and Sales, 1988).

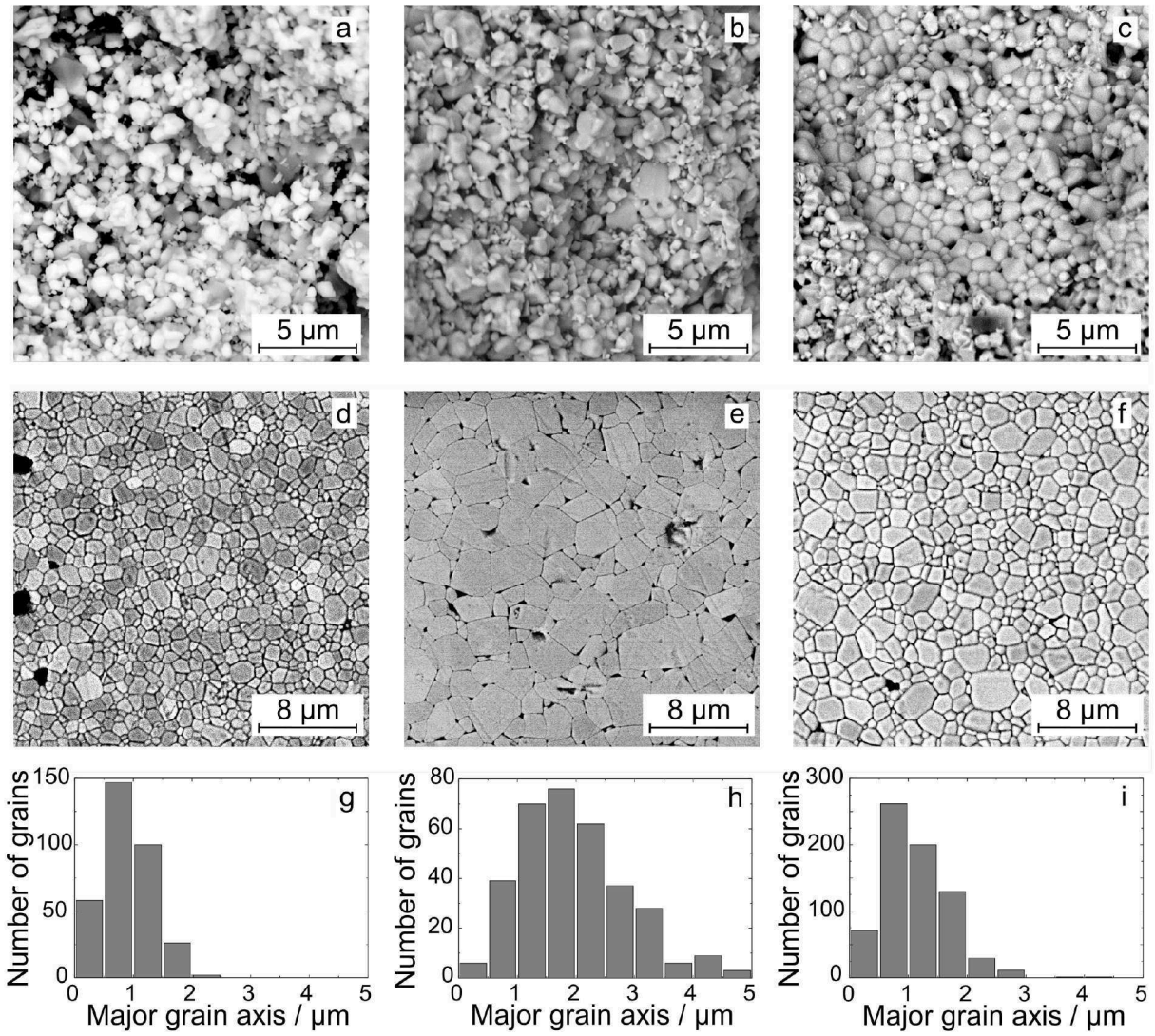

Figure 3.38 SEM micrographs and grain size distributions of LaPr with $x = 0$ (a,d,g), $x = 0.5$ (b,e,h) and $x = 1$ (c,f,i) after Thust *et al.* (2017). Note that in contrast to a-c, figures d-f show polished sections of corresponding ceramics. While all pre-ceramics (a-c) show similar grain sizes, final ceramics of intermediate compositions have larger grains (e) compared to end-members (d,f) which is highlighted by grain size distributions (g-i) obtained by the method of the best fitting ellipses by Heilbronner and Barrett (2013).

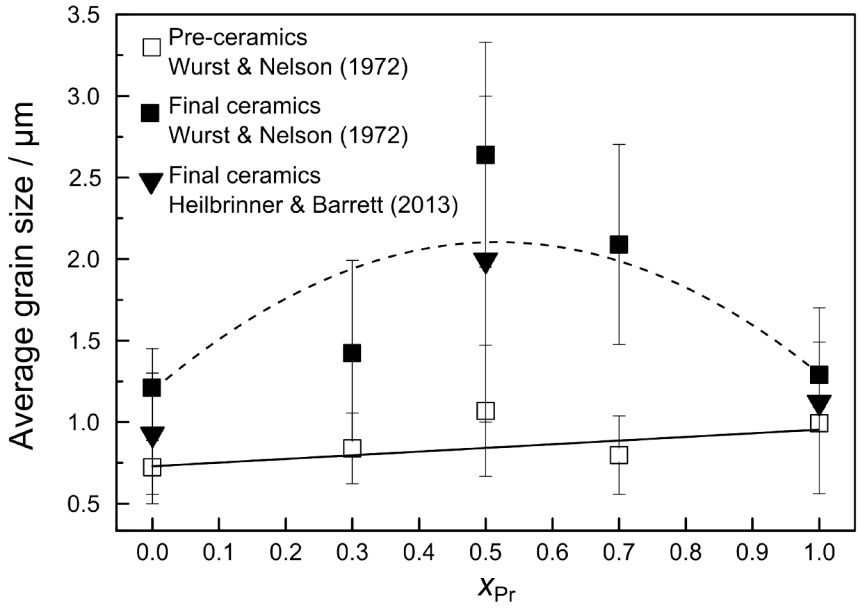

Figure 3.39 Average grain size of LaPr ceramics after Thust *et al.* (2017). Grain sizes of the pre-ceramics (open squares) and final ceramics (filled squares) were determined using the intercept method (Wurst and Nelson, 1972). Grain sizes for the final ceramics determined using the best fitting ellipses (Heilbronner and Barrett, 2013) are represented as filled triangles. Dashed and continuous lines are guides to the eye.

The pre-ceramics are not suitable as a nuclear waste form due to their small grain sizes, high porosity and their fragility. As a repository matrix, the waste form needs to have a high mechanical stability and low (open) porosity in order to resist fracturing and to withstand water influx and corrosion. Bregiroux *et al.* (2009) investigated the sintering behaviour of $LaPO_4$ obtained by solid state reaction according to Bregiroux *et al.* (2007a) stating an optimum sintering temperature between 1723 and 1773 K to achieve the maximum densification. Although their sintering temperature is higher than the one used here, the resulting ceramics show comparable grain sizes (up to 4 μm) and densities (higher than 92 % compared to the theoretical density).

3.3.2.2 Thermal expansion from HT-XRD

The diffractograms show a shift of the peaks with increasing temperature (fig. 3.40): the 2θ values become smaller indicating an increase of the lattice parameters.

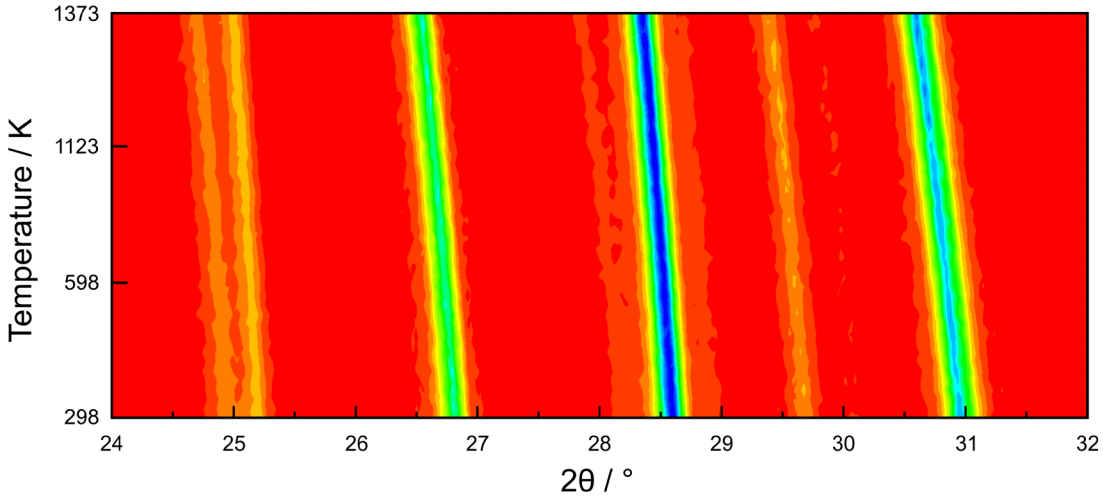

Figure 3.40 Two-dimensional contour plot (heat plot) of the HT-diffraction data for $LaPO_4$ in the 2θ range of 24-32° during heating from 298 K to 1373 K (see subsection 2.2.3.3) after Thust *et al.* (2017). Measurements were performed every 25 K. Background is given in red, while increasing blue colour indicates higher counts.

The change in the normalised lattice parameters and the volume is shown in figure 3.41 for $La_{0.5}Pr_{0.5}PO_4$. The results for the other four samples are comparable. The percentage change of $\vec{a}$, $\vec{b}$, $\vec{c}$, β, and V throughout the whole solid solution was calculated via:

$$a_i[\%] = \frac{a_i \cdot 100}{a_{i,0}} - 100 \tag{3.7}$$

and presented in table 3.6. Within the solid solution, β remains almost unchanged, all other lattice parameters increase with increasing temperature. The longest axis, $\vec{b}$, undergoes the smallest relative change, the shortest axis, $\vec{c}$, shows the largest relative increase. This can be attributed to the chain structure parallel to [001] in monazite (see chapter 1.3.1): Since all polyhedra are linked to each other in the $\vec{a}$-$\vec{b}$-plane, the $\vec{c}$ direction is more affected meaning that the expansion along the chain structure is easier than perpendicular to it (Asuvathraman and Kutty, 2014).

Table 3.6 Percentage change in the lattice parameters between 298 K and 1373 K of five LaPr compositions. Errors are given in brackets. All values are in %. The $\vec{b}$ axis shows the smallest relative change, while the $\vec{c}$ axis shows the largest change.

x_{Pr}	$\lvert\vec{a}\rvert$	$\lvert\vec{b}\rvert$	$\lvert\vec{c}\rvert$	β	V
0.0	1.14(1)	0.85(1)	1.34(1)	0.09(1)	3.33(1)
0.2	1.07(1)	0.81(1)	1.27(1)	0.08(1)	3.14(2)
0.5	1.08(1)	0.83(1)	1.24(1)	0.06(1)	3.15(2)
0.8	1.06(1)	0.83(1)	1.19(1)	0.05(1)	3.10(2)
1.0	1.06(2)	0.86(2)	1.15(2)	0.03(1)	3.09(3)
mean	1.08(1)	0.84(1)	1.24(1)	0.06(1)	3.16(2)

The coefficients of thermal expansion, α, were calculated at $T_{\mathrm{ref}} = 298\,\mathrm{K}$ as described in section 2.2.3.4. For $\vec{a}$, $\vec{b}$, $\vec{c}$, and β, they are shown in figure 3.42 and in table A.33 in the Appendix. The volume-derived linear expansion coefficient (α_m) is used for comparison with the dilatometric data. Again, α_c shows the highest values. However, within the uncertainties, these findings are only slightly significant, although there might be a slight decrease with Pr content of α_a and α_c.

There are two approaches to correlate the observations with other parameters. The first one is based on the melting temperatures of monazites ($LaPO_4$: 2345(20) K; $PrPO_4$: 2211(20) K; Hikichi and Nomura, 1987). Generally, with increasing temperature, lattice vibrations are increasing. With increasing mass of the components, the anharmonicity of these lattice vibrations increases, too (Kingery *et al.*, 1976): In LaPr, the mass of PO_4 remains constant, while the mass from La to Pr increases, *i.e.* the total mass of the formula unit in the solid solution series increases. Thus, the anharmonicity increases, yielding lower melting temperatures. Therefore, Pr richer compositions might show smaller α values. However, this approach is unlikely correct because the mass change is very small.

The second and more likely approach concerns bond characteristics of the monazite structure by Li *et al.* (2009) as described before in section 3.3.1: The higher the lattice energy of a certain bond, the stronger the interactions between the two ions, resulting in smaller bond lengths. Consequently, higher energies attributed to a specific bond yield lower coefficients of thermal expansion. Since the *Ln*-O bonds in monazite are longer than the P-O bonds, the influence of the latter on the expansion behaviour is rather small ($\alpha_{La-O} = 10.48 - 11.55 \cdot 10^{-6}\,\mathrm{K}^{-1}$; $\alpha_{Pr-O} = 10.29 - 11.42 \cdot 10^{-6}\,\mathrm{K}^{-1}$; $\alpha_{P-O} = 0.89 - 0.92 \cdot 10^{-6}\,\mathrm{K}^{-1}$; Li *et al.*, 2009). For $LaPO_4$ and $PrPO_4$, these bonding characteristics yield α values of $7.78 \cdot 10^{-6}\,\mathrm{K}^{-1}$ and $7.66 \cdot 10^{-6}\,\mathrm{K}^{-1}$, respectively (Li *et al.*, 2009). Although the calculations of Li *et al.* (2009) are significantly lower than the results obtained here, the observation is the same: with increasing Pr content α decreases. The deviation between α_m and the values calculated by Li *et al.* (2009) is rather small and within errors.

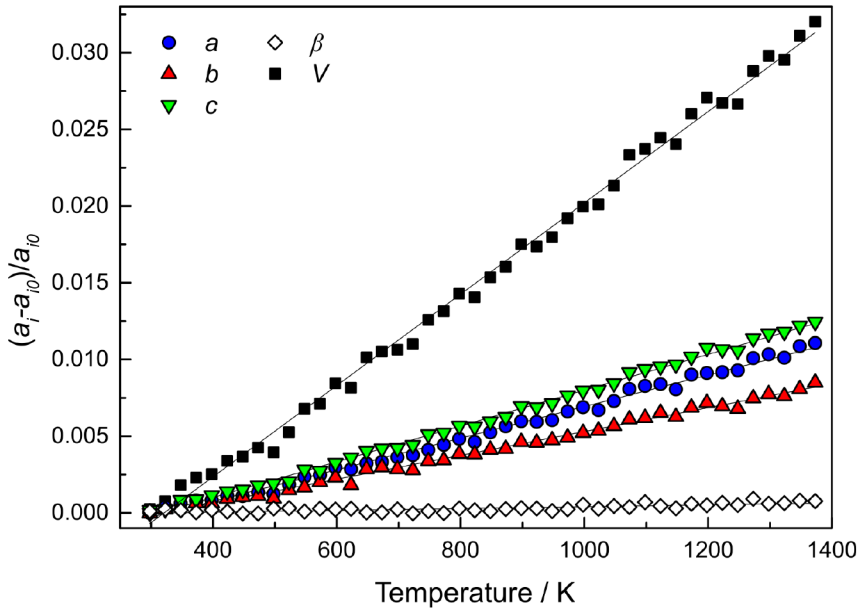

Figure 3.41 Temperature dependence of the lattice parameter changes a_i and the unit cell volume normalised to the parameter value at 300 K ($a_{i,0}$) of $La_{0.5}Pr_{0.5}PO_4$ after Thust *et al.* (2017). Solid lines correspond to first-order-polynomial fits. Error bars are smaller than the symbols.

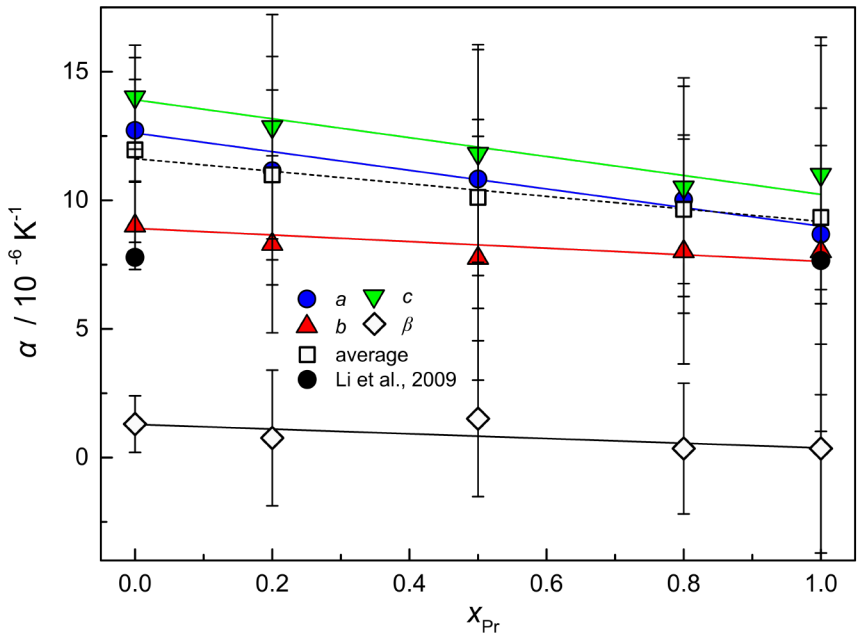

Figure 3.42 Coefficients of thermal expansion (α) of the lattice parameters and the average value (calculated by $\alpha_V/3$) of LaPr vs. the Pr content x_{Pr} in comparison to Li *et al.* (2009). Lines are linear fits to the data.

3.3.2.3 Thermal expansion from dilatometry

The ceramics were subjected to dilatometric measurements. The information obtained hereby are important because the industrial use of nuclear waste forms would focus on ceramics which are easier to produce and to handle.
In the dilatometric measurements, the pre-ceramics show a high deviation between heating and cooling which is due to shrinkage upon sintering because of grain growth. As expected, the final ceramics show almost identical behaviour for the heating and cooling run indicating that no further sintering occurred. The results for the final ceramics were used to calculate α as described in section 2.2.6.
The α values obtained by dilatometry and by HT XRD are shown in figure 3.43 in comparison to literature data. Both, α from dilatometry and from HT XRD, show similar values. While the volume-derived linear expansion coefficient for the lattice parameters, α_m, of the powder XRD decreases as described before, the values obtained via dilatometry for the ceramics range between 11.3 and $12.0 \cdot 10^{-6}\,\mathrm{K}^{-1}$ and show no systematic dependence on the composition.
The microstructure of ceramics depends on the synthesis route and conditions of the powder, which will influence the reactivity of the powders during sintering. Furthermore, different sintering profiles will also influence the microstructure (grain and pore size, grain shape etc.). Perriere *et al.* (2007) used solid state reaction as done in this work, while Morgan and Marshall (1995) and Hikichi *et al.* (1997) used precipitation from aqueous solution and Thust *et al.* (2015) synthesised the samples hydrothermally. All of them report to have pure monazite in the end of their synthesis procedures which is supported by the comparable α values. For sintering, Hikichi *et al.* (1997) and Thust *et al.* (2015) used 1573 K, whereas Perriere *et al.* (2007) sintered at 1773 K and Morgan and Marshall (1995) at 1973 K. However, all of them calculated the thermal expansion coefficients from dilatometric measurements on ceramic samples. Li *et al.* (2009) calculated the α values from lattice energies. In comparison to these literature data, the values for the thermal expansion in the present study are slightly higher.
The values α_m from HT XRD reflect the behaviour of the lattice parameters since they are directly calculated from these. In contrast, α values from dilatometry are calculated from the length change of a bulk ceramic sample. Therefore, they are clearly influenced by the microstructure in terms of grain size and shape, pores and defects as well as grain boundaries (Li *et al.*, 2009). These influences on the ceramic samples mask the compositional differences observed in X-ray experiments.

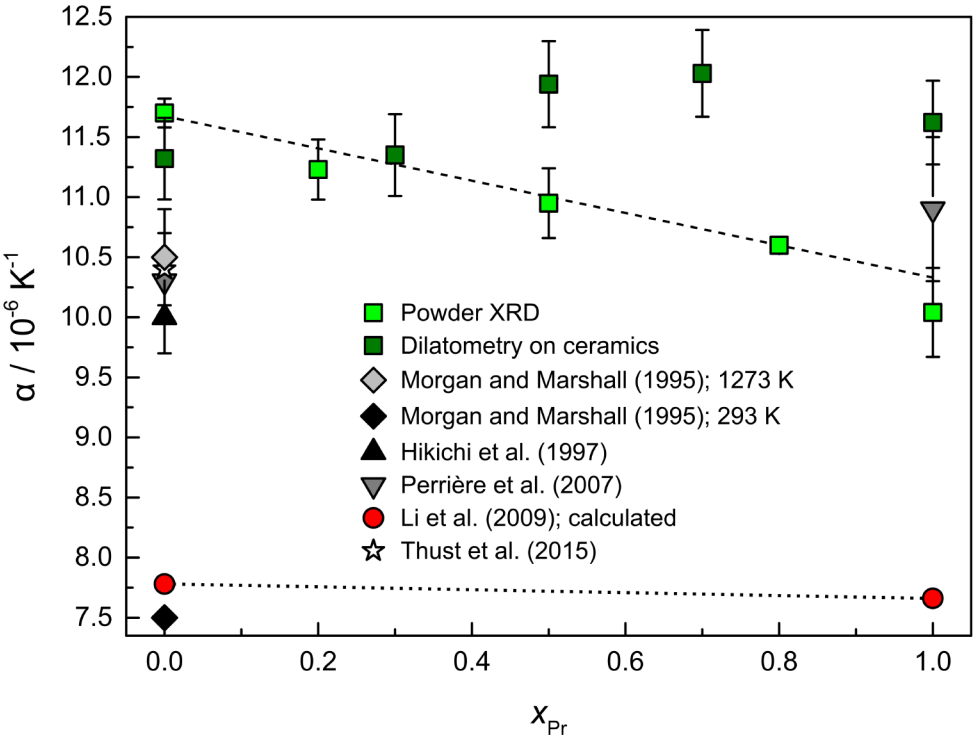

Figure 3.43 Linear thermal expansion coefficients (α) from powder XRD (α_m) and from dilatometry of the final ceramics of LaPr at 1273 K in comparison to literature data after Thust *et al.* (2017). The dashed line represents a linear fit to the average α_m values of the powders. The dotted line at the bottom is the connection of the α values calculated from lattice energies by Li *et al.* (2009).

3.3.2.4 Mechanical properties

Figure A.18 in the Appendix shows, exemplarily, the results of a plane-wave/parallel-plate ultrasound spectroscopy measurement (see subsection 2.2.4.3) on the final ceramic of $LaPO_4$. The measurements on the other ceramics look similar. Table A.32 in the Appendix shows the densities, porosities and stiffness coefficients of the samples. Resonances were not detected for any of the pre-ceramics. This was because their high porosities dissipate the ultrasound signal considerably. As described in section 2.2.3.4, longitudinal and shear waves are used to determine the interval between adjacent resonances (Δf). Afterwards, the elastic stiffness coefficients are calculated to assess the mechanical properties: bulk modulus K, Young's modulus E, shear modulus G and Poisson's ratio η (fig. 3.44). All of these mechanical properties decrease with increasing ionic radius which is supported by the literature values (Thust *et al.*, 2015; Perriere *et al.*, 2007; Feng *et al.*, 2013; Du *et al.*, 2009; Wang *et al.*, 2005; Li *et al.*, 2009; Lacomba-Perales *et al.*, 2010). Measurements on samples of LaEu and LaPr (Thust *et al.*, 2015, 2017) with the same compositions show different values due to different macroscopic densities. This may also explain the differences between the values from the literature and the ones obtained here.
As the *Ln* radius and the *Ln*-O bond lengths increase, the interatomic bond strength

decreases, yielding an decrease of E as described by Du *et al.* (2009) and Feng *et al.* (2013). Though the trends for LaEu and LaPr are consistent, some literature values show a large dispersion. These differences are most probably due to different sample preparation techniques as stated by Du *et al.* (2009). The elastic properties are in the same range as those for SynRoc (*e.g.* K; 110-160 GPa; E: 140-200 GPa according to Campbell *et al.*, 1982). Industrial glasses, however, show lower values in all elastic properties. Borosilicate glasses and SiO_2 glasses from Schott and Saint-Gobain are in a K range of 30-45 GPa and an E range of 60-80 GPa (Rouxel, 2007).

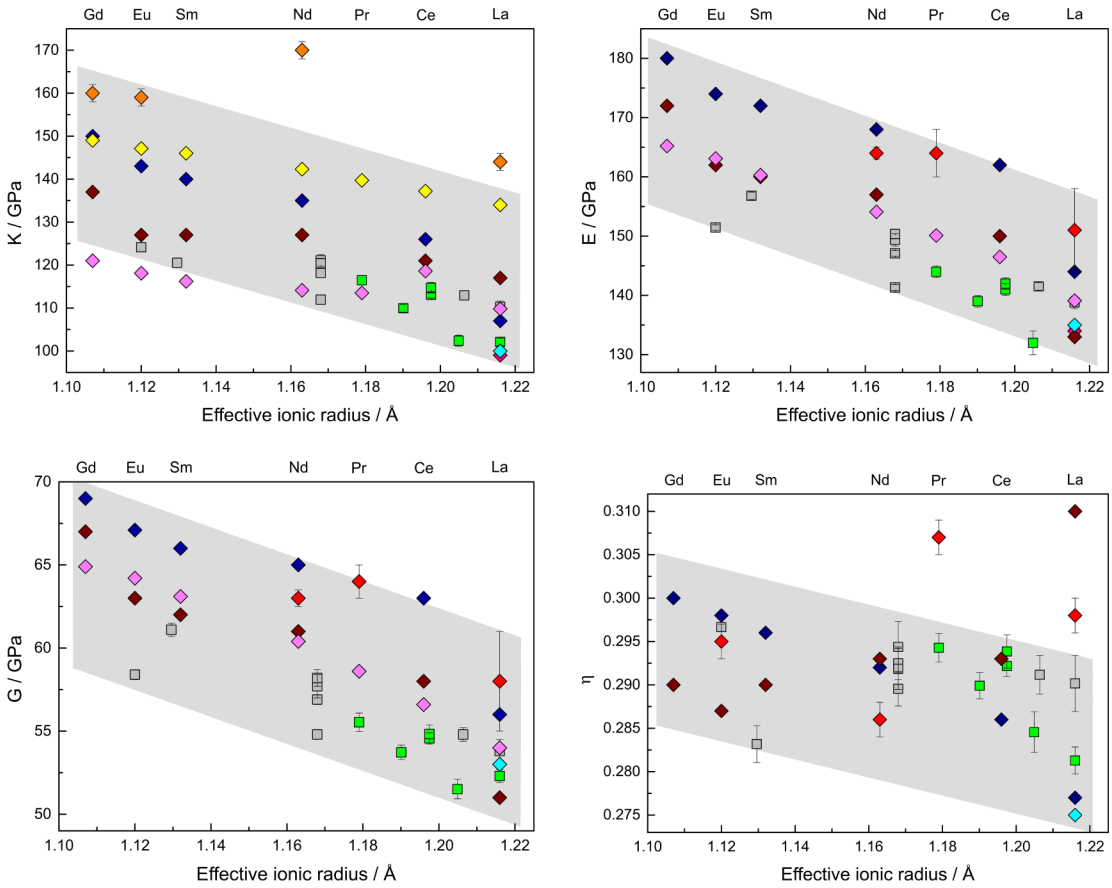

Figure 3.44 Bulk modulus K, Young's modulus E, shear modulus G, and Poisson's ratio η of LaPr and LaEu calculated from c_{11} and c_{44} in comparison to literature data vs. composition. For the explanation of the symbols see table 3.7. The shaded area shows the decrease of the data.

Table 3.7 Legend for figures 3.44 and 3.45 containing the symbol, the composition in terms of the abbreviated formula of the solid solution or the end members and the references.

Symbol	Chemistry	Reference
■	LaPr	Thust *et al.* (2017), this work
■	LaEu	Thust *et al.* (2015)
◇	end members	Morgan and Marshall (1995)
◆	end members	Wang *et al.* (2005)
◆	end members	Perriere *et al.* (2007)
◆	end members	Li *et al.* (2009), cal.
◆	end members	Du *et al.* (2009)
◆	end members	Lacomba-Perales *et al.* (2010)
◆	end members	Feng *et al.* (2013), exp.
◆	end members	Feng *et al.* (2013), cal.
◆	end members	Kowalski and Li (2016), cal.

Using the empirical relationship between the shear modulus G and the Vickers micro hardness H_V by Jiang *et al.* (2011):

$$G = 6.78 H_V \tag{3.8}$$

the hardness of the ceramics was calculated and compared to literature values (fig. 3.45 on the left). All samples show a relatively low hardness H_V between 7 and 10 GPa. These values are comparable to *Ln*-bearing Zr-pyrochlores (9-11 GPa), but smaller than for *Ln*-bearing Sn-pyrochlores or double perovskites (10–15 GPa and 12–14 GPa, respectively, Feng *et al.*, 2011a,b, 2012, 2013) which are also possible nuclear waste host matrices. The values are also comparable to SynRoc (8–11.7 GPa), but higher than for industrial glasses like borosilicate and SiO_2 (4–5 GPa, Campbell *et al.*, 1982; Rouxel, 2007). In contrast, NaCl shows a far lower value of 2.1 GPa according to Gilmore and Katz (1982), while diamond reaches values of over 100 GPa (*e.g.* Blank *et al.*, 1998; Vepřek, 1999; Solozhenko *et al.*, 2009).
When considered as a potential nuclear waste form, the low hardness and the weak bonding make monazite an ideal candidate because both properties are essential for machinable ceramics (Davis *et al.*, 1998). In general as described by Pugh (1954), the resistance to plastic deformation is proportional to G, while the fracture strength is proportional to the lattice parameters and K. The Pugh's ratio (K/G) can be used as an indicator for malleability (Pugh, 1954). Generally, if K/G is larger than 1.75, the material is ductile, while smaller Pugh's ratios indicate brittle behaviour. Industrial borosilicate glasses from Schott and SiO_2 glass from Saint-Gobain yields K/G values between 1.1 and 1.3 (calculated after Rouxel, 2007), while K/G for SynRoc is >2 (calculated after Campbell *et al.*, 1982). In addition to the Pugh's ratio, a rather high Poissons' ratio (η) is an indicator for the 'softness' of a specific material (Feng *et al.*, 2013). For monazite, the low hardness and

the weak bonding resulting from the mixture of covalent and ionic bonds, both influence the Poisson's ratio. As described by Feng *et al.* (2013), η for ionic and covalent-ionic materials is usually found to be 0.2-0.25. For monazite, because of the relatively low shear modulus G, this value is around 0.275-0.3, which is comparable to steel and SynRoc (Stang *et al.*, 1946; Campbell *et al.*, 1982). The correlation between Pugh's and Poissons' ratio was determined by Pugh (1954):

$$\frac{K}{G} = \frac{2(1+\eta)}{3(1-2\eta)}. \tag{3.9}$$

This equation was used to calculate K/G from literature values in order to obtain more data for comparison. The results are shown in figure 3.45 on the right. The values are found to be around 2. This means that both, Poissons' ratio and Pugh's ratio, demonstrate the ductility and good machinability of monazite as described for the end-members by Davis *et al.* (1998), Hay and Marshall (2003), and Feng *et al.* (2013).

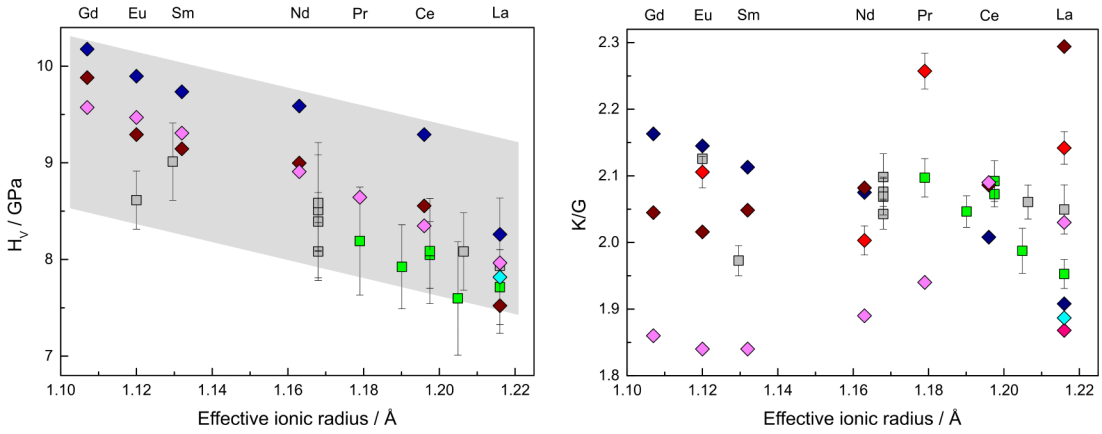

Figure 3.45 Calculated Vickers hardness (H_V, left) and Pugh's ratio (K/G, right) of LaPr and LaEu vs. effective ionic radius in comparison to literature values. H_V was calculated from the shear modulus (G) after Jiang *et al.* (2011). The shaded area shows the decrease of the data. For the explanation of the symbols see table 3.7.

3.3.3 Summary on non-ambient characterisation of monazite

HP studies on $LaPO_4$ single crystals show a decrease of the lattice parameters with increasing pressure up to 27.1 GPa. The $\vec{a}$-axis shows the highest shortening. At 27.1 GPa, the structure is rearranged: the *Ln*-O bond lengths increase and the coordination of the *Ln* atom increases from nine to twelve, while the PO_4 tetrahedra remain unchanged. The HP phase is isotypic to post-barite with the space group $P2_12_12_1$.
HT investigations focussed on powders and ceramics. For the latter, high densities were achieved in a two-step sintering profile. With increasing temperature, the lattice parameters of the monazite powders increase. The thermal expansion coefficient of the powders decrease with increasing Pr content. This change can be ascribed to the following: with increasing lattice energy, the increasing interactions lead to smaller *Ln*-O bond lengths and, by this, to decreasing thermal expansion coefficients. In contrast to the results from powder XRD, the thermal expansion measured by dilatometry on and the elastic properties obtained from ultrasound spectroscopy on the ceramics are highly affected by the density of the sample.

3.4 Thermodynamic properties of monazite

High-temperature (HT) and low-temperature (LT) calorimetric data are presented in the following section. For powder samples, HT calorimetry yields enthalpies of formation and mixing, while LT calorimetry on single crystals gives insight into the influence of Pr^{3+} on the molar heat capacity.

3.4.1 HT solution calorimetry

HT solution calorimetry, as described in Hirsch *et al.* (2017), was performed to answer the following two questions:

- How do the standard enthalpies of formation from the oxides ($\Delta H^0_{\mathrm{f,ox}}$) and from the elements ($\Delta H^0_{\mathrm{f,el}}$) change with composition?
- Does the standard enthalpy of mixing (ΔH_{mix}) change within the solid solution?

When considering the thermochemical cycle (table 3.8) for calculating the enthalpies, the oxidation of Pr needs to be included. As shown by Ushakov *et al.* (2001), the stable species of Pr in the solvent ($3\,Na_2O \cdot MoO_3$) is $PrO_{1.83}$ instead of Pr_2O_3. This change is a result of the oxidising conditions upon which Pr^{3+} nominally changes to $Pr^{3.66+}$ in the solvent. The enthalpy of solution, ΔH_{ds} (LaPr), obtained from the measured heat-flow (see subsection 2.2.7), is given as (i) in table 3.8, which consists of the reaction of monazite with oxygen to La_2O_3, $PrO_{1.83}$ and P_2O_5, the three dissolved component oxides in the melt. The dissolution and standard formation enthalpies of these compounds (ΔH_{ds} and ΔH^0_f) were determined by Cheng and Navrotsky (2003), Ushakov *et al.* (2001) and Robie *et al.* (1979) (see (ii)-(ix) in table 3.8). Then, the standard formation enthalpy from the oxides and from the elements ($\Delta H^0_{\mathrm{f,ox}}$ and $\Delta H^0_{\mathrm{f,el}}$) can be calculated, indicated as (x) and (xi) in table 3.8. For more details, see Hirsch *et al.* (2017). The results are given in table 3.9.

Table 3.8 Thermochemical cycle of LaPr for the determination of enthalpy of formation from oxides and elements after Hirsch *et al.* (2017). $\Delta H(n)$ refers to the ΔH term in roman numbering. The subscripts correspond to: s = solid, sln = solution, ds = drop solution, f = formation, cr = crystalline, g = gaseous. Data from Cheng and Navrotsky (2003) [a] , Ushakov *et al.* (2001) [b] and Robie *et al.* (1979) [c] was used for the calculation. Numbers in brackets at the start of the line are corresponding to the ΔH terms

		Reaction	ΔH[kJ/mol]
(i)	ΔH_{ds} ($La_{1-x}Pr_xPO_4$)	$La_{1-x}Pr_xPO_{4(s,298\,K)}$ + x 0.165 $O_{2(g,298\,K)}$ → 0.5 (1-x) $La_2O_{3(sln,973\,K)}$ + x $PrO_{1.83(sln,973\,K)}$ + 0.5 $P_2O_{5(sln,973\,K)}$	see table 3.9
(ii)	ΔH_{ds} (La_2O_3)	$La_2O_{3(cr,298\,K)} \rightarrow La_2O_{3(sln,973\,K)}$	-225.1 ± 3.16[a]
(iii)	ΔH_{ds} ($PrO_{1.83}$)	$PrO_{1.83(cr,298\,K)} \rightarrow PrO_{1.83(sln,973\,K)}$	-41.6 ± 1.0[b]
(iv)	$\Delta H_{(298-973\,K)}$ (O_2)	$O_{2(g,298\,K)} \rightarrow O_{2(g,973\,K)}$	21.7[c]
(v)	ΔH_{ds} (P_2O_5)	$P_2O_{5(cr,298\,K)} \rightarrow P_2O_{5(sln,973\,K)}$	-164.6 ± 0.5[b]
(vi)	ΔH^0_{f} (Pr_2O_3)	2 $Pr_{(s,298\,K)}$ + 1.5 $O_{2(g,298\,K)} \rightarrow Pr_2O_{3(s,298\,K)}$	-1809.6 ± 6.7[c]
(vii)	ΔH^0_{f} ($PrO_{1.83}$)	$Pr_{(s,298\,K)}$ + 0.915 $O_{2(g,298\,K)} \rightarrow PrO_{1.83(s,298\,K)}$	-952.3 ± 3.4[c]
(viii)	ΔH^0_{f} (La_2O_3)	2 $La_{(s,298\,K)}$ + 1.5 $O_{2(g,298\,K)} \rightarrow La_2O_{3(s,298\,K)}$	-1791.6 ± 1.6[c]
(ix)	ΔH^0_{f} (P_2O_5)	2 $P_{(s,298\,K)}$ + 2.5 $O_{2(g,298\,K)} \rightarrow P_2O_{5(s,298\,K)}$	-1504 ± 0.5[c]
(x)	$\Delta H^0_{\mathrm{f,ox}}(La_{1-x}Pr_xPO_4)$	0.5 (1-x) $La_2O_{3(s,298\,K)}$ + 0.5 x $Pr_2O_{3(s,298\,K)}$ + 0.5 $P_2O_{5(s,298\,K)}$ → $La_{1-x}Pr_xPO_{4(s,298\,K)}$	see table 3.9
	ΔH(x) = -ΔH(i) + 0.5 (1-x) ΔH(ii) + x(ΔH(iii) - 0.165 ΔH(iv) + ΔH(vii) - 0.5 ΔH(vi)) + 0.5 ΔH(v)		
(xi)	$\Delta H^0_{\mathrm{f,el}}(La_{1-x}Pr_xPO_4)$	(1-x) $La_{(s,298\,K)}$ + x $Pr_{(s,298\,K)}$ + $P_{(s,298\,K)}$ + 2 $O_{2(g,298\,K)} \rightarrow La_{1-x}Pr_xPO_{4(s,298\,K)}$	see table 3.9
	ΔH(xi) = 0.5 (1-x) ΔH(viii) + 0.5 x ΔH(vi) + 0.5 ΔH(ix) + ΔH(x)		

Table 3.9 HT solution calorimetry results for LaPr in $3\,Na_2O \cdot 4\,MoO_3$ at 973 K as a function of molar fraction of Pr (x): n = number of measurements; $\Delta H_{ds,973\,K}$ = enthalpies of solution; $\Delta H^0_{f,ox}$and $\Delta H^0_{f,el}$ = standard enthalpies of formation from oxides and elements at 298 K, ΔH_{mix} = enthalpy of mixing. All enthalpies in kJ/mol after Hirsch *et al.* (2017).

x	n	$\Delta H_{ds,973\,K}$	$\Delta H^0_{f,ox}$	$\Delta H^0_{f,el}$	ΔH_{mix}
0.00(0)	10	151(2)	-346(4)	-1994(4)	—
0.08(3)	8	149(1)	-342(3)	-1991(4)	-2(1)
0.28(3)	9	149(1)	-338(3)	-1989(5)	-1(1)
0.53(5)	8	147.1(7)	-332(2)	-1985(6)	-2(1)
0.72(5)	8	149(1)	-330(2)	-1985(6)	+1(1)
0.81(2)	9	145.8(7)	-325(2)	-1980(6)	-3(1)
0.90(2)	6	150(1)	-327(2)	-1983(7)	+2(2)
0.91(2)	8	151(2)	-328(2)	-1985(7)	+4(2)
0.94(0)	8	151(1)	-327(2)	-1984(7)	+3(2)
1.00(0)	8	148(1)	-323(1)	-1980(7)	—

In figure 3.46, the $\Delta H_{ds,973\,K}$ values are presented as a function of the Pr content in LaPr (on the top left) and in comparison to literature values (on the top right) from Neumeier *et al.* (2017) and Ushakov *et al.* (2001) and to LaNd by Kegler (pers.comm., 2017). The ideal mixing behaviour for LaPr is given as a dotted line. A second-order polynomial (dashed line, $R^2 = 0.21$) and fourth-order polynomial (continuous line, $R^2 = 0.63$) was used to fit the data. The latter polynomial was calculated without using the composition $x = 0.81$ as it seems to be an outlier. From the thermochemical point of view a second-order fit would be more reasonable because the deviation from ideal mixing is expected to yield a parabolic trend. However, the fourth-order polynomial was used because it was the polynomial of the lowest order yielding an 'acceptable' fit representing the data which is probably due to the rather pronounced scattering.
There is a clear deviation for $LaPO_4$ from the data reported by Ushakov *et al.* (2001) as seen in figure 3.46 on the top right. The measurements on $LaPO_4$ in the solid solutions LaEu and LaGd from Neumeier *et al.* (2017) and LaNd by Kegler (pers.comm., 2017) show the same values as the one presented here (see fig. 3.46 on the top right). All of these samples were obtained by co-precipitation. Hence, different synthesis routes yield highly comparable results. Thus, the original $LaPO_4$ sample from Ushakov *et al.* (2001) was remeasured. This remeasured value is in very good agreement with the one presented here (fig. 3.46 on the top left). According to Ushakov (pers. comm., 2016), the difference is probably due to different measurement set-ups (like the 'bubbling' rate). The value of the $PrPO_4$ sample measured first was close to the one originally published by Ushakov *et al.* (2001). However, an XRD measurement of the $PrPO_4$ samples used here revealed an impurity phase of PrP_3O_9 which could be removed by heating the sample for 12 h at 1773 K. Afterwards, the calorimetric measurement yielded values closer to the other ones

of the solid solution. This implies that the Pr sample measured by Ushakov *et al.* (2001) might also contain impurities and is not pure $PrPO_4$.
In general, $\Delta H_{\mathrm{ds,973\,K}}$ increases with increasing effective ionic radius which is seen in figure 3.46 (top right), the pure end members by Ushakov *et al.* (2001) and solid solutions LaEu and LaGd by Neumeier *et al.* (2017) and LaNd by Kegler (pers.comm., 2017).
To calculate the enthalpy of mixing ΔH_{mix}, the difference between the ideal behaviour (dotted line in fig. 3.46 on the top left) and the measured ΔH_{ds} was determined. The results are shown in figure 3.46 (bottom). There is no statistically significant deviation from the ideal mixing within uncertainties: all deviations are smaller than 2.5 % and two standard deviations (see table 3.9). Still minor impurity phases with $\ll 2\,\mathrm{wt\%}$ may be present, below the detection limits of EPMA and XRD, yielding the observed scatter. However, since the deviations from the ideal behaviour are rather small, there is no indication for a miscibility gap. Hence, LaPr can be considered an almost ideal solid solution.

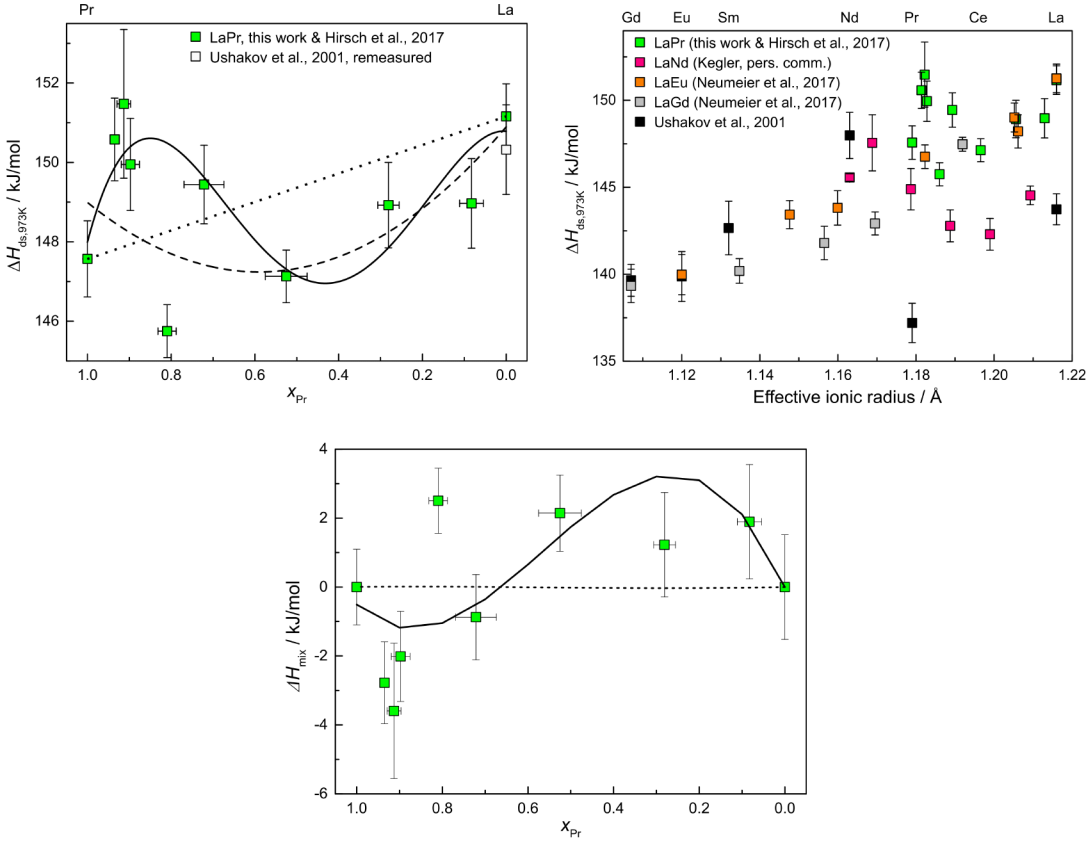

Figure 3.46 Enthalpy of solution $\Delta H_{\mathrm{ds,973\,K}}$ versus Pr content x_{Pr} (top left) after Hirsch *et al.* (2017) and versus the effective ionic radius (top right). Standard enthalpy of mixing ΔH_{mix} of LaPr versus Pr content x_{Pr} (bottom). The dotted line in $\Delta H_{\mathrm{ds,973\,K}}$ represents ideal mixing, the dashed line shows a second-order polynomial fit, while the continuous line is a fourth-order polynomial fit. The dotted line in ΔH_{mix} represents ideal mixing, the continuous line is a fourth-order polynomial fit. Where not visible, error bars are smaller than the symbols used.

3.4.2 Microcalorimetry and fluorescence spectroscopy

In this section, the following aspects are addressed:

- What is the molar heat capacity ($C_{p,m}$) of the LaPr single crystals?
- What are the energy levels of the Pr^{3+} ion in the monazite structure?

Lattice vibrations caused by thermal excitations of the ions influence the $C_{p,m}$ values. However, since Pr possesses $4f$ electrons, their thermal excitation potentially influences the heat capacity and causes an excess heat capacity called 'Schottky anomaly' or 'Schottky contribution' (Westrum, 1985). Results presented in this chapter were published in Bauer *et al.* (2016).

3.4.2.1 Heat capacity

The heat capacities for the end members $LaPO_4$ and $PrPO_4$ are given in figure 3.47. As described in subsection 2.2.8, three temperature ranges were fitted with two seventh order polynomials and one Haas-Fisher function. As an inset, the normalised heat capacity difference ($\Delta C_{p,m}/C_{p,m,cal} = (C_{p,m,obs}\text{-}C_{p,m,cal})/C_{p,m,cal}$) is given for the La end member. At high temperatures, the deviation between the measured values and the fit is very small, but even at lower temperatures the deviation is within the range of precision. For clearer presentation, the lower temperature part of the $C_{p,m}$ curves is given in figure 3.48 for all six analysed compositions. The general behaviour of the samples is the same, while a clear increase of the overall molar heat capacity with increasing Pr content is observed.

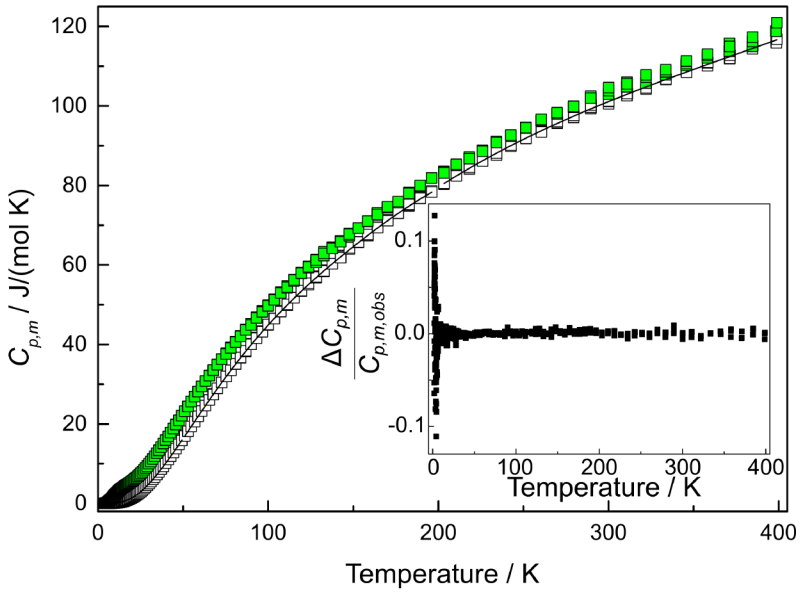

Figure 3.47 Molar heat capacity of $LaPO_4$ (white) and $PrPO_4$ (green) with increasing temperature. At each temperature, three measurements were performed. The inset shows the difference ($\Delta C_{p,m}$) of the observed data ($C_{p,m,obs}$) and the fitted curve ($C_{p,m,cal}$, black line) normalised to $C_{p,m,obs}$ for $LaPO_4$ after Bauer *et al.* (2016). The deviation at high temperatures is very small, but even at lower temperatures, the deviation is within the range of precision.

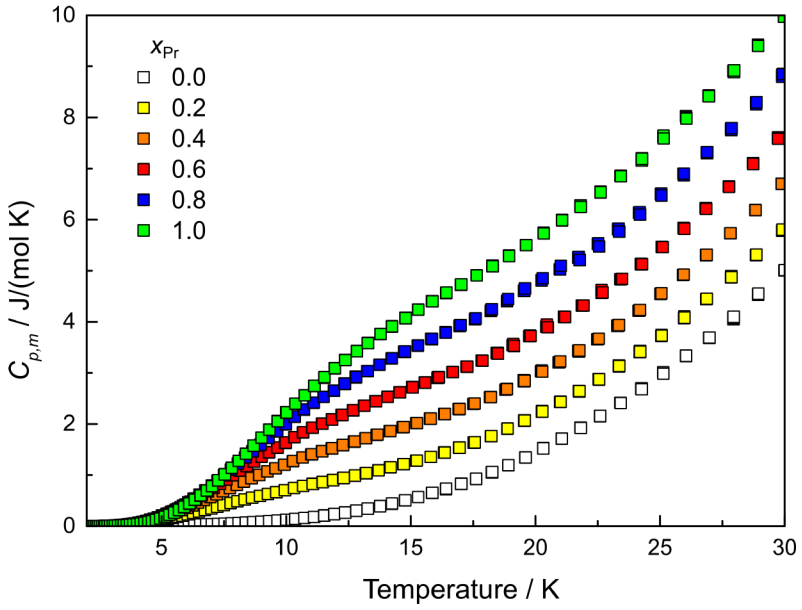

Figure 3.48 Molar heat capacity ($C_{p,m}$) of LaPr with increasing temperature up to 30 K after Bauer *et al.* (2016). The data are from white (pure $LaPO_4$) to green (pure $PrPO_4$) with increasing $\Delta x_{Pr} = 0.2$. The behaviour of the solid solution members is the same but with higher Pr content the $C_{p,m}$ increases.

As shown in figure 3.49, the molar heat capacity at 298.15 K ($C_{p,298.15\,\mathrm{K}}$) of LaPr agrees with published data on the end members by Thiriet *et al.* (2005), Gavrichev *et al.* (2008), Kowalski and Li (2016), Thust *et al.* (2015), and Gavrichev *et al.* (2016). There is a decrease in the $C_{p,298.15\,\mathrm{K}}$ values within increasing *Ln* radius from Eu to La. Differences in the values for the end members arise from the different preparation techniques. In this work, measurements were done on single crystals. Thiriet *et al.* (2005) and Thust *et al.* (2015) used ceramics, while Gavrichev *et al.* (2008, 2016) measured $C_{p,298.15\,\mathrm{K}}$ on not-sintered compacted powder. Data from Kowalski and Li (2016) were obtained via calculations. Apart from the Schottky contribution shown in figure 3.48, there is no additional excess heat capacity.

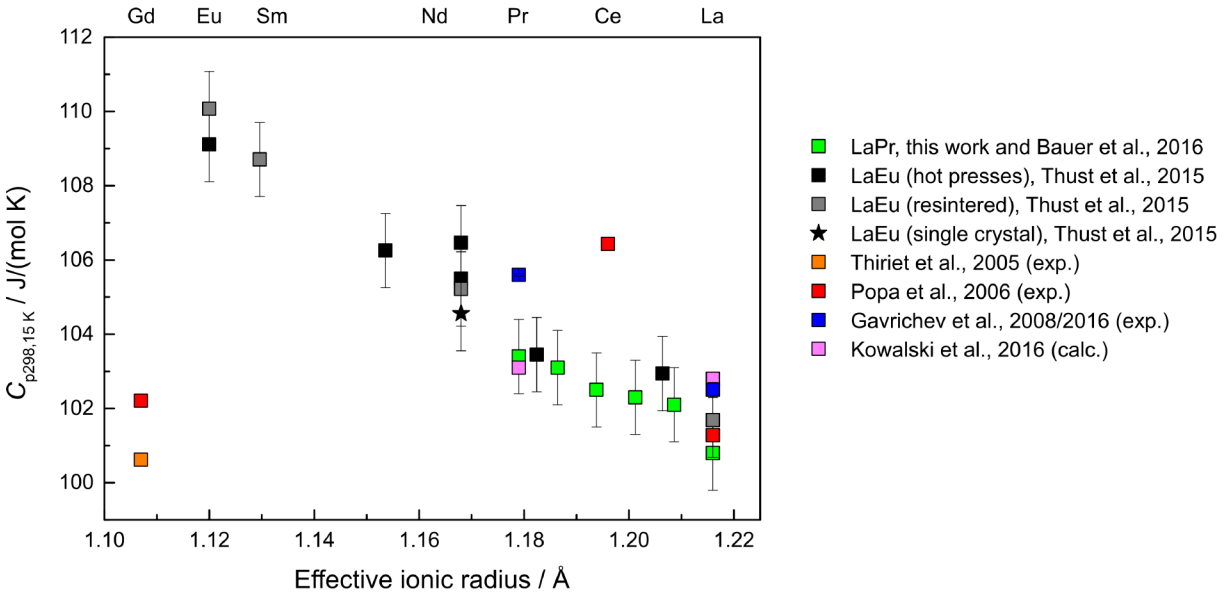

Figure 3.49 Molar heat capacity at 298.15 K ($C_{p,298.15\,\mathrm{K}}$) of the solid solutions LaPr and LaEu after Bauer *et al.* (2016) and Thust *et al.* (2015) in comparison to literature data. Differences in comparison to the literature values arise from different samples types like single crystals, ceramics and powders.

To determine the standard molar entropy $S^0_{298.15\,\mathrm{K}}$ and the enthalpy change $\Delta H_{298.15\,\mathrm{K}}$, the following formulas were used:

$$\Delta H_{298.15\,\mathrm{K}} = \int_{0\,K}^{298.15\,\mathrm{K}} C_p dT \tag{3.10}$$

$$S^0_{298.15\,\mathrm{K}} = \int_{0\,K}^{298.15\,\mathrm{K}} \frac{C_p}{T} dT \tag{3.11}$$

The results are shown in figure 3.50 in comparison to literature values of the end members and to LaEu from Thust *et al.* (2015). Both solid solutions show the same decreasing trend with increasing ionic radius as the $C_{p,298.15\,\mathrm{K}}$ data. Although the slope for LaPr and LaEu is different and even more pronounced in $S^0_{298.15\,\mathrm{K}}$ than in $\Delta H_{298.15\,\mathrm{K}}$, the values for the members of each solid solution lie in between those of their end members measured

by Thiriet *et al.* (2005). Within uncertainties, the values for the end members are comparable to those from the literature. Differences, again, arise from the different preparation techniques.

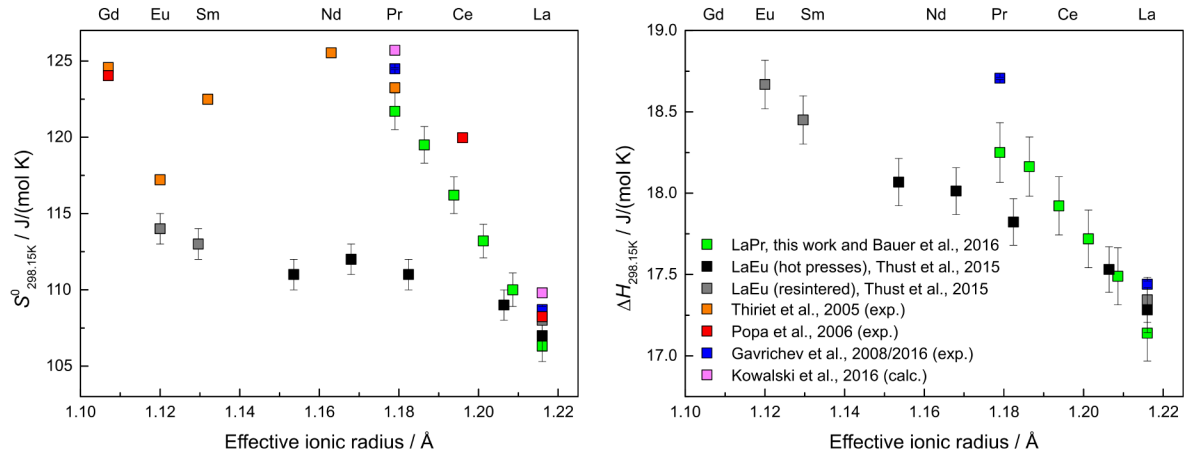

Figure 3.50 Standard molar entropy ($S^0_{298.15\,\mathrm{K}}$, left) and molar enthalpy change ($\Delta H_{298.15\,\mathrm{K}}$, right) of LaPr after Bauer *et al.* (2016). Included are data points from the literature for the end members. The legend belongs to both figures.

3.4.2.2 Schottky contribution

The Schottky contribution (C_{ex}, also known as $\Delta C_{p,m}$) to the heat capacity is given by the excess compared to the lattice heat capacity (C_{latt}) (Schottky, 1922). Due to its electron configuration, Pr^{3+} has partially filled $4f$ orbitals. The Stark effect induces a splitting of the electronic levels due to the influence of the crystal field. When the electrons are excited, the low energy electronic states ($^3H_4$ ground state) contribute to the heat capacity at lower temperatures. This contribution can be calculated via:

$$C_{ex} = \frac{\Sigma_i g_i \epsilon^2 exp(-\epsilon_i/RT)}{QRT^2} - \frac{(\Sigma_i g_i \epsilon_i exp(-\epsilon_i/RT))^2}{Q^2RT^2} \tag{3.12}$$

where ϵ_i is the energy of the i^{th} state with degeneracy g_i and the partitioning function Q:

$$Q = \Sigma_i g_i exp(-\epsilon_i/RT) \tag{3.13}$$

where R is the gas constant and T temperature (Justice and Westrum Jr., 1963).

Usually, $C_{\mathrm{latt}}(Ln\mathrm{PO_4})$ can be calculated from the molar volume and the heat capacity. C_{ex} is calculated from these lattice vibrations and the molar heat capacity of each sample according to Westrum Jr. (1983) and Gavrichev *et al.* (2016):

$$C_{ex} = C_p(Ln\mathrm{PO_4}) - C_{\mathrm{latt}}(Ln\mathrm{PO_4}). \tag{3.14}$$

The C_p contribution from the lattice vibration is then calculated as a linear interpolation for Pr monazite between La and Gd as they are the largest and the smallest Ln cation crystallising in the monazite structure type (Westrum Jr., 1983; Gavrichev *et al.*, 2016):

$$C_{\text{latt}}(Ln\text{PO}_4) = (1-f)C_p(\text{GdPO}_4) + fC_p(\text{LaPO}_4) \tag{3.15}$$

where f is the proportionality factor as defined by Westrum Jr. (1983) with the unit cell volumes of La, Pr and Gd monazite, respectively (Gavrichev *et al.*, 2016):

$$f = \frac{V(\text{PrPO}_4) - V(\text{LaPO}_4)}{V(\text{GdPO}_4) - V(\text{LaPO}_4)}. \tag{3.16}$$

However, since the difference in C_{latt} (eq. 3.15) at 298.15 K between LaPO_4 and PrPO_4 is rather small (0.6 %), the compositional change can be neglected. C_{ex} was then calculated by assuming C_{latt} to be equal in all samples and set to be the molar heat capacity of LaPO_4 which was subtracted from the other measurements. The resulting excess heat capacities are shown in figure 3.51. The maximum of the Schottky anomaly in each sample is at 50-60 K. The Schottky contribution increases with increasing Pr content yielding the highest value for PrPO_4 with 6.2-6.3 J/(mol K). This value is in good agreement with the findings on the pure end member PrPO_4 of Gavrichev *et al.* (2016) who reported 6.06 J/(mol K) for 50 K and 6.27 J/(mol K) for 60 K.

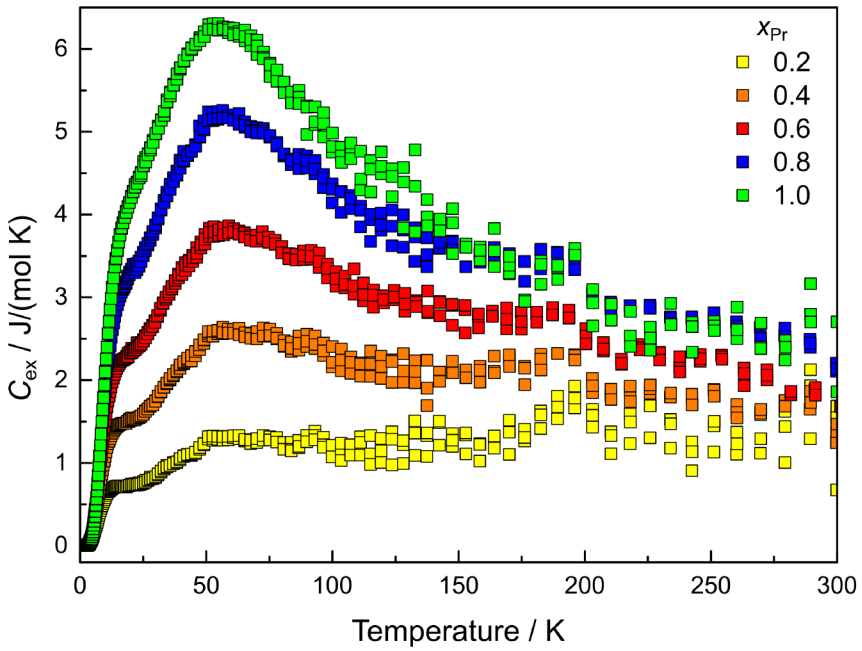

Figure 3.51 Schottky contribution or excess molar heat capacity (C_{ex}) of LaPr after Bauer *et al.* (2016). With increasing Pr content, the Schottky contribution increases while the maximum remains constant at around 50-60 K.

3.4.2.3 Energy level scheme of Pr^{3+}

For explaining the observed Schottky anomaly, fluorescence spectroscopy was used to analyse the energy levels of Pr^{3+}. With this method, the splitting of the ground state ($^3H_4$) of Pr^{3+} can be seen because of the transitions $^3H_4 \leftarrow {}^3P_0$. Generally, these

transitions range from 20,000 to 21,000 cm^{-1} (Gusowski *et al.*, 2007; Sokólska *et al.*, 2000; Horchani-Naifer and Férid, 2009). In $PrPO_4$, Horchani-Naifer and Férid (2009) determined the $^3H_4 \rightarrow ^3P_0$ transition to be at a wave number of $\approx 20,500\,cm^{-1}$. As described in section 1.3.1, *Ln* is at Wyckoff position 4*e* and, therefore, has a low site symmetry. According to Bünzli (1989), this symmetry results in nine energy levels (Stark sublevels) due to the splitting of $^3H_4$. All of these Stark levels should be seen as nine $^3H_4 \leftarrow ^3P_0$ transitions (Bünzli, 1989).
Figure 3.52 shows the results including the fitted barycenter positions. Seven peaks were unambiguously assigned leading to the conclusion that two of the nine transitions are not observed or the resolution is not enough for a clearer assignment.

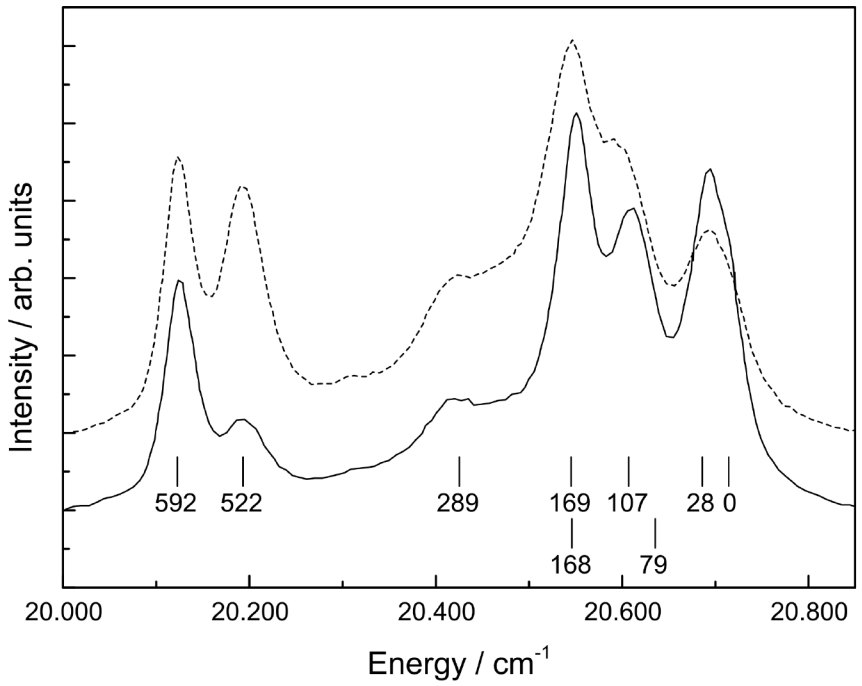

Figure 3.52 Fluorescence spectra of a $La_{0.8}Pr_{0.2}PO_4$ single crystal measured in two orientations (continuous and dashed line) showing the $^3H_4 \leftarrow ^3P_0$ transition after Bauer *et al.* (2016). Tic marks in the upper row show barycenters from fitting Lorentzian functions, while tic marks on the bottom are two additional energy levels obtained from fitting the Schottky anomaly. All energies are given in cm^{-1}. Note that the energies given for the tic marks are relative to the peak with the highest energy which is indicated as 0.

Fluorescence results are compared to literature values in figure 3.53. Thiriet *et al.* (2005) obtained their values by rescaling the crystal field parameters for $NdPO_4$ to $PrPO_4$ to consider the different shapes of the 4*f* orbitals assuming that the crystal field is comparable in all monazites. Kowalski *et al.* (2015) used $LaCl_3$:Ln^{3+} to determine the energy level splitting. Since Ln^{3+} does have a higher site symmetry in this environment, the Stark levels are partly degenerate.
From the literature data, the Schottky contribution for $PrPO_4$ was calculated using equation 3.12. The results are given in figure 3.54.

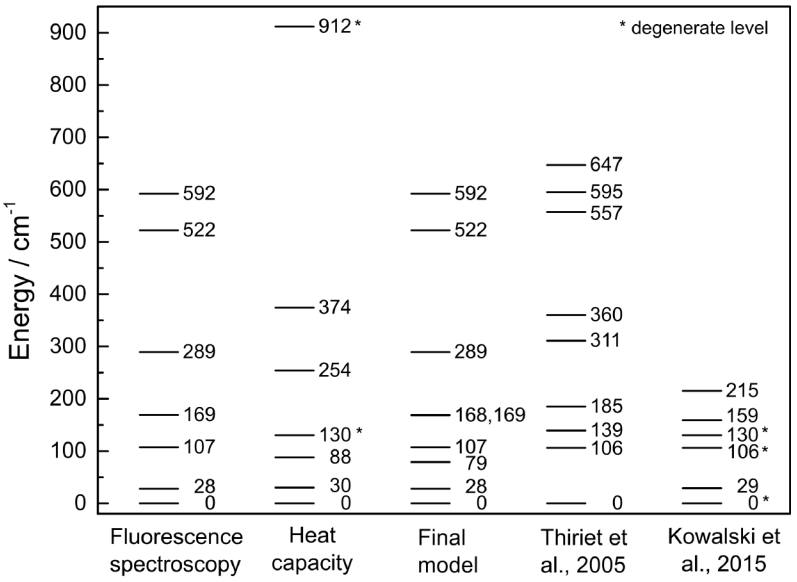

Figure 3.53 Energy level schemes for $^3H_4$ ground state of Pr^{3+} ion obtained by determining the barycenters from fluorescences spectroscopy and by fitting the heat capacity using equation 3.12 (see text). The final model after Bauer *et al.* (2016) is a fit using the seven energy levels from fluorescences spectroscopy and two additional energy levels. Literature data from Thiriet *et al.* (2005) and Kowalski *et al.* (2015) are added.

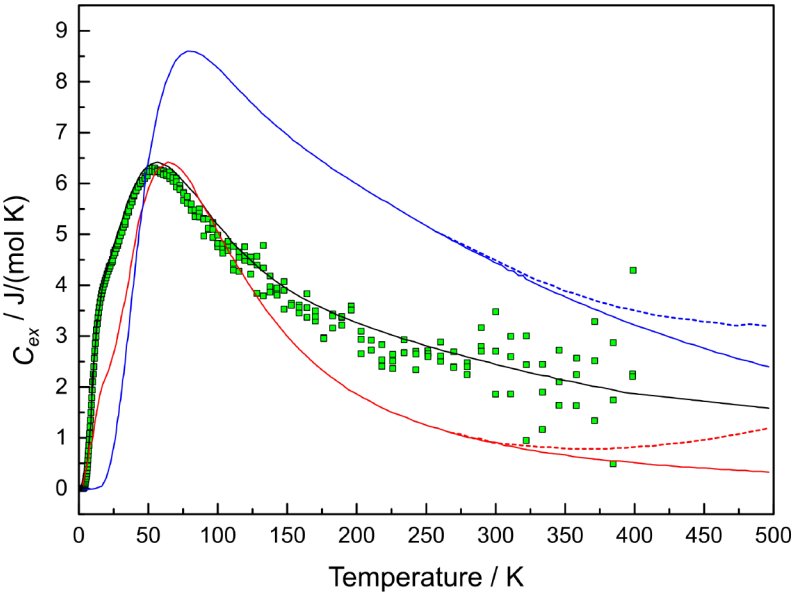

Figure 3.54 Schottky contribution (C_{ex}) of $PrPO_4$ after Bauer *et al.* (2016). Green symbols mark the experimental values, lines give the calculations. The black line is the fit from Bauer *et al.* (2016) using seven energy levels from fluorescence spectroscopy and two additionally fitted levels. The blue and red lines are calculated on the basis of Thiriet *et al.* (2005) and Kowalski *et al.* (2015), respectively, where solid lines give the calculation only based on $^3H_4$ only and dashed lines include $^3H_5$.

Note that solid lines were calculated by taking into account only the electronic levels of the $^3H_4$ ground state while dashed lines were calculated adding $^3H_5$ energy levels. Since the latter levels are at energies $\gg 2000\,\mathrm{cm}^{-1}$, the effect can only be seen at higher temperatures. Using the values of Thiriet *et al.* (2005), the calculation does not reproduce the experiment: on the one hand, the maximum of the curve occurs at a significantly higher temperature (80 K instead of 50-60 K) and also shows a higher C_{ex} value (8.6 J/(mol K) instead of 6.27 J/(mol K)). On the other hand, the part below 50 K is underestimated while the part above 50 K is overestimated. The fit based on the values of Kowalski *et al.* (2015) is closer to the data obtained here with a comparable maximum of 6.4 J/(mol K) at slightly higher temperatures (65 K). However, the deviations in the temperature part below 50 K and above 100 K are still notable. The best fit was achieved using eq. 3.12 with nine $^3H_4$ ground state levels as shown in figure 3.52, figure 3.54 and table 3.10.

Table 3.10 Energy levels of the $^3H_4$ ground state of the Pr^{3+} ion after Bauer *et al.* (2016): Observed barycenters in fluorescence spectroscopy and the fit of heat capacity data yield a combined final model with all energy levels from fluorescence and two additional ones. For more explanation, see the text. Comparison to literature data from Thiriet *et al.* (2005) and Kowalski *et al.* (2015). Errors are given in brackets.

Fluorescence	Heat Capacity	Final model	Thiriet *et al.* (2005)	Kowalski *et al.* (2015)
0(3)	0	0(3)	0	0
28(3)	30(1)	28(3)	106	0
-	88(2)	79(3)	139	29
107(3)	130(2)	107(3)	185	106
-	130(2)	168(3)	311	106
169(3)	254(10)	169(3)	360	130
289(3)	374(16)	289(3)	557	130
522(3)	912(26)	522(3)	595	156
592(3)	912(26)	592(3)	647	215

Two energy levels in the fit of the heat capacity data are very similar ($\approx 130\,\mathrm{cm}^{-1}$) so that they were constrained to be equivalent to ensure numerical stability. This is not related to symmetry or degeneracy but completely accidental as described in Bauer *et al.* (2016). Additionally, the fit yielded two levels at higher energies ($> 900\,\mathrm{cm}^{-1}$). Since they could not be distinguished from each other because of the high scattering of the data at around $T > 250$ K, both levels were also constrained to be equal. A second fit using equation 3.12 was done taking the seven levels obtained by fluorescence as fixed values and adding two more levels to the fit to obtain the complete set of energy levels. The fit can be seen in figure 3.54. The nine energy levels resulting from this fit are given

in table 3.10 and figure 3.53.
The final model contains two levels at $\approx 170\,\mathrm{cm}^{-1}$ which again is accidental. The degeneracy is not related to symmetry of the crystal field but could not be resolved within the measurement uncertainties. However, the model is consistent and robust, and demonstrates that the combination of microcalorimetry and fluorescence spectroscopy can be used to obtain Stark levels.
Perriere *et al.* (2007) pointed out that a high specific heat capacity and low thermal conductivity would limit the temperature increase, which occurs due to nuclear disintegration of the radionuclides. Additionally, the temperature-induced annealing of radiation defects is limited too. This has to be taken into account when aiming to use monazite as a nuclear waste matrix.

3.4.3 Summary on thermodynamic properties of monazite

HT calorimetry showed an increase of the measured ΔH_{ds} as well as the deduced $\Delta H^0_{\mathrm{f,el}}$ and $\Delta H^0_{\mathrm{f,ox}}$ with increasing Ln radius. Results showed that this technique is highly sensitive to impurities which might influence the results.
In LT calorimetry, a decrease of standard molar heat capacity, molar enthalpy change and standard molar entropy was found with increasing Ln radius. Additionally, an increasing Schottky contribution to the C_p value with increasing Pr content was observed. This was attributed to the f-orbital electrons of the Pr^{3+} ion. Its energy levels were determined using a combination of fluorescence spectroscopy and fits to the measure heat capacity.

Chapter 4: Summary and Conclusion

Monazite is considered as a potential nuclear waste host matrix for the immobilisation of long-lived radionuclides such as Pu or the minor actinides (Am, Cm, Np). The aim of this work was to obtain insight into the structural, chemical, and physical behaviour of monazite at ambient and non-ambient conditions. Six monazite solid solutions ($La_{1-x}Pr_xPO_4$, $Pr_{1-x}Nd_xPO_4$, $Pr_{1-x}Sm_xPO_4$, $Nd_{1-x}Eu_xPO_4$, $Nd_{1-x}Sm_xPO_4$, and $Sm_{1-x}Gd_xPO_4$) were synthesised as powder samples, single crystals, and ceramics. Lanthanides were used as surrogates for actinides, since monazites containing lanthanides have almost the same chemical and physical properties as those containing trivalent actinides due to their similar ionic radii (*e.g.* Terra *et al.*, 2003). The findings can be used to predict the properties and the behaviour of actinide-bearing monazites. In the solid state reaction for the preparation of powder samples, rare earth oxides were mixed with an excess of $NH_4H_2PO_4$ to assure the formation of pure monazite. These powders were used to grow single crystals via the high-temperature solution method using a Li_2MoO_4 flux and Pt crucibles. Single crystals were grown via temperature reduction and/or via evaporation of the flux material. Additionally, some of the powder was used to prepare ceramics, by pressing it isostatically and sintering at two temperatures.

The samples were characterised extensively using different methods: Room-temperature characterisation on the powder samples was performed via electron micro-probe analyses (EPMA), scanning electron microscopy (SEM; both for the chemical composition), X-ray diffraction (for structure investigation), and infra-red and Raman spectroscopy (for the characterisation of the vibrational modes of the PO_4 tetrahedra). Single crystals were characterised at room temperature via EPMA and XRD. Optical absorption spectroscopy was employed to evaluate the influence of the Pr^{3+} ion on the crystal field of $LaPO_4$.

Studies at non-ambient conditions using XRD and second-harmonic generation were used to investigate the high-pressure behaviour of LaPO4 single crystals. The thermal behaviour of powders and ceramics was studied via high-temperature XRD and dilatometry, respectively. The microstructure and mechanical properties of the ceramics were characterised with SEM and ultrasound spectroscopy. Additionally, thermodynamic properties were studied on powders using high-temperature calorimetry and on single crystals using low-temperature microcalorimetry and fluorescence spectroscopy.

The results on LaPr powders are published in Hirsch *et al.* (2017), while the LaPr ceramics are presented in Thust *et al.* (2017). The high-pressure investigations are published in Ruiz-Fuertes *et al.* (2016). The results from the low-temperature microcalorimetry are

summarised in Bauer *et al.* (2016).
Many of the analytical techniques are sensitive to impurities which may influence the results of the measured properties. Hence, it is important to assure a pure synthesis product. Yet, the solid state reaction, used in this work, may be unfavourable for the processing for nuclear waste disposal since dust contamination needs to be avoided in industrial use (*e.g.* Dacheux *et al.*, 2013). However, the powder-synthesis procedure used here yields pure monazite samples which is important for the further characterisation.
The powders were found to be chemically homogeneous. The impurities, found in only very few samples, were PO_4-surplus phases. The lattice parameters $\vec{a}$, $\vec{b}$, and $\vec{c}$, as well as the unit cell volume and the *Ln*-O bond lengths increased linearly with increasing *Ln* radius, while β decreases. The P-O bond lengths did not change with varying composition. Hence, the PO_4 tetrahedra were considered as 'rigid bodies'. IR spectra did not reveal substantial changes in the modes. The wave numbers of the PO_4-related Raman modes decreased with increasing *Ln* radius. This was attributed to the decrease of the force constants and the increase in the *Ln*-O bond lengths (Santos *et al.*, 2007).
The single crystals grown using the flux method were inclusion-free. The initial composition of the flux components seemed to influence the habit of the crystals: A higher MoO_3 content yields smaller crystals. This was probably due to the formation of larger PO_4 complexes in the flux which inhibits the growth (Cherniak *et al.*, 2004). A flux composed of Li_2MoO_4 and MoO_3 yielded isometric crystals, whereas flux composed of Li_2CO_3 and MoO_3 yielded platelets. The LaPr single crystals investigated using EPMA did not show any signs of zoning. Structural investigations using XRD showed an increasing distortion of the LnO_9 polyhedra with increasing *Ln* radii. This distortion was attributed to an increasing distortion resulting from the oxygen atoms connecting the LnO_9 polyhedra to the PO_4 tetrahedra within the chains along the $\vec{c}$ direction. However, the equatorial plane built by five oxygen atoms around the *Ln* ion can adapt easily to changes of the ionic *Ln* radius and its distortion remains constant. The optical absorption spectra of $La_{1-x}Pr_xPO_4$ did not reveal significant changes upon the increase of the Pr amount.
High-pressure single-crystal XRD on $LaPO_4$ revealed a phase transformation to the post-barite-type structure ($P2_12_12_1$) at 27.1 GPa. This structural change was due to a rearrangement of the atoms resulting in an increase of the *Ln*-O bond lengths and a *Ln* coordination number change from nine to twelve oxygens, accompanied by a rapid decrease in the unit cell volume.
Homogeneous ceramics were obtained using a two-step sintering process without any special sintering programme. Densities of up to 95 % of the theoretical densities were reached. This good response to sintering is an advantage for the application of monazite as a nuclear waste form (Dacheux *et al.*, 2013). The thermal expansion coefficients obtained from powder XRD showed an increase with increasing *Ln* radius. However, the thermal expansion coefficients from dilatometry, measured on the ceramics, did not show a trend with increasing ionic radii even though they showed comparable values. This was because the measurements were done on the bulk ceramic samples which were strongly influenced by the microstructure of the samples in terms of porosity and grain sizes. The elastic moduli calculated from ultrasound spectra showed a decrease with increasing *Ln* radius. Both, the thermal expansion coefficients and the elastic moduli depended on the density of the ceramics and, hence, on the degree of sintering.

High-temperature drop solution calorimetry showed that the enthalpy of solution as well as the deduced standard formation enthalpies increased with increasing *Ln* radius. This method was highly sensitive to impurities which significantly influences the results: the enthalpies measured on these samples were considerably lower. Low-temperature microcalorimetry measurements showed that the molar heat capacity, the standard molar entropy and the molar entropy change decreased with increasing *Ln* radius. An excess to the molar heat capacity was observed (Schottky contribution). This corresponded to the excitation of *f*-orbital electrons of the Pr^{3+}. The Schottky contribution increased with increasing Pr content and was modelled using the energy levels obtained by a combination of fluorescence spectroscopy and the measurements of the heat capacity.
The extensive investigations and the comparison to other solid solutions and end members of the monazite type show that monazite can form thermodynamically stable, ideal solid solutions from La to Gd without a miscibility gap. This is essential when considering monazite as a potential host for nuclear waste.

Chapter 5: Outlook

The results from this work can be used to extrapolate structural, thermal and physical properties from end members to solid solutions. This can help to predict the behaviour of actinide-bearing monazite.
High-pressure studies should investigate the phase transition from monazite to post-barite on other LnO_9 compounds with changing ionic radii.
Further research should now concern actinide-containing monazites. This is important since the behaviour of the actinides might still differ from that of the lanthanides. The results can support and extend the knowledge about the structural, chemical and physical properties of monazite. Additionally, studies with radioactive samples or on irradiated samples will be needed to investigate the influence of radiation damage on the structure and on the performance of monazite as a potential nuclear waste form. In particular, gaining insight into the amorphisation and recrystallisation are important to evaluate the performance of a monazite-based waste form in a repository. Although this thesis focussed on polycrystalline samples, fundamental research on single crystals could help understanding structural behaviour of monazite during leaching and the (anisotropy of) reaction kinetics. The presented systematic investigations on monazite single-crystal growths can be used for future experiments. Long-term leaching experiments using different solutions will then help to investigate the performance of monazite under repository conditions. Additionally, the radiation tolerance of monazite needs to be addressed. For this, ceramics and single crystals have to be exposed to (internal and external) radiation. Follow-up experiments should focus on the structural changes in monazite generated by this irradiation as well as on the mechanical stability and annealing processes in the material to further evaluate monazite as a nuclear waste matrix.

Chapter 6: Appendix

Table A.1 Reactants used for the synthesis of the solid solutions listed in table 2.1. *Ln* oxides marked with * were annealed before weighing.

Reactant	Manufacturer	Purity	Loss on ignition
La_2O_3	Rhône-Poulenc	95 %	14 – 14.5 %
Pr_2O_3	Sigma-Aldrich	99.9 %	-2.5 – -2.9 %
Nd_2O_3	Sigma Chemical Co.	99.9 %	10.2 –12.1 % / *
Sm_2O_3	Alfa Aesar	99.9 %	*
Eu_2O_3	Alfa Aesar	99.9 %	*
Gd_2O_3	Alfa Aesar	99.99+ %	*
$NH_4H_2PO_4$	Alfa Aesar	98 %	-

Table A.2 Reactants used as flux material for the single crystal growth experiments listed in table A.22. T_m, T_b: melting and boiling temperature, respectively.

Reactant	Manufacturer	Purity	T_m / K	T_b / K
MoO_3	Merck	99.5 %	1068	1438
Li_2CO_3	Merck	99 %	720	1583
Li_2MoO_4	Sigma-Aldrich	99.9 %	975	-

Table A.3 Results of all EPMA analyses for composition (x), Ln_1/Ln_2 and ΣLn/P ratios in $La_{1-x}Pr_xPO_4$ (LaPr), $Pr_{1-x}Sm_xPO_4$ (PrSm), and $Nd_{1-x}Sm_xPO_4$(NdSm) solid solutions. The nomial (nom.) and calculated values are presented. Uncertainties (standard deviations) are given in brackets reffering to the last digit.

x (nom.)	x_{Pr} (LaPr)	x_{Sm} (PrSm)	x_{Sm} (NdSm)	Ln_1/Ln_2 (nom.)	La/Pr (LaPr)	Pr/Sm (PrSm)	Nd/Sm (NdSm)	ΣLn/P (nom.)	(La+Pr)/P (LaPr)	(Pr+Sm)/P (PrSm)	(Nd+Sm)/P (NdSm)
0.0	0.00(1)	0.00(1)	0.00(1)	-	-	-	-	1	1.1(2)	1.05(4)	0.99(6)
0.1	0.08(2)	0.09(3)	0.10(4)	9	12(5)	22(71)	11(6)	1	0.96(1)	1.00(4)	0.99(3)
0.2	0.3(2)	0.20(5)	0.20(9)	4	4(3)	5(6)	10(35)	1	0.95(3)	0.98(5)	1.0(2)
0.3	0.31(9)	0.30(4)	0.29(6)	2.33	2.5(8)	2.5(8)	3(2)	1	0.95(2)	1.0(1)	0.99(2)
0.4	0.4(1)	0.40(6)	0.43(9)	1.5	1.5(6)	2(2)	1.4(4)	1	0.95(1)	0.99(3)	1.0(1)
0.5	0.54(9)	0.51(6)	0.6(2)	1	0.9(3)	1.0(4)	1.0(8)	1	0.96(3)	1.00(3)	1.0(2)
0.6	0.65(8)	0.62(5)	0.7(2)	0.67	0.6(2)	0.6(2)	0.6(4)	1	0.96(3)	1.0(1)	1.0(3)
0.7	0.74(9)	0.7(1)	0.8(1)	0.43	0.4(1)	0.4(7)	0.4(2)	1	0.96(3)	0.98(8)	1.0(2)
0.8	0.81(2)	0.8(1)	0.86(9)	0.25	0.24(3)	2(15)	0.2(1)	1	0.96(1)	1.02(2)	1.1(4)
0.9	0.91(2)	0.91(2)	0.9(1)	0.11	0.10(2)	0.10(2)	0.2(4)	1	0.9(1)	0.99(3)	0.98(3)
1.0	1.00(1)	1.00(1)	1.00(1)	-	-	-	-	1	0.97(1)	0.99(2)	1.0(2)

Table A.4 Lattice parameters of LaPr obtained from Synchrotron powder XRD. Results are shown in the figures 3.5 and 3.6 in subsection 3.1.3 and in Hirsch *et al.* (2017).

Sample	x_{Pr}	r_{Ln}	$\vec{a}$	$\vec{b}$	$\vec{c}$	β	V_{uc}
LaPr00	0.0	1.2160	6.8413(2)	7.0759(2)	6.5123(2)	103.289(3)	306.81(2)
LaPr01	0.1	1.2123	6.8345(2)	7.0698(2)	6.5051(2)	103.305(2)	305.88(1)
LaPr02	0.2	1.2086	6.8290(3)	7.0626(3)	6.4999(3)	103.334(3)	305.04(2)
LaPr03	0.3	1.2049	6.8238(3)	7.0561(3)	6.4945(2)	103.356(3)	304.25(2)
LaPr04	0.4	1.2012	6.8157(3)	7.0456(3)	6.4870(3)	103.389(3)	303.04(2)
LaPr05	0.5	1.1975	6.8081(3)	7.0349(3)	6.4808(3)	103.428(4)	301.91(3)
LaPr06	0.6	1.1938	6.7984(2)	7.0252(2)	6.4699(2)	103.449(3)	300.53(2)
LaPr07	0.7	1.1901	6.7929(2)	7.0172(2)	6.4648(2)	103.481(2)	299.67(2)
LaPr08	0.8	1.1864	6.7862(2)	7.0089(2)	6.4583(2)	103.505(2)	298.69(1)
LaPr09	0.9	1.1827	6.7776(2)	6.9983(2)	6.4498(2)	103.529(2)	297.43(1)
LaPr10	1.0	1.1790	6.7708(1)	6.9902(2)	6.4427(2)	103.553(2)	296.43(1)

Table A.5 Lattice parameters of PrSm obtained from powder XRD for this thesis by Bigdeli (2016). Results are shown in the figures 3.5 and 3.6 in subsection 3.1.3.

Sample	x_{Sm}	r_{Ln}	$\vec{a}$	$\vec{b}$	$\vec{c}$	β	V_{uc}
DB001	0.0	1.1790	6.7691(4)	6.9863(4)	6.4421(4)	103.563(4)	296.16(3)
DB005	0.1	1.1743	6.7605(3)	6.9774(3)	6.4344(3)	103.590(4)	295.02(2)
DB017	0.2	1.1696	6.7523(4)	6.9687(4)	6.4269(4)	103.624(5)	293.91(3)
DB016	0.3	1.1649	6.7446(5)	6.9598(5)	6.4204(5)	103.652(6)	292.87(4)
DB015	0.4	1.1602	6.7364(4)	6.9500(4)	6.4136(4)	103.684(5)	291.75(3)
DB010	0.5	1.1555	6.7284(5)	6.9403(5)	6.4062(5)	103.716(6)	290.62(4)
DB009	0.6	1.1508	6.7195(6)	6.9297(6)	6.3982(6)	103.752(8)	289.39(5)
DB008	0.7	1.1461	6.7123(4)	6.9210(5)	6.3914(5)	103.786(6)	288.37(4)
DB007	0.8	1.1414	6.7040(5)	6.9110(5)	6.3836(5)	103.815(7)	287.20(3)
DB006	0.9	1.1367	6.6962(4)	6.9009(4)	6.3764(4)	103.845(5)	286.09(3)
DB011	1.0	1.1320	6.6894(3)	6.8910(3)	6.3708(3)	103.869(4)	285.11(2)

Table A.6 Lattice parameters of PrNd obtained from powder XRD for this thesis by Claßen, pers.comm. (2015). Results are shown in the figures 3.5 and 3.6 in subsection 3.1.3.

Sample	x_{Nd}	r_{Ln}	$\vec{a}$	$\vec{b}$	$\vec{c}$	β	V_{uc}
CCPrPO4_5g	0.0	1.179	6.7592(1)	6.9771(1)	6.4340(1)	103.555(2)	294.97(2)
CCPrNd02	0.1	1.1774	-	-	-	-	-
CCPrNd03	0.2	1.1758	-	-	-	-	-
CCPrNd11	0.3	1.1742	6.7541(1)	6.9706(1)	6.4274(1)	103.579(2)	294.15(2)
CCPrNd05	0.4	1.1726	6.7529(2)	6.9683(1)	6.4248(1)	103.609(2)	293.84(2)
CCPrNd01	0.5	1.171	6.7569(1)	6.9735(1)	6.4268(1)	103.615(1)	294.32(2)
CCPrNd06	0.6	1.1694	6.7468(1)	6.9603(1)	6.4179(1)	103.641(2)	292.88(2)
CCPrNd07	0.7	1.1678	6.7439(1)	6.9559(1)	6.4142(1)	103.642(2)	292.40(2)
CCPrNd08	0.8	1.1662	6.7420(1)	6.9546(1)	6.4123(1)	103.652(1)	292.20(2)
CCPrNd09	0.9	1.1646	6.7397(1)	6.9554(2)	6.4073(1)	103.656(2)	291.86(2)
CCPrNd10	1.0	1.163	6.7413(1)	6.9530(1)	6.4114(1)	103.673(1)	292.00(2)

Table A.7 Lattice parameters of NdSm obtained from powder XRD for this thesis by Kuleci (2015). Results are shown in the figures 3.5 and 3.6 in subsection 3.1.3.

Sample	x_{Sm}	r_{Ln}	$\vec{a}$	$\vec{b}$	$\vec{c}$	β	V_{uc}
NdPO4	0.0	1.1630	6.748(1)	6.961(1)	6.418(1)	103.68(1)	292.9(1)
Sm01Nd09PO4	0.1	1.1599	6.743(2)	6.954(1)	6.414(2)	103.69(2)	292.3(1)
Sm02Nd08PO4	0.2	1.1568	6.740(1)	6.950(1)	6.412(1)	103.71(1)	291.8(1)
Sm03Nd07PO4	0.3	1.1537	6.732(1)	6.945(1)	6.406(1)	103.74(2)	291.1(1)
Sm04Nd06PO4	0.4	1.1506	6.729(1)	6.937(1)	6.404(1)	103.76(2)	290.4(2)
Sm05Nd05PO4	0.5	1.1475	6.722(2)	6.930(2)	6.398(2)	103.77(3)	289.5(2)
Sm06Nd04PO4	0.6	1.1444	6.715(2)	6.923(2)	6.394(2)	103.81(2)	288.6(2)
Sm07Nd03PO4	0.7	1.1413	6.711(2)	6.917(2)	6.391(2)	103.83(1)	288.1(1)
Sm08Nd02PO4	0.8	1.1382	6.706(2)	6.910(2)	6.387(2)	103.85(2)	287.3(2)
Sm09Nd01PO4	0.9	1.1351	6.699(2)	6.902(2)	6.380(2)	103.86(2)	286.4(2)
SmPO4	1.0	1.1320	6.696(2)	6.898(2)	6.378(2)	103.87(1)	286.0(1)

Table A.8 Lattice parameters of NdEu obtained from powder XRD for this thesis by Schumacher (2016). Results are shown in the figures 3.5 and 3.6 in subsection 3.1.3.

Sample	x_{Eu}	r_{Ln}	$\vec{a}$	$\vec{b}$	$\vec{c}$	β	V_{uc}
NdPO4	0.0	1.1630	6.7419(2)	6.9568(2)	6.4088(3)	103.671(3)	292.08(2)
Nd0.9Eu0.1PO4	0.1	1.1587	6.7338(3)	6.9473(3)	6.4030(3)	103.704(4)	291.02(2)
Nd0.8Eu0.2PO4	0.2	1.1544	6.7257(2)	6.9375(2)	6.3972(3)	103.734(4)	289.97(2)
Nd0.7Eu0.3PO4	0.3	1.1501	6.7184(3)	6.9292(3)	6.3925(3)	103.767(4)	289.04(2)
Nd0.6Eu0.4PO4	0.4	1.1458	6.7100(3)	6.9193(3)	6.3865(3)	103.789(4)	287.97(2)
Nd0.5Eu0.5PO4	0.5	1.1415	6.7024(3)	6.9098(3)	6.3802(3)	103.812(4)	286.94(2)
Nd0.4Eu0.6PO4	0.6	1.1372	6.6944(2)	6.9002(2)	6.3742(3)	103.843(4)	285.89(2)
Nd0.3Eu0.7PO4	0.7	1.1329	6.6877(3)	6.8915(3)	6.3686(3)	103.866(4)	284.97(2)
Nd0.2Eu0.8PO4	0.8	1.1286	6.6803(3)	6.8824(3)	6.3623(3)	103.894(4)	283.96(2)
Nd0.1Eu0.9PO4	0.9	1.1243	6.6727(2)	6.8720(3)	6.3563(2)	103.922(3)	282.91(2)
EuPO4	1.0	1.1200	6.6672(2)	6.8659(2)	6.3522(2)	103.941(3)	282.22(2)

Table A.9 Lattice parameters of SmGd obtained from powder XRD for this thesis by Ladenthin (2017). Results are shown in the figures 3.5 and 3.6 in subsection 3.1.3.

Sample	x_{Gd}	r_{Ln}	$\vec{a}$	$\vec{b}$	$\vec{c}$	β	V_{uc}
SmPO4	0.0	1.1320	6.6897(1)	6.8940(1)	6.3703(1)	103.872(1)	285.2(1)
Sm0.9Gd0.1PO4	0.1	1.1295	6.6864(1)	6.8896(1)	6.3673(1)	103.883(1)	284.8(1)
Sm0.8Gd0.2PO4	0.2	1.1270	6.6824(1)	6.8845(1)	6.3636(1)	103.896(1)	284.2(1)
Sm0.7Gd0.3PO4	0.3	1.1245	6.6785(1)	6.8798(1)	6.3598(1)	103.911(1)	283.6(1)
Sm0.6Gd0.4PO4	0.4	1.1220	6.6738(1)	6.8750(1)	6.3558(1)	103.925(1)	283.0(1)
Sm0.5Gd0.5PO4	0.5	1.1195	6.6701(1)	6.8704(1)	6.3528(1)	103.942(2)	282.5(1)
Sm0.4Gd0.6PO4	0.6	1.1170	6.6664(1)	6.8656(1)	6.3492(1)	103.952(2)	282.0(1)
Sm0.3Gd0.7PO4	0.7	1.1145	6.6621(1)	6.8605(1)	6.3452(1)	103.968(2)	281.4(1)
Sm0.2Gd0.8PO4	0.8	1.1120	6.6586(1)	6.8563(1)	6.3416(1)	103.976(1)	280.9(1)
Sm0.1Gd0.9PO4	0.9	1.1095	6.6545(1)	6.8508(1)	6.3373(1)	103.988(2)	280.3(1)
GdPO4	1.0	1.1070	6.6499(1)	6.8463(1)	6.3338(1)	104.002(2)	279.8(1)

Table A.10 Individual and mean *Ln*-O bond lengths for LaPr from Synchrotron powder XRD at 293 K. Oxygen atoms are named according to Mullica *et al.* (1984) and Ni *et al.* (1995) and are shown in figure 1.7 in section 1.3.1.

x_{Pr}	O^1	$O^{1'}$	O^2	$O^{2'}$	$O^{2''}$	O^3	$O^{3'}$	O^4	$O^{4'}$	mean
0	2.501(9)	2.459(8)	2.827(8)	2.655(7)	2.589(9)	2.600(8)	2.515(7)	2.544(7)	2.467(7)	2.573(8)
0.1	2.518(6)	2.471(5)	2.797(5)	2.651(4)	2.594(6)	2.601(6)	2.494(5)	2.523(5)	2.468(5)	2.569(5)
0.2	2.52(1)	2.473(9)	2.791(9)	2.657(8)	2.59(1)	2.604(9)	2.480(8)	2.505(8)	2.471(8)	2.566(9)
0.3	2.516(8)	2.451(8)	2.793(8)	2.656(6)	2.585(8)	2.605(8)	2.493(7)	2.509(7)	2.460(7)	2.563(7)
0.4	2.476(8)	2.448(9)	2.771(9)	2.657(7)	2.59(1)	2.600(9)	2.499(1)	2.488(8)	2.470(8)	2.555(8)
0.5	2.517(1)	2.420(9)	2.780(9)	2.654(8)	2.568(1)	2.599(9)	2.482(8)	2.508(9)	2.453(9)	2.553(7)
0.6	2.502(8)	2.455(7)	2.745(7)	2.656(6)	2.586(8)	2.580(7)	2.469(6)	2.454(7)	2.488(7)	2.548(7)
0.7	2.506(8)	2.429(7)	2.762(7)	2.650(6)	2.574(7)	2.580(7)	2.464(6)	2.464(6)	2.475(6)	2.545(7)
0.8	2.487(6)	2.461(6)	2.761(6)	2.641(5)	2.577(6)	2.555(6)	2.465(5)	2.470(5)	2.461(5)	2.542(6)
0.9	2.494(8)	2.424(7)	2.762(7)	2.637(6)	2.559(8)	2.573(7)	2.457(6)	2.505(7)	2.427(7)	2.537(7)
1	2.492(7)	2.411(6)	2.783(6)	2.612(5)	2.554(6)	2.562(6)	2.435(5)	2.518(6)	2.425(6)	2.532(6)

Table A.11 Individual and mean P-O bond lengths for LaPr from Synchrotron powder XRD at 293 K. Oxygen atoms are named according to Mullica *et al.* (1984) and Ni *et al.* (1995) and are shown in figure 1.7 in section 1.3.1.

x_{Pr}	O^1	O^2	O^3	O^4	mean
0	1.577(9)	1.55(1)	1.559(8)	1.55(1)	1.559(9)
0.08(2)	1.559(6)	1.563(7)	1.567(5)	1.548(7)	1.559(6)
0.19(6)	1.56(1)	1.56(1)	1.563(9)	1.56(1)	1.56(1)
0.28(3)	1.579(8)	1.555(9)	1.547(7)	1.555(9)	1.559(9)
0.40(3)	1.59(1)	1.55(1)	1.554(8)	1.551(1)	1.562(8)
0.52(5)	1.56(1)	1.56(1)	1.536(9)	1.56(1)	1.56(1)
0.63(5)	1.569(8)	1.559(9)	1.538(7)	1.538(9)	1.559(9)
0.72(5)	1.585(7)	1.553(8)	1.537(6)	1.547(8)	1.555(8)
0.81(2)	1.552(6)	1.550(7)	1.555(5)	1.548(7)	1.551(6)
0.91(2)	1.587(8)	1.554(9)	1.543(6)	1.550(9)	1.559(8)
1	1.584(7)	1.560(7)	1.569(6)	1.540(7)	1.563(7)

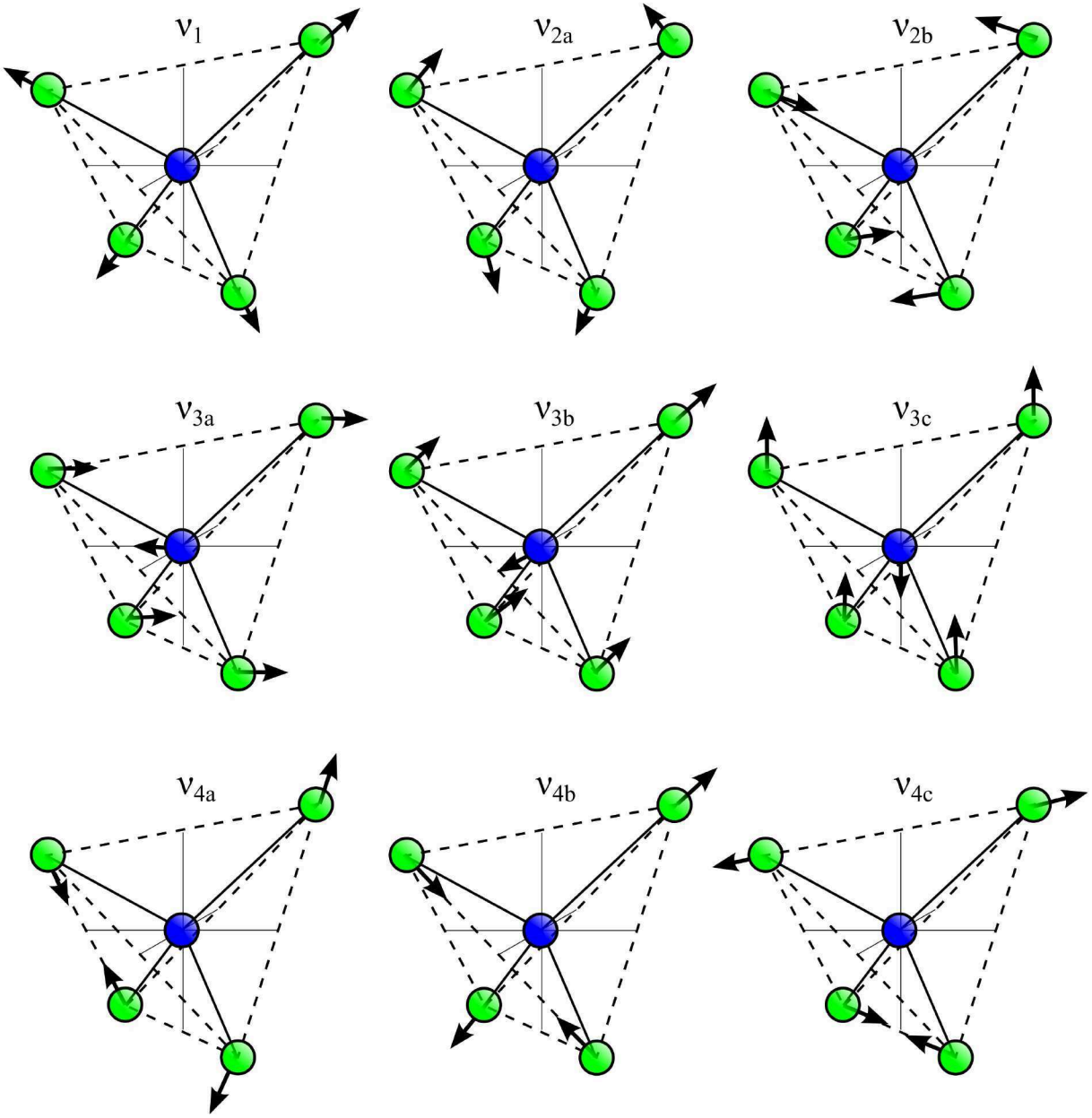

Figure A.1 Vibrational modes of PO_4 after Herzberg (1945): ν_1 and ν_3 are symmetric and asymmetric stretching modes, respectively, while ν_2 and ν_4 are symmetric and asymmetric bending modes, respectively.

Table A.12 Wave numbers (cm^{-1}) of LaPr solid solutions (x_{Pr}: Pr content) obtained via IR spectroscopy at room temperature by locating the peak minima.

Sample	x_{Pr}	ν_3	ν_3	ν_3	ν_3	ν_1	ν_4	ν_4	ν_4	ν_4	ν_2
La002	0.0	1092(2)	1059(2)	1015(2)	993(2)	953(2)	621(2)	577(2)	563(2)	538(2)	488(2)
LaPr003	0.1	1090(2)	1059(2)	1016(2)	993(2)	953(2)	617(2)	577(2)	563(2)	538(2)	488(2)
LaPr004	0.2	1092(2)	1059(2)	1016(2)	993(2)	953(2)	617(2)	577(2)	563(2)	538(2)	488(2)
LaPr005	0.3	1092(2)	1059(2)	1016(2)	993(2)	953(2)	617(2)	577(2)	563(2)	538(2)	488(2)
LaPr006	0.4	1092(2)	1059(2)	1018(2)	993(2)	953(2)	617(2)	577(2)	563(2)	538(2)	488(2)
LaPr002	0.5	1092(2)	1059(2)	1018(2)	995(2)	955(2)	619(2)	577(2)	565(2)	540(2)	488(2)
LaPr007	0.6	1092(2)	1061(2)	1020(2)	995(2)	955(2)	619(2)	579(2)	565(2)	540(2)	488(2)
LaPr008	0.7	1092(2)	1059(2)	1020(2)	995(2)	955(2)	619(2)	579(2)	565(2)	540(2)	488(2)
LaPr009	0.8	1092(2)	1061(2)	1022(2)	995(2)	955(2)	619(2)	579(2)	565(2)	540(2)	488(2)
LaPr010	0.9	1094(2)	1061(2)	1022(2)	997(2)	957(2)	619(2)	579(2)	565(2)	540(2)	488(2)
Pr002	1.0	1094(2)	1061(2)	1026(2)	997(2)	957(2)	617(2)	579(2)	565(2)	540(2)	488(2)

Table A.13 Wave numbers (cm^{-1}) for Raman lines of LaPr, PrSm, and NdSm solid solutions at room temperature in comparison to Begun *et al.* (1981). The explanation of the Mulliken representations are given in table A.14.

				(LaPr)		(PrSm)		(NdSm)	
No.[a]	Symbol[b]	Assignment[c]	La[a]	La	Pr	Pr	Sm	Nd	Sm
25A	B_g	Lattice	90(1.6)						
24A	A_g	Lattice	100(0.6)						
23A	B_g	-	118(0.2)	121(4))		114.7(5)	122.4(3)	118(1)	119.1(3)
22A	B_g	-	131(0.4)	129.3(3)	126.7(2)	126.0(2)		127.3(3)	127.3(1)
20A	A_g	Lattice	151(0.5)	148.8(2)	151.7(3)	148.4(3)	149.2(8)	149(2)	150.3(5)
19A	B_g	Lattice	170(0.5)	167.5(2)	173.1(2)	154.6(2)	164.4(6)	158.0(4)	166.7(5)
18A	A_g	Lattice	183(0.3)	180.2(1)		171.6(2)	177.1(5)	175.2(4)	178.1(4)
17A	B_g	Lattice	220(1.0)	219.8(1)	221.91(7)	220.3(1)	224.16(5)	221.6(5)	225.76(4)
16A	B_g	Lattice	227(1.1)				236.1(1)		237.67(9)
15A	A_g	Lattice	255(0.4)	256.3(5)	255.6(3)	253.6(4)	258.6(1)	256.9(2)	259.5(2)
14A	A_g	Lattice	271(1.0)	269.3(2)	275.8(2)	274.4(2)	291.3(3)	280.2(3)	288.6(3)
12A	B_g	Lattice	394(0.9)	392.86(9)	393.5(1)	391.7(1)	395.76(7)	393.1(1)	397.04(9)
11A	A_g	Lattice	414(1.5)	410.61(6)	412.41(7)	410.95(7)	417.31(5)	413.72(9)	418.65(6)
10A	A_g	ν_2	465(1.7)	462.74(4)	464.72(4)	463.19(5)	466.45(4)	466.00(7)	467.73(4)
9A	A_g	-	537(0.4)	535.0(3)	533.3(3)	531.7(3)	532.3(4)	532.8(5)	533.6(3)
8A	A_g	-	572(0.5)	568.9(5)	567.0(2)	565.9(2)	568.9(1)	567.9(3)	570.1(2)
7A	B_g	-	589(0.3)	586.7(2)	586.9(6)	586.0(5)	589.3(3)	587.5(5)	590.6(3)
6A	A_g/B_g	ν_4	619(0.8)	616.545(4)	617.99(9)	616.28(8)	621.48(7)	619.0(1)	622.72(9)
1A	A_g	ν_1	967(10.0)	964.96(7)	969.61(6)	968.31(5)	975.95(4)	971.65(5)	977.26(5)
2A	A_g	-	991(1.7)	988.5(4)	989.2(4)	988.4(4)	993.5(5)	991.1(4)	994.8(7)
3A	B_g	-	1025(0.4)	1022.4(1)	1024.5(4)	1023.3(4)	1029.6(5)	1026.4(3)	1031.0(1)
4A	A_g	ν_3	1055(2.9)	1053.3(3)	1054.04(9)	1052.83(6)	1059.2(1)	1056.45(6)	1060.7(2)
?	B_g	-	1065(0.4)	1063(3)					
5A	B_g	-	1073(0.8)	1070(2)	1070.6(2)	1069.6(2)	1078.6(3)	1073.6(2)	1079.6(5)

[a] according to Begun *et al.* (1981).
[b] Mulliken representation from Begun *et al.* (1981), Silva *et al.* (2006) and Ruschel *et al.* (2012); the more specific symmetry declaration was used.
[c] according to Silva *et al.* (2006).

Table A.14 Explanation of the Mulliken representations used in table A.13 after Mulliken (1955).

Symbol	Description
A	singly degenerate state which is symmetric with respect to the rotation around the principal axis
B	singly degenerate state which is antisymmetric with respect to the rotation around the principal axis
$_g$	(gerade, symmetric) the sign of the wave function does not change on inversion through the centre of the atom
$_u$	(ungerade, antisymmetric) the sign of the wave function changes on inversion through the centre of the atom

Table A.15 Wave numbers (cm^{-1}) of LaPr obtained via Raman spectroscopy at room temperature. The results are presented in figure 3.15 in subsection 3.1.4.

x_{Pr}	r_{Ln}	ν_1	ν_2	ν_3	ν_4
0.0	1.216	964.96(7)	462.75(4)	1053.3(3)	616.55(4)
0.1	1.212	965.06(8)	462.70(5)	1053.0(2)	616.1(1)
0.2	1.209	965.94(6)	462.84(6)	1053.22(9)	-
0.3	1.205	966.51(6)	463.24(4)	1053.46(8)	616.84(7)
0.4	1.201	967.02(8)	463.38(4)	1053.51(8)	616.88(7)
0.5	1.198	967.49(7)	463.74(4)	1053.55(7)	616.95(7)
0.6	1.194	968.33(8)	464.45(3)	1054.10(8)	617.58(7)
0.7	1.190	968.24(7)	463.92(3)	1053.59(7)	617.13(5)
0.8	1.186	969.33(8)	464.92(3)	1054.5(1)	617.97(8)
0.9	1.183	969.68(7)	464.42(9)	1054.50(7)	618.02(5)
1.0	1.179	969.61(6)	464.72(4)	1054.04(9)	618.0(1)

Table A.16 Wave numbers (cm^{-1}) of PrSm obtained via Raman spectroscopy at room temperature. The results are presented in figure 3.15 in subsection 3.1.4.

x_{Sm}	r_{Ln}	ν_1	ν_2	ν_3	ν_4
0.0	1.179	968.32(5)	463.19(5)	1052.83(6)	616.26(8)
0.1	1.174	968.85(4)	463.17(4)	1053.06(4)	612.29(6)
0.2	1.170	970.34(5)	464.02(3)	1054.22(5)	617.28(6)
0.3	1.165	971.06(4)	464.88(5)	1054.92(4)	617.9(1)
0.4	1.160	971.26(4)	464.29(4)	1054.99(4)	617.82(8)
0.5	1.156	972.71(5)	465.22(4)	1056.25(4)	619.04(8)
0.6	1.151	973.22(4)	465.56(5)	1056.54(3)	619.1(1)
0.7	1.146	973.95(5)	465.46(3)	1057.29(5)	619.79(7)
0.8	1.141	974.42(5)	465.70(4)	1057.73(5)	620.10(8)
0.9	1.137	975.35(4)	466.16(3)	1058.67(7)	620.93(7)
1.0	1.132	975.95(4)	466.45(4)	1059.2(1)	621.48(7)

Table A.17 Wave numbers (cm^{-1}) of NdSm obtained via Raman spectroscopy at room temperature. The results are presented in figure 3.15 in subsection 3.1.4.

x_{Sm}	r_{Ln}	ν_1	ν_2	ν_3	ν_4
0.0	1.163	971.65(5)	466.00(7)	1056.45(6)	619.0(1)
0.1	1.160	972.01(5)	465.13(4)	1056.71(8)	618.87(7)
0.2	1.157	972.01(5)	465.13(4)	1056.48(5)	618.88(7)
0.3	1.154	973.24(4)	466.14(4)	1057.60(6)	619.98(7)
0.4	1.151	973.72(4)	466.6(2)	1057.68(4)	619.60(1)
0.5	1.148	973.72(4)	466.10(5)	1057.68(4)	619.94(1)
0.6	1.144	974.10(3)	465.78(3)	1057.88(4)	620.27(7)
0.7	1.141	975.19(4)	466.92(5)	1058.74(4)	621.12(1)
0.8	1.138	975.59(4)	466.70(5)	1058.99(4)	621.3(1)
0.9	1.135	976.51(4)	467.29(4)	1059.88(7)	622.14(8)
1.0	1.132	977.26(5)	467.73(4)	1060.7(2)	622.72(9)

Table A.18 Full-width of half maximum (FWHM; cm^{-1}) of Raman modes in LaPr at room temperature. The results are presented in figure 3.17 in subsection 3.1.4.

x_{Pr}	r_{Ln}	ν_1	ν_2	ν_3	ν_4
0.0	1.216	7.9(5)	15.7(5)	8.0(5)	9.3(5)
0.1	1.2123	9.0(5)	16.9(5)	9.0(5)	10.2(5)
0.2	1.2086	9.1(5)	16.3(5)	9.1(5)	-
0.3	1.2049	9.0(5)	16.2(5)	9.0(5)	10.2(5)
0.4	1.2012	9.2(5)	16.2(5)	9.3(5)	10.1(5)
0.5	1.1975	9.3(5)	16.6(5)	9.4(5)	10.3(5)
0.6	1.1938	9.2(5)	16.8(5)	9.3(5)	10.1(5)
0.7	1.1901	9.7(5)	16.7(5)	9.7(5)	10.5(5)
0.8	1.1864	9.2(5)	16.8(5)	9.8(5)	10.1(5)
0.9	1.1827	9.4(5)	17.1(5)	9.4(5)	10.3(5)
1.0	1.179	9.2(5)	17.3(5)	9.3(5)	10.3(5)

Table A.19 Full-width of half maximum (FWHM; cm^{-1}) of Raman modes in PrSm at room temperature. The results are presented in figure 3.17 in subsection 3.1.4.

x_{Sm}	r_{Ln}	ν_1	ν_2	ν_3	ν_4
0.0	1.179	7.3(5)	17.0(5)	7.5(5)	8.5(5)
0.1	1.174	7.9(5)	17.7(5)	8.1(5)	9.0(5)
0.2	1.170	7.8(5)	17.0(5)	8.1(5)	8.9(5)
0.3	1.165	8.1(5)	17.6(5)	8.3(5)	9.0(5)
0.4	1.160	8.4(5)	17.2(5)	8.7(5)	9.4(5)
0.5	1.156	8.0(5)	16.3(5)	8.5(5)	8.9(5)
0.6	1.151	8.9(5)	16.4(5)	9.0(5)	9.7(5)
0.7	1.146	8.3(5)	16.1(5)	8.6(5)	9.2(5)
0.8	1.141	8.4(5)	16.1(5)	8.6(5)	9.3(5)
0.9	1.137	8.0(5)	15.5(5)	8.1(5)	8.8(5)
1.0	1.132	7.9(5)	15.3(5)	7.8(5)	8.9(5)

Table A.20 Full-width of half maximum (FWHM; cm^{-1}) of Raman modes in NdSm at room temperature. The results are presented in figure 3.17 in subsection 3.1.4.

x_{Sm}	r_{Ln}	ν_1	ν_2	ν_3	ν_4
0.0	1.163	7.5(5)	18.1(5)	7.5(5)	8.7(5)
0.1	1.156	8.0(5)	17.1(5)	8.2(5)	9.1(5)
0.2	1.157	8.0(5)	17.1(5)	8.1(5)	9.1(5)
0.3	1.154	7.8(5)	16.7(5)	8.0(5)	8.8(5)
0.4	1.151	8.6(5)	16.4(5)	8.5(5)	9.2(5)
0.5	1.148	8.6(5)	17.2(5)	8.5(5)	9.2(5)
0.6	1.144	8.4(5)	16.3(5)	8.4(5)	9.2(5)
0.7	1.141	8.2(5)	16.1(5)	8.2(5)	8.9(5)
0.8	1.138	8.2(5)	16.1(5)	8.2(5)	9.1(5)
0.9	1.135	8.0(5)	15.6(5)	8.0(5)	8.9(5)
1.0	1.132	7.6(5)	15.1(5)	7.4(5)	8.4(5)

Table A.21 Flux growth conditions: No: Number of the experiment; Name and Composition: Abbreviation of the chemical formula of the solid solutions. Single crystals of PrSm, NdEu and NdSm were grown by Bigdeli (2016), Schumacher (2016) and Kuleci (2015), respectively, and used for this thesis. Crystal growth experiments of PrNd and LaNd done by Claßen and Schoel (pers.comm.) were included. LaPr single crystals were used in Ruiz-Fuertes *et al.* (2016)[1] and Bauer *et al.* (2016)[2].

No	Name	Composition	Sample
1	LaPr	x_{Pr}=0	Ansatz 1 AH-La-002
2	PrSm	x_{Sm}=0; 0.2; 0.4; 0.6; 0.8	David Bigdeli DB-007; DB-009; DB-015 DB-017; DB-001
3	NdEu	x_{Eu}=0; 0.5; 1	AH-La-002 Ansatz 1
4	PrNd	x_{Nd}=0.2; 0.5; 0.8; 1	Christa Claßen CCPr20Nd80; CCPr50Nd50; CCPr80Nd20; CCPr00Nd100
5	LaPr	x_{Pr}=0; 0.2; 0.5; 0.8; 1	Ansatz 2 AH-La-003; AH-LaPr-004; AH-LaPr-001; AH-LaPr-009; AH-Pr-002
6	LaPr	x_{Pr}=0	Ansatz 4a AH-La-006
7	LaPr	x_{Pr}=0	Ansatz 4b AH-La-006
8	LaPr	x_{Pr}=0	Ansatz 4c AH-La-006
9	LaPr	x_{Pr}=0	Ansatz 4d AH-La-007
10	NdSm	x_{Sm}=0; 0.2; 0.4; 0.6; 0.8; 1	Zafer Kuleci: Nd0.0; Nd0.2; Nd0.4; Nd0.6; Nd0.8; Nd1.0
11	LaPr	x_{Pr}=0.2; 0.4; 0.6 0.8	Ansatz 5 LR-M-003; LR-M-005; LR-M-007; LR-M-009
12	LaNd	x_{Nd}=0.5	Jörg Schoel JS012
13	LaNd	x_{Nd}=0.5	Jörg Schoel JS021
14	LaNd	x_{Nd}=0.5 (doped with 100ppm Eu)	Jörg Schoel JS037
15	LaPr	x_{Pr}=0.5	Ansatz 3 AH-LaPr-005
16	LaPr	x_{Pr}=0.5	Ansatz 3 AH-LaPr-012

Table A.22 Flux growth conditions: No: Number of the experiment (see table A.21; molar fractions according to table 2.1; composition and molar ratio of the flux component(s) and monazite (Mon); T_{start}, T_{end}: start, end temperature in K; ramp: cooling ramp in K/h; lid: Y = yes (closed crucible; *: welded), N = no (open crucible); crystal habit (P = platelet; N = needle; I = isometric): Y = yes (crystals found in this form), - = no crystals found in this shape; Max: longest dimension in mm; ‡: large crystal broke during removing from crucible. Single crystals of PrSm, NdEu and NdSm were grown by Bigdeli (2016), Schumacher (2016) and Kuleci (2015) [a,b,c], respectively, and used for this thesis. Crystal growth experiments of PrNd and LaNd done by Claßen and Schoel [d,e: pers.comm.] were included. LaPr single crystals were used in Ruiz-Fuertes *et al.* (2016)[1] and Bauer *et al.* (2016)[2].

No	Li_2CO_3	Li_2MoO_4	MoO_3	Mon	T_{start}	T_{end}	Ramp	Lid	P	N	I	Max	Reference
1	25	-	75	2	1623	1143	3	N	Y	Y	-	1	[1]
2	25	-	75	2	1623	1143	3	Y	Y	-	Y	3	[a]
3	25	-	75	2	1623	1143	3	Y	Y	-	-	2	[b]
4	25	-	75	2	1623	1143	2	Y	Y	-	-	8 (fig. 3.19 right)	[d]
5	25	-	75	2	1623	1143	1	N	Y	Y	-	1	[1,2]
6	-	25	50	1	1623	1143	1.5	Y	-	-	-	1	-
7	-	25	50	2	1623	1143	1.5	Y	Y	Y	-	5	-
8	-	25	50	4	1623	1143	1.5	Y	-	-	-	13‡ (fig. 3.19 left)	-
9	-	25	50	8	1623	1143	1.5	Y	-	-	Y	2 (fig. 3.19 middle)	-
10	-	25	75	2	1623	1143	3	Y	-	-	Y	1	[c]
11	-	25	75	2	1623	1073	1.5	Y	-	-	Y	2 (fig. 3.20)	[2]
12	-	15	75	2	1623	1143	2	Y	-	Y	Y	5	[e]
13	-	15	75	2	1623	1143	1	Y*	Y	-	Y	3	[e]
14	-	15	75	2	1273	1273	-	N	-	-	-	10‡	[e]
15	50	-	50	1	1273	1073	1	Y	-	-	-	-	-
16	-	100	-	2	1273	1073	1	Y	-	-	-	-	-

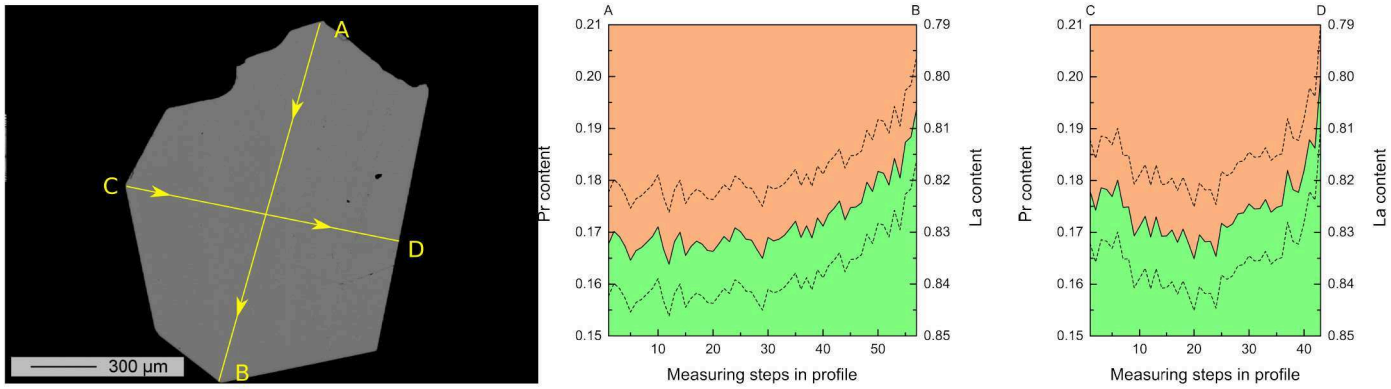

Figure A.2 Atomic fraction of La (orange) and Pr (green) along the cross-sections (A-B: left; C-D: right) of the $La_{0.8}Pr_{0.2}PO_4$ single crystal in figure 3.21 on the right. The solid black line represents the measured values while the dashed lines represent the error range of $\pm 1\,\%$. There is no significant change in the composition within the errors in both profiles.

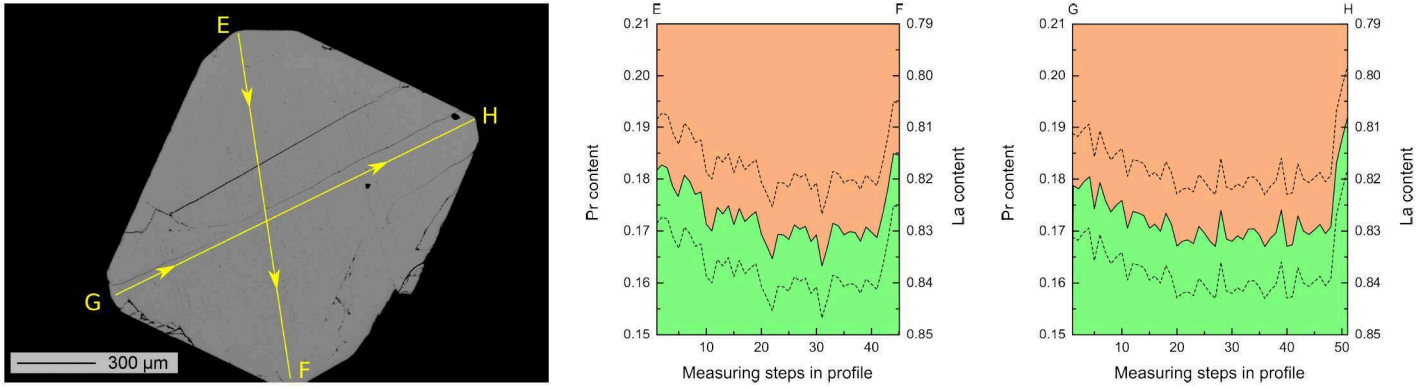

Figure A.3 Atomic fraction of La (orange) and Pr (green) along the cross-sections (E-F: left; G-H: right) of the $La_{0.8}Pr_{0.2}PO_4$ single crystal in figure 3.21 on the right. The solid black line represents the measured values while the dashed lines represent the error range of $\pm 1\,\%$. There is no significant change in the composition within the errors in both profiles.

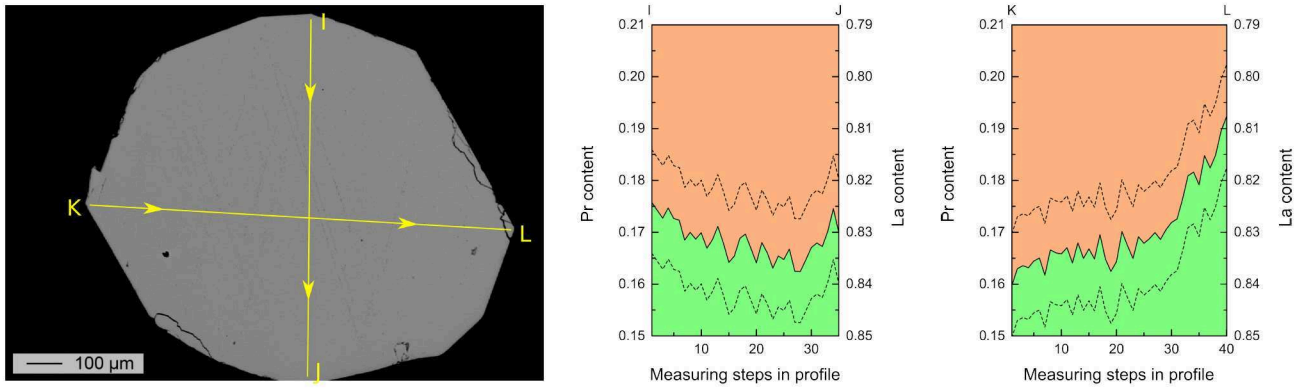

Figure A.4 Atomic fraction of La (orange) and Pr (green) along the cross-sections (I-J: left; K-L: right) of the $La_{0.8}Pr_{0.2}PO_4$ single crystal in figure 3.21 on the right. The solid black line represents the measured values while the dashed lines represent the error range of $\pm 1\,\%$. There is no significant change in the composition within the errors in both profiles.

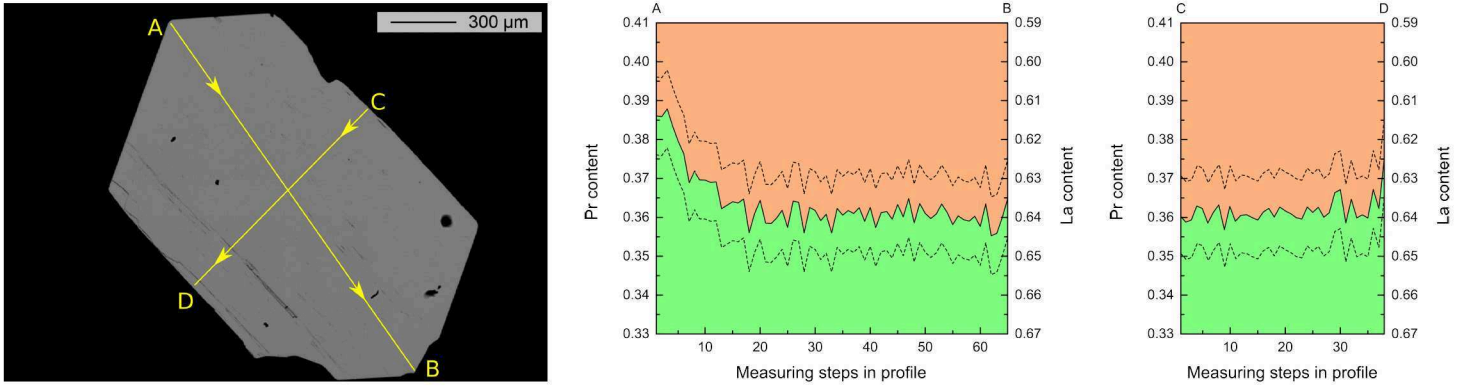

Figure A.5 Atomic fraction of La (orange) and Pr (green) along the cross-sections (A-B: left; C-D: right) of the $La_{0.6}Pr_{0.4}PO_4$ single crystal in figure 3.21 on the right. The solid black line represents the measured values while the dashed lines represent the error range of $\pm 1\,\%$. There is no significant change in the composition within the errors in both profiles.

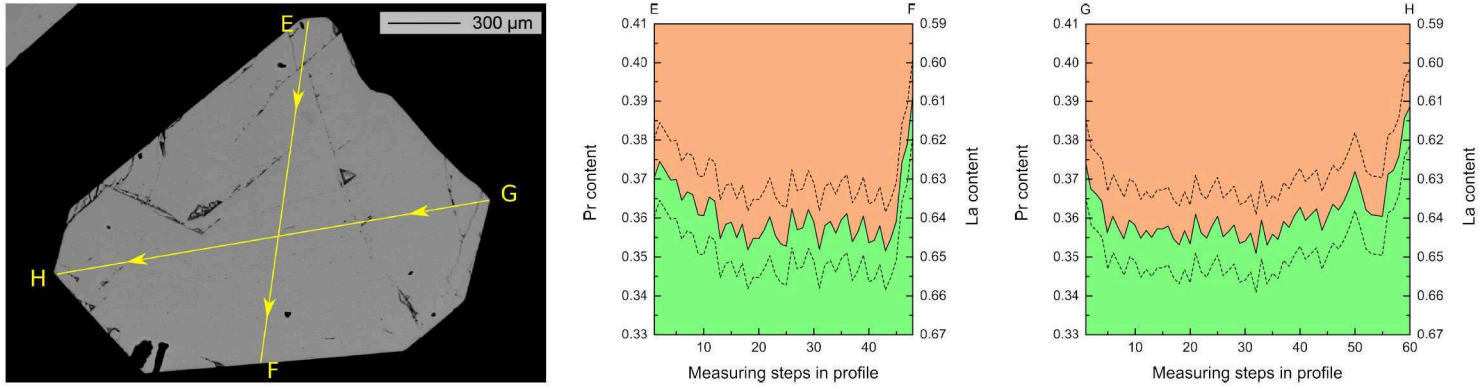

Figure A.6 Atomic fraction of La (orange) and Pr (green) along the cross-sections (E-F: left; G-H: right) of the $La_{0.6}Pr_{0.4}PO_4$ single crystal in figure 3.21 on the right. The solid black line represents the measured values while the dashed lines represent the error range of $\pm 1\,\%$. There is no significant change in the composition within the errors in both profiles.

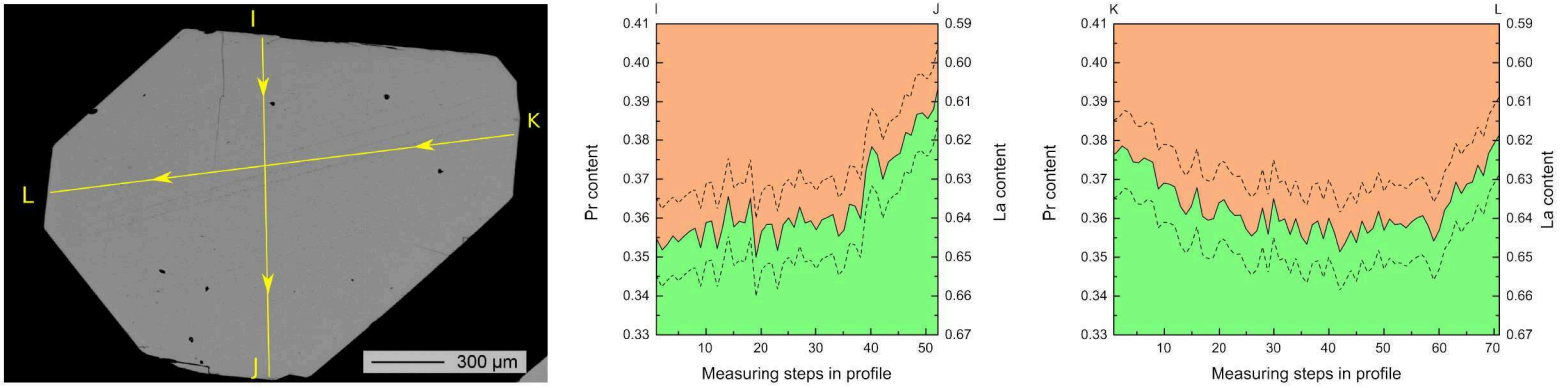

Figure A.7 Atomic fraction of La (orange) and Pr (green) along the cross-sections (I-J: left; K-L: right) of the $La_{0.6}Pr_{0.4}PO_4$ single crystal in figure 3.21 on the right. The solid black line represents the measured values while the dashed lines represent the error range of $\pm 1\,\%$. There is no significant change in the composition within the errors in both profiles.

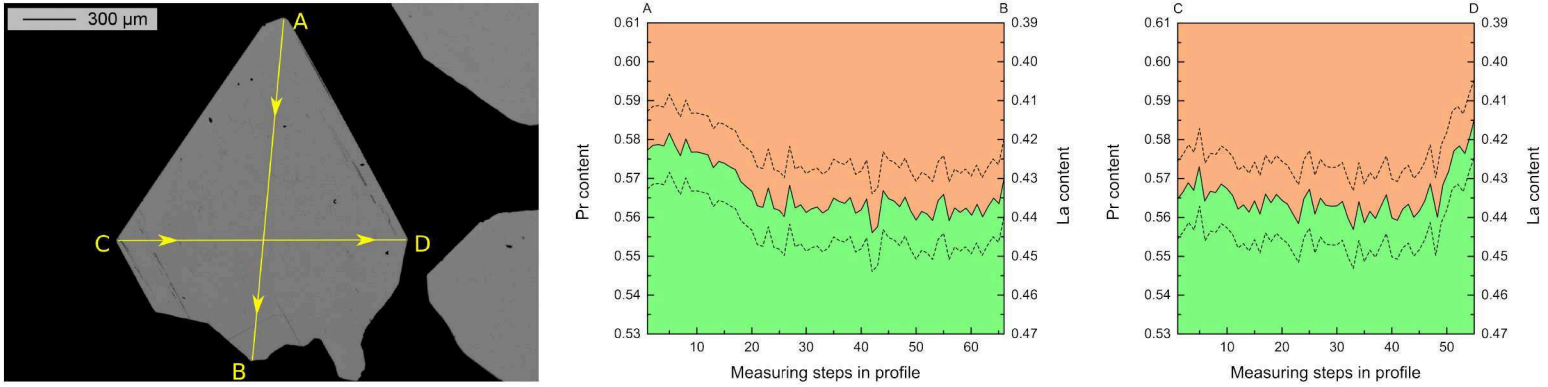

Figure A.8 Atomic fraction of La (orange) and Pr (green) along the cross-sections (A-B: left; C-D: right) of the $La_{0.4}Pr_{0.6}PO_4$ single crystal in figure 3.21 on the right. The solid black line represents the measured values while the dashed lines represent the error range of $\pm 1\,\%$. There is no significant change in the composition within the errors in both profiles.

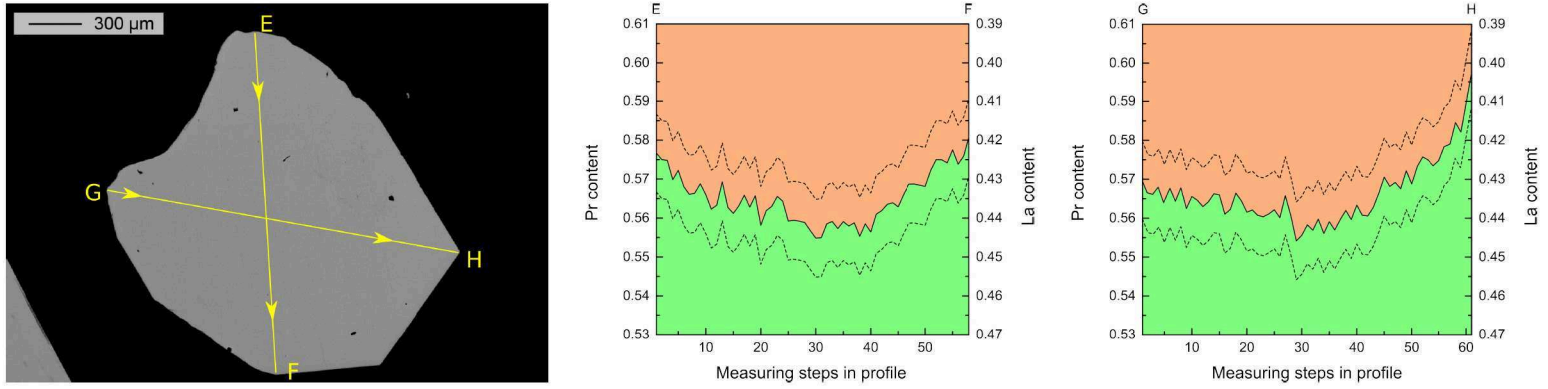

Figure A.9 Atomic fraction of La (orange) and Pr (green) along the cross-sections (E-F: left; G-H: right) of the $La_{0.4}Pr_{0.6}PO_4$ single crystal in figure 3.21 on the right. The solid black line represents the measured values while the dashed lines represent the error range of $\pm 1\,\%$. There is no significant change in the composition within the errors in both profiles.

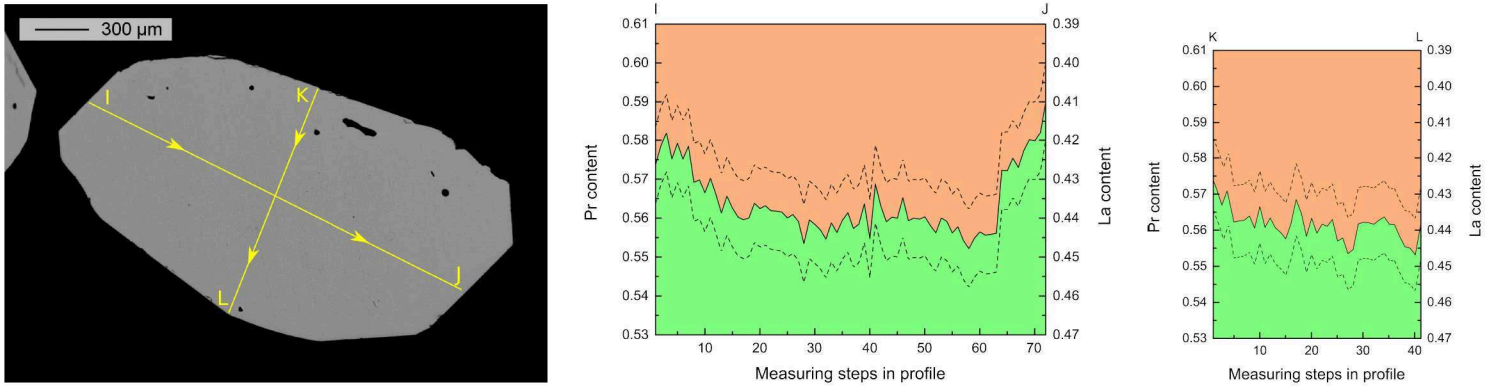

Figure A.10 Atomic fraction of La (orange) and Pr (green) along the cross-sections (I-J: left; K-L: right) of the $La_{0.4}Pr_{0.6}PO_4$ single crystal in figure 3.21 on the right. The solid black line represents the measured values while the dashed lines represent the error range of $\pm 1\,\%$. There is no significant change in the composition within the errors in both profiles.

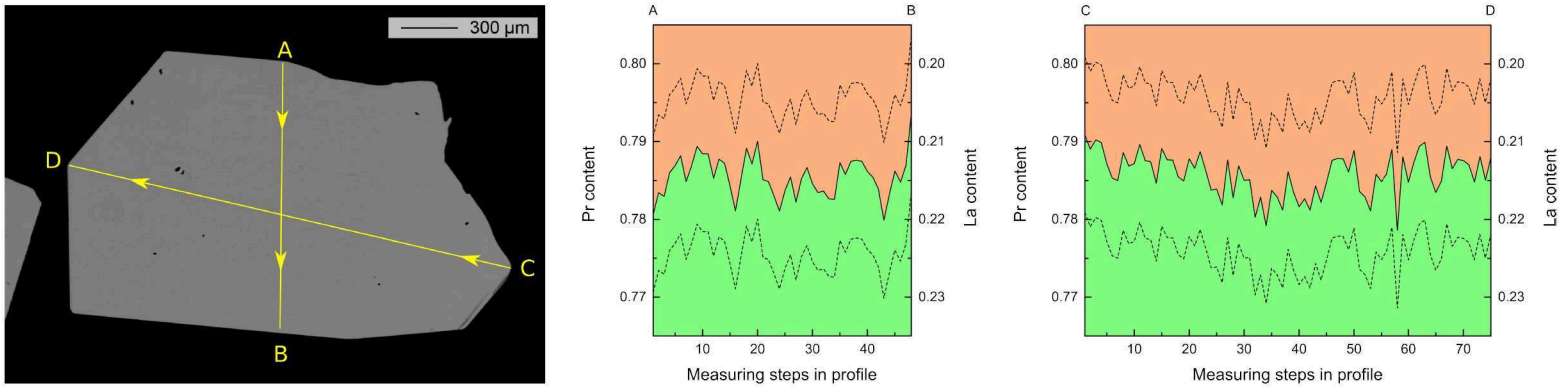

Figure A.11 Atomic fraction of La (orange) and Pr (green) along the cross-sections (A-B: left; C-D: right) of the $La_{0.2}Pr_{0.8}PO_4$ single crystal in figure 3.21 on the right. The solid black line represents the measured values while the dashed lines represent the error range of $\pm 1\,\%$. There is no significant change in the composition within the errors in both profiles.

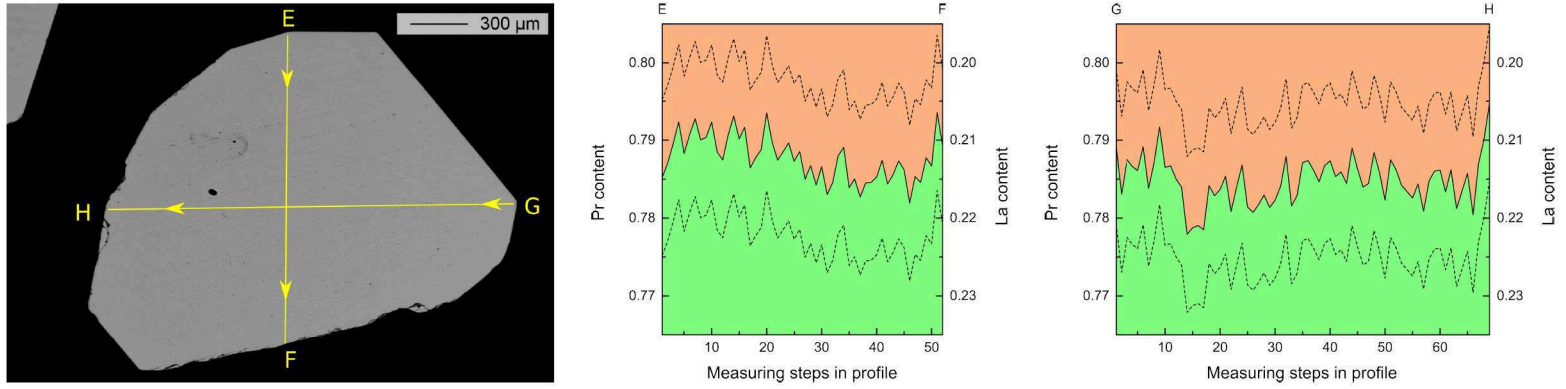

Figure A.12 Atomic fraction of La (orange) and Pr (green) along the cross-sections (E-F: left; G-H: right) of the $La_{0.2}Pr_{0.8}PO_4$ single crystal in figure 3.21 on the right. The solid black line represents the measured values while the dashed lines represent the error range of $\pm 1\,\%$. There is no significant change in the composition within the errors in both profiles.

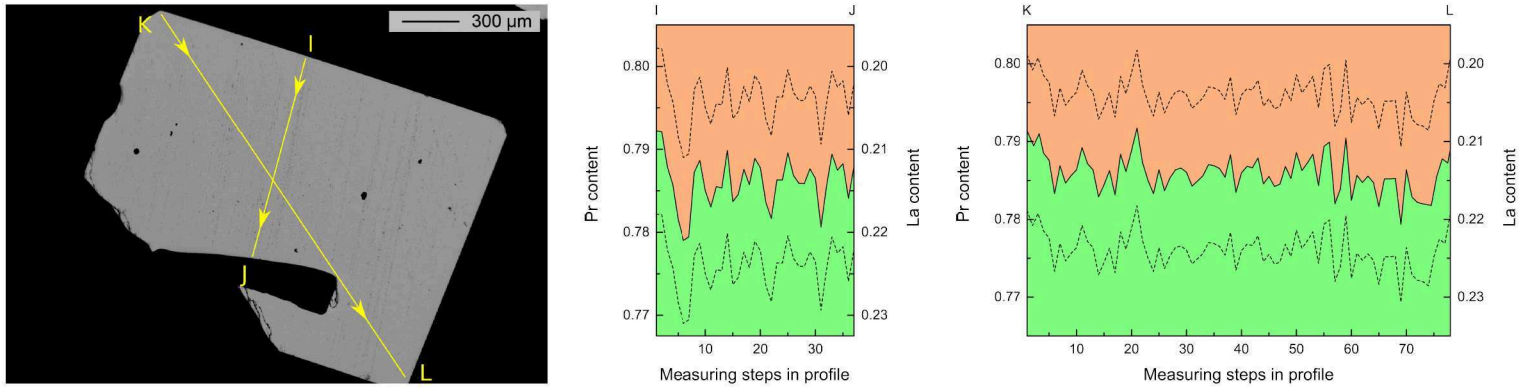

Figure A.13 Atomic fraction of La (orange) and Pr (green) along the cross-sections (I-J: left; K-L: right) of the $La_{0.2}Pr_{0.8}PO_4$ single crystal in figure 3.21 on the right. The solid black line represents the measured values while the dashed lines represent the error range of $\pm 1\,\%$. There is no significant change in the composition within the errors in both profiles.

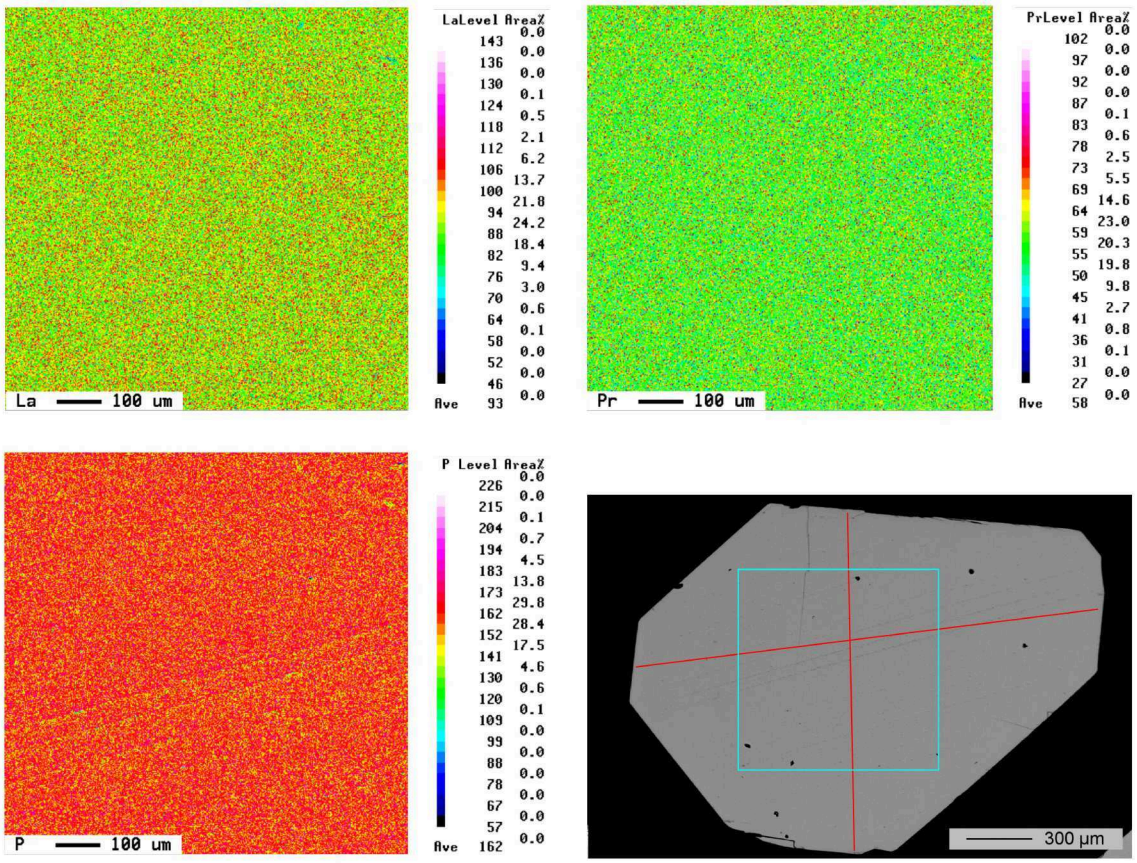

Figure A.14 Chemical analyses of the mapping on a $La_{0.6}Pr_{0.4}PO_4$ single crystal (La: top left, Pr: top right, P: bottom left. Mapped area as blue box: bottom right). No indication for zoning can be found.

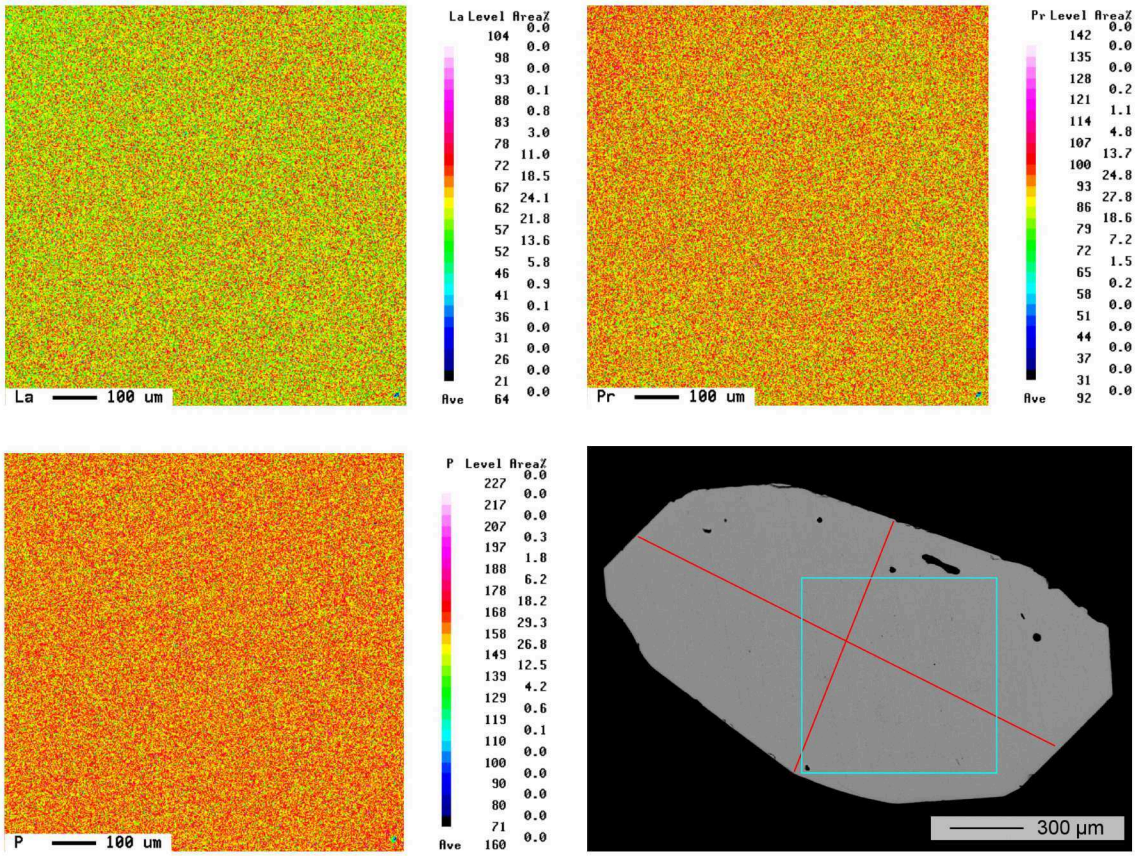

Figure A.15 Chemical analyses (La: top left, Pr: top right, P: bottom left) on the mapping on a $La_{0.4}Pr_{0.6}PO_4$ single crystal (bottom right). No indication for zoning can be found.

Table A.23 Lattice parameters and fractional coordinates of the atoms in the asymmetric unit of three compositions of LaPr from single crystal XRD. For growth conditions, see table A.22. Details of the data collection are given: n_{obs} and n_{un} are the number of observed and unique reflections, respectively, and n_{prm} is the number of parameters used in the refinement; R^1, ωR^2, and GoF are quality criteria for Rietveld analyses (unweighted and weighted residual R-value, Goodness of fit).

x_{Pr}		0	0.2	0.4	0.6
Space group		$P2_1/n$	$P2_1/n$	$P2_1/n$	$P2_1/n$
$\vec{a}$		6.84130(10)	6.8290(10)	6.81570(10)	6.79830(10)
$\vec{b}$		7.07590(10)	7.0626(9)	7.04560(10)	7.02520(10)
$\vec{c}$		6.51230(10)	6.4999(9)	6.48700(10)	6.46990(10)
β		103.2892(9)	103.334(10)	103.3892(11)	103.4487(9)
Ln	x	0.28168(6)	0.28167(9)	0.28171(9)	0.28187(18)
	y	0.16031(6)	0.15999(8)	0.15958(9)	0.15964(19)
	z	0.10074(7)	0.10041(9)	0.10038(8)	0.10017(19)
P	x	0.3052(3)	0.3047(5)	0.3045(4)	0.3042(9)
	y	0.1642(3)	0.1634(4)	0.1635(4)	0.1623(9)
	z	0.6126(3)	0.6123(4)	0.6122(4)	0.6117(9)
O^1	x	0.2544(10)	0.2550(15)	0.2540(14)	0.248(3)
	y	0.0063(10)	0.0064(14)	0.0049(14)	0.004(3)
	z	0.4505(10)	0.4514(15)	0.4487(14)	0.452(3)
O^2	x	0.3802(10)	0.3806(14)	0.3815(13)	0.390(3)
	y	0.3304(9)	0.3316(11)	0.3315(12)	0.338(3)
	z	0.4982(10)	0.4973(14)	0.4971(13)	0.489(3)
O^3	x	0.4731(10)	0.4745(13)	0.4751(13)	0.474(3)
	y	0.1066(10)	0.1070(13)	0.1073(13)	0.106(3)
	z	0.8011(10)	0.8023(13)	0.8044(13)	0.807(3)
O^4	x	0.1258(11)	0.1229(15)	0.1243(13)	0.123(3)
	y	0.2219(10)	0.2197(14)	0.2202(13)	0.217(3)
	z	0.7119(11)	0.7129(14)	0.7088(12)	0.713(3)
n_{obs}		1052	1040	1031	1028
n_{un}		935	977	933	890
n_{prm}		35	25	25	25
R^1		0.0461	0.0762	0.0699	0.1156
ωR^2		0.0585	0.926	0.0807	0.1466
GoF		4.41	7.45	6.19	10.34
Threshold		$I > 3\sigma$	$I > 3\sigma$	$I > 3\sigma$	$I > 3\sigma$

Table A.24 Lattice parameters and fractional coordinates of the atoms in the asymmetric unit of three compositions of NdSm from single crystal XRD after Kuleci (2015). For growth conditions, see table A.22. Details of the data collection are given: R^1, ωR^2, and GoF are quality criteria for Rietveld analyses (unweighted and weighted residual R-value, Goodness of fit).

		0	0.2	0.4	0.6	0.8	1
Space group		$P2_1/n$	$P2_1/n$	$P2_1/n$	$P2_1/n$	$P2_1/n$	$P2_1/n$
$\vec{a}$		6.721(2)	6.681(2)	6.705(2)	6.689(2)	6.663(2)	6.659(2)
$\vec{b}$		6.934(2)	6.910(2)	6.907(2)	6.900(2)	6.900(2)	6.869(2)
$\vec{c}$		6.383(1)	6.374(1)	6.368(2)	6.365(2)	6.355(2)	6.348(2)
β		103.68(2)	103.67(2)	103.72(2)	103.79(2)	103.57(2)	103.79(2)
Ln	x	0.28188(4)	0.28182(6)	0.28175(8)	0.28171(6)	0.28182(8)	0.28171(5)
	y	0.15806(4)	0.15776(7)	0.15748(8)	0.15714(7)	0.15683(8)	0.15650(5)
	z	0.09959(5)	0.09920(7)	0.09913(3)	0.09874(6)	0.09841(9)	0.09829(5)
P	x	0.3034(2)	0.3032(3)	0.3042(4)	0.3033(3)	0.3035(4)	0.3031(3)
	y	0.1625(2)	0.1628(3)	0.1623(4)	0.1625(3)	0.1618(4)	0.1620(3)
	z	0.6125(2)	0.6128(3)	0.6141(4)	0.6129(3)	0.6132(5)	0.6130(3)
O^1	x	0.249(1)	0.248(1)	0.250(1)	0.250(1)	0.248(1)	0.249(1)
	y	0.005(1)	0.004(1)	0.005(1)	0.004(1)	0.003(1)	0.003(1)
	z	0.441(1)	0.440(1)	0.438(1)	0.441(1)	0.440(1)	0.440(1)
O^2	x	0.381(1)	0.383(1)	0.382(1)	0.381(1)	0.386(1)	0.382(1)
	y	0.332(1)	0.333(1)	0.334(1)	0.335(1)	0.335(1)	0.335(1)
	z	0.498(1)	0.500(1)	0.499(1)	0.500(1)	0.500(1)	0.500(1)
O^3	x	0.474(1)	0.476(1)	0.475(1)	0.473(1)	0.474(1)	0.475(1)
	y	0.104(1)	0.107(1)	0.105(1)	0.103(1)	0.103(1)	0.105(1)
	z	0.808(1)	0.808(1)	0.809(1)	0.809(1)	0.810(1)	0.810(1)
O^4	x	0.123(1)	0.125(1)	0.125(1)	0.123(1)	0.122(1)	0.123(1)
	y	0.212(1)	0.210(1)	0.211(1)	0.213(1)	0.212(1)	0.213(1)
	z	0.713(1)	0.714(1)	0.712(1)	0.713(1)	0.713(1)	0.714(1)
ωR^2		0.071	0.116	0.1072	0.0969	0.1297	0.0956
R^1		0.0265	0.0431	0.04	0.038	0.0502	0.0365
Threshold		$I > 3\sigma$	$I > 3\sigma$	$I > 3\sigma$	$I > 3\sigma$	$I > 3\sigma$	$I > 3\sigma$

Table A.25 Lattice parameters and fractional coordinates of the atoms in the asymmetric unit of three compositions of NdEu from single crystal XRD after Schumacher (2016). For growth conditions, see table A.22. Details of the data collection are given: n_{obs} and n_{un} are the number of observed and unique reflections, respectively, and n_{prm} is the number of parameters used in the refinement; R^1, ωR^2, and GoF are quality criteria for Rietveld analyses (unweighted and weighted residual R-value, Goodness of fit).

x_{Eu}		0	0.5	1
Space group		$P2_1/n$	$P2_1/n$	$P2_1/n$
$\vec{a}$		6.741(1)	6.702(1)	6.668(1)
$\vec{b}$		6.9559(9)	6.9097(9)	6.866(1)
$\vec{c}$		6.4082(8)	6.3801(8)	6.252(1)
β		103.67(1)	103.81(1)	103.94(1)
Ln	x	0.2819(2)	0.2815(2)	0.282(2)
	y	0.1580(2)	0.1570(2)	0.156(2)
	z	0.0996(2)	0.0984(2)	0.0974(2)
P	x	0.306(1)	0.3046(9)	0.3040(8)
	y	0.161(1)	0.1620(1)	0.1626(8)
	z	0.614(1)	0.612(1)	0.6141(7)
O^1	x	0.254(3)	0.257(3)	0.262(3)
	y	0.001(3)	0.001(2)	-0.003(2)
	z	0.451(3)	0.446(2)	0.444(3)
O^2	x	0.382(3)	0.383(2)	0.383(2)
	y	0.334(3)	0.335(2)	0.334(2)
	z	0.502(2)	0.501(3)	0.502(2)
O^3	x	0.471(3)	0.470(2)	0.473(2)
	y	0.102(2)	0.101(2)	0.106(2)
	z	0.810(3)	0.810(3)	0.812(2)
O^4	x	0.114(3)	0.115(3)	0.118(2)
	y	0.219(2)	0.215(2)	0.218(2)
	z	0.707(4)	0.715(3)	0.713(2)
n_{obs}		345	247	1133
n_{un}		282	191	684
n_{prm}		55	55	50
R^1		0.0642	0.0225	0.0833
ωR^2		0.0756	0.0208	0.0861
GoF		5.52	1.49	3.82
Threshold		$I > 3\sigma$	$I > 3\sigma$	$I > 3\sigma$

Table A.26 Individual and mean *Ln*-O bond lengths obtained by single crystals XRD at RT for LaPr, PrSm, and NdSm. For growth conditions, see table A.22. Oxygen atoms are named according to Mullica *et al.* (1984) and Ni *et al.* (1995) and are shown in figure 1.7 in subsection 1.3.1.

			Oxygen atoms involved in the chain				Oxygen atoms involved in the equatorial plane				
Name	x_{Ln}	r_{Ln}	O^1	O^2	O^3	O^4	$O^{1'}$	$O^{2'}$	$O^{2''}$	$O^{3'}$	$O^{4'}$
LaPr	0.0	1.216	2.563(8)	2.786(7)	2.610(8)	2.550(7)	2.468(8)	2.668(7)	2.594(7)	2.503(7)	2.437(7)
LaPr	0.2	1.209	2.57(1)	2.789(9)	2.609(9)	2.537(9)	2.47(1)	2.666(9)	2.586(8)	2.498(9)	2.43(1)
LaPr	0.4	1.201	2.55(9)	2.783(8)	2.59(1)	2.554(8)	2.46(1)	2.655(9)	2.580(9)	2.488(9)	2.430(8)
LaPr	0.6	1.194	2.58(2)	2.75(2)	2.57(2)	2.52(2)	2.44(2)	2.59(2)	2.55(2)	2.48(2)	2.43(2)
NdSm	0.0	1.163	2.480(7)	2.750(6)	2.532(7)	2.474(6)	2.423(7)	2.525(7)	2.525(7)	2.426(7)	2.410(7)
NdSm	0.2	1.157	2.476(7)	2.763(6)	2.523(7)	2.458(6)	2.409(7)	2.590(7)	2.514(7)	2.421(7)	2.415(7)
NdSm	0.4	1.151	2.455(7)	2.759(6)	2.522(7)	2.468(6)	2.416(7)	2.605(7)	2.503(7)	2.416(7)	2.420(7)
NdSm	0.6	1.144	2.475(7)	2.768(6)	2.511(7)	2.462(6)	2.411(7)	2.604(7)	2.489(7)	2.408(7)	2.398(7)
NdSm	0.8	1.138	2.474(7)	2.770(6)	2.498(7)	2.461(6)	2.405(7)	2.564(7)	2.499(7)	2.399(7)	2.390(7)
NdSm	1.0	1.132	2.468(7)	2.764(6)	2.501(7)	2.447(6)	2.396(7)	2.586(7)	2.476(7)	2.396(7)	2.390(6)
NdEu	0.0	1.163	2.55(2)	2.79(1)	2.52(2)	2.54(2)	2.41(2)	2.62(2)	2.53(2)	2.43(2)	2.34(2)
NdEu	0.5	1.142	2.51(1)	2.78(2)	2.50(2)	2.47(2)	2.40(1)	2.59(1)	2.50(1)	2.41(1)	2.35(2)
NdEu	1.0	1.120	2.49(2)	2.78(1)	2.47(2)	2.45(2)	2.37(2)	2.58(1)	2.47(2)	2.40(2)	2.36(2)

Table A.27 Individual and mean P-O bond lengths obtained by single crystals XRD at RT for LaPr, PrSm, and NdSm. For growth conditions, see table A.22. Oxygen atoms are named according to Mullica *et al.* (1984) and Ni *et al.* (1995) and are shown in figure 1.7 in subsection 1.3.1.

Name	x_{Ln}	r_{Ln}	O^1	O^2	O^3	O^4
LaPr	0.0	1.216	1.519(8)	1.538(8)	1.530(8)	1.563(8)
LaPr	0.2	1.209	1.51(1)	1.555(9)	1.539(8)	1.58(1)
LaPr	0.4	1.201	1.51(1)	1.55(1)	1.547(8)	1.56(1)
LaPr	0.6	1.194	1.51(2)	1.65(2)	1.55(2)	1.57(2)
NdSm	0.0	1.163	1.528(7)	1.539(7)	1.536(6)	1.539(7)
NdSm	0.2	1.157	1.537(7)	1.538(7)	1.533(6)	1.518(8)
NdSm	0.4	1.151	1.542(7)	1.548(8)	1.528(6)	1.517(8)
NdSm	0.6	1.144	1.528(7)	1.543(7)	1.530(6)	1.532(8)
NdSm	0.8	1.138	1.536(7)	1.560(8)	1.534(6)	1.531(8)
NdSm	1.0	1.132	1.530(7)	1.544(7)	1.531(6)	1.529(8)
NdEu	0.0	1.163	1.51(2)	1.52(2)	1.53(2)	1.59(2)
NdEu	0.5	1.142	1.52(2)	1.54(2)	1.53(2)	1.61(2)
NdEu	1.0	1.120	1.55(2)	1.53(2)	1.48(2)	1.56(2)

Table A.28 P-O angles obtained by single crystals XRD at RT for LaPr, PrSm, and NdSm. For growth conditions, see table A.22. Oxygen atoms are named according to Mullica *et al.* (1984) and Ni *et al.* (1995) and are shown in figure 1.7 in subsection 1.3.1.

Name	x_{Ln}	r_{Ln}	O^1-P-O^2	O^1-P-O^3	O^1-P-O^4	O^2-P-O^3	O^2-P-O^4	O^3-P-O^4
LaPr	0.0	1.216	105.8(4)	111.7(4)	113.8(4)	108.5(4)	112.2(4)	104.8(4)
LaPr	0.2	1.209	106.0(5)	111.9(5)	113.5(5)	108.1(5)	112.8(5)	104.6(5)
LaPr	0.4	1.201	105.7(5)	112.3(5)	113.4(5)	107.9(5)	112.6(5)	104.9(5)
LaPr	0.6	1.194	107(1)	113(1)	112(1)	108(1)	115(1)	103(1)
NdSm	0.0	1.163	104.8(4)	113.5(3)	112.3(4)	108.4(4)	114.6(4)	103.3(4)
NdSm	0.2	1.157	105.2(4)	114.2(4)	112.3(4)	107.1(4)	115.3(4)	103.0(4)
NdSm	0.4	1.151	104.1(4)	114.2(4)	112.5(4)	108.1(4)	114.4(4)	103.8(4)
NdSm	0.6	1.144	105.4(4)	113.2(4)	112.8(4)	108.7(4)	113.8(4)	103.1(4)
NdSm	0.8	1.138	105.5(4)	113.8(3)	112.2(4)	107.8(4)	114.6(4)	103.2(4)
NdSm	1.0	1.132	105.3(4)	114.0(4)	113.0(4)	107.8(4)	114.0(4)	103.0(4)
NdEu	0.0	1.163	105(1)	111.2(9)	116(1)	108.2(5)	113.1(9)	103(1)
NdEu	0.5	1.142	106.7(8)	111.4(9)	113.5(9)	109.5(9)	113.6(9)	102.3(9)
NdEu	1.0	1.120	108(1)	112(1)	112(1)	109(1)	111(1)	105(1)

Table A.29 Bond-length distortion (BLD) for $Ln\mathrm{O}_9$ and PO_4 polyhedra, tetrahedral angle variance (TAV) and angular distortion (AD) for O-P-O angles according to Renner and Lehmann (1986), Robinson *et al.* (1971) and Baur (1974) calculated from data obtained by single crystals XRD at RT for LaPr, PrSm, and NdSm according to the equations 3.1, 3.2 and 3.3 given in subsection 3.2.3. Results are shown in figures 3.28 and 3.29. For growth conditions, see table A.22.

Name	x_{Ln}	r_{Ln}	BLD (P-O)/%	TAV (OPO)/°	AD (OPO)/%	BLD (Ln-O)/%
LaPr	0.0	1.216	0.8(8)	13(1)	2.8(4)	3.1(3)
LaPr	0.2	1.209	1(1)	14(2)	3.0(5)	3.1(4)
LaPr	0.4	1.201	0.7(1)	14(2)	3.0(5)	3.0(4)
LaPr	0.6	1.194	3(2)	19(4)	3(1)	2.8(8)
NdSm	0.0	1.163	0.4(2)	3.19(6)	22(2)	3.6(4)
NdSm	0.2	1.157	0.7(2)	3.16(9)	26(2)	4.0(4)
NdSm	0.4	1.151	1.1(2)	3.2(1)	24(2)	3.8(4)
NdSm	0.6	1.144	0.5(2)	3.29(9)	20(2)	3.5(4)
NdSm	0.8	1.138	1.0(2)	3.12(1)	22(2)	3.7(4)
NdSm	1.0	1.132	0.5(2)	3.36(8)	23(2)	3.8(4)
NdEu	0.0	1.163	1(2)	8(3)	2(1)	2.6(8)
NdEu	0.5	1.142	2(2)	19(4)	3.1(9)	3.4(7)
NdEu	1.0	1.120	2(2)	24(4)	3.6(9)	3.5(7)

Table A.30 Polyhedral angle variance (PAV) for the O-*Ln*-O angles in $LnO_9$and angular distortion (AD) for O-P-O angles calculated from data obtained by single crystals XRD at RT for LaPr, PrSm, and NdSm according to the equations 3.4, 3.6 and 3.5 given in subsection 3.2.3. Results are shown in figures 3.30. For growth conditions, see table A.22.

Name	x_{Ln}	r_{Ln}	PAV(T)	PAV(F)	PAV(A)
LaPr	0.0	1.216	1992(8)	1456(5)	1001(2)
LaPr	0.2	1.209	1964(7)	1428(8)	999(3)
LaPr	0.4	1.201	1958(10)	1470(8)	998(3)
LaPr	0.6	1.194	1870(23)	1486(17)	999(7)
NdSm	0.0	1.163	1917(8)	1462(2)	991(2)
NdSm	0.2	1.157	1926(8)	1461(2)	992(2)
NdSm	0.4	1.151	1916(8)	1464(2)	991(2)
NdSm	0.6	1.144	1910(8)	1460(2)	991(2)
NdSm	0.8	1.138	1881(8)	1462(2)	990(2)
NdSm	1.0	1.132	1897(8)	1461(6)	990(2)
NdEu	0.0	1.163	1887(23)	1453(17)	990(7)
NdEu	0.5	1.142	1872(21)	1452(13)	990(6)
NdEu	1.0	1.120	1873(20)	1456(15)	990(6)

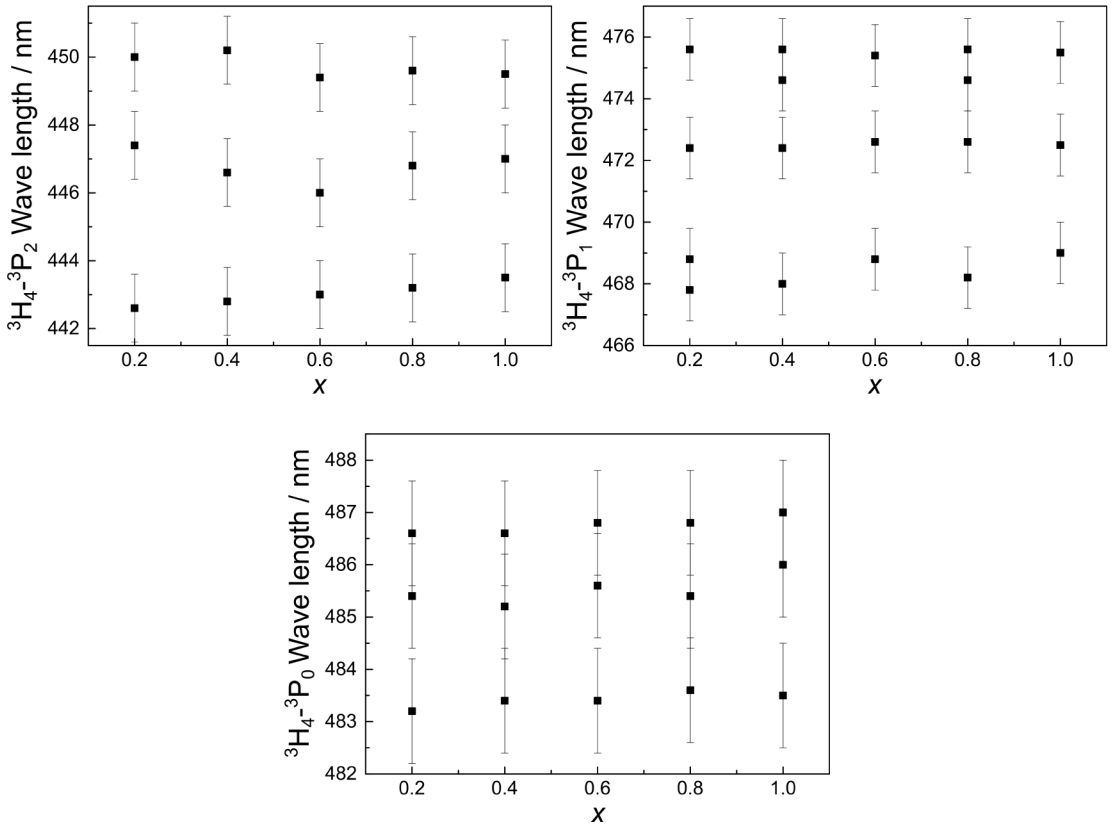

Figure A.16 Wave length of peak positions from optical absorption spectroscopy of the ${}^3H_4 \rightarrow {}^3P_2, {}^3P_1, {}^3P_0$ $4f-4f$ electron transitions of Pr^{3+} in LaPr against the Pr content x. For the spectra, see figure 3.31 in subsection 3.2.4. Within the error, there is no change with increasing Pr.

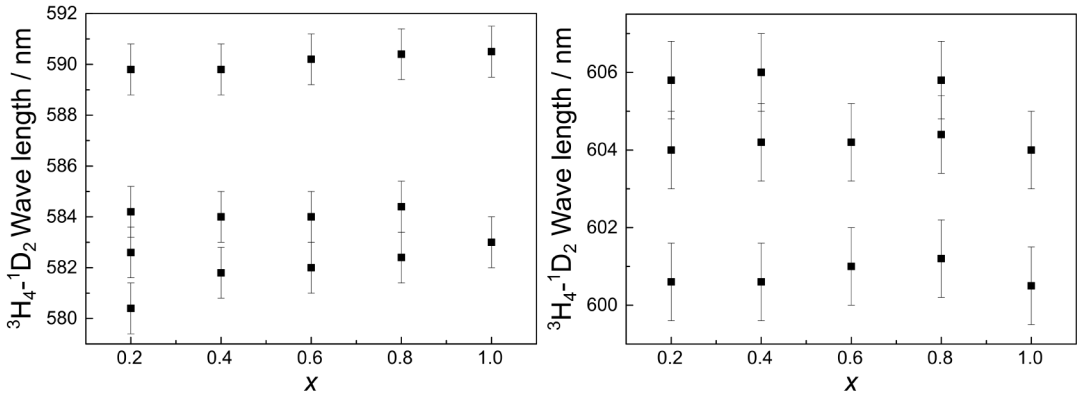

Figure A.17 Wave length of peak positions from optical absorption spectroscopy of the ${}^3H_4 \rightarrow {}^3D_2$ $4f-4f$ electron transitions of Pr^{3+} in LaPr against the Pr content x. For the spectra, see figure 3.31 in subsection 3.2.4. Within the error, there is no change with increasing Pr.

Table A.31 Lattice parameters and fractional coordinates of the atoms in the asymmetric unit of $LaPO_4$ in the monazite and post-barite structure from HP synchrotron single crystal XRD at 27.1 GPa after Ruiz-Fuertes *et al.* (2016) (supplemental material). For more details on the experimental set-up, see subsection 2.2.3.6. Details of the data collection are given: n_{obs} and n_{un} are the number of observed and unique reflections, respectively, and n_{prm} is the number of parameters used in the refinement; R_{int}, R^1, ωR^2, and GoF are quality criteria for Rietveld analyses (internal, unweighted and weighted residual R-value, Goodness of fit). Note that this is a compact representation of the coordinates of both structures and the two data sets cannot be compared directly due to the different metrics of the lattices.

		Monazite	Post-barite
Space group		$P2_1/n$	$P2_12_12_1$
	$\vec{a}$	6.4055(17)	5.9054(13)
	$\vec{b}$	6.7158(15)	6.6672(14)
	$\vec{c}$	6.182(14)	6.221(13)
	β	101.70(8)	90
La	x	0.2696(2)	0.5341(2)
	y	0.16209(19)	0.8802(2)
	z	0.1178(6)	0.1605(8)
P	x	0.2966(11)	0.4916(10)
	y	0.1679(9)	0.8623(9)
	z	0.626(3)	0.659(3)
O^1	x	0.235(2)	0.438(3)
	y	0.004(2)	0.695(3)
	z	0.450(7)	0.513(11)
O^2	x	0.375(3)	0.551(3)
	y	0.343(2)	1.046(3)
	z	0.505(8)	0.517(12)
O^3	x	0.489(3)	0.694(3)
	y	0.120(2)	0.820(3)
	z	0.825(8)	0.794(10)
O^4	x	0.115(3)	0.287(3)
	y	0.216(3)	0.905(3)
	z	0.752(9)	0.807(10)
n_{obs}		1188	1073
n_{un}		562	357
R_{int}		0.1621	0.0888
n_{prm}		26	36
R^1		0.1621	0.0771
ωR^2		0.3546	0.2085
GoF		141 1.110	1.121
Threshold I/σ		> 2	> 2

Table A.32 Sample thickness d, expected (theoretical) and measured densities ρ_e (see eq. 2.12 in subsection 2.2.5) and ρ_m, porosities Φ (see eq. 2.13 in subsection 2.2.5), and elastic stiffness coefficients c_{11} and c_{44} (from longitudinal and shear wave, respectively) of LaPr for pre-ceramics and final ceramics for five compositions x_{Pr} at the sintering temperature T after Thust *et al.* (2017). Errors for d, ρ_e, and ρ_m are standard deviations from 3-6 measurements, while errors in Φ, c_{11}, and c_{44} are from error propagation.

x_{Pr}	T/K	d / mm	ρ_e / g/cm^3	ρ_m / g/cm^3	Φ / %	c_{11} /GPa	c_{44} / GPa
pre-ceramics							
0.0	1273	12.288(8)	5.08	3.0(5)	41(10)	-	-
0.3	1273	8.525(11)	5.15	2.9(2)	43(4)	-	-
0.5	1273	9.504(6)	5.19	3.2(1)	39(3)	-	-
0.5	1273	9.616(15)	5.19	3.2(1)	39(1)	-	-
0.7	1273	10.625(13)	5.24	3.1(3)	42(5)	-	-
1.0	1273	6.918(1)	5.31	3.4(3)	36(6)	-	-
final ceramics							
0.0	1573	6.955(2)	5.08	5.015(6)	1.3(1)	172(1)	52.3(4)
0.3	1573	7.213(1)	5.15	4.959(6)	3.7(1)	170(1)	51.5(6)
0.5	1573	5.315(3)	5.19	5.106(6)	1.7(1)	186(1)	54.6(4)
0.5	1573	8.143(1)	5.19	5.158(6)	0.7(1)	188(1)	54.8(5)
0.7	1573	7.619(2)	5.24	5.104(6)	2.6(1)	182(1)	53.7(5)
1.0	1573	4.724(4)	5.31	5.227(6)	1.5(1)	191(1)	55.5(7)

Table A.33 Coefficients of thermal expansion (α) of the lattice parameters of LaPr as a function of the Pr content: α_a for $\vec{a}$, α_b for $\vec{b}$, α_c for $\vec{c}$, α_β for β. The average α_m calculated by $\alpha_V/3$ is added.

x_{Pr}	α_a	α_b	α_c	α_β	α_m
0.0	13(2)	9(2)	14(2)	1(1)	12(4)
0.2	11(4)	8(3)	13(4)	1(3)	11(3)
0.5	11(5)	8(5)	12(4)	2(3)	10(3)
0.8	10(4)	8(4)	11(4)	0(3)	10(3)
1.0	9(8)	8(6)	11(5)	0(4)	9(3)

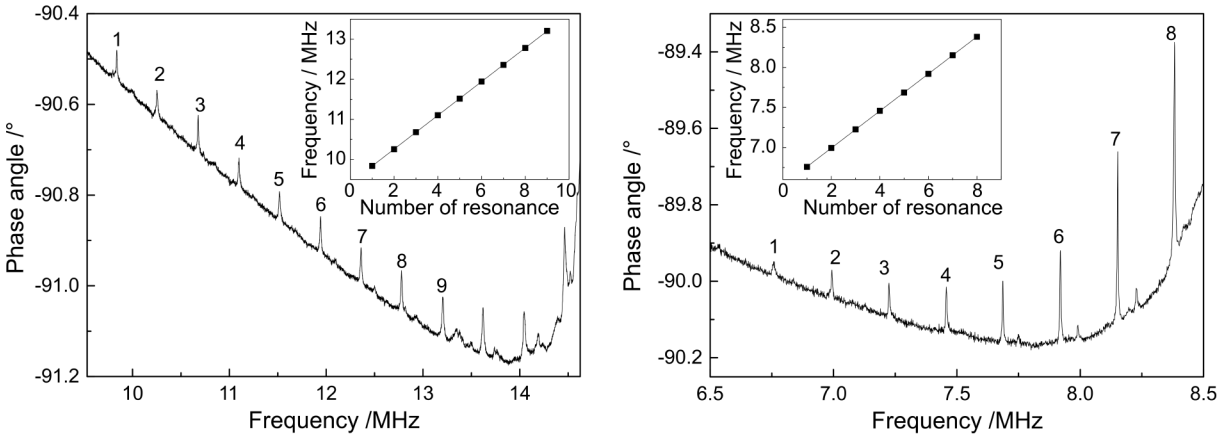

Figure A.18 Ultrasound resonance spectra of $LaPO_4$ with the longitudinal (left) and the shear wave (right) used to determine the elastic stiffness coefficients c_{11} and c_{44}, respectively (after Thust *et al.*, 2017). Inset: Frequency vs. number of the resonances used to determine the resonant frequencies Δf.

Bibliography

Abdelouas, A. (2006). Uranium mill tailings: Geochemistry, mineralogy, and environmental impact. *Elements* **2** 335–341

Agilent (2013). *CrysAlisPro software system.* Agilent Technologies UK Ltd., Oxford, UK, first edition

Ali, K., Arya, A., Ghosh, P. and Dey, G. (2016). A first principle study of the pressure dependent elastic properties of monazite $LaPO_4$. In *International Conference on Condensed Matter and Applied Physics (ICC 2015): Proceeding of International Conference on Condensed Matter and Applied Physics*, volume 1728, 020090. AIP Publishing

Aloy, A., Kovarskala, E., Koltsova, T., Samoylov, S., Rovnyi, G. and LJ, J. (2001). Immobilization of ^{241}Am, formed under Plutonium Metal Conversion, into Monazite-type ceramics. Technical report, Lawrence Livermore National Lab., CA (US)

Amezawa, K., Maekawa, H., Tomii, Y. and Yamamoto, N. (2001). Protonic conduction and defect structures in Sr-doped $LaPO_4$. *Solid State Ionics* **145** 233–240

Arbeck, D., Haussühl, E., Bayarjagal, L., Winkler, B., Paulsen, N., Haussühl, S. and Milman, V. (2010). Piezoelastic properties of retgersite determined by ultrasonic measurements. *The European Physical Journal B* **73** 167–175

"Arbeitskreis Abfallmanagement" des VGB (Vereinigung der Großkesselbesitzer) PowerTech e.V. (2011). Entsorgung von Kernkraftwerken - Eine technisch gelöste Aufgabe. Technical report, VGB PowerTech e.V., Klinkestraße 27-31, 45136 Essen

Arinicheva, Y., Bukaemskiy, A., Neumeier, S., Modolo, G. and Bosbach, D. (2014). Studies on thermal and mechanical properties of monazite-type ceramics for the conditioning of minor actinides. *Progress in nuclear energy* **72** 144–148

Armstrong, J. T. (1995). *Citzaf*-A package of correction programs for the quantitative electron microbeam X-ray-analysis of thick polished materials, thin-films, and particles. *Microbeam Analysis* **4** 177–200

Asuvathraman, R. and Kutty, K. G. (2014). Thermal expansion behaviour of a versatile monazite phase with simulated HLW: A high temperature X-ray diffraction study. *Thermochimica Acta* **581** 54–61

Baran, E. J. and Lavat, A. E. (1982). Schwingungseigenschaften des PO_4^{3-} Ions im Monazit- und Zirkon-Gitter. *Zeitschrift für Naturforschung A* **37 a** 380–382

Bauer, J., Hirsch, A., Bayarjargal, L., Peters, L., Roth, G. and Winkler, B. (2016). Schottky contribution to the heat capacity of monazite type (La,Pr)PO_4 from low temperature calorimetry and fluorescence measurements. *Chemical Physics Letters* **654** 97–102

Baur, W. (1974). The geometry of polyhedral distortions. Predictive relationships for the phosphate group. *Acta Crystallographica Section B: Structural Crystallography and Crystal Chemistry* **30** 1195–1215

Bayarjargal, L. and Winkler, B. (2014). Second harmonic generation measurements at high pressures on powder samples. *Zeitschrift für Kristallographie. Crystalline materials* **229** 92–100

Bayarjargal, L., Winkler, B., Haussühl, E. and Boehler, R. (2009). Influence of deviatoric stress on the pressure-induced structural phase transition of ZnO studied by optical second harmonic generation measurements. *Applied Physics Letters* **95** 061907

Beall, G. W., Boatner, L. A., Mullica, D. F. and Milligan, W. O. (1981). The Structure of Cerium Orthophosphate, a synthetic Analog of Monazite. *Journal of Inorganic & Nuclear Chemistry* **43** 101–105

Begun, G. M., Beall, G. W., Boatner, L. A. and Gregor, W. J. (1981). Raman-spectra of the Rare-earth Orthophosphates. *Journal of Raman Spectroscopy* **11** 273–278

Bělina, P., Myšková, V. and Šulcová, P. (2009). Comparison of the crystallisation and solid state reaction methods for the preparation of rare-earth orthophosphates. *Journal of thermal analysis and calorimetry* **96** 949–954

Bělina, P., Šulcová, P., Trojan, M. and Mazurek, P. (2007). Thermal synthesis and characterization of $Al_xLa_{1-x}P_3O_9$. *Open Chemistry* **5** 706–714

Bérar, J.-F. and Lelann, P. (1991). E.S.D.'s and estimated probable error obtained in Rietveld refinements with local correlations. *Journal of applied crystallography* **24** 1–5

Bernstein, L. R. (1982). Monazite from North Carolina having the Alexandrite Effect. *American Mineralogist* **67** 356–359

de Biasi, R. S., Fernandes, A. A. R. and Oliveira, J. C. S. (1987). Cell Volumes of $LaPO_4$-$CePO_4$ Solid-solutions. *Journal of Applied Crystallography* **20** 319–320

Bigdeli, D. (2016). *Master thesis: Synthese und Charakterisierung von Monazit-Mischkristallen im System Pr_2O_3 - Sm_2O_3 - P_2O_5*. RWTH Aachen University

Blank, V., Popov, M., Pivovarov, G., Lvova, N., Gogolinsky, K. and Reshetov, V. (1998). Ultrahard and superhard phases of fullerite C60: Comparison with diamond on hardness and wear. *Diamond and Related Materials* **7** 427–431

Bo, L., Liya, S., Xiaozhen, L., Shuihe, Z., Yumei, Z., Tianmin, W., Sasaki, Y., Ishii, K., Kashiwaya, Y., Takahashi, H. *et al.* (2001). Sol-gel synthesis of monazite-type cerous phosphate for fiber coating. *Journal of materials science letters* **20** 1071–1075

Boakye, E. E., Hay, R. S., Mogilevsky, P. and Douglas, L. (2001). Monazite coatings on fibers: II, coating without strength degradation. *Journal of the American Ceramic Society* **84** 2793–2801

Boatner, L., Beall, G., Abraham, M., Finch, C., Huray, P. and Rappaz, M. (1980). Monazite and other lanthanide orthophosphates as alternate actinide waste forms. In *Scientific Basis for Nuclear Waste Management. Advances in Nuclear Science & Technology* (Ed. C. Northrup), 289–296. Springer, Boston, MA

Boatner, L. and Sales, B. (1988). Monazite. In *Radioactive waste forms for the future* (Eds. W. Lutze and R. Ewing), 495–564. Elsevier Science Publishers Co., Inc., New York (USA)

Boatner, L. A. (2002). Synthesis, structure, and properties of monazite, pretulite, and xenotime. *Reviews in mineralogy and geochemistry* **48** 87–121

Botto, I. and Baran, E. (1982). Characterization of the monoclinic rare earth orthoarsenates. *Journal of the Less Common Metals* **83** 255–261

Bregiroux, D., Audubert, F. and Bernache-Assollant, D. (2009). Densification and grain growth during solid state sintering of $LaPO_4$. *Ceramics International* **35** 1115–1120

Bregiroux, D., Audubert, F., Charpentier, T., Sakellariou, D. and Bernache-Assollant, D. (2007a). Solid-state synthesis of monazite-type compounds $Ln\mathrm{PO}_4$ (Ln = La to Gd). *Solid State Sciences* **9** 432–439

Bregiroux, D., Belin, R., Valenza, P., Audubert, F. and Bernache-Assollant, D. (2007b). Plutonium and americium monazite materials: Solid state synthesis and X-ray diffraction study. *Journal of Nuclear Materials* **366** 52–57

Broegger, W. (1893). Amorf. *Salmonsens store illustrerede Konversationslexikon* **1** 742–743

Bruno, J. and Ewing, R. C. (2006). Spent nuclear fuel. *Elements* **2** 343–349

Buck, E. C., Hanson, B. D. and McNamara, B. K. (2004). The geochemical behaviour of Tc, Np and Pu in spent nuclear fuel in an oxidizing environment. *Geological Society, London, Special Publications* **236** 65–88

Bünzli, J.-C. (1989). *Lanthanide probes in life, chemical and earth sciences: Theory and Practice*, chapter Luminescent Probes, 219–293. Elsevier, Amsterdam

Campbell, J., Hoenig, C., Bazan, F., Ryerson, F., Guinan, M., Van Konynenburg, R. and Rozsa, R. (1982). Properties of synroc-d nuclear waste form: A state-of-the-art review. *Lawrence Livermore National Laboratory (LLNL), Rept. UCRL-53240*

Carvajal, J. J., Pujol, M. C. and Díaz, F. (2010). High-Temperature Solution Growth: Application to Laser and Nonlinear Optical Crystals. In *Springer Handbook of Crystal Growth* (Eds. G. Dhanaraj, K. Byrappa, V. Prasad and M. Dudley), 725–757. Springer, Berlin, Heidelberg

Chall, M., Knorr, K., Ehm, L. and Depmeier, W. (2000). Estimating intensity errors of powder diffraction data from area detectors. *International Journal of High Pressure Research* **17** 315–323

Chen, G., Hölsä, J. and Peterson, J. (1997). A luminescence study of single-crystal $EuPO_4$ at high pressure. *Journal of Physics and Chemistry of Solids* **58** 2031–2037

Chen, P. and Mah, T.-I. (1997). Synthesis and characterization of lanthanum phosphate sol for fibre coating. *Journal of materials science* **32** 3863–3867

Cheng, J. and Navrotsky, A. (2003). Enthalpies of Formation of LaBO$_3$ Perovskites (B= Al, Ga, Sc, and In). *Journal of materials research* **18** 2501–2508

Cherniak, D., Pyle, J. and Rakovan, J. (2004). Synthesis of REE and Y phosphates by Pb-free flux methods and their utilization as standards for electron microprobe analysis and in design of monazite chemical U-Th-Pb dating protocol. *American Mineralogist* **89** 1533–1539

Cho, I.-S., Choi, G. K., An, J.-S., Kim, J.-R. and Hong, K. S. (2009). Sintering, microstructure and microwave dielectric properties of rare earth orthophosphates, REPO$_4$ (RE= La, Ce, Nd, Sm, Tb, Dy, Y, Yb). *Materials Research Bulletin* **44** 173–178

Chun-hua, L., Jie, H., Zhongzi, X. and Yaru, N. (2007). Preparation and IR spectra study of rare earth orthophosphates. *Journal of Rare Earths* **25** 273–276

Clavier, N., Podor, R. and Dacheux, N. (2011). Crystal chemistry of the monazite structure. *Journal of the European Ceramic Society* **31** 941–976

Coelho, A. (2000). Topas V 2.0: General profile and structure analysis software for powder diffraction data.

Copeland, P., Parrish, R. R. and Harrison, T. M. (1988). Identification of inherited radiogenic Pb in monazite and its implications for U–Pb systematics. *Nature* **333** 760–763

Dabkowska, H. A. and Dabkowski, A. B. (2010). Crystal growth of oxides by optical floating zone technique. In *Springer Handbook of Crystal Growth* (Eds. G. Dhanaraj, K. Byrappa, V. Prasad and M. Dudley), 367–391. Springer, Berlin, Heidelberg

Dacheux, N., Clavier, N. and Podor, R. (2013). Monazite as a promising long-term radioactive waste matrix: Benefits of high-structural flexibility and chemical durability. *American Mineralogist* **98** 833–847

Davis, D., Vance, E. and McCarthy, G. (1981). Crystal chemistry and phase relations in the synthetic minerals of ceramic waste forms. II. Studies of uranium-containing monazites. In *Scientific basis for nuclear waste management.* (Ed. J. Moore), volume 3, 197–200. Plenum Press, New York

Davis, J., Marshall, D. and Morgan, P. (2000). Monazite-containing oxide/oxide composites. *Journal of the European Ceramic Society* **20** 583–587

Davis, J. B., Marshall, D. B., Housley, R. M. and Morgan, P. E. (1998). Machinable ceramics containing rare-earth phosphates. *Journal of the American Ceramic Society* **81** 2169–2175

Deissmann, G., Neumeier, S., Modolo, G. and Bosbach, D. (2012). Durability of potential plutonium waste forms under repository conditions. *Mineralogical Magazine* **76** 2911–2918

Deutsche Arbeitsgemeinschaft Endlagerforschung (DAEF) (2014). Aspekte eines Standortauswahlverfahrens für ein Endlager für Wärme entwickelnde Abfälle

Deutsches Atomforum e. V. (DAtF) (2016). Kernkraftwerke in Deutschland. http://www.kernenergie.de/kernenergie/themen/strom/Zahlen-und-Fakten/01_index.php

Ditmars, D., Ishihara, S., Chang, S., Bernstein, G. and West, E. (1982). Enthalpy and heat-capacity standard reference material: Synthetic sapphire (α-Al_2O_3) from 10 to 2250 K. *Journal of Research of the National Bureau of Standards* **87** 159–163

Donald, I., Metcalfe, B. and Taylor, R. (1997). The immobilization of high level radioactive wastes using ceramics and glasses. *Journal of Materials Science* **32** 5851–5887

Dong, H., Liu, Y., Yang, P., Wang, W. and Lin, J. (2010). Controlled synthesis and characterization of $LaPO_4$, $LaPO_4$: Ce^{3+} and $LaPO_4$: Ce^{3+}, Tb^{3+} by EDTA assisted hydrothermal method. *Solid state sciences* **12** 1652–1660

Dooley Jr, J. and Hathaway, J. (1961). Two occurrences of thorium-bearing minerals with rhabdophane-like structure. *US Geological Survey Professional Paper* **424** C339–C341

Du, A., Wan, C., Qu, Z. and Pan, W. (2009). Thermal Conductivity of Monazite-Type $RE$$PO_4$ (RE= La, Ce, Nd, Sm, Eu, Gd). *Journal of the American Ceramic Society* **92** 2687–2692

Elwell, D. (1980). High-Temperature Solid Growth. In *Crystal Growth* (Ed. B. Pamplin), volume 16 of *International Series in the Science of the Solid State*, chapter 12, 421–483. Pergamon Press Ltd, Oxford, UK

Elwell, D. and Scheel, H. (2000). *Crystal Growth from High-Temperature Solutions, 1975*. Academic Press, London

Emeis, R. (1954). Tiegelfreies Ziehen von Silicium-Einkristallen. *Zeitschrift Naturforschung Teil A* **9** 67

Ewing, R. C. (1975). The crystal chemistry of complex niobium and tantalum oxides. IV. The metamict state: Discussion. *American Mineralogist* **60** 728–733

Ewing, R. C. (1977). Metamict minerals: Alteration and radiation damage effects. In *ERDA Report Conf-770102* (Eds. D. W. Ready and C. R. Cooley), 139–146

Ewing, R. C. (2006). The nuclear fuel cycle: A role for mineralogy and geochemistry. *Elements* **2** 331–334

Ewing, R. C. (2007). Ceramic matrices for plutonium disposition. *Progress In Nuclear Energy* **49** 635–643

Ewing, R. C. and Haaker, R. (1980). The metamict state: Implications for radiation damage in crystalline waste forms. *Nuclear and Chemical Waste Management* **1** 51–57

Ewing, R. C. and Lutze, W. (1991). High-level Nuclear Waste Immobilization with Ceramics. *Ceramics International* **17** 287–293

Ewing, R. C., Weber, W. and Clinard, F. (1995). Radiation effects in nuclear waste forms for high-level radioactive waste. *Progress in nuclear energy* **29** 63–127

Feigelson, R. S. (1964). Synthesis and Single-crystal Growth of Rare-earth Orthophosphates. *Journal of the American Ceramic Society* **47** 257–258

Feng, J., Xiao, B., Qu, Z. X., Zhou, R. and Pan, W. (2011a). Mechanical properties of rare earth stannate pyrochlores. *Applied Physics Letters* **99** 201909

Feng, J., Xiao, B., Wan, C., Qu, Z., Huang, Z., Chen, J., Zhou, R. and Pan, W. (2011b). Electronic structure, mechanical properties and thermal conductivity of $Ln_2Zr_2O_7$ (Ln = La, Pr, Nd, Sm, Eu and Gd) pyrochlore. *Acta Materialia* **59** 1742 – 1760

Feng, J., Xiao, B., Zhou, R. and Pan, W. (2013). Anisotropy in elasticity and thermal conductivity of monazite-type $REPO_4$ (RE= La, Ce, Nd, Sm, Eu and Gd) from first-principles calculations. *Acta Materialia* **61** 7364–7383

Feng, J., Xiao, B., Zhou, R., Pan, W. and Clarke, D. R. (2012). Anisotropic elastic and thermal properties of the double perovskite slab-rock salt layer $Ln_2SrAl_2O_7$ (Ln = La, Nd, Sm, Eu, Gd or Dy) natural superlattice structure. *Acta Materialia* **60** 3380 – 3392

Ferhi, M., Horchani-Naifer, K. and Ferid, M. (2008). Hydrothermal synthesis and photoluminescence of the monophosphate $LaPO_4$: Eu (5%). *Journal of Luminescence* **128** 1777–1782

Floran, R., Abraham, M., Boatner, L. and Rappaz, M. (1981). Geologic stability of monazite and its bearing on the immobilization of actinide wastes. In *Scientific basis for nuclear waste management. Volume 3* (Ed. J. Moore), 507–514. Plenum Press, New York

Gallini, S., Jurado, J. and Colomer, M. (2005). Synthesis and characterization of monazite-type Sr:$LaPO_4$ prepared through coprecipitation. *Journal of the European Ceramic Society* **25** 2003 – 2007

Gardés, E., Jaoul, O., Montel, J., Seydoux-Guillaume, A. and Wirth, R. (2006). Pb diffusion in monazite: An experimental study of $Pb^{2+} + Th^{4+} \Leftrightarrow 2Nd^{3+}$ interdiffusion. *Geochimica et Cosmochimica Acta* **70** 2325–2336

Gavrichev, K., Gurevich, V., Ryumin, M., Tyrin, A. and Komissarova, L. (2016). Low-temperature heat capacity and thermodynamic properties of $PrPO_4$. *Geochemistry International* **54** 362–368

Gavrichev, K., Ryumin, M., Tyurin, A., Gurevich, V. and Komissarova, L. (2008). Refined heat capacity of $LaPO_4$ in the temperature range 0–1600 K. *Thermochimia Acta* **474** 47–51

Geckeis, H., Röhlig, K.-J. and Mengel, K. (2012). Endlagerung radioaktiver Abfälle. *Chemie in unserer Zeit* **46** 282–293

Gilmore, R. and Katz, J. (1982). Elastic properties of apatites. *Journal of Materials Science* **17** 1131–1141

Gompper, K., Geist, A. and Geckeis, H. (2010). Actinoidenabtrennung aus hochradioaktiven Abfällen. *Nachrichten aus der Chemie* **58** 1015–1019

Gouadec, G. and Colomban, P. (2007). Raman Spectroscopy of nanomaterials: How spectra relate to disorder, particle size and mechanical properties. *Progress in Crystal Growth and Characterization of Materials* **53** 1–56

Gramaccioli, C. and Segalstad, T. (1978). A uranium-and thorium-rich monazite from a south-alpine pegmatite at Piona, Italy. *American Mineralogist* **63** 757–761

Grambow, B. (2006). Nuclear waste glasses - How durable? *Elements* **2** 357–364

Gusowski, M., Dominiak-Dzik, G., Solarz, P., Lisiecki, R. and Ryba-Romanowski, W. (2007). Luminescence and energy transfer in K_3GdF_6:Pr^{3+}. *Journal of Alloys and Compounds* **438** 72 – 76

Haaker, R. F. and Ewing, R. C. (1981). Naturally occurring crystalline phases: Analogues for radioactive waste forms. Technical report, Battelle Pacific Northwest Labs., Richland, WA (USA)

Haas Jr., J. L. and Fisher, J. R. (1976). Simultaneous evaluation and correlation of thermodynamic data. *American Journal of Science* **276** 525–545

Hammersley, A., Svensson, S., Hanfland, M., Fitch, A. and Hausermann, D. (1996). Two-dimensional detector software: From real detector to idealised image or two-theta scan. *High Pressure Research* **14** 235–248

Harrison, M., Scales, C. and Maddrell, E. (2008). Progress in the assessment of wasteforms for the immobilisation of UK civil plutonium. In *Proceedings Waste Management 2008 Conference, February 24–28, Phoenix, AZ*, 24–28. WM Symposia, 1628 E. Southern Avenue, Suite 9-332, Tempe, AZ 85282 (United States)

Haussühl, E. and Tillmanns, E. (1997). Physical properties and phase transitions of bis (guanidinium) zirconium bis (nitrilotriacetate) hydrate $[C(NH_2)_3]_2Zr[N(CH_2COO)_3]_2 \cdot H_2O$. *Zeitschrift Fur Kristallographie* **212** 826–831

Haussühl, S. (1983). *Kristallographie*. Physik Verlag, Weinheim

Hay, R. and Marshall, D. (2003). Deformation twinning in monazite. *Acta Materialia* **51** 5235 – 5254

Hedin, A. (1997). Spent nuclear fuel–how dangerous is it. Technical report, Swedish Nuclear Fuel and Waste Management Co.

Heilbronner, R. and Barrett, S. (2013). *Image Analysis in Earth Sciences: Microstructures and Textures of Earth Materials*, volume 129. Springer Science & Business Media, Berlin, Heidelberg

Herzberg, G. (1945). *Infrared and Raman spectra*. D. Van Nostrand Company.; New York

Heuser (2015). *Keramiken des Monazit-Typs zur Immobilisierung von minoren Actinoiden und Plutonium*. Ph.D. thesis, RWTH Aachen University

Hezel, A. and Ross, S. (1966). Forbidden transitions in the infra-red spectra of tetrahedral anions – III. Spectra-structure correlations in perchlorates, sulphates and phosphates of the formula MXO_4. *Spectrochimica Acta* **22** 1949–1961

Hikichi, Y. (1991). Synthesis of monazite (RPO_4, R=La, Ce, Nd, or Sm) by solid state reaction. *Mineralogical Journal* **15** 268–275

Hikichi, Y., Hukuo, K. and Shiokawa, J. (1980). Solid state Reactions between Rare-earth Orthophosphate and Oxide. *Bulletin of the Chemical Society of Japan* **53** 1455–1456

Hikichi, Y., Hukuo, K. I. and Shiokawa, J. (1978a). Solid solutions in the Systems Monazite ($CePO_4$) Huttonite ($ThSiO_4$), and Monazite $Ca_{0.5}Th_{0.5}PO_4$. *Nippon Kagaku Kaishi* **10** 1635–1640

Hikichi, Y., Hukuo, K. I. and Shiokawa, J. (1978b). Syntheses of Rare-earth Ortho-phosphates. *Bulletin of the Chemical Society of Japan* **51** 3645–3646

Hikichi, Y. and Nomura, T. (1987). Melting temperatures of monazite and xenotime. *Journal of the American Ceramic Society* **70** C–252

Hikichi, Y., Nomura, T., Tanimura, Y., Suzuki, S. and Miyamoto, M. (1990). Sintering and Properties of Monazite-Type $CePO_4$. *Journal of the American Ceramic Society* **73** 3594–3596

Hikichi, Y., Ota, T. and Hattori, T. (1997). Thermal, mechanical and chemical properties of sintered monazite-(La, Ce, Nd or Sm). *Mineralogical Journal* **19** 123–130

Hirsch, A., Kegler, P., Alencar, I., Ruiz-Fuertes, J., Shelyug, A., Peters, L., Schreinemachers, C., Neumann, A., Neumeier, S., Liermann, H.-P., Navrotsky, A. and Roth, G. (2017). Structural, vibrational, and thermochemical properties of the monazite-type solid solution $La_{1-x}Pr_xPO_4$. *Journal of Solid State Chemistry* **245** 82–88

Hobart, D. E., Begun, G. M., Haire, R. G. and Hellwege, H. E. (1983). Raman-spectra of the Transplutonium Orthophosphates and Trimetaphosphates. *Journal of Raman Spectroscopy* **14** 59–62

Horchani-Naifer, K. and Férid, M. (2009). Crystal structure, energy band and optical characterizations of praseodymium monophosphate $PrPO_4$. *Inorganica Chimica Acta* **362** 1793 – 1796

Hou, Z. Y., Zhang, M. L., Wang, L. L., Lian, H. Z., Chai, R. T., Zhang, C. M., Cheng, Z. Y. and Lin, J. (2009). Preparation and luminescence properties of Ce^{3+} and/or Tb^{3+} doped $LaPO_4$ nanofibers and microbelts by electrospinning. *Journal of Solid State Chemistry* **182** 2332–2332

Huittinen, N., Arinicheva, Y., Kowalski, P., Vinograd, V., Neumeier, S. and Bosbach, D. (2017). Probing structural homogeneity of $La_{1-x}Gd_xPO_4$ monazite-type solid solutions by combined spectroscopic and computational studies. *Journal of Nuclear Materials* **486** 148 – 157

Hutton, C. (1951). Uranoan Thorite and Thorian Monazite from Blacksand Paystraks, San-Mateo County, California. In *Geological Society of America Bulletin*, volume 62, 1518–1519

International Atomic Energy Agency (IAEA) (2016). Nuclear Technology Review 2016. https://www.iaea.org/sites/default/files/16/08/ntr2016.pdf

Ishizawa, N., Miyata, T., Minato, I., Marumo, F. and Iwai, S. (1980). A structural investigation of α-Al_2O_3 at 2170 K. *Acta Crystallographica Section B: Structural Crystallography and Crystal Chemistry* **36** 228–230

Jarosewich, E. and Boatner, L. (1991). Rare-earth element reference samples for electron microprobe analysis. *Geostandards Newsletter* **15** 397–399

Jiang, X., Zhao, J. and Jiang, X. (2011). Correlation between hardness and elastic moduli of the covalent crystals. *Computational Materials Science* **50** 2287 – 2290

Jones, W. J. (1963). The infra-red spectra of simple molecules. In *Infra-red spectroscopy and molecular structure* (Ed. M. Davies). Elevier Publishing Company, Amsterdam, London, New York

Justice, B. H. and Westrum Jr., E. F. (1963). Thermophysical properties of the lanthanide oxides. I. Heat capacities, tthermodynamic properties, and some energy levels of lanthanum(III) and neodymium(III) oxides from 5 to 350 K. *Journal of Physical Chemistry* **67** 339–345

Karkhanavala, M. (1956). The synthesis of huttonite and monazite. *Current Science (India)* **25** 166–167

Kato, T. (1958). A study on monazite from the Ebisu mine, Gifu prefecture. *Mineralogical Journal* **2** 224–235

Keck, P. H. and Golay, M. J. E. (1953). Crystallization of silicon from a floating liquid zone. *Physical Review* **89** 1297–1297

Keller, C. (1963). Untersuchungen über die Germanate und Silikate des Typs ABO_4 der vierwertigen Elemente Thorium bis Americium. *Nukleonik* **5** 41–48

Kelly, K., Beall, G., Young, J. and Boatner, L. (1981). Valence states of actinides in synthetic monazites. In *The scientific basis for nuclear waste management* (Ed. J. Moore), volume 3., 189–195. Plenum Press, New York

Kingery, W., Bowen, H. and Uhlmann, D. (1976). *Introduction to ceramics*. John Wiley & Sons, New York

Kitaev, D., Volkov, Y. and Orlova, A. (2004). Orthophosphates of tetravalent Ce, Th, U, Np, and Pu with the monazite structure. *Radiochemistry* **46** 211–217

Kitamura, N., Amezawa, K., Tomii, Y., Yamamoto, N. and Hanada, T. (2004). Protonic conduction in Sr-doped $(La_{1-x}Sm_x)PO_4$). *Solid State Ionics* **175** 563 – 567

Kitamura, N., Amezawa, K., Uchimoto, Y., Tomii, Y., Hanada, T. and Yamamoto, N. (2006). Electrical conduction properties of rare earth orthophosphates under reducing conditions. *Solid State Ionics* **177** 2369–2373

Kleykamp, H. (1985). The chemical state of the fission products in oxide fuels. *Journal of Nuclear Materials* **131** 221–246

Klotz, S., Chervin, J., Munsch, P. and Le Marchand, G. (2009). Hydrostatic limits of 11 pressure transmitting media. *Journal of Physics D: Applied Physics* **42** 075413

Kolitsch, U. and Holtstam, D. (2004). Crystal chemistry of $REEXO_4$ compounds (X = P, As, V). II. Review of $REEXO_4$ compounds and their stability fields. *European Journal of Mineralogy* **16** 117–126

Kowalski, P. M., Beridze, G., Vinograd, V. L. and Bosbach, D. (2015). Heat capacities of lanthanide and actinide monazite-type ceramics. *Journal of Nuclear Materials* **464** 147–154

Kowalski, P. M. and Li, Y. (2016). Relationship between the thermodynamic excess properties of mixing and the elastic moduli in the monazite-type ceramics. *Journal of the European Ceramic Society* **36** 2093–2096

Krishnan, R., Srinivasan, R. and Devanarayanan, S. (1979). *Thermal Expansion of Crystals*, volume 12 of *International Series in the Science of the solid state*. Pergamon Press Ltd., Oxford, UK

Kropiwnicka, J. and Znamierowska, T. (1988). Phase equilibria in the system La_2O_3-Na_2O-P_2O_5. I. side system La_2O_3-P_2O_5. *Polish Journal of Chemistry* **62** 587–594

Kuleci, Z. (2015). *Master thesis: Synthese und Charakterisierung von Monazit-Typ Mischkristallen im System Nd_2O_3 - Sm_2O_3 - P_2O_5*. RWTH Aachen University

Lacomba-Perales, R., Errandonea, D., Meng, Y. and Bettinelli, M. (2010). High-pressure stability and compressibility of APO$_4$ (A= La, Nd, Eu, Gd, Er, and Y) orthophosphates: An X-ray diffraction study using synchrotron radiation. *Physical Review B* **81** 064113

Ladenthin, N. (2017). *Bachelor thesis: Synthese und Charakterisierung von Monazit-Typ-Mischkristallen im System (Sm,Gd)PO_4*

Lashley, J., Hundley, M., Migliori, A., Sarrao, J., Pagliuso, P., Darling, T., Jaime, M., Cooley, J., Hults, W., Morales, L., Thoma, D., Smith, J., Boerio-Goates, J., Woodfield, B., Stewart, G., Fisher, R. and Phillips, N. (2003). Critical examination of heat capacity measurements made on a Quantum Design physical property measurement system. *Cryogenics* **43** 369 – 378

Leonardos, O. (1974). Origin and provenance of fossil and recent monazite deposits in Brazil. *Economic Geology* **69** 1126–1128

Levine, B. (1973). Bond susceptibilities and ionicities in complex crystal structures. *The Journal of Chemical Physics* **59** 1463–1486

Levy, M., Bass, H., Stern, R., Furr, L. and Keppens, V. (2001). *Handbook of Elastic Properties of Solids, Liquids, and Gases: Elastic Properties of Solids: Biological and Organic Materials, Earth and Marine Sciences. Volume III*. Academic Press, Oxford

Li, H., Zhang, S., Zhou, S. and Cao, X. (2009). Bonding Characteristics, Thermal Expansibility, and Compressibility of RXO_4 (R = Rare Earths, X = P, As) within Monazite and Zircon Structures. *Inorganic Chemistry* **48** 4542–4548

Lucas, S., Champion, E., Bernache-Assollant, D. and Leroy, G. (2004a). Rare earth phosphate powders RePO$_4$ · nH$_2$O (Re=La, Ce or Y) II. Thermal behavior. *Journal of Solid State Chemistry* **177** 1312 – 1320

Lucas, S., Champion, E., Bregiroux, D., Bernache-Assollant, D. and Audubert, F. (2004b). Rare earth phosphate powders RePO$_4$ · nH$_2$O (Re= La, Ce or Y) - Part I. Synthesis and characterization. *Journal of Solid State Chemistry* **177** 1302–1311

Lucas, S., Champion, E., Penot, C., Leroy, G. and Bernache-Assollant, D. (2002). Synthesis and characterization of rare earth phosphate powders. In *Key Engineering Materials*, volume 206, 47–50. Trans Tech Publications, Switzerland

Lumpkin, G. R. (2006). Ceramic waste forms for actinides. *Elements* **2** 365–372

Mao, H., Xu, J.-A. and Bell, P. (1986). Calibration of the ruby pressure gauge to 800 kbar under quasi-hydrostatic conditions. *Journal of Geophysical Research: Solid Earth* **91** 4673–4676

Marples, J. A. C. (1988). The preparation, properties, and disposal of vitrified high level waste from nuclear fuel reprocessing. *Glass technology, Society of Glass Technology* **29** 230–247

Masui, T., Tategaki, H., Furukawa, S. and Imanaka, N. (2004). Synthesis and characterization of new environmentally-friendly pigments based on cerium phosphate. *Journal of the Ceramic Society of Japan* **112** 646–649

McCarthy, G. J. (1977). High-level waste ceramics: Materials considerations, process simulation, and product characterization. *Nuclear Technology* **32** 92–105

McCarthy, G. J., White, W. B. and Pfoertsch, D. E. (1978a). Synthesis of Nuclear Waste Monazites, Ideal Actinide Hosts For Geologic Disposal. *Materials Research Bulletin* **13** 1239–1245

McCarthy, G. J., White, W. B., Roy, R., Scheetz, B. E., Komarneni, S., Smith, D. K. and Roy, D. M. (1978b). Interactions Between Nuclear Waste and Surrounding Rock. *Nature* **273** 216–217

Meldrum, A., Boatner, L. A. and Ewing, R. C. (1997a). Displacive radiation effects in the monazite- and zircon-structure orthophosphates. *Physical Review B* **56** 13805–13814

Meldrum, A., Boatner, L. A. and Ewing, R. C. (1997b). Electron-irradiation-induced nucleation and growth in amorphous $LaPO_4$, $ScPO_4$, and zircon. *Journal of Materials Research* **12** 1816–1827

Meldrum, A., Boatner, L. A. and Ewing, R. C. (2000). A comparison of radiation effects in crystalline ABO_4-type phosphates and silicates. *Mineralogical Magazine* **64** 185–194

Meldrum, A., Boatner, L. A., Weber, W. J. and Ewing, R. C. (1998). Radiation damage in zircon and monazite. *Geochimica Et Cosmochimica Acta* **62** 2509–2520

Meldrum, A., Wang, L. M. and Ewing, R. C. (1996). Ion beam induced amorphization of monazite. *Nuclear Instruments and Methods in Physics Research Section B: Beam Interactions With Materials and Atoms* **116** 220–224

Meldrum, A., Zinkle, S. J., Boatner, L. A. and Ewing, R. C. (1999). Heavy-ion irradiation effects in the ABO_4 orthosilicates: Decomposition, amorphization, and recrystallization. *Physical Review B* **59** 3981–3992

Men, D., Patel, M. K., Usov, I. O., Toiammou, M., Monnet, I., Pivin, J. C., Porter, J. R. and Mecartney, M. L. (2013). Radiation damage in multiphase ceramics. *Journal of Nuclear Materials* **443** 120 – 127

Meyssamy, H., Riwotzki, K., Kornowski, A., Naused, S. and Haase, M. (1999). Wet-chemical synthesis of doped colloidal nanomaterials: Particles and fibers of $LaPO_4$:Eu, $LaPO_4$:Ce, and $LaPO_4$:Ce,Tb. *Advanced Materials* **11** 840–844

Milligan, W., Mullica, D., Beall, G. and Boatner, L. (1982). Structural investigations of YPO_4, $ScPO_4$, and $LuPO_4$. *Inorganica Chimica Acta* **60** 39 – 43

Milligan, W., Mullica, D., Beall, G. and Boatner, L. (1983a). Structures of $ErPO_4$, $TmPO_4$, and $YbPO_4$. *Acta Crystallographica Section C: Crystal Structure Communications* **39** 23–24

Milligan, W., Mullica, D., Beall, G. and Boatner, L. (1983b). The structures of three lanthanide orthophosphates. *Inorganica Chimica Acta* **70** 133 – 136

Mitchell, R. (1965). Rhabdopahne from Champion Pegmatite Amelia County Virginia. *American Mineralogist* **50** 231

Mogilevsky, P., Boakye, E. E. and Hay, R. S. (2007). Solid Solubility and Thermal Expansion in a $LaPO_4$–YPO_4 System. *Journal of the American Ceramic Society* **90** 1899–1907

Montel, J.-M., Glorieux, B., Seydoux-Guillaume, A.-M. and Wirth, R. (2006). Synthesis and sintering of a monazite-brabantite solid solution ceramic for nuclear waste storage. *Journal of Physics and Chemistry of Solids* **67** 2489–2500

Mooney, R. C. (1948). Crystal structures of a series of rare earth phosphates. *Journal of Chemical Physics* **16** 1003–1003

Morgan, P. E. D. and Marshall, D. B. (1995). Ceramic composites of monazite and alumina. *Journal of the American Ceramic Society* **78** 1553–1563

Muller, I., Weber, W. J., Vance, E., Wicks, G. and Karraker, D. (2002). *Advances in plutonium chemistry: 1967-2000*, chapter Glass, ceramics, and composites, 260–297. American Nuclear Society, La Grange Park, IL, USA

Mullica, D. F., Grossie, D. A. and Boatner, L. A. (1985a). Coordination Geometry and Structural Determinations of $SmPO_4$, $EuPO_4$ and $GdPO_4$. *Inorganica Chimica Acta* **109** 105–110

Mullica, D. F., Grossie, D. A. and Boatner, L. A. (1985b). Structural Refinements of Praseodymium and Neodymium Orthophosphate. *Journal of Solid State Chemistry* **58** 71–77

Mullica, D. F., Lok, C. K. C. and Grossie, D. A. (1986). A new nine-coordination system: Pentagonal interpenetrating tetrahedral polyhedron. *Journal of Solid State Chemistry* **63** 452 – 454

Mullica, D. F., Milligan, W. O., Grossie, D. A., Beall, G. W. and Boatner, L. A. (1984). Nine-fold coordination $LaPO_4$: Pentagonal interpenetrating tetrahedral polyhedron. *Inorganica Chimica Acta* **95** 231 – 236

Mullica, D. F., Sappenfield, E. L. and Boatner, L. A. (1990). A structural investigation of several mixed lanthanide orthophosphates. *Inorganica Chimica Acta* **174** 155 – 159

Mulliken, R. S. (1955). Report on notation for the spectra of polyatomic molecules. *The Journal of Chemical Physics* **23** 1997–2011

Myasoedov, B., Kirby, H. and Tananaev, I. (2010). *The Chemistry of the Actinide and Transactinide Elements: Volumes 1-6*, Volume 2, Chapter Proactinium, 699–1397. Springer Science & Business Media, Berlin, Heidelberg

Navrotsky, A. (1977). Progress and new directions in high temperature calorimetry. *Physics and Chemistry of Minerals* **2** 89–104

Navrotsky, A. (1997). Progress and new directions in high temperature calorimetry revisited. *Physics and Chemistry of Minerals* **24** 222–241

Navrotsky, A. (2014). Progress and new directions in calorimetry: A 2014 perspective. *Journal of the American Ceramic Society* **97** 3349–3359

Neumeier, S., Kegler, P., Arinicheva, Y., Shelyug, A., Kowalski, P. M., Schreinemachers, C., Navrotsky, A. and Bosbach, D. (2017). Thermochemistry of $La_{1-x}Ln_xPO_4$-monazites (Ln = Gd, Eu). *The Journal of Chemical Thermodynamics* **105** 396–403

Ni, Y. X., Hughes, J. M. and Mariano, A. N. (1995). Crystal-chemistry of the Monazite and Xenotime Structures. *American Mineralogist* **80** 21–26

Nuñez, N. O., Liviano, S. R. and Ocaña, M. (2010). Citrate mediated synthesis of uniform monazite $Ln PO_4$ (Ln= La, Ce) and Ln: $LaPO_4$ (Ln= Eu, Ce, Ce+Tb) spheres and their photoluminescence. *Journal of colloid and interface science* **349** 484–491

Oelkers, E. and Montel, J. (2008). Phosphates and nuclear waste storage. *Elements* **4** 113–116

OriginLab (n.d.). *Origin*. OriginLab, Nothampton, MA, USA

Oversby, V. M. (1994). *Materials Science and Technology: A Comprehensive Treatment*, volume 10B, chapter Nuclear waste materials, 391 –442. VCH Verlagsgesellschaft mbH, Wiley Online Library, New York

Pamplin, B. R. (1980). *Crystal growth*, volume 6 of *International Series of Monographs in the Solid State*. Pergamon Press Ltd, Oxford, UK

Parker, J., Feldman, D. and Ashkin, M. (1967). Raman scattering by silicon and germanium. *Physical Review* **155** 712–714

Peiffert, C., Brouand, M., Cuney, M. and Podor, R. (1996). La monazite: De l'indicateur de „fertilité“ des granites pour les gîtes d'uranium à la matrice de stockage. In *Rapport Sientifique*. CEA Centre d'Etudes Nucleaires de Saclay

Perriere, L., Bregiroux, D., Naitali, B., Audubert, E., Champion, E., Smith, D. S. and Bernache-Assollant, D. (2007). Microstructural dependence of the thermal and mechanical properties of monazite $Ln PO_4$ (Ln = La to Gd). *Journal of the European Ceramic Society* **27** 3207–3213

Petek, M., Abraham, M. M. and Boatner, L. A. (1981). Lanthanide orthophosphates as a matrix for solidified radioactive defense and reactor wastes. In *Symposium D – Scientific Basis for Nuclear Waste Management IV*, volume 6 of *MRS Proceedings*

Petříček, V., Dušek, M. and Palatinus, L. (2008). Jana2006 (version 03/11/2014). Institute of Physics, Academy of Sciences of the Czech Republic, Praha; http://jana.fzu.cz/

Phillips, J. (1970). Ionicity of the chemical bond in crystals. *Reviews of Modern Physics* **42** 317

Podor, R. (1995). Raman spectra of the actinide-bearing monazites. *European Journal of Mineralogy* **7** 1353–1360

Poitrasson, F., Oelkers, E., Schott, J. and Montel, J.-M. (2004). Experimental determination of synthetic $NdPO_4$ monazite end-member solubility in water from 21°C to 300°C: Implications for rare earth element mobility in crustal fluids. *Geochimica et Cosmochimica Acta* **68** 2207 – 2221

Popa, K., Konings, R. J. M. and Geisler, T. (2007). High-temperature calorimetry of $(La_{1-x}Ln_x)PO_4$ solid solutions. *Journal of Chemical Thermodynamics* **39** 236–239

Pugh, S. (1954). XCII. Relations between the elastic moduli and the plastic properties of polycrystalline pure metals. *The London, Edinburgh, and Dublin Philosophical Magazine and Journal of Science* **45** 823–843

Raison, P. E., Jardin, R., Bouexiere, D., Konings, R. J. M., Geisler, T., Pavel, C. C., Rebizant, J. and Popa, K. (2008). Structural investigation of the synthetic $CaAn(PO_4)_2$ (An = Th and Np) cheralite-like phosphates. *Physics and Chemistry of Minerals* **35** 603–609

Rajesh, K., Mukundan, P., Pillai, P. K., Nair, V. and Warrier, K. (2004). High-surface-area nanocrystalline cerium phosphate through aqueous sol-gel route. *Chemistry of materials* **16** 2700–2705

Rapp, R. P. and Watson, E. B. (1986). Monazite solubility and dissolution kinetics: Implications for the thorium and light rare earth chemistry of felsic magmas. *Contributions to Mineralogy and Petrology* **94** 304–316

Rappaz, M., Abraham, M. M., Ramey, J. O. and Boatner, L. A. (1981). Electron-paramagnetic-res Spectroscopic Characterization of Gd^{3+} in the Monazite-type Rare-earth Ortho-phosphates - $LaPO_4$, $CePO_4$, $PrPO_4$, $NdPO_4$, $SmPO_4$, and $EuPO_4$. *Physical Review B* **23** 1012–1030

Rappaz, M., Boatner, L. and Abraham, M. (1980). EPR investigations of Gd^{3+} in single crystals and powders of the zircon–structure orthophosphates YPO_4, $ScPO_4$, and $LuPO_4$. *The Journal of Chemical Physics* **73** 1095–1103

Rasband, W. (1997-2016). ImageJ. U. S. National Institutes of Health, Bethesda, Maryland, USA; https://imagej.nih.gov/ij/

Renner, B. and Lehmann, G. (1986). Correlation of angular and bond length distortions in TO_4 units in crystals. *Zeitschrift für Kristallographie-Crystalline Materials* **175** 43–60

Rietveld, H. M. (1967). Line profiles of neutron powder-diffraction peaks for structure refinement. *Acta Crystallographica* **22** 151–152

Ringwood, A. E., Kesson, S. E., Ware, N. G., Hibberson, W. and Major, A. (1979a). Immobilisation of high level nuclear reactor wastes in SYNROC. *Nature* **278** 219–223

Ringwood, A. E., Kesson, S. E., Ware, N. G., Hibberson, W. O. and Major, A. (1979b). The SYNROC process: A geochemical approach to nuclear waste immobilization. *Geochemical Journal* **13** 141–165

Robie, R., Hemingway, B. and Fisher, J. (1979). Thermodynamic properties of minerals and related substances at 298.15 K and 1 bar (10^5 Pa) pressure and at higher temperatures. *U.S. Geolical Survey Bulletin* **1452** 456

Robinson, K., Gibbs, G. V. and Ribbe, P. H. (1971). Quadratic elongation: A quantitative measure of distortion in coordination polyhedra. *Science* **172** 567–570

Röhlig, K.-J., Geckeis, H. and Mengel, K. (2012). Endlagerung radioaktiver Abfälle. *Chemie in unserer Zeit* **46** 140–149

Rothkirch, A., Gatta, G. D., Meyer, M., Merkel, S., Merlini, M. and Liermann, H.-P. (2013). Single-crystal diffraction at the Extreme Conditions Beamline P02. 2: Procedure for collecting and analyzing high-pressure single-crystal data. *Journal of synchrotron radiation* **20** 711–720

Rouxel, T. (2007). Elastic properties and short-to medium-range order in glasses. *Journal of the American Ceramic Society* **90** 3019–3039

Roy, R. (1982). *Radioactive Waste Disposal: The waste package*, Volume 1. Pergamon Press Ltd, Oxford, UK

Ruiz-Fuertes, J., Hirsch, A., Friedrich, A., Winkler, B., Bayarjargal, L., Morgenroth, W., Peters, L., Roth, G. and Milman, V. (2016). High-pressure phase of $LaPO_4$ studied by X-ray diffraction and second harmonic generation. *Physical Review B* **94** 134109

Ruschel, K., Nasdala, L., Kronz, A., Hanchar, J. M., Többens, D. M., Skoda, R., Finger, F. and Moller, A. (2012). A Raman spectroscopic study on the structural disorder of monazite-(Ce). *Mineralogy and Petrology* **105** 41–55

Sales, B. C., White, C. W. and Boatner, L. A. (1983). A Comparison of the Corrosion Characteristics of Synthetic Monazite and Borosilicate Glass Containing Simulated Nuclear Defense Waste. *Nuclear and Chemical Waste Management* **4** 281–289

Santamaría-Pérez, D., Gracia, L., Garbarino, G., Beltrán, A., Chulia-Jordan, R., Gomis, O., Errandonea, D., Ferrer-Roca, C., Martínez-García, D. and Segura, A. (2011). High-pressure study of the behavior of mineral barite by X-ray diffraction. *Physical Review B* **84** 054102

Santos, C., Silva, E., Ayala, A., Guedes, I., Pizani, P., Loong, C.-K. and Boatner, L. A. (2007). Raman investigations of rare earth orthovanadates. *Journal of Applied Physics* **101** 053511

Schärer, U. and Deutsch, A. (1990). Isotope systematics and shock-wave metamorphism: II. U-Pb and Rb-Sr in naturally shocked rocks; the Haughton Impact Structure, Canada. *Geochimica et Cosmochimica Acta* **54** 3435 – 3447

Schildknecht, H. (1964). *Zonenschmelzen.* Number 75 in Monographien zu „Angewandte Chemie“ und „Chemie-Ingenieur-Technik“. Verlag Chemie GmbH, Weinheim/Bergstraße

Schlenz, H., Heuser, J., Neumann, A., Schmitz, S. and Bosbach, D. (2013). Monazite as a suitable actinide waste form. *Zeitschrift für Kristallographie* **228** 113–123

Schlenz, H., Neumeier, S., Hirsch, A., Peters, L. and Roth, G. (2017). Submitted: Phosphates as safe containers for radionuclides. In *Highlights in Applied Mineralogy* (Eds. S. Heuss-Aßbichler, G. Amthauer and M. John). De Gruyter, Berlin

Schottky, W. (1922). Über die Drehung von Atomachsen in festen Körpern. (Mit magnetischen, thermischen und chemischen Beziehungen). *Physikalsiche Zeitschrift* **23** 448–455

Schumacher, A. (2016). *Bachelor thesis: Synthese und Charakterisierung der Monazit-Typ-Orthophosphate (Nd,Eu)PO_4*. RWTH Aachen University

Scott, H. (1983). The estimation of standard deviations in powder diffraction Rietveld refinements. *Journal of Applied Crystallography* **16** 159–163

Seydoux-Guillaume, A.-M., Montel, J.-M., Bingen, B., Bosse, V., Parseval, P., Paquette, J.-L., Janots, E. and Wirth, R. (2012). Low-temperature alteration of monazite: Fluid mediated coupled dissolution-precipitation, irradiation damage, and disturbance of the U–Pb and Th–Pb chronometers. *Chemical Geology* **330–331** 140–158

Seydoux-Guillaume, A.-M., Wirth, R., Deutsch, A. and Schärer, U. (2004). Microstructure of 24–1928 Ma concordant monazites; implications for geochronology and nuclear waste deposits. *Geochimica et Cosmochimica Acta* **68** 2517–2527

Seydoux-Guillaume, A. M., Wirth, R., Nasdala, L., Gottschalk, M., Montel, J. M. and Heinrich, W. (2002). An XRD, TEM and Raman study of experimentally annealed natural monazite. *Physics and Chemistry of Minerals* **29** 240–253

Shannon, R. D. (1976). Revised effective ionic radii and systematic studies of interatomic distances in halides and chalcogenides. *Acta Crystallographica Section A* **32** 751–767

Sheldrick, G. M. (2008). A short history of SHELX. *Acta Crystallographica Section A: Foundations of Crystallography* **64** 112–122

Sheldrick, G. M. (2015). Crystal structure refinement with SHELXL. *Acta Crystallographica Section C: Structural Chemistry* **71** 3–8

Silva, E. N., Ayala, A. P., Guedes, I., Paschoal, C. W. A., Moreira, R. L., Loong, C. . K. and Boatner, L. A. (2006). Vibrational spectra of monazite-type rare-earth orthophosphates. *Optical Materials* **29** 224–230

Smith, S. and Wanklyn, B. (1974). Flux growth of rare earth vanadates and phosphates. *Journal of Crystal Growth* **21** 23 – 28

Sokólska, I., Gołb, S., Bałuka, M. and Ryba-Romanowski, W. (2000). Quenching of Pr^{3+} emission in single crystals of $K_5Pr_xLa_{1-x}Li_2F_{10}$. *Journal of Luminescence* **91** 79 – 86

Solozhenko, V. L., Kurakevych, O. O., Andrault, D., Le Godec, Y. and Mezouar, M. (2009). Ultimate metastable solubility of boron in diamond: Synthesis of superhard diamond-like BC5. *Physical review letters* **102** 015506

Stang, A. H., Greenspan, M. and Newman, S. B. (1946). Poisson's ratio of some structural alloys for large strains. *Journal of Research of the National Bureau of Standards* **37** 211–221

Stefanovsky, S., Yudintsev, S., Gieré, R. and Lumpkin, G. (2004). Nuclear waste forms. In *Geological Society Special Publications, 236.: Energy, Waste, and the Environment: A Geochemical Perspective* (Eds. R. Gieré and P. Stille), 37–63. Geological Society, London.

Stoe & Cie GmbH (2012). X-red32 (version 1.58). *Stoe & Cie, Darmstadt, Germany*

Stoe & Cie GmbH (2013). X-area (version 1.68). *Stoe & Cie, Darmstadt, Germany*

Terra, O., Clavier, N., Dacheux, N. and Podor, R. (2003). Preparation and characterization of lanthanum-gadolinium monazites as ceramics for radioactive waste storage. *New Journal of Chemistry* **27** 957–967

Terra, O., Dacheux, N., Audubert, F. and Podor, R. (2006). Immobilization of tetravalent actinides in phosphate ceramics. *Journal of Nuclear Materials* **352** 224–232

Terra, O., Dacheux, N., Clavier, N., Podor, R. and Audubert, F. (2008). Preparation of Optimized Uranium and Thorium Bearing Brabantite or Monazite/Brabantite Solid Solutions. *Journal of the American Ceramic Society* **91** 3673–3682

Theuerer, H. (1962). Method of processing semiconductive materials. U.S.Patent 3060123. *Trans. Am. Inst. Mining Met Engrs.* **206** 1316

Thiriet, C., Konings, R., Javorsky, P., Magnani, N. and Wastin, F. (2005). The low temperature heat capacity of $LaPO_4$ and $GdPO_4$, the thermodynamic functions of the monazite-type $Ln PO_4$ series. *Journal of Chemical Thermodynamics* **37** 131–139

Thompson, P., Cox, D. E. and Hastings, J. B. (1987). Rietveld refinement of Debye–Scherrer synchrotron X-ray data from Al_2O_3. *Journal of Applied Crystallography* **20** 79–83

Thust, A., Arinicheva, Y., Haussühl, E., Ruiz-Fuertes, J., Bayarjargal, L., Vogel, S. C., Neumeier, S. and Winkler, B. (2015). Physical Properties of $La_{1-x}Eu_xPO_4$, $0 \leq x \leq 1$, Monazite-Type Ceramics. *Journal of the American Ceramic Society* **98** 4016–4021

Thust, A., Hirsch, A., Haussühl, E., Schrodt, N., Loison, L., Schott, P., Peters, L., Roth, G. and Winkler, B. (2017). Physical properties and microstructures of $La_{1-x}Pr_xPO_4$ monazite-ceramics. *Physics and Chemistry of Minerals* 1–10

Trachenko, K. (2004). Understanding resistance to amorphization by radiation damage. *Journal of Physics: Condensed Matter* **16** R1491

Ushakov, S. V., Helean, K. B., Navrotsky, A. and Boatner, L. A. (2001). Thermochemistry of rare-earth orthophosphates. *Journal of Materials Research* **16** 2623–2633

Van Emden, B., Thornber, M. R., Graham, J. and Lincoln, F. (1996). Solid solution behaviour of synthetic monazite and xenotime from structure refinement of powder data. In *Advances in X-ray Analysis–the Proceedings of the 45th X-ray Conferences, Denver, Colorado, USA*, 2–15

Vepřek, S. (1999). The search for novel, superhard materials. *Journal of Vacuum Science & Technology A: Vacuum, Surfaces, and Films* **17** 2401–2420

Wang, J., Zhou, Y. and Lin, Z. (2005). First-principles elastic stiffness of $LaPO_4$ monazite. *Applied Physics Letters* **87** 051902

Wang, X., Teng, Y., Huang, Y., Wu, L. and Zeng, P. (2014). Synthesis and structure of $Ce_{1-x}Eu_xPO_4$ solid solutions for minor actinides immobilization. *Journal of Nuclear Materials* **451** 147–152

Wanklyn, B. (1972). Flux growth of some complex oxide materials. *Journal of Materials Science* **7** 813–821

Wanklyn, B. (1977). The prediction of starting compositions for the flux growth of complex oxide crystals. *Journal of Crystal Growth* **37** 334–342

Wanklyn, B. (1978). Effects of modifying starting compositions for flux growth. *Journal of Crystal Growth* **43** 336–344

Wanklyn, B. (1983). The present status of flux growth. *Journal of Crystal Growth* **65** 533–540

Waseda, Y., Hirata, K. and Ohtani, M. (1975). High-temperature thermal expansion of platinum, tantalum, molybdenum, and tungsten measured by X-ray diffraction. *High Temperature High Pressure* **7** 221–226

Weber, W. J., Navrotsky, A., Stefanovsky, S., Vance, E. R. and Vernaz, E. (2009). Materials Science of High-Level Nuclear Waste Immobilization. *MRS Bulletin* **34** 46–53

Weigelt, S. (2011). *Bachelor thesis: Synthese und Charakterisierung von Seltenerd-Phosphaten und -Phosphosilikaten mit Monazit-Struktur als Speichermedium zur Immobilisierung von Actinoiden*. RWTH Aachen University

Westrum, E. F. (1985). Schottky contributions in chemical thermodynamics. *Journal of thermal analysis* **30** 1209–1215

Westrum Jr., E. F. (1983). Lattice and Schottky contributions to the morphology of lanthanide heat capacities. *Journal of Chemical Thermodynamics* **15** 305–325

Wickham, D. (1962). Use of lead pyrophosphate as a flux for crystal growth. *Journal of Applied Physics* **33** 3597–3598

Wicks, G. G. (1985). Nuclear waste glasses. In *Glass IV Treatise on Materials Science and Technology* (Eds. M. Tomozawa and R. H. Doremus), volume 26 of *Treatise on Materials Science & Technology*, 57 – 118. Elsevier, Amsterdam

Wicks, G. G. and Bickford, D. F. (1989). High level radioactive waste: Doing something about it. Technical report, Du Pont de Nemours (EI) and Co., Aiken, SC (USA). Savannah River Lab.

Wilke, K. T. (1963). *Methoden der Kristallzüchtung*. VEB Deutscher Verlag für Wissenschaft, Berlin

Wilke, K. T. and Bohm, J. (1988). *Kristallzüchtung*. VEB Deutscher Verlag für Wissenschaft, Berlin

Winkler, B. and Milman, V. (2014). Density functional theory based calculations for high pressure research. *Zeitschrift für Kristallographie–Crystalline Materials* **229** 112–122

Wurst, J. and Nelson, J. (1972). Lineal Intercept Technique for Measuring Grain Size in Two-Phase Polycrystalline Ceramics. *Journal of the American Ceramic Society* **55** 109–109

Yadawa, P., Singh, D., Pandey, D. and Yadav, R. (2009). Elastic and acoustic properties of heavy rare-earth metals. *Open Acoustics Journal* **2** 61–67

Yaiphaba, N., Ningthoujam, R., Singh, N. S., Vatsa, R. and Singh, N. R. (2010). Probing of inversion symmetry site in Eu^{3+}-doped $GdPO_4$ by luminescence study: Concentration and annealing effect. *Journal of Luminescence* **130** 174–180

Yan, B., Gu, J. and Xiao, X. (2010). $Ln PO_4$: RE^{3+} (Ln= La, Gd; RE= Eu, Tb) nanocrystals: solvo-thermal synthesis, microstructure and photoluminescence. *Journal of Nanoparticle Research* **12** 2145–2152

Yang, H., Teng, Y., Ren, X., Wu, L., Liu, H., Wang, S. and Xu, L. (2014). Synthesis and crystalline phase of monazite-type $Ce_{1-x}Gd_xPO_4$ solid solutions for immobilization of minor actinide curium. *Journal of Nuclear Materials* **444** 39–42

Yang, P., Quan, Z., Li, C., Hou, Z., Wang, W. and Lin, J. (2009). Solvothermal synthesis and luminescent properties of monodisperse $LaPO_4$:Ln (Ln=Eu^{3+}, Ce^{3+}, Tb^{3+}) particles. *Journal of Solid State Chemistry* **182** 1045 – 1054

Zaddach, J. (2013). *Master thesis: Synthese und Charakterisierung von Seltenerd-Erdalkali-Phosphosilikatphasen*. RWTH Aachen University

Zeng, P., Teng, Y., Huang, Y., Wu, L. and Wang, X. (2014). Synthesis, phase structure and microstructure of monazite-type $Ce_{1-x}Pr_xPO_4$ solid solutions for immobilization of minor actinide neptunium. *Journal of Nuclear Materials* **452** 407–413

Zhang, S., Li, H., Li, H., Zhou, S. and Cao, X. (2007a). Calculation of the bulk modulus of simple and complex crystals with the chemical bond method. *The Journal of Physical Chemistry B* **111** 1304–1309

Zhang, S., Li, H., Li, L. and Zhou, S. (2007b). Calculation of bulk modulus on carbon nitrides with chemical bond method. *Applied Physics Letters* **91** 1905

Zhang, Y.-W., Yan, Z.-G., You, L.-P., Si, R. and Yan, C.-H. (2003). General synthesis and characterization of monocrystalline lanthanide orthophosphate nanowires. *European Journal of Inorganic Chemistry* **2003** 4099–4104

Zhou, R.-S. and Snyder, R. L. (1991). Structures and transformation mechanisms of the η, γ and θ transition aluminas. *Acta Crystallographica Section B: Structural Science* **47** 617–630

List of Publications

H. Schlenz, S. Neumeier, A. Hirsch, L. Peters, G. Roth (2017) *Phosphates as safe containers for radionuclides* in *Highlights in Applied Mineralogy* (S. Heuss-Aßbichler, G. Amthauer, M. John (Ed.)), De Gruyter, Berlin (in press)

A. Thust, A. Hirsch, E. Haussühl, N. Schrodt, L. Loison, P. Schott, L. Peters, G. Roth, B. Winkler (2017). Physical properties and microstructures of $La_1 - xPr_xPO_4$ monazite-ceramics *Physics and Chemistry of Minerals* 1-10

A. Hirsch, P. Kegler, I. Alencar, J. Ruiz-Fuertes, L. Peters, C. Schreinemachers, A. Shelyug, A. Neumann, S. Neumeier, H.-P. Liermann, A. Navrotsky, G.Roth (2017). Structural, vibrational, and thermochemical properties of the monazite-type solid solution $La_{1-x}Pr_xPO_4$. *Journal of Solid State Chemistry* **245** 82-88

A. Hirsch, L. Peters, G. Roth (2016). Fachlicher Schlussbericht des BMBF Forschungsvorhabens "Verbundprojekt: Grundlegende Untersuchungen zur Immobilisierung langlebiger Radionuklide mittels Einbau in endlagerrelevante Keramiken (Conditioning)": Teilprojekt E.

J. Ruiz-Fuertes, A. Hirsch, A. Friedrich, B. Winkler, L. Bayarjargal, W. Morgenroth, L. Peters, G. Roth, V. Milman (2016). High-pressure phase of $LaPO_4$ studied by X-ray diffraction and second harmonic generation. *Physical Review B*, **94** 134109

J.D. Bauer, A. Hirsch, L. Bayarjargal, L. Peters, G. Roth, B. Winkler (2016). Schottky contribution to the heat capacity of monazite type (La,Pr)PO_4 from low temperature calorimetry and fluorescence measurements. *Chemical Physics Letters* **654** 97-102

Attended schools and conferences

Conferences

Talks

25. Jahrestagung der Deutschen Gesellschaft für Kristallographie (DGK), Karlsruhe, Germany, March 2017: A. Hirsch, P. Kegler, I. Alencar, J. Ruiz-Fuertes, A. Thust, J. Bauer, C. Schausten, L. Peters, G. Roth. *Synthesis and characterisation of monazite solid solution series.* Zeitschrift für Kristallographie. Supplement Volume 37

24. Jahrestagung der Deutschen Gesellschaft für Kristallographie (DGK), Stuttgart, Germany, March 2016: J. Ruiz-Fuertes, A. Hirsch, B. Winkler, A. Friedrich, L. Bayarjargal, W. Morgenroth, L. Peters, G. Roth. *Structural solution of the high-pressure phase of LaPO4.* Zeitschrift für Kristallographie, Supplement Volume 36

MRS - Scientific Basis for Nuclear Waste Management XXXIX, Montpellier, France, November 2015: A. Thust, A. Hirsch, E. Haussühl, Y. Arinicheva, M. Klinkenberg, S. Neumeier, G. Roth, B. Winkler. *Microstructural properties of monazite-type ceramics.*

MRS - Scientific Basis for Nuclear Waste Management XXXIX, Montpellier, France, November 2015: C. Schausten, A. Thust, A. Hirsch, Y. Arinicheva, A. Wätjen, A. Neumann, R. Telle). *Sintering behaviour and microstructure of rare earth phosphates $REPO_4$ (with RE = La, Ce, Pr).*

MRS - Scientific Basis for Nuclear Waste Management XXXIX, Montpellier, France, November 2015: A. Hirsch, A. Thust, I. Alencar, J. Ruiz-Fuertes, C. Schausten, L. Peters, G. Roth. *Structura, vibrational and thermochemical characterization of (La,Pr)PO_4 monazite.*

22. Jahrestagung der Deutschen Gesellschaft für Kristallographie (DGK), Berlin, Germany, March 2014: A. Hirsch, A. Neumann, A. Wätjen, J. Heuser, A. Thust, L.Peters, G. Roth. *Synthesis and characterisation of (La,Pr) monazite solid solution series.* Zeitschrift für Kristallographie, Supplement Volume 34.

Posters

25. Jahrestagung der Deutschen Gesellschaft für Kristallographie (DGK), Karlsruhe, Germany, March 2017: A. Hirsch, P. Kegler, I. Alencar, J. Ruiz-Fuertes, A. Thust, J. Bauer, C. Schausten, L. Peters, G. Roth. *Synthesis and characterisation of monazite solid solution series.* Zeitschrift für Kristallographie. Supplement Volume 37

24. Jahrestagung der Deutschen Gesellschaft für Kristallographie (DGK), Stuttgart, Germany, March 2016: J.D. Bauer, A. Hirsch, L. Bayarjargal, L. Peters, G. Roth, B. Winkler. *Schottky contribution to the heat capacity of monazite type (La,Pr)PO_4 from low temperature calorimetry and fluorescence measurements.* Zeitschrift für Kristallographie, Supplement Volume 36

European Materials Research Society (E-MRS) - Spring Meeting, Lille, France, May 2015: A. Neumann, L. Loison, J.M. Simons, F. Greffrath, C. Schausten, A. Hirsch, J. Heuser, L. Peters, R. Telle, G. Roth. *High temperature investigations of the phase relation in the binary system Sm_2O_3 - P_2O_5.*

23. Jahrestagung der Deutschen Gesellschaft für Kristallographie (DGK), Göttingen, Germany, March 2015: A. Hirsch, A. Neumann, C. Schausten, A. Thust, L. Peters, G. Roth. *(La,Pr)PO_4- A model system for ceramic radioactive waste matrices.* Zeitschrift für Kristallographie. Supplement Volume 35

23rd Congress and General Assembly of the International Union of Crystallography, Montreal, Canada, August 2014: A. Hirsch, A. Neumann, A. Wätjen, J. Heuser, A. Thust, L. Peters, G. Roth. *Synthesis and characterisation of (La,Pr) monazite solid solution series.* Acta Cryst. (2014). A70, C1106

8th European Summer School on Separation Chemistry and Conditioning as well as Supramolecular, Intermolecular, Interaggregate Interactions, Bonn, Germany, July 2014: A. Hirsch, L. Peters, G. Roth. *Optical Floating Zone Method vs. Accerlerated Crucible Rotation Technique - A comparison of two methods.*

24th Goldschmidt Conference, Sacramento, CA, USA, July 2014: A. Neumann, A. Hirsch, J. Heuser, P.C. Jung, J. Zaddach, S. Neumeier, H. Schlenz, D. Bosbach, L. Peters, G. Roth. *Phase relations of the solid solution Sm(Ca,Ce)PO_4 and La(Sr,Ce)PO_4.* http://goldschmidt.info/2014/uploads/abstracts/finalPDFs/1791.pdf

22. Jahrestagung der Deutschen Gesellschaft für Kristallographie (DGK),Berlin, Germany, March 2014: A. Neumann, A. Hirsch, R. Faust, H. Schlenz, D. Bosbach, L. Peters, G. Roth. *Phase relations in the binary system Sm_2O_3 - P_2O_5.* Zeitschrift für Kristallographie, Supplement Volume 34

22. Jahrestagung der Deutschen Gesellschaft für Kristallographie (DGK),Berlin, Germany, March 2014: A. Neumann, A. Hirsch, J. Heuser, P.C. Jung), J. Zad-

dach, S. Neumeier, H. Schlenz, D. Bosbach, L. Peters, G.Roth. *(La, Sr, Ce) and (Sm, Ca, Ce) Monazite Solid Solutions.* Zeitschrift für Kristallographie, Supplement Volume 34

23rd Goldschmidt Conference, Florenz, Italy, August 2013: J. Heuser, A. A. Bukaemskiy, S. Neumeier, F. Brandt, H. Schlenz, N. Dacheux, N. Clavier, A. Neumann, A. Hirsch, D. Bosbach. *Raman and IR spectroscopy of Monazite-type Ceramics used for Nuclear Waste Management.* Progress in Nuclear Energy 72 (2014) 149-155

Attended Schools

2nd Lab Meeting of the Young Crystallographers of the DGK, Darmstadt, Germany (2017)

JCNS Neutron Laboratory Course, Forschungszentrum Jülich und MLZ Garching, Germany (2015)

8th European Summer School on Separation Chemistry and Conditioning as well as Supramolecular, Intermolecular, Interaggregate Interactions, Bonn, Germany (2014)

Radiation damage in structures - Relevance for nuclear waste disposal, Hamburg, Germany (2014)

Powder Diffraction and Rietveld Refinement School 2014, Durham, UK (2014)